Isogeometric analysis and shape optimization in electromagnetism

Nguyen, Dang Manh

Publication date:
2012

Document Version
Publisher's PDF, also known as Version of record

TECHNICAL UNIVERSITY OF DENMARK

DEPARTMENT OF MATHEMATICS

Isogeometric Analysis and Shape Optimization in Electromagnetism

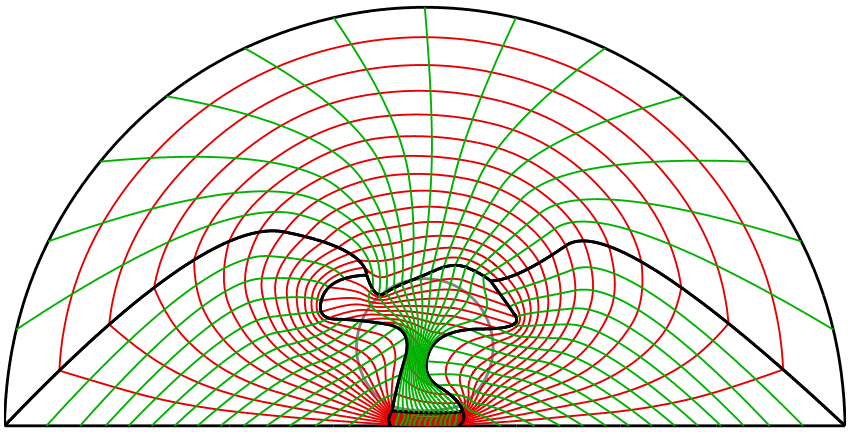

Ph.D. Thesis

Nguyen Dang Manh

February 2012

Isogeometric Analysis and Shape Optimization in Electromagnetism

Nguyen Dang Manh

Department of Mathematics

Technical University of Denmark

Title of Thesis:
Isogeometric Analysis and Shape Optimization in Electromagnetism

Ph.D. student:
Nguyen Dang Manh
Department of Mathematics
Technical University of Denmark
Address: Matematiktorvet, Building 303S, DK-2800 Lyngby, Denmark
E-mail: D.M.Nguyen@mat.dtu.dk

Supervisors:
Jens Gravesen
Department of Mathematics
Technical University of Denmark
Address: Matematiktorvet, Building 303S, DK-2800 Lyngby, Denmark
E-mail: J.Gravesen@mat.dtu.dk

Anton Evgrafov
Department of Mathematics
Technical University of Denmark
Address: Matematiktorvet, Building 303S, DK-2800 Lyngby, Denmark
E-mail: A.Evgrafov@mat.dtu.dk

Summary

In this thesis a recently proposed numerical method for solving partial differential equations, isogeometric analysis (IGA), is utilized for the purpose of shape optimization, with a particular emphasis on applications to two-dimensional design problems arising in electromagnetic applications. The study is motivated by the fact that in contrast with most commonly utilized finite element approximations, IGA allows one to exactly represent geometries arising in computer aided design applications with relatively few variables using splines.

The following problems coming from theoretical considerations or engineering applications are solved in the thesis utilizing IGA:

- finding a shape having a few prescribed eigenvalues of the Laplace operator;
- shape optimization of sub-wavelength micro-antennas for energy concentration;
- shape optimization of nano-antennas for field enhancement;
- economical design of magnetic density separators.

From the point of view of method development, several heuristic approaches for extending a valid parametrization of the boundary onto the domain's interior are examined in the thesis. The parametrization approaches and a method for validating a spline parametrization are combined into an iterative algorithm for shape optimization of two dimensional electromagnetic problems. The algorithm may also be relevant for problems in other engineering disciplines.

Using the methods developed in this thesis, remarkably we have obtained antennas that perform one million times better than an earlier topology optimization result. This shows a great potential of shape optimization using IGA in the area of electromagnetic antenna design in particular, and for electromagnetic problems in general. Our conclusion is that IGA is well suited for shape optimization.

Resumé (in Danish)

I denne afhandling bliver en ny numerisk metode til løsning af partielle differentialligninger, isogeometrisk analyse (IGA), benyttet til formoptimering, specielt med henblik på to-dimensionelle design problemer der optrder i elektromagnetiske anvendelser.

Studiet er motiveret af den kendsgerning, at i modstning til traditionelle finite elementer, tillader IGA ved brug af splines, at reprsenterer de geometrier, der optrder i "computer aided design" systemer eksakt og med relativ få variable.

De følgende problemer, der dels kommer fra teoretiske overvejelser og dels fra konkrete ingeniørvidenskabelige anvendelser, bliver i afhandlingen løst ved brug af IGA:

- bestem en form der har et lille antal givne værdier af Laplace operatoren;
- formoptimering af mikroantenner til energikoncentration på områder der er mindre end bølgelængden;
- formoptimering af nanoantenner til forstærkning af det elektromagnetisk felt;
- økonomisk design af magnetisk densitet separatorer.

Fra et metode udviklings synspunkt, bliver flere heuristiske fremgangsmåder til at udvide en parametrisering fra randen til det indre af et område undersøgt i denne afhandling.

Disse parametriserings metoder og en metode til sikring af gyldigheden en spline parametrisering bliver kombineret til en itterativ algoritme til formoptimering af to-dimensionele elektromagnetiske problemer. Algoritmen kan også være relevant i andre ingeniørvidenskabelige discipliner.

Blandt de nævnte problemer opnår vi bemærkelsesværdig nok, en antenne der er en million gange bedre end tidligere resultater af topologioptimering. Dette viser det store potentiale for brugen af IGA i formoptimering, af specielt antenner; men også indenfor generelle elektromagnetiske problemer. Vores konklusion er, at isogeometrisk analyse er særdeles velegnet til formoptimering.

Preface

This thesis is submitted in partial fulfillment of the requirements for obtaining the degree of Ph.D. at the Technical University of Denmark. The Ph.D. project was funded by the Technical University of Denmark and carried out at the Department of Mathematics during the period February 15$^{\text{th}}$ 2009 - February 14$^{\text{st}}$ 2012. Supervisors on the project were Associate Professor Jens Gravesen and Associate Professor Anton Evgrafov from the Department of Mathematics. During the first year of the study period, Allan Roulund Gersborg from the Department of Mechanical Engineering also acted as a supervisor for this project.

List of publications

The following research papers and manuscripts have been written during the three years of the Ph.D. study

1. Nguyen D. M., A. Evgrafov, A.R. Gersborg, J. Gravesen, Isogeometric shape optimization of vibrating membranes, *Computer Methods in Applied Mechanics and Engineering*, vol. 200, pp. 1343-1353, 2011.

2. J. Gravesen, A. Evgrafov, Nguyen D. M., On the sensitivities of multiple eigenvalues, *Structural and Multidisciplinary Optimization*, vol. 44, pp. 583-587, 2011.

3. Nguyen D. M., A. Evgrafov, J. Gravesen, Shape optimization of sub-wavelength antenna using isogeometric analysis, *International Journal for Numerical Methods in Engineering*, submitted, August, 2011.

4. Nguyen D. M., A. Evgrafov, J. Gravesen, D. Lahaye, Economical designs of magnetic density separators using isogeometric analysis and shape optimization, *Structural and Multidisciplinary Optimization*, in preparation, 2012.

Other publications by the author

1. Nguyen D. M., A. Evgrafov, J. Gravesen, J. S. Jensen, Isogeometric analysis toward shape optimization in electromagnetics, *Proceedings of NSCM-23: the* 23^{rd} *Nordic Seminar on Computational Mechanics*, A. Erikson and G. Tibert eds., pp. 18-21, 2010.

2. J. Gravesen, A. Evgrafov, A.R. Gersborg, Nguyen D.M., P. N. Nielsen, Isogeometric analysis and shape optimization, *Proceedings of NSCM-23: the* 23^{rd} *Nordic Seminar on Computational Mechanics*, A. Erikson and G. Tibert eds., pp. 14-17, 2010.

Acknowledgments

First of all, I would like to deliver my sincere thanks to my supervisors for leading me instructively to my present research field. In particular, I would like to express my deep gratitude to

Jens Gravesen for giving me the opportunity to develop my career at DTU and guiding me gradually to the world of splines, isogeometric analysis and shape optimization; from him I have learned, indeed, invaluable mathematical knowledge. Furthermore, I am grateful to Anton Evgrafov, who has always helped me a lot from a scientific issue to a matter of the real life, and with whom I alway enjoy every discussion. And, I would like to give special thanks to Allan R. Gersborg for conveying his enthusiasm to me and always looking after me even he has not working at DTU recently.

Moreover, I would like to sincerely thank Sergey I. Bozhevolnyi and Morten Willatzen, University of Southern Denmark, for teaching me further electromagnetic knowledge and encouraging me a lot during the working period on the nano-antenna problem. I truly want to continue our collaboration in future.

Next, I would like to gratefully thank Domenico Lahaye, Delft University of Technology, for his wonderful support to me during the time I visited the Delft University of Technology. Besides the scientific support in the magnetic density separator problem, I have also received invaluable helps from him in other matters, especially his introduction of me to several post-doc positions from his collaborators.

During the three years of my Ph.D. study, my work has been done with lots of helps from my colleagues. In particular, I would like to give many thanks to my officemate Peter N. Nielsen for helping me many times with his fluent or even expert knowledge of UNIX, FORTRAN, LATEX, English and for exchanging our daily stories. I would like to thank Vagn L. Hansen, Steen Markvorsen, Peter Røgen, David Brander, Martin Carlsen for helping me on many occasions and collaborating with me in teaching activities. I have received great helps from Poul-Erik Madsen with my constant use of the department's clusters. I would like to thank him a lot. Furthermore, I would like to thank Ole Christensen, Tom Høholdt, Peter Beelen, Ulla Louring, Wanja Andersen and Dorte Lundsgaard for making my administrative activities easier. And, my special thanks are given to all players of the department's indoor football group who have helped me to refresh my brain quickly.

I would like to thank all members of the TopOpt group for creating a scientifically and friendlily "optimized" atmosphere. I especially thank Ole Sigmund, Jakob S. Jensen and Mathias Stolpe for fruitful discussions on my antenna problem. In particular, I would like to thank Niels Aage, DTU-Mechanics, for helping me get acquainted with the antenna problem and for his effort on validating one of our resulting antennas with his code. Furthermore, I would like to thank Julia Borghoff and Oded Amir for assisting me with some latex data and techniques for me to write this thesis.

I would like to use this opportunity to say that I am grateful: to my high school advisor Vi Duc Cuong, High School of Bac Son, Lang Son; to my undergraduate advisor Tran Duc Long, Hanoi University of Science; to my graduate advisor Do Ngoc Diep, Institute of Mathematics, Vietnam, for building up the base for my future career.

Finally, I would like to send my deep gratitude: to my father Nguyen Dang Hieu, to my mother Le Thi Thiem and to my sister Nguyen Thi Hong for their lifetime supports to me; to Dinh Thi Thao for helping me overcome many stressful occasions with her love and her dream of a future happy family.

Kgs. Lyngby, February 2011

Nguyen Dang Manh

Contents

Notation and abbreviations

C^r : Continuously differentiable r times

$\mathbf{d}$: The vector that contains all coordinates of design control points

$\widehat{\mathbf{d}}$: The vector that contains all coordinates of the parametrization control points

$\mathrm{int}(\Omega)$: The interior of the domain Ω

$\mathbb{N}$: The set of natural numbers which does not contain 0

$\mathbb{N}_0$: The set of natural numbers which contains 0

$\mathbb{R}$: The set of real numbers

2D : 2-dimensional Euclidean space

3D : 3-dimensional Euclidean space

CAD : Computer-aided design

EM : Electromagnetic

FEA : Finite element analysis

FEM : Finite element method

FESO : Finite element method-based shape optimization

IGA : Isogeometric analysis

IBC : Impedance boundary condition

IGSO : Isogeometric shape optimization

MDS : Magnetic density separator

NURBS : Non-uniform rational B-splines

PDE : Partial differential equation

Introduction

This study was motivated by the recent development of isogeometric analysis (IGA, c.f. [1]), which is a new numerical method for numerically approximating solutions to PDEs proposed by T.J.R. Hughes, J.A. Cottrell, and Y. Bazilevs. Similarly to the traditional finite element method (FEM), the underlying principle of IGA is the use of the Galerkin method [2]. However, one of the advantages of IGA is its ability to represent exactly domains with a piecewise-NURBS boundary. Furthermore, in comparison with basis functions considered by the traditional FEM, the basis functions utilized in IGA may be easily constructed to have arbitrarily high smoothness, which for PDE problems with smooth solutions translates into improved accuracy per degree of freedom (dof) when compared with traditional FEM by the virtue of k-refinement in IGA, see [3, 4, 5]. Another advantage of IGA is the ability of representing very complicated shapes utilizing relatively few parameters (control points in the terminology of IGA). Furthermore, these shapes are piecewise smooth and may be relatively easily imported to a computer-aided design (CAD) system for manufacturing [6, 7]. Additionally, the direct involvement of CAD allows the utilization of well studied and powerful tools for regularizing the parametrization and the shapes under consideration [8, 9, 10]. This makes IGA a very promising tool for shape optimization. As a result, in recent years isogeometric analysis-based shape optimization (IGSO) has attained intensive developments and applications towards various engineering disciplines [11, 12, 13, 9, 14, 15, 16, 10].

However, the incorporation of IGA into shape optimization is not a trivial task due to the fact that the parametrization control points need to be determined as smooth functions of the design control points in such a way, that they form a valid parametrization of the physical domain, which is one of the main topics of this thesis. In previous works on this subject, the problem was somewhat avoided by introducing unnecessary restrictions on the variations of the shape under consideration. Several examples of such an approach include a circle of a varying radius [17, 18], a family of super-elliptical shapes [19, 20], or only small local variations of the boundary [21, 17, 11, 13]. In this thesis, we aim at enabling large variations of the shapes from the initial configuration while having shape optimization applications in mind. Several heuristic approaches for extending a valid parametrization of the boundary onto the domains interior are examined. While our approach requires certain restrictions on shape variations, it is a big improvement compared to the aforementioned works.

The parametrization approaches and a method for validating a spline parametrization are combined into an iterative algorithm for shape optimization of two dimensional electromagnetic problems. The developments are summarized as follows:

- A heuristic algorithm using two approaches, namely a spring model and a quasi-conformal deformation, for extending a parametrization onto the domains interior are examined in Chapter 3.

- An improved heuristic algorithm for the same purpose based on minimizing the quadratic approximation of Winslow functional is examined in Chapters 5 and 6.

- An iterative algorithm using a class of parametrization extension methods including the quasi-conformal deformation and the linearized Winslow functional is described in Chap-

ters 2 and 7. We recommend interested readers to use this algorithm if they are to choose between the listed options.

Structure of the thesis

This thesis is organized as follows

- *Part I*: In this part we present the necessary mathematical background for the rest of the thesis. In *Chapter 1* we recall some important properties of spline curves that are often utilized in the thesis. In *Chapter 2*, we outline our shape optimization algorithm.
- *Part II*: In this part we consider a model problem of shape optimization of vibrating membranes using IGA. On this model problem, we examine two numerical methods, a spring model and a quasi-conformal deformation, for extending a parametrization onto the domains interior. The examination is presented in *Chapter 3*. Some issues arising from the need for dealing with double eigenvalues are discussed in *Chapter 4*.
- *Part III*: In this part we consider the problem of designing the shapes of electromagnetic antennas toward different engineering applications, from micro-antennas for energy concentration presented in *Chapter 5* to nano-antennas for field enhancement presented in *Chapter 6*. In this part we also experiment with the use of a heuristic algorithm for shape optimization using IGA.
- *Part IV*: In this part we improve the efficiency of a device called a magnetic density separator. The IGA-based modeling of the device and an improved algorithm for performing shape optimization on the problem are presented in *Chapter 7*.

Part I

Isogeometric analysis and shape optimization

Chapter 1

Isogeometric analysis

Isogeometric analysis (IGA) has been recently introduced by Hughes et al. [6] and has already found many applications in a variety of engineering disciplines [7]. The original paper of IGA [6] and the textbook [7] are the recommended materials for readers who would like to study IGA. In this chapter, we rather focus on utilization of B-splines for IGA. To this end, let us first recall the concept of B-splines and their basic properties.

1.1 B-splines

In this section, we define B-splines via a recursive formula, which requires no advanced knowledge and is straightforward to implement. For further properties of B-splines, we recall polar forms of polynomials. The notation used in this section, e.g., p for the degree of a B-spline, $n+p+1$ for the number of knots in a knot vector, is borrowed from [6, 7]; in our experience, it simplifies the indexing process in the implementation of IGA. The main reference for the section is [22]; see also [23, 24].

1.1.1 Definition and basis properties

***Definition* 1.** A sequence of real numbers $\Xi = \{t_1, \ldots, t_{n+p+1}\}$ is called a *knot vector* if its elements form a monotonically non-decreasing sequence

$$t_1 \leq \ldots \leq t_{p+1} < t_{p+2} \leq \ldots \leq t_n < t_{n+1} \leq \ldots \leq t_{n+p+1}.$$

Each element of the knot vector is called a *knot*. A knot t_r is said to have *multiplicity* ν if $t_{r-1} < t_r = \ldots = t_{r+\nu-1} < t_{r+\nu}$.

***Definition* 2.** *B-splines* of degree p with the knot vector $\Xi = \{t_1, \ldots, t_{n+p+1}\}$ are the functions $N_1^p, \ldots, N_n^p$ defined recursively as follows: for $i = 1, \ldots, n+p$ we put

$$N_i^0(t) = \begin{cases} 1 & \text{if} \quad t \in [t_i, t_{i+1}[, \\ 0 & \text{otherwise}, \end{cases} \tag{1.1}$$

and for $1 \leq k \leq p$, $i = 1, \ldots, n+p-k$

$$N_i^k(t) = \frac{t - t_i}{t_{i+k} - t_i} N_i^{k-1}(t) + \frac{t_{i+k+1} - t}{t_{i+k+1} - t_{i+1}} N_{i+1}^{k-1}(t), \quad t \in [t_i, t_{i+1}[. \tag{1.2}$$

***Definition* 3.** Let $N_1^p, \ldots, N_n^p$ be the B-splines with a knot vector $\Xi = \{t_1, \ldots, t_{n+p+1}\}$. Further, let $\mathbf{c}_1, \ldots, \mathbf{c}_n$ be points in $\mathbb{R}^d$. The following parametrized curve

$$\mathbf{r} : [t_{p+1}, t_{n+1}] \ni t \mapsto \mathbf{c}_1 N_1^p(t) + \ldots \mathbf{c}_n N_n^p(t) \in \mathbb{R}^d$$

is called a *spline curve* with *control points* $\mathbf{c}_1, \ldots, \mathbf{c}_n$.

Remark 1. It is straightforward from (1.2) that

(i) B-splines are piecewise polynomials of degree p.

(ii) B-splines are non-negative.

(iii) B-splines are compactly supported. To be precise, the support of N_i^p is $[t_i, t_{i+p+2}]$, $i = 1, \ldots, n$. Consequently, for $p+1 \leq r \leq n$, only the B-splines $N_{r-p}^p, \ldots, N_r^p$ are supported on $[t_r, t_{r+1}]$.

To present further important properties of B-splines, let us first derive the fundamental de Boor's algorithm. Let $\mathbf{r}(t) = \mathbf{c}_1 N_1^p(t) + \ldots \mathbf{c}_n N_n^p(t)$ be a *spline curve*, with $t \in [t_r, t_{r+1}]$, $p+1 \leq r \leq n$. Utilizing Remark 1(iii) and Equation (1.2) we have the following equalities

$$\begin{aligned}
\mathbf{r}(t) &= \sum_{i=r-p}^{r} \mathbf{c}_i N_i^p(t) && (1.3)\\
&= \sum_{i=r-p+1}^{r} \left(\Big(1 - \frac{t-t_i}{t_{i+p}-t_i}\Big)\mathbf{c}_{i-1} + \frac{t-t_i}{t_{i+p}-t_i}\mathbf{c}_i \right) N_i^{p-1}(t) = \sum_{i=r-p+1}^{r} \mathbf{c}_i^{(1)} N_i^{p-1}(t)\\
&= \ldots\\
&= \sum_{i=r-p+k}^{r} \left(\Big(1 - \frac{t-t_i}{t_{i+p-k+1}-t_i}\Big)\mathbf{c}_{i-1}^{(k-1)} + \frac{t-t_i}{t_{i+p-k+1}-t_i}\mathbf{c}_i^{(k-1)} \right) N_i^{p-k}(t) = \sum_{i=r-p+k}^{r} \mathbf{c}_i^{(k)} N_i^{p-k}(t)\\
&= \ldots\\
&= \mathbf{c}_r^{(p)} N_r^0(t) = \mathbf{c}_r^{(p)}. && (1.4)
\end{aligned}$$

In (1.4), the intermediate control points $\mathbf{c}_i^{(k)}$ are given by

$$\mathbf{c}_i^{(0)} = \mathbf{c}_i, \quad i = r-p, \ldots, r \tag{1.5a}$$

$$\mathbf{c}_i^{(k)} = (1-\alpha_i^{(k)})\mathbf{c}_{i-1}^{(k-1)} + \alpha_i^{(k)}\mathbf{c}_i^{(k-1)}, \quad r = 1, \ldots, p, \quad i = r-p-r, \ldots, r, \tag{1.5b}$$

where $\alpha_i^{(k)} = \frac{t-t_i}{t_{i+p-k+1}-t_i}$. Note that $1-\alpha_i^{(k)}$ and $\alpha_i^{(k)}$ are barycentric coordinates of t in the interval $[t_i, t_{i+p-k+1}]$, i.e., $t = (1-\alpha_i^{(k)})t_i + \alpha_i^{(k)} t_{i+p-k+1}$. By (1.5), we have derived the *de Boor's algorithm*.

Remark 2. With the help of de Boor algorithm (1.5), we can now prove other important properties of B-splines:

(i) The point $\mathbf{r}(t)$ with $t \in [t_r, t_{r+1}]$, $p+1 \leq r \leq n$, always belongs to the convex hull of the control points $\mathbf{c}_{r-p}, \ldots, \mathbf{c}_r$, and consequently a spline curve is completely contained in the convex hull of its control points. This is due to the fact that in the k^{th} step of de Boor's algorithm (1.5), a new control point $\mathbf{c}_i^{(k)}$ is a convex combination of the control points $\mathbf{c}_i^{(k-1)}$ from the previous step.

(ii) Letting all control points in the de Boor's algorithm (1.5) equal to 1, it follows that the B-splines form a *partition of unity*. That is

$$N_1(t) + \ldots + N_n(t) = 1, \quad \text{for all } t \in [t_{p+1}, t_{n+1}[.$$

Note that if the knot t_{n+1} of the knot vector $\boldsymbol{\Xi}$ has multiplicity $p+1$ then it is straightforward from Definition 2 that all the B-splines N_i^p vanish at the knot. An example is the case where $\boldsymbol{\Xi}$ is an *open* knot vector, i.e., the knots t_{p+1} and t_{n+1} have multiplicity $p+1$.

However, this does not cause any problem for isogeometric analysis if the numerical integrations under considerations are calculated using the Gaussian quadratures [25]. This is owing to the fact that the quadratures only require the values of the B-splines at the interiors of knot intervals.

However, from the definition 2, it is not straightforward to explain, why a B-spline is $C^{p-\nu}$ at an inner knot with multiplicity ν, or what new control points are if one extra knot is inserted. To this end, let us invoke the following concept of polar forms.

1.1.2 Polar form of a polynomial

We shall see that each polynomial can be put into $1:1$ correspondence with a mapping called the polar form (also known as the blossom). This provides a powerful tool for exploring B-splines.

***Definition* 4.** The *polar form* f of a polynomial F of degree p is a mapping $f : \mathbb{R}^p \to \mathbb{R}$ satisfying the following conditions

(i) f is symmetric, that is, f is invariant under any permutation of its arguments.

(ii) f is p-affine, i.e., f is affine with respect to each variable.

(iii) The restriction of f to the diagonal of $\mathbb{R}^n$ is F, i.e., $f(t,\dots,t) = F(t)$.

By looking at the Taylor expansion of $F(t)$ at a point $t_0 \in \mathbb{R}$

$$F(t) = \sum_{k=0}^{p} \frac{F^{(k)}(t_0)}{k!}(t-t_0)^k,$$

one can find a polar form of F, thereby proving the *existence of the polar form*, as follow

$$f_{t_0}(t_1,\dots,t_p) = \sum_{k=0}^{p} \frac{F^{(k)}(t_0)}{k!}\binom{p}{k}^{-1} \sum_{(i_1,\dots,i_k)\in I_k} (t_{i_1}-t_0)\dots(t_{i_k}-t_0), \tag{1.6}$$

where $I_k = \{(i_1,\dots,i_k) \subset \{1,\dots,p\} : i_1 < \dots < i_k\}$. The uniqueness of *the* polar form follows from the following theorem

Theorem 1 (de Boor's algorithm)**.** *Let $f : \mathbb{R}^p \to \mathbb{R}$ be symmetric and p-affine, and let $s_1 \le \dots \le s_{2p}$ be real numbers satisfying $s_p < s_{p+1}$. Then f is determined uniquely by the values $f(s_{i+1},\dots,s_{i+p})$, $i = 0,\dots,p$. Furthermore, for given $t_1,\dots,t_p$, $f(t_1,\dots,t_p)$ is determined by the following recursive* de Boor's algorithm*: for $1 \le k \le p$ and $k \le i \le p$*

$$\begin{aligned} f(t_1,\dots,t_k,s_{i+1},\dots,s_{i+p-k}) = \; & (1-\alpha_i^{(k)})f(t_1,\dots,t_{k-1},s_i,\dots,s_{i+p-k}) \\ & +\alpha_i^{(k)} f(t_1,\dots,t_{k-1},s_{i+1},\dots,s_{i+p-k+1}), \end{aligned} \tag{1.7}$$

where $\alpha_i^{(k)} = \frac{t_k - s_i}{s_{i+p-k+1}-s_i}$.

Proof. For each $1 \le k \le p$, (1.7) is obtained by utilizing the hypothesis for f and using the expression $t_k = (1-\alpha_i^{(k)})s_i + \alpha_i^{(k)} s_{i+p-k+1}$. In the recursive formula (1.7), if we let k run from 1 to p, we end up with $f(t_1,\dots,t_p)$. □

We will now address the relations of the degree of continuity at a joint point between two polynomials to their polar forms.

Theorem 2. *Given two polynomials f and g of degree p, let F and G be their polar forms. Then for $t \in \mathbb{R}$ and $r \in \mathbb{N}_0$, the following two statements are equivalent*

(i) $F^{(k)}(t) = G^{(k)}(t), \quad k = 0, \ldots, r.$

(ii) $f(t, \ldots, t, t_1, \ldots, t_r) = g(t, \ldots, t, t_1, \ldots, t_r), \quad$ *for all* $t_1, \ldots, t_r \in \mathbb{R}$.

Proof. Applying the chain rule to the Taylor expansion-based polar form (1.6), we arrive at the equality

$$F'(t) = \frac{p}{b-a}\big(f(t, \ldots, t, b) - f(t, \ldots, t, a)\big), \tag{1.8}$$

where $a \neq b$ are arbitrary real numbers. Differentiating both sides of (1.8) $k-1$ times with respect to t results in the following equality

$$F^{(k)}(t) = \sum_{i=0}^{k} C_i(p, k, a, b) f(t, \ldots, t, t_1, \ldots, t_k), \tag{1.9}$$

where $t_1, \ldots, t_k \in \{a, b\}$ and $C_i(p, k, a, b)$ are coefficients which only depend on p, k, a, and b. The equation (1.9) clearly still holds if F and f are substituted by G and g respectively, and therefore the theorem is proven. □

We are now ready to explain afore mentioned properties of B-splines.

1.1.3 B-splines in terms of polar forms and their further properties

The following theorem provides a powerful tool for establishing further properties of B-splines.

Theorem 3 (Alternative definition for B-splines)**.** *Let* $\mathbf{r}(t)$ *be a spline curve with knot vector* $\Xi = \{t_1, \ldots, t_{n+p+1}\}$ *and control points* $\mathbf{c}_1, \ldots, \mathbf{c}_n$*. On each knot span* $[t_r, t_{r+1}]$ *with* $t_r < t_{r+1}$*, let* f_r *be the symmetric and* p*-affine mapping defined by assigning its values to each of the* $p+1$ *sets of* p *consecutive knots in the sequence of* $2p$ *knots* $t_{r-p+1}, \ldots, t_r, t_{r+1}, \ldots, t_{n+r}$ *as follows*

$$f_r(t_{r-p+i}, \ldots, t_{r-1+i}) = \mathbf{c}_{r-p+i-1}, \quad i = 1, \ldots, p+1. \tag{1.10}$$

Then in $[t_r, t_{r+1}]$*,* f_r *is the polar form of* $\mathbf{r}$*. That is*

$$\mathbf{r}(t) = f_r(t, \ldots, t) \quad \textit{for all } t \in [t_r, t_{r+1}]. \tag{1.11}$$

Proof. If we put

$$\begin{aligned} \mathbf{c}_i^{(0)} &= \mathbf{c}_i, \quad i = r-p, \ldots, r \\ \mathbf{c}_i^{(k)} &= f_r(\underbrace{t, \ldots, t}_{k \text{ times}}, t_{i+1}, \ldots, t_{i+p-k}), \quad k = 1, \ldots, p, \quad i = k, \ldots, p, \end{aligned}$$

then the de Boor's algorithm given by (1.7) gives the same relations of the intermediate control points $\mathbf{c}_i^{(k)}$ as given in (1.5). The former results in the right-hand side of (1.11), while the later leads to the left-hand side of (1.11). □

Remark 3. As a consequence of Theorem 3, each B-spline N_i^p, $i = 1, \ldots, n$, can be defined in terms of polar forms by using the set of control points $c_j = \delta_{ij}$, $j = 1, \ldots, n$.

We will now present one of the most important properties of B-splines.

Corollary 1. *Let* t_r *be an inner knot, i.e.,* $p+2 \leq r \leq n$*, with multiplicity* ν*. Then any spline curve of degree* p *is* $C^{n-\nu}$ *at* t_r*.*

Proof. Assume that

$$t_{r-\nu} < t = t_{r-\nu+1} = \ldots = t_r < t_{r+1}.$$

If we let $f_{r-\nu}$ and f_r be polar forms of the spline curve in the intervals $[t_{r-\nu}, t]$ and $[t, t_{r+1}]$ respectively, then $f_{r-\nu}$ and f_r have the same values at every sets of p consecutive knots of the $2p$-knot sequence $\{t_{r-p+1}, \ldots, t_{r-\nu}, t, \ldots, t, t_{r+1}, \ldots, t_{r-\nu+p}\}$. That is, at every set of p consecutive knots containing i knots in front of $t = t_{r-\nu+1}$ and containing $p - \nu - i$ knots after $t = t_r$, $i = 0, \ldots, p - \nu$, $f_{r-\nu}$ and f_r satisfy the following equalities

$$f_{r-\nu}(t_{r-\nu-i+1}, \ldots, t_{r-\nu}, t, \ldots, t, t_{r+1}, \ldots, t_{r+p-\nu-i}) = f_r(t_{r-\nu-i+1}, \ldots, t_{r-\nu}, t, \ldots, t, t_{r+1}, \ldots, t_{r+p-\nu-i}). \quad (1.12)$$

If we put

$$g_{r-\nu}(s1, \ldots, s_{p-\nu}) = f_{r-\nu}(t, \ldots, t, s1, \ldots, s_{p-\nu}) \quad (1.13)$$

$$g_r(s1, \ldots, s_{p-\nu}) = f_r(t, \ldots, t, s1, \ldots, s_{p-\nu}), \quad (1.14)$$

for $s_1, \ldots, s_{p-\nu} \in \mathbb{R}$, then $g_{r-\nu}$ and g_r are symmetric and $(p - \nu)$-affine. By Theorem 1, $g_{r-\nu}$ and g_r are uniquely determined by their values at all sets of $p - \nu$ consecutive knots of the set $\{t_{r-\nu+1}, \ldots, t_{r-\nu}, t_{r+1}, \ldots, t_{r+p}\}$. Therefore, the equalities given by (1.12) ensure that $g_{r-\nu} = g_r$. That is

$$f_{r-\nu}(t, \ldots, t, s_1, \ldots, s_{p-\nu}) = f_r(t, \ldots, t, s_1, \ldots, s_{p-\nu}), \quad \text{for all } s_1, \ldots, s_{p-\nu} \in \mathbb{R}.$$

By Theorem 2, we conclude that the spline curve is $C^{n-\nu}$ at $t = t_r$. □

Figure 1.1 demonstrates the continuity property of B-splines. Another direct consequence of

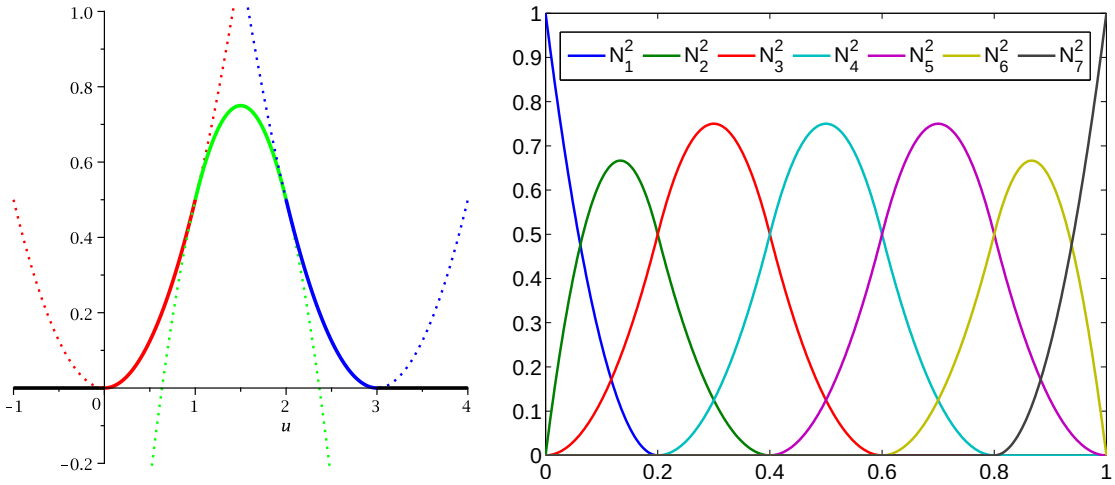

Figure 1.1: To the left: a quadratic B-spline composed of polynomial "pieces" (shown in different colors). The alignments of the dashed-straight lines show that the B-spline is C^1-continuous at the joint points. To the right: quadratic B-splines with the knot vector $\{0, 0, 0, 0.2, 0.4, 0.6, 0.8, 1, 1, 1\}$.

Theorem 3 is the following fundamental result on basis representation of spline functions.

Corollary 2 (Basis representation of spline functions)**.** *Let F be a piecewise polynomial of degree p defined in a domain $[\xi_1, \xi_N]$ and associated with a strictly increasing sequence of real numbers $\xi_1 < \ldots < \xi_N$ as follows: F is $C^{p-\nu_i}$ at each ξ_i, $2 \le i \le N-1$. Then F has a unique representation in terms of B-splines with the knot vector containing ξ_1 and ξ_N as boundary knots with multiplicity $p+1$ respectively, and containing ξ_i, $2 \le i \le N-1$, as inner knots with multiplicity ν_i.*

With the help of polar forms, it is now easy to derive the knot insertion rule.

Corollary 3 (Knot insertion)**.** *Let $\mathbf{c}_1, \ldots, \mathbf{c}_n$ be the control points of a spline curve of degree p with knot vector $\boldsymbol{\Xi} = \{t_1, \ldots, t_{n+p+1}\}$. If one extra knot $t^* \in [t_r, t_{r+1}]$, with $t_{p+1} \leq t_r < t_{r+1} \leq t_{n+1}$, is inserted to the knot sequence then the spline curve with the new knot vector is represented by the following new control points*

$$\mathbf{c}_i^* = \begin{cases} \mathbf{c}_i & i = 1, \ldots, r-p \qquad (1.15) \\ (1-\alpha_i)\mathbf{c}_{i-1} + \alpha_i \mathbf{c}_i & i = r-p+1, \ldots, r \qquad (1.16) \\ \mathbf{c}_{i-1} & i = r+1, \ldots, n+1, \qquad (1.17) \end{cases}$$

where $\alpha_i = \dfrac{t^* - t_i}{t_{i+p} - t_i}$.

Proof. As only B-splines $N_{r-p}^p, \ldots, N_r^p$ are supported on $[t_r, t_{r+1}]$, all the control points except $\mathbf{c}_{r-p}, \ldots, \mathbf{c}_r$ are unchanged. Furthermore, $\mathbf{c}_{r-p}$ and $\mathbf{c}_r$ are associated to the sets of p consecutive knots $t_{r-p+1}, \ldots, t_r$ and $t_{r+1}, \ldots, t_{r+p}$, respectively. The sets of knots are not affected by the knot insertion, thus $\mathbf{c}_{r-b}$ and $\mathbf{c}_r$ are unchanged as well. Therefore, (1.15) and (1.17) hold. It now remains (1.16) to be determined.

Let f_r be the polar form of the spline curve defined in the interval $[t_r, t_{r+1}]$. For each set of p consecutive knots containing i knots in front of t^* and $p-i-1$ knots after t^*, $0 \leq i \leq p-1$,

$$\mathbf{c}_{r-i}^* = f_r(t_{r-i+1}, \ldots, t_r, t^*, t_{r+1}, \ldots, t_{r+p-i-1}). \qquad (1.18)$$

Expressing $t^* = (1-\alpha_{r-i})t_{r-i} + \alpha_{r-i}t_{r+p-i}$, where $\alpha_{r-i} = \frac{t^* - t_{r-i}}{t_{r+p-i} - t_{r-i}}$, and utilizing the p-affine and symmetric property of f_r, (1.18) becomes

$$\mathbf{c}_{r-i}^* = (1-\alpha_{r-i})\mathbf{c}_{r-i-1} + \alpha_{r-i}\mathbf{c}_{r-i}, \quad 0 \leq i \leq p-1. \qquad (1.19)$$

Substituting $r-i$ by i in (1.19), we reach the conclusion (1.16), thereby completing the proof. □

Finally, let us discuss the B-spline representation of the derivative of a spline curve.

Corollary 4 (Derivative of B-splines)**.** *Let $\mathbf{r}$ be a spline curve of degree p with knot vector $\boldsymbol{\Xi} = \{t_1, \ldots, t_{n+p+1}\}$ and control points $\mathbf{c}_1, \ldots, \mathbf{c}_n$. Then the derivative $\mathbf{r}'$ is a spline curve of degree $p-1$ with the same knot vector and the following control points*

$$\mathbf{c}_i' = \frac{p}{t_{i+p} - t_i}\big(\mathbf{c}_i - \mathbf{c}_{i-1}\big), \quad i = 1, \ldots, n+1. \qquad (1.20)$$

Consequently, the derivatives of B-splines are given by

$$\frac{\mathrm{d}}{\mathrm{d}t} N_i^p = \frac{p}{t_{i+p} - t_i} N_i^{p-1} - \frac{p}{t_{i+p+1} - t_{i+1}} N_{i+1}^{p-1}, \quad i = 1, \ldots, n. \qquad (1.21a)$$

Proof. By Corollary 2, $\mathbf{r}'$ is a spline curve of degree $p-1$ with, for convenience, the same knot vector $\boldsymbol{\Xi}$. Let us now determine the control points $\mathbf{c}_i'$, $1 \leq i \leq n-1$. Let f_r be the polar form of $\mathbf{r}$ in the interval $[t_r, t_{r+1}]$, where r satisfies $i+1 \leq r \leq i+p$. From the Taylor expansion-based representation of a polar form (1.6), it follows that the polar form g_r of $\mathbf{r}'$ in $[t_r, t_{r+1}]$ is given by

$$g_r(\xi_1, \ldots, \xi_{p-1}) = \frac{p}{b-a}\big(f_r(\xi_1, \ldots, \xi_{p-1}, b) - f_r(\xi_1, \ldots, \xi_{p-1}, a)\big), \qquad (1.22)$$

for all $\xi_1, \ldots, \xi_{p-1} \in \mathbb{R}$ and real numbers $a \neq b$. Substituting $(\xi_1, \ldots, \xi_{p-1}) = (t_{i+1}, \ldots, t_{i+p-1})$, $b = t_{i+p}$, and $a = t_i$ to (1.22), we arrive at the conclusion (1.20).

For each $1 \leq i \leq n$, applying (1.20) to the set of control points $c_k = \delta_{ik}$, $k = 1, \ldots, n$, (1.21) is established. □

1.2 Isogeometric analysis

In this section, we first state IGA precisely. Enforcement of C^0-continuity of the numerical solution when using a model with multiple IGA patches is then discussed.

1.2.1 Isogeometric analysis: Basis functions for analysis

Let us again consider a simply connected open domain $\Omega \subset \mathbb{R}^2$. We are looking for a B-spline parametrization of Ω, that is, for a *bijective* map $\mathbf{F} : [0,1]^2 \to \Omega$ of the form

$$\mathbf{F}(u,v) = \big(x(u,v), y(u,v)\big) = \sum_{i=1}^{\widehat{m}} \sum_{j=1}^{\widehat{n}} \widehat{\mathbf{d}}_{i,j} \widehat{M}_i^p(u) \widehat{N}_j^q(v), \tag{1.23}$$

where $\widehat{M}_i^p$ and $\widehat{N}_i^q$ are B-splines of degree p and q with knot vectors $\widehat{\boldsymbol{\Xi}}_u$ and $\widehat{\boldsymbol{\Xi}}_v$, respectively. By composing the inverse $\mathbf{F}^{-1}$ with some basis functions on the parameter (reference) domain $]0,1[^2$ we obtain basis functions defined on the physical domain Ω.

We let $\widetilde{M}_i^{\widetilde{p}}$, $i = 1, \ldots, \widetilde{m}$ and $\widetilde{N}_j^{\widetilde{q}}$, $j = 1, \ldots, \widetilde{n}$ be B-splines of degree $\widetilde{p}$ and $\widetilde{q}$ (not necessary equal to p and q) with knot vector $\widetilde{\boldsymbol{\Xi}}_u$ and $\widetilde{\boldsymbol{\Xi}}_v$, respectively. The basis functions on the parameter domain are defined as the tensor product splines

$$\widetilde{R}_k^{\widetilde{p},\widetilde{q}}(u,v) = \widetilde{M}_i^{\widetilde{p}}(u) \widetilde{N}_j^{\widetilde{q}}(v),\ k = (\widetilde{n}-1)i + j. \tag{1.24}$$

Thus, the basis functions on the physical domain Ω are given as

$$\phi_k(x,y) = (\widetilde{R}_k^{\widetilde{p},\widetilde{q}} \circ \mathbf{F}^{-1})(x,y), \quad k = 1, \ldots, \widetilde{m}\widetilde{n}. \tag{1.25}$$

An integral over Ω can be now transformed to an integral over $]0,1[^2$ as

$$\iint_{\Omega} f(x,y)\,\mathrm{d}x\,\mathrm{d}y = \iint_{]0,1[^2} f(x(u,v),y(u,v))\ \det(\mathbf{J})\,\mathrm{d}u\,\mathrm{d}v, \tag{1.26}$$

where $\mathbf{J}$ is the Jacobian of the variable transformation $\mathbf{F}$, and we have assumed that $\det(\mathbf{J}) > 0$.

Furthermore, to ensure that we can approximate any function in $H^1(\Omega)$ [26] sufficiently well, we may want to use an even finer (when compared to $\widehat{\boldsymbol{\Xi}}_u$ and $\widehat{\boldsymbol{\Xi}}_v$) pair of knot vectors $\widetilde{\boldsymbol{\Xi}}_u$ and $\widetilde{\boldsymbol{\Xi}}_v$ for the analysis, see Fig. 1.2.

Remark 4. As a consequence of the formula (1.26), one may evaluate integrals over Ω entering a variational form of a given boundary value problem by computing the integrals over the parameter domain instead. Thus an "IGA assembly routine" may be implemented as a loop over elements defined by the knot vectors $\widetilde{\boldsymbol{\Xi}}_u$ and $\widetilde{\boldsymbol{\Xi}}_v$, see Fig. 1.2.

1.2.2 Multiple patches: Enforcement of the C^0-continuity of the numerical solution

1.2.2.1 Theory

Often, it is convenient or even necessary to consider domains subdivided into several patches. Examples include non-simply connected domains or physical models involving several materials. For enforcing the C^0-continuity of the numerical solution across patch boundaries, we need the following property of spline curves.

Lemma 1. *Let* $\mathbf{r}$ *be a spline curve of degree* p *with knot vector* $\boldsymbol{\Xi} = \{t_1, \ldots, t_{n+p+1}\}$ *and control points* $\mathbf{c}_1, \ldots, \mathbf{c}_n$. *Then the following curve*

$$[0,1] \ni t \mapsto \mathbf{r}(a(1-t)+bt) \in \mathbb{R}^d, \quad t_{p+1} \le a \ne b \le t_{n+1},$$

is a spline curve,

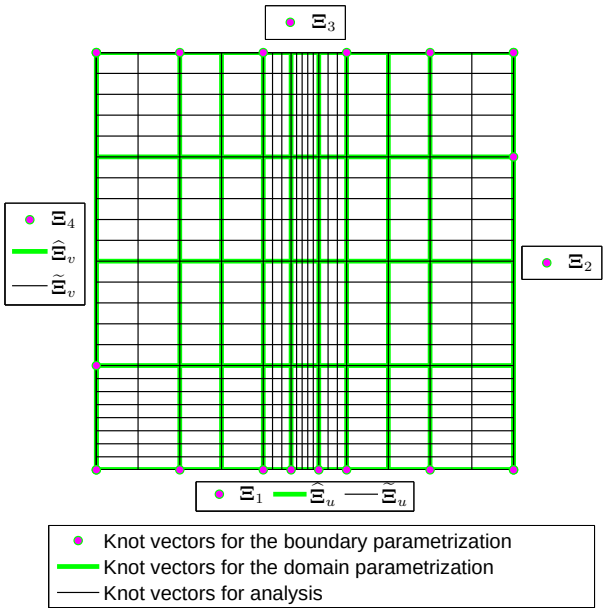

Figure 1.2: The three types of knot vectors of an IGA model used in the present work.

(i) if $b > a$, with the knot vector

$$\boldsymbol{\Xi}_{a,b} = \{\frac{t_1 - a}{b-a}, \ldots, \frac{t_{n+p+1} - a}{b-a}\} \tag{1.27}$$

and with the control points $\mathbf{c}_1, \ldots, \mathbf{c}_n$.

(ii) if $b < a$, with the knot vector

$$\boldsymbol{\Xi}_{a,b} = \{\frac{a - t_{n+p+1}}{a-b}, \ldots, \frac{a - t_1}{a-b}\} \tag{1.28}$$

and with the control points $\mathbf{c}_n, \ldots, \mathbf{c}_1$.

Proof. Let us prove the conclusion (ii), the conclusion (i) is then proven using similar arguments. Let $\boldsymbol{\gamma}_{a,b}$ be the spline curve of degree p with knot vector $\boldsymbol{\Xi}_{a,b}$ given by (1.28) and the control points $\mathbf{c}_n, \ldots, \mathbf{c}_1$. We need to show that

$$\boldsymbol{\gamma}_{a,b}(t) = \mathbf{r}(a(1-t) + bt), \quad \text{for all } 0 \leq t \leq 1. \tag{1.29}$$

Indeed, let f_r be the polar form of $\mathbf{r}$ in the knot interval $[t_r, t_{r+1}]$ with $t_r < t_{r+1}$, and let f_r^* be the polar form of $\boldsymbol{\gamma}_{a,b}$ in the knot interval $[\frac{a - t_{r+1}}{a-b}, \frac{a-t_r}{a-b}]$. By Theorem 3 we have the following equalities

$$\mathbf{c}_i = f_r(t_{r-p+i}, \ldots, t_{r+i-1}) = f_r^*(\frac{a - t_{r+i-1}}{a-b}, \ldots, \frac{a - t_{r-p+i}}{a-b}), \quad i = 1, \ldots, p+1. \tag{1.30}$$

If we let $g_r(s_1, \ldots, s_p) = f_r^*(\frac{a-s_1}{a-b}, \ldots, \frac{a-s_p}{a-b})$, $s_1, \ldots, s_p \in \mathbb{R}$, then g_r is also a symmetric and p-affine mapping. From Theorem 1 and (1.30) it follows that $g_r = f_r$. That is,

$$f_r^*(\frac{a-s_1}{a-b}, \ldots, \frac{a-s_p}{a-b}) = f_r(s_1, \ldots, s_p), \quad s_1, \ldots, s_p \in \mathbb{R}. \tag{1.31}$$

Substituting $s_1 = \ldots = s_p = a(1-t)+bt$ to (1.31), we arrive at the expected equality (1.29). □

The C^0-continuity of the numerical solution across boundaries between patches can be enforced as follows

- We parametrize all patches in the counter-clockwise fashion, i.e., a valid parametrization of this type has positive Jacobian determinant everywhere.
- *At a boundary Γ between two patches*, let spline curves $\mathbf{r}_i$ with knot vectors $\mathbf{\Xi}_i = \{t_1^{(i)}, \ldots, t_{n_i+p+1}^{(i)}\}$ and control points $\mathbf{c}_1^i, \ldots, \mathbf{c}_{n_i}^i$, $i = 1, 2$, be the induced parametrizations of the two parametrizations of the two patches of Γ, respectively. According to the direction of increasing parameter of the induced parametrizations, there are two cases, see Fig. 7.6 for illustrations,

  (i) $\mathbf{r}_1'(t) \cdot \mathbf{r}_2'(t) > 0$ for all $0 < t < 1$, i.e., $\mathbf{r}_1$ and $\mathbf{r}_2$ have co-directional tangent vectors. The criteria for the numerical solution to be continuous across Γ are
    1. *The two parametrizations are continuous across* Γ, i.e., $\mathbf{r}_1(t) = \mathbf{r}_2(t)$ for all $t \in \mathbf{F}^{-1}{}_i(\Gamma)$. This criterion is formulated as follows. First we find the "union" knot vector $\mathbf{\Xi}$ of $\mathbf{\Xi}_1$ and $\mathbf{\Xi}_2$, i.e., the knot vector whose inner knots are all inner knots of both knot vectors with maximum multiplicity. Let $\mathbf{R}_i$ be the refinement matrices [24] obtained when inserting knots into $\mathbf{\Xi}_i$ to have $\mathbf{\Xi}$, $i = 1, 2$. The C^0-continuity of the parametrizations now can be enforced by the following linear constraints on the control points
    $$\mathbf{R}_1[x_1^1, \ldots, x_{n_1}^1]^T = \mathbf{R}_2[x_1^2, \ldots, x_{n_2}^2]^T, \tag{1.32}$$
    where x_j^i is one of the coordinates of the control points $\mathbf{c}_j^i$.
    2. The same conditions as in (1.32) are enforced for the *state variables*, i.e., the coefficients of the representation of the numerical solution in terms of the basis functions given by (1.25).

  (ii) $\mathbf{r}_1'(t) \cdot \mathbf{r}_2'(t) < 0$ for all $0 < t < 1$, i.e., the tangent vectors of $\mathbf{r}_1$ and $\mathbf{r}_2$ are the vectors with opposite directions. The criteria for the numerical solution to be continuous across Γ are
    1. *The two parametrizations are "continuous" across* Γ, i.e., $\mathbf{r}_1(1-t) = \mathbf{r}_2(t)$ for all $t \in \mathbf{F}_i^{-1}(\Gamma)$. This criterion is formulated as follows. Applying Lemma 1 with $a = 1$ and $b = 0$ for $\mathbf{r}_1$ to get the new knot vector $\mathbf{\Xi}_{1,1,0} = \{1 - t_{n_i+p+1}^{(1)}, \ldots, 1 - t_1^{(1)}\}$. Then similar to the previous case, we find the "union" knot vector $\mathbf{\Xi}$ of $\mathbf{\Xi}_{1,1,0}$ and $\mathbf{\Xi}_2$. Let $\mathbf{R}_1$ and $\mathbf{R}_2$ be the refinement matrices obtained when inserting knots into $\mathbf{\Xi}_{1,1,0}$ and $\mathbf{\Xi}_i$ to have $\mathbf{\Xi}$, respectively. The linear constraints for the "C^0-continuity" of the parametrizations are
    $$\mathbf{R}_1[x_{n_1}^1, \ldots, x_1^1]^T = \mathbf{R}_2[x_1^2, \ldots, x_{n_2}^2]^T, \tag{1.33}$$
    where x_j^i is one of the coordinates of the control points $\mathbf{c}_j^i$.
    2. The same conditions as in (1.33) are enforced for the *state variables*.

- Let $\mathbf{Ch} = \mathbf{c}$ be the constraints, discussed above, on state variables $\mathbf{h}$. Let $\mathbf{Kh} = \mathbf{f}$ be the global discretization of the linear system, resulting from assembling matrices from all patches. Then $\mathbf{h}$ can be determined via the stationary point of the following Lagrange function with Lagrange multipliers $\boldsymbol{\lambda}$ [27]
$$\Lambda(\mathbf{h}, \boldsymbol{\lambda}) = \frac{1}{2}\mathbf{h}^T\mathbf{K}\mathbf{h} - \mathbf{h}^T\mathbf{f} + \boldsymbol{\lambda}^T(\mathbf{C}\mathbf{h} - \mathbf{c}). \tag{1.34}$$
That is,
$$\begin{bmatrix} \mathbf{K} & \mathbf{C}^T \\ \mathbf{C} & \mathbf{0} \end{bmatrix} \begin{bmatrix} \mathbf{h} \\ \boldsymbol{\lambda} \end{bmatrix} = \begin{bmatrix} \mathbf{f} \\ \mathbf{c} \end{bmatrix}. \tag{1.35}$$

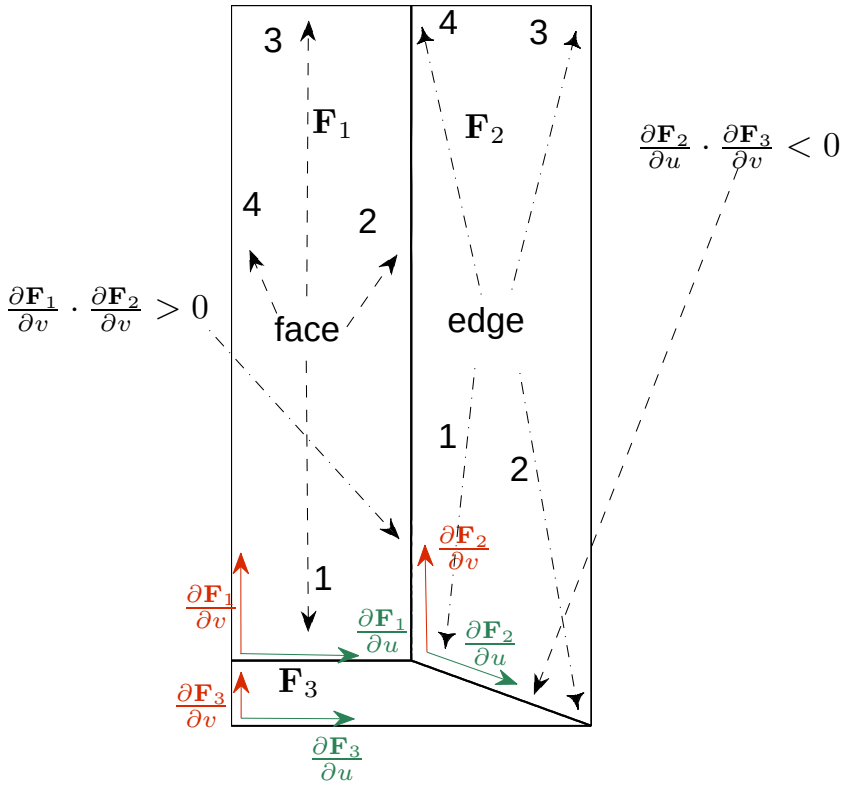

Figure 1.3: Implementing configuration used for enforcing the C^0-continuity of the numerical solution in a domain comprised of multiple IGA patches. In the picture, $\mathbf{F}_i(u,v)$ denotes the parametrization of the patch i, $i = 1,2,3$, $(u,v) \in [0,1]^2$. The rules of numbering the faces and edges of a patch are given in Section 1.2.2.2. In the present example, the tangent vectors of face 2 of patch 1 and face 4 of patch 2 at the same point are co-directional, whereas those of face 1 of patch 2 and face 2 of patch 3 at the same point are with opposite directions.

1.2.2.2 Implementation

It is important to note that if we collect the linear constraints, as defined by (1.32) and (1.33) but for state variables, from each boundary between two patches to a global matrix constraint $\mathbf{Ch} = \mathbf{c}$, then the rows of $\mathbf{C}$ are not linearly independent if there exists a joint corner between more than 2 patches in 2D, or a joint edge between more than 2 patches in 3D. To overcome this, we detect all such joint corners or joint edges automatically and eliminate linearly dependent constraints using the detection. Thus, we enforce the C^0-continuity of the numerical solution by the following scheme

- *Input*: Control points of all patches that satisfy the conditions (1.32) and (1.33).
- *Detect the connectivities between patches*: Let $\mathbf{F}_i(u,v)$ is the parametrization of the patch i, $i = 1,\ldots,N$. We refer each boundary component of one patch to a *face* numbered as follows: $\mathbf{F}_i(u,0)$: face 1, $\mathbf{F}_i(1,v)$: face 2, $\mathbf{F}_i(u,1)$: face 3, and $\mathbf{F}_i(0,v)$: face 4. Furthermore, we call each intersection set of two faces an *edge* and name the edges as follows: $\mathbf{F}_i(0,0)$: edge 1; $\mathbf{F}_i(1,0)$: edge 2; $\mathbf{F}_i(1,1)$: edge 3; $\mathbf{F}_i(0,1)$: edge 4. The terms *face* and *edge* are

to make the arguments be generalized to 3D without changing terminologies. Fig. 7.6 illustrates the numbering rules. We then calculate the following data

1. *The connectivity matrix*: Let $\mathbf{M}_{\text{con}}$ denote the matrix with 5 columns and rows each of which represents a boundary between two patches. If a face f_1 of a patch i_1 and a face f_2 of a patch i_2 are the same, then the row in $\mathbf{M}_{\text{con}}$ that representing the boundary reads
$$[i_1, i_2, f_1, f_2, \chi],$$
where $\chi = 1$ if the two faces are tangentially co-directional, and $\chi = -1$ otherwise.
2. *The array of joint edges*: Let $\mathbf{A}_{\text{je}}$ be an array whose element representing a joint edge of more than 2 patches. If the edges e_k of patches i_k are the same, $k = 1, \ldots, N_e$, then the element of $\mathbf{A}_{\text{je}}$ representing the joint edge may read
$$\begin{bmatrix} i_1 & \ldots & i_{N_e} \\ e_1 & \ldots & e_{N_e} \end{bmatrix}.$$

- *Assemble the global linear constraints on state variables* $\mathbf{Ch} = \mathbf{c}$: This is done as follows
  1. Using $\mathbf{M}_{\text{con}}$ to assemble linear constraints with respect to each boundary of two patches specified by a row of $\mathbf{M}_{\text{con}}$.
  2. Using $\mathbf{A}_{\text{je}}$ to eliminate linearly dependent constraints from the global assembled constraints obtained by the step above.
- *Enforce the resulting linearly independent constraints for the state variables by solving the linear system* (1.35).

Chapter 2

Shape optimization using isogeometric analysis

In this chapter, we first describe techniques for handling spline parametrizations. We then present an iterative algorithm for incorporating isogeometric analysis into shape optimization that has been tested with the design problem of magnetic density separators in Chapter 7 and with the antenna design problem in Part III. A parametrization setting and sensitivity analysis for a general shape optimization problem are described afterwards.

2.1 B-spline parametrization

In this section, we recall techniques for handling B-spline parametrizations in isogeometric analysis while having their utilizations for shape optimization in mind. For more details, see [28, 29, 30, 10].

2.1.1 Jacobian determinant of a parametrization as a spline

In order to ensure the validity of a parametrization of Ω when some of the control points $\widehat{\mathbf{d}}_{i,j}$, $i = 1,\dots,\widehat{n}$, $j = 1,\dots,\widehat{m}$ are design variables, we employ the following approach. The determinant of the Jacobian of $\mathbf{F}$ given by (1.23) is computed as

$$\det(\mathbf{J}) = \sum_{i,j=1}^{\widehat{m},\widehat{n}} \sum_{k,\ell=1}^{\widehat{m},\widehat{n}} \det[\widehat{\mathbf{d}}_{i,j}, \widehat{\mathbf{d}}_{k,\ell}] \, \frac{\mathrm{d}\widehat{M}_i^p(u)}{\mathrm{d}u} \, \widehat{N}_j^q(v) \, \widehat{M}_k^p(u) \, \frac{\mathrm{d}\widehat{N}_\ell^q(v)}{\mathrm{d}v}, \tag{2.1}$$

where $\det[\widehat{\mathbf{d}}_{i,j}, \widehat{\mathbf{d}}_{k,\ell}]$ is the determinant of the 2×2 matrix with columns $\widehat{\mathbf{d}}_{i,j}$, $\widehat{\mathbf{d}}_{k,\ell}$. Equation (2.1) defines a piecewise polynomial of degree $2p-1$ in u and degree $2q-1$ in v, with the differentiability at a knot lower by 1 in u and also lower by 1 in v. Such a map can be written in terms of B-splines $\mathcal{M}_k^{2p-1}$ and $\mathcal{N}_\ell^{2q-1}$ of degree $2p-1$ and $2q-1$ with the knot vectors obtained from $\widehat{\boldsymbol{\Xi}}_u$ and $\widehat{\boldsymbol{\Xi}}_v$ by raising the multiplicities of the inner u-knots and v-knots by p and q, respectively. That is

$$\det(\mathbf{J}) = \sum_{k,\ell=1}^{M,N} c_{k,\ell} \, \mathcal{M}_k^{2p-1}(u) \, \mathcal{N}_\ell^{2q-1}(v). \tag{2.2}$$

As B-splines are non-negative, the positivity of the determinant can be ensured by the positivity of the coefficients $c_{k,\ell}$. Let $(\mathcal{N}_\ell^{2q-1})^*$ be a function having the following form

$$(\mathcal{N}_\ell^{2q-1})^* = \alpha_1 \mathcal{N}_1^{2q-1} + \dots \alpha_N \mathcal{N}_N^{2q-1}, \tag{2.3}$$

and satisfying the conditions

$$\langle (\mathcal{N}_\ell^{2q-1})^*, \mathcal{N}_j^{2q-1} \rangle = \sum_{i=1}^{N} \alpha_k \int_0^1 \mathcal{N}_i^{2q-1}(v)\, \mathcal{N}_j^{2q-1}(v)\, \mathrm{d}v = \delta_{\ell,j}, \quad j = 1, \ldots, N. \tag{2.4}$$

$(\mathcal{N}_\ell^{2q-1})^*$ is called the *dual functional* of $\mathcal{N}_\ell^{2q-1}$, and may be determined by solving the system of linear equations (2.4) for unknowns $\alpha_1, \ldots, \alpha_N$. Utilizing the fact that $(\mathcal{M}_k^{2p-1}\mathcal{N}_\ell^{2q-1})^* = (\mathcal{M}_k^{2p-1})^*(\mathcal{N}_\ell^{2q-1})^*$, and substituting (2.1) to the relation $c_{k,\ell} = \langle (\mathcal{M}_k^{2p-1}\mathcal{N}_\ell^{2q-1})^*, \det(\mathbf{J}) \rangle$ we arrive at the following

$$c_{k,\ell} = \sum_{i,j=1}^{\widehat{m},\widehat{n}} \sum_{\alpha,\beta=1}^{\widehat{m},\widehat{n}} \det[\widehat{\mathbf{d}}_{i,j}, \widehat{\mathbf{d}}_{\alpha,\beta}] \, \langle \, (\mathcal{M}_k^{2p-1})^* \, , \, \frac{\mathrm{d}\widehat{M}_i^p}{\mathrm{d}u} \, \widehat{M}_\alpha^p \, \rangle \, \langle \, (\mathcal{N}_\ell^{2q-1})^* \, , \, \widehat{N}_j^q \frac{\mathrm{d}\widehat{N}_\beta^q}{\mathrm{d}v} \, \rangle. \tag{2.5}$$

If we let $\widehat{\mathbf{d}}$ denote the vector containing coordinates of the control points $\widehat{\mathbf{d}}_{i,j}$, then (2.5) shows that $c_{k,\ell}$ are quadratic forms of $\widehat{\mathbf{d}}$. The equation (2.5) also specifies coefficients of the matrices, denoted by $\mathbf{Q}_{k,\ell}$, of the quadratic forms. Thus we can write

$$c_{k,\ell} = \widehat{\mathbf{d}}^T \mathbf{Q}_{k,\ell} \widehat{\mathbf{d}}. \tag{2.6}$$

We now look for a linear method for extending a spline parametrization of the boundary of the physical domain onto the domain interior. By the term *linear*, we mean that that the resulting inner control points from the method are *affine* mappings of boundary control points. The linear method used in this work does not only depend on the knot vectors for the domain parametrization $\boldsymbol{\Xi}_u$ and $\boldsymbol{\Xi}_v$ but also depends on a reference parametrization of the domain. We obtain the reference parametrization by a minimization problem related to a so-called the Winslow functional [31]. We then "linearize" the Winslow functional to obtain the linear method. The approach for obtaining a reference parametrization of the domain and the derivation of the linear method are presented as follows.

2.1.2 Obtaining a B-spline parametrization

None of the linear methods presented in [29, 30] for extending the parametrization of the boundary into the interior of the domain can in general guarantee that the resulting map $\mathbf{F}$ will satisfy $\det(\mathbf{J}) > 0$ everywhere on $[0,1]^2$. Therefore, during some shape optimization iterations we have to utilize a more expensive non-linear method for improving the distribution of the interior control points $\widehat{\mathbf{d}}_{i,j}$. In a view of (2.2), a natural approach to ensure that $\det(\mathbf{J})$ is bounded away from zero is to solve the following optimization problem:

$$\begin{aligned} &\underset{\widehat{\mathbf{d}}_{i,j}, z}{\text{maximize}} \quad z, \\ &\text{subject to} \quad c_{k,\ell}\big(\widehat{\mathbf{d}}_{i,j}\big) \geq z, \end{aligned} \tag{2.7}$$

where $\widehat{\mathbf{d}}_{i,j}$ are inner control points as stated in (1.23), $c_{k,\ell}$ are given by (2.2), and z is an auxiliary optimization variable. If z resulting from approximately solving (2.7) to local optimality is positive then we are guaranteed to have a valid parametrization. Unfortunately, the quality of the parametrization obtained in this fashion needs not to be very high. We can further improve the parametrization by trying to approximate a conformal map. That is, ideally we would like $\mathbf{g} = \mathbf{J}^T\mathbf{J}$ to be an identically diagonal matrix (e.g., see [32]).

Let λ_1 and λ_2 be the eigenvalues of the matrix $\mathbf{g}$. Then $\mathbf{g}$ satisfies the ideal condition if and only if $\lambda_1 = \lambda_2$. The identity

$$\frac{(\sqrt{\lambda_1} - \sqrt{\lambda_2})^2}{\sqrt{\lambda_1 \lambda_2}} = \frac{\lambda_1 + \lambda_2}{\sqrt{\lambda_1 \lambda_2}} - 2 \tag{2.8}$$

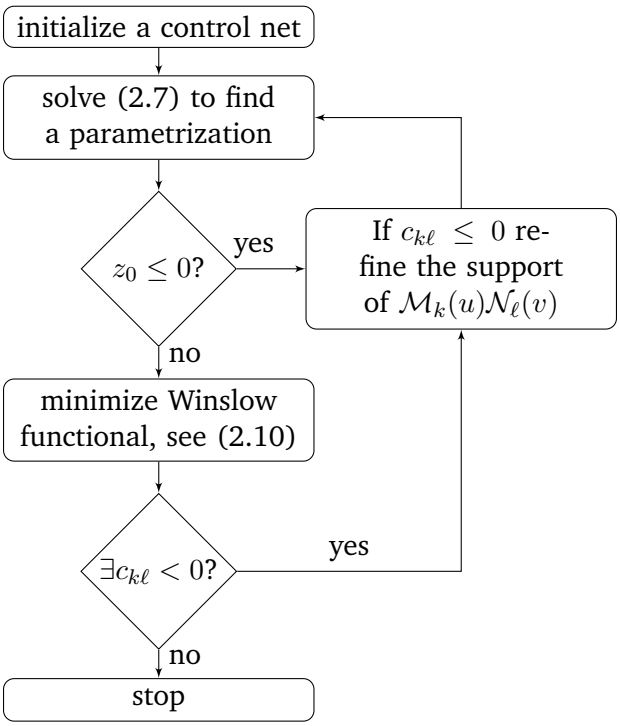

Figure 2.1: The algorithm for extending a boundary parametrization to the interior.

gives rise to *Winslow functional* [31]

$$W = \frac{\lambda_1 + \lambda_2}{\sqrt{\lambda_1 \lambda_2}} = \frac{\operatorname{trace}(\mathbf{g})}{\sqrt{\det(\mathbf{g})}} = \frac{\|\mathbf{F}_u\|^2 + \|\mathbf{F}_v\|^2}{\det[\mathbf{F}_u, \mathbf{F}_v]}. \tag{2.9}$$

In order to make $\mathbf{g}$ "as identically diagonal as possible" we would like to minimize W; however, to ensure the positivity of the determinant we consider the following constrained optimization problem:

$$\begin{aligned} \underset{\widehat{\mathbf{d}}_{i,j}}{\text{minimize}} \quad & \int_0^1 \int_0^1 W\big(\widehat{\mathbf{d}}_{i,j}\big)\,\mathrm{d}u\,\mathrm{d}v, \\ \text{subject to} \quad & c_{k\ell}\big(\widehat{\mathbf{d}}_{i,j}\big) \geq \delta z_0. \end{aligned} \tag{2.10}$$

In (2.10), $z_0 > 0$ is computed by approximately solving (2.7) and $\delta \in [0, 1]$ is a fixed relaxation parameter.

In our numerical experiments we utilize the interior point algorithm constituting a part of Optimization Framework in Matlab [33] for solving the optimization problems (2.7) and (2.10) to approximate stationarity. Also, we set $\delta = 0$ in (2.10). The whole process is outlined in Fig. 2.1.

2.1.3 Linearized Winslow functional

The algorithm for finding a valid domain parametrization described above has to be executed at every iteration of an "outer" shape optimization algorithm. Firstly, this process is rather computationally expensive, as it requires solving two non-linear programming problems at every shape optimization iteration. Secondly, as we solve the said optimization problems only approximately, it is not possible to find the derivatives of the inner control points with respect to changes of boundary control points. The latter does not allow us to use gradient based optimization algorithms for the "outer" shape optimization problem.

To avoid this difficulty, we linearize the process of computing a domain parametrization. Namely, we can Taylor-expand the Winslow functional as

$$\mathcal{W}(\widehat{\mathbf{d}}) = \iint_\Omega W(\widehat{\mathbf{d}})\,\mathrm{d}u\,\mathrm{d}v \approx \mathcal{W}(\widehat{\mathbf{d}}_0) + (\widehat{\mathbf{d}} - \widehat{\mathbf{d}}_0)^T\,\mathbf{G}(\widehat{\mathbf{d}}_0) + \frac{1}{2}(\widehat{\mathbf{d}} - \widehat{\mathbf{d}}_0)^T\,\mathbf{H}(\widehat{\mathbf{d}}_0)\,(\widehat{\mathbf{d}} - \widehat{\mathbf{d}}_0), \quad (2.11)$$

where $\widehat{\mathbf{d}}$ is a vector with all control points $\widehat{\mathbf{d}}_{i,j}$, $\widehat{\mathbf{d}}_0$ is the control points for a reference parametrization obtained by solving (2.10), and $\mathbf{G}$ and $\mathbf{H}$ are the gradient and Hessian of $\mathcal{W}$ respectively. If we split the control points $\widehat{\mathbf{d}} = (\widehat{\mathbf{d}}_1\ \widehat{\mathbf{d}}_2)^T$ into the part $\widehat{\mathbf{d}}_2$ that is given (typically the boundary control points) and the part $\widehat{\mathbf{d}}_1$ that has to be determined (typically the inner control points), then we can write (2.11) as

$$\begin{aligned}\mathcal{W}(\widehat{\mathbf{d}}) \approx \mathcal{W}(\widehat{\mathbf{d}}_0) + \begin{pmatrix}\widehat{\mathbf{d}}_1 - \widehat{\mathbf{d}}_{1,0} & \widehat{\mathbf{d}}_2 - \widehat{\mathbf{d}}_{2,0}\end{pmatrix}\begin{pmatrix}\mathbf{G}_1\\ \mathbf{G}_2\end{pmatrix} \\ + \frac{1}{2}\begin{pmatrix}\widehat{\mathbf{d}}_1 - \widehat{\mathbf{d}}_{1,0} & \widehat{\mathbf{d}}_2 - \widehat{\mathbf{d}}_{2,0}\end{pmatrix}\begin{pmatrix}\mathbf{H}_{11} & \mathbf{H}_{12}\\ \mathbf{H}_{21} & \mathbf{H}_{22}\end{pmatrix}\begin{pmatrix}\widehat{\mathbf{d}}_1 - \widehat{\mathbf{d}}_{1,0}\\ \widehat{\mathbf{d}}_2 - \widehat{\mathbf{d}}_{2,0}\end{pmatrix}. \quad (2.12)\end{aligned}$$

The minimum of the right hand side of (2.12) is obtained when $\widehat{\mathbf{d}}_1$ satisfies the *linear equation*

$$\mathbf{H}_{11}(\widehat{\mathbf{d}}_1 - \widehat{\mathbf{d}}_{1,0}) = -\mathbf{G}_1 - \mathbf{H}_{12}(\widehat{\mathbf{d}}_2 - \widehat{\mathbf{d}}_{2,0}). \quad (2.13)$$

This gives us a fast method for computing the domain parametrization and its derivatives with respect to the boundary control points. We use this method as long as we obtain a valid parametrization, but if the parametrization at some point fails the test described in Section 2.1.1 then we restart the "outer" shape optimization algorithm with a new reference parametrization $\widehat{\mathbf{d}}_0$ found by the method described in Section 2.1.2.

The given control points $\widehat{\mathbf{d}}_2$ can further be split into the set of fixed control points $\widehat{\mathbf{d}}_f$ and control points $\mathbf{R}\mathbf{d}$ obtained from the design variables (control points) $\mathbf{d}$ by knot insertion (refinement).

2.1.4 The quasi-conformal deformation

Assume we have found a reference control net with desirable properties, in particular of being a parametrization of the domain. Let $\widehat{\mathbf{v}}$ and $\widehat{\mathbf{w}}$ be two adjacent edges of the control net as depicted in Fig. 2.2. The rotation matrix $\mathbf{R}(\widehat{\theta})$, with $\widehat{\theta}$ being the angle between $\widehat{\mathbf{v}}$ and $\widehat{\mathbf{w}}$, enjoys

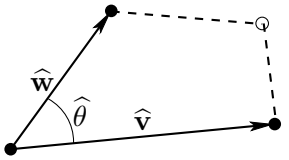

Figure 2.2: A local configuration in a reference control net

the identity

$$\|\widehat{\mathbf{w}}\|\mathbf{R}(\widehat{\theta})\widehat{\mathbf{v}} = \|\widehat{\mathbf{v}}\|\widehat{\mathbf{w}}. \quad (2.14)$$

Consider now a new control net with $\mathbf{v}$ and $\mathbf{w}$ being the adjacent edges corresponding to $\widehat{\mathbf{v}}$ and $\widehat{\mathbf{w}}$ of the reference control net. For each such pair of edges we consider linear equations

$$\|\widehat{\mathbf{w}}\|\mathbf{R}(\widehat{\theta})\mathbf{v} = \|\widehat{\mathbf{v}}\|\mathbf{w}. \quad (2.15)$$

The resulting linear system is overdetermined (there are $8(\widehat{m}-2)(\widehat{n}-2)$ equations with only $2(\widehat{m}-2)(\widehat{n}-2)$ unknown nodal positions) and is solved in the least squares sense.

2.1.5 Multiple patches

Let us discuss the case where a physical domain is configured by several patches. In any case, the parametrization of the domain boundary is given. Thus, the task of extending the parametrization into the interior is the same as in the one patch case except the parametrizations of inner patch boundaries are unknown. For such a domain, the optimization problems (2.7), (2.10), and the linear system (2.13) should account for the control points with respect to the inner boundaries as design variables while maintaining C^0-continuities across the boundaries by linear constraints on the control points. The constraints are obtained using the approach discussed in Section 1.2.2.1.

2.2 Shape optimization algorithm

Let us consider the following shape optimization problem using isogeometric analysis

$$\underset{\mathbf{d}\in\Omega_{\mathbf{d}}}{\text{minimize}} \quad f(\mathbf{d}) \tag{2.16}$$

where $\Omega_{\mathbf{d}} \subset \mathbb{R}^n$ is the space of design variables, and $\mathbf{d}$ are typically coordinates of boundary control points of spline patches. We solve the problem by the following iterative algorithm

- Start the algorithm with a guess $\mathbf{d}_0 \in \text{int}(\Omega_{\mathbf{d}})$.
- Let $\mathbf{A}_{\mathbf{d}_0}$ and $\mathbf{B}_{\mathbf{d}_0}$ be the matrices of an affine mapping that represent an approach for extending a parametrization of the boundary of the physical domain under consideration onto the domain interior. That is, the approach results in all control points $\widehat{\mathbf{d}}$ from $\mathbf{d}$ according to the following relation

  $$\widehat{\mathbf{d}}(\mathbf{d}) = \mathbf{A}_{\mathbf{d}_0}\mathbf{d} + \mathbf{B}_{\mathbf{d}_0}, \quad \mathbf{d} \in \Omega_{\mathbf{d}}. \tag{2.17}$$

  Assume $\mathbf{A}_{\mathbf{d}_0}$ and $\mathbf{B}_{\mathbf{d}_0}$ satisfy the condition that $\widehat{\mathbf{d}}(\mathbf{d}_0) = \mathbf{A}_{\mathbf{d}_0}\mathbf{d}_0 + \mathbf{B}_{\mathbf{d}_0}$ corresponds to a valid parametrization. Thus with a sufficient subdivision of the Jacobian determinant surface, c.f. (2.1), its representing control points $c_{k,\ell}$ given by (2.2) are positive. For simplicity let us assume that without further subdivision, the control points $c_{k,\ell}$ are positive. According to (2.6)

  $$c_{k,\ell}(\mathbf{d}) = (\mathbf{A}_{\mathbf{d}_0}\mathbf{d} + \mathbf{B}_{\mathbf{d}_0})^T \mathbf{Q}_{k,\ell}(\mathbf{A}_{\mathbf{d}_0}\mathbf{d} + \mathbf{B}_{\mathbf{d}_0}). \tag{2.18}$$

  The control points $c_{k,\ell}$ are obviously continuous functions of $\mathbf{d}$, thus there exists a neighborhood $B_{\mathbf{d}_0} \subset \Omega_{\mathbf{d}_0}$ of $\mathbf{d}_0$ such that

  $$c_{k,\ell}(\mathbf{d}) > 0 \quad \forall \mathbf{d} \in B_{\mathbf{d}_0},\, \forall k, \ell. \tag{2.19}$$

- We then would like to solve the following sub-optimization problem

  $$\mathbf{d}_1 = \underset{\mathbf{d}\in B_{\mathbf{d}_0}}{\text{argmin}} \quad f(\mathbf{d}), \tag{2.20}$$

  where argmin denotes the argument of the minimum of a function. In practice, it is difficult to determine $B_{\mathbf{d}_0}$, especially the "maximal" one, i.e., the largest neighborhood satisfying (2.19). Instead, we find $\mathbf{d}_1$ as the solution to the following problem

  $$\underset{\mathbf{d}\in\Omega_{\mathbf{d}}}{\text{minimize}} \quad f(\mathbf{d}), \tag{2.21a}$$

  $$\text{such that} \quad c_{k,\ell}(\mathbf{d}) \geq \varepsilon, \tag{2.21b}$$

  where ε is some positive constant. Note that the values and sensitivities of the constraints (2.21b) are very easy to compute using (2.18).

- Repeat the steps above by replacing $\mathbf{d}_0$ with $\mathbf{d}_1$, and stop when convergence.

Remark 5. We note that

(i) The linearized Winslow functional presented in Section 2.1.3 and the quasi-conformal deformation presented in Section 2.1.4 are among the methods that fulfill the condition related to (2.17).

(ii) In J. Gravesen et al. [28], any parametrization of a 2D B-spline patch with a corner having angle more than π is invalid. Therefore, it is necessary to constrain the angles. Fortunately, they are already included in the constraints (2.21b) as those on the corner control points of the Jacobian determinant ensure the "validity" of the corresponding angles.

(iii) One problem of shape optimization using isogeometric analysis has been encountered in fluid mechanics is the clustering of control points [28]. This requires some special treatment [28]. Interestingly, without extra efforts the algorithm above avoids this issue. Indeed, since the the boundary control points of the Jacobian determinant are constrained to be positive, the boundary parametrization must be locally regular.

2.3 Multiple methods of extending parametrization from boundary to interior

For some problems, there are regions which can be parametrized in a simple and effective way. For such a case, it is not necessary to employ more complicated and expensive methods to extend the parametrization from the boundaries to the interiors of those regions. Thus in general we can have different parametrization extension methods for different regions. See Fig. 7.10 and Fig. 7.13 for illustrations of the argument.

For the sake of deriving sensitivity later on and implementation, let us formulate the general configuration. Let Ω be a connected domain. Assume that according to parametrization extension, Ω can be partitioned into N sub-domains Ω_k, $k = 1, \ldots, N$. Each sub-domains are comprised of several spline patches. Let $\mathbf{d}$ be the design variable vector and $\mathbf{d}_k$ be the control point vector of $\partial\Omega_k$. The first task for the algorithm is to determine affine maps that sending $\mathbf{d}$ to $\mathbf{d}_k$ as

$$\mathbf{d}_k = \mathbf{a}_k\mathbf{d} + \mathbf{b}_k. \tag{2.22}$$

The next task will be to derive affine transformations that map $\mathbf{d}_k$ to unknown inner control points of Ω_k, and therefore to the control point vector $\mathbf{d}_k$ of Ω_k

$$\widehat{\mathbf{d}}_k = \mathbf{A}_k\mathbf{d}_k + \mathbf{B}_k = \mathbf{A}_k\mathbf{a}_k\mathbf{d} + \mathbf{A}_k\mathbf{b}_k + \mathbf{B}_k. \tag{2.23}$$

Note that the refinement matrices [24] obtained when inserting knots into the boundary knot vectors to have parametrization knot vectors are already taken into account in $\mathbf{A}_k$. If for some sub-domain Ω_k, the parametrization extension method used in this domain is guaranteed to result in a valid parametrization then the constraints (2.21b) with respect to this domain should be removed to reduce computational time consume.

2.4 Sensitivity analysis

Let the governing system of linear algebraic equations for the numerical model under consideration be the following

$$\mathbf{K}\mathbf{h} = \mathbf{f}, \tag{2.24}$$

where $\mathbf{h}$ is the vector of state variables, i.e., the coefficients of the representation of the numerical solution in terms of the basis functions given by (1.25). If the objective function or a

constraint of the considered shape optimization relates to an integral over a domain Ω_0, then very often we can keep the parametrization of Ω_0 fixed, i.e., independent from changes of design control points, e.g., see Fig. 7.11. Thus to determine the partial derivative of a function with respect to a design variable $\hat{d}_i$, we only need to determine $\frac{\partial \mathbf{h}}{\partial \hat{d}_i}$. Differentiating both sides of (2.24), the partial derivative is in turn the solution to the following linear system

$$\mathbf{K}\frac{\partial \mathbf{h}}{\hat{d}_i} = -\frac{\partial \mathbf{K}}{\hat{d}_i}\mathbf{h} + \frac{\partial \mathbf{f}}{\hat{d}_i}. \tag{2.25}$$

In (2.25), the partial derivatives of $\mathbf{K}$ and $\mathbf{f}$ with respect to $\hat{d}_i$ can often be calculated straightforwardly. Finally, as we employ linear parametrization methods formulated in (2.23), the desired sensitivities are

$$\frac{\partial I}{\partial \mathbf{d}} = \mathbf{a}_1^T \mathbf{A}_1^T \frac{\partial I}{\partial \widehat{\mathbf{d}}_1} + \ldots + \mathbf{a}_N^T \mathbf{A}_N^T \frac{\partial I}{\partial \widehat{\mathbf{d}}_N}. \tag{2.26}$$

Part II

Prescription for first few eigenvalues of the Laplacian operator

Chapter 3

Isogeometric shape optimization of vibrating membranes

Nguyen D. M., A. Evgrafov, A.R. Gersborg, J. Gravesen, Isogeometric shape optimization of vibrating membranes, *Computer Methods in Applied Mechanics and Engineering*, vol. 200, pp. 1343-1353, 2011.

Abstract. We consider a model problem of isogeometric shape optimization of vibrating membranes whose shapes are allowed to vary freely. The main obstacle we face is the need for robust and inexpensive extension of a spline parametrization from the boundary of a domain onto its interior, a task which has to be performed in every optimization iteration. We experiment with two numerical methods (one is based on the idea of constructing a quasi-conformal mapping, whereas the other is based on a spring-based mesh model) for carrying out this task, which turn out to work sufficiently well in the present situation. We perform a number of numerical experiments with our isogeometric shape optimization algorithm and present smooth, optimized membrane shapes. Our conclusion is that isogeometric analysis fits well with shape optimization.

Keywords: Isogeometric analysis, shape optimization, spline parametrization, vibrating membrane, eigenvalue.

3.1 Introduction

Shape optimization is a classical mathematical problem with a multitude of applications in engineering disciplines; see for example the monographs [34, 35] and references therein. From the theoretical perspective, the most interesting cases occur when the shapes under consideration are not restricted to be diffeomorphic to each other, that is, when changes in the topology are allowed. Such problems are often treated by parametrizing the shape indirectly, using for example the coefficients of the partial differential equation governing an engineering model under consideration (control in the coefficients, homogenization, or topology optimization approaches, see [36, 37]) or auxiliary surfaces such as in level-set methods, see [38]. All the mentioned methods gain their computational efficiency from the fact that they are based on fixed grids, which provides a tremendous advantage particularly in 3D.

Having industrial applications in mind, it would be convenient to integrate geometry optimization into CAD environments. For this to be possible one needs to utilize a direct CAD-like representations of the boundary. Such a representation should be maintained at every optimization iteration by shape optimization methods at the expense of needing to re-generate or

to update frequently the volumetric mesh, which is needed for solving equations governing a given system. This expense imposes a computational penalty on the total performance of shape optimization methods.

One promising method of combining the efficiency of the computations on a fixed grid with the demand of a direct CAD-like parametrization of the boundary within the shape optimization framework is utilizing isogeometric analysis (IGA) for numerically solving the equations governing a given engineering system [6, 39, 40, 41, 11, 18, 42, 13]. In this way one keeps all the computations on a fixed mesh on a parameter domain while gaining the advantage that optimized geometries can be easily processed in CAD systems for manufacturing [6, 7].

In the present paper we utilize isogeometric analysis-based shape optimization (IGSO) for designing vibrating membranes with prescribed eigenvalues. We treat vibrating membranes as as a model problem for more general spectral shape optimization problems of systems governed by elliptic operators [43, 44]. It is also closely related to eigenfrequency optimization problems of vibrating plates with holes [19, 20, 45]. The problem of designing vibrating membranes is by no means a novel one: for example Hutchinson and Niordson [46] computed shapes of drums where the first few eigenvalues were prescribed. In particular, they considered the design problem of a harmonic drum, namely, a membrane whose first four eigenfrequencies form a ratio of 2:3:3:4. (The reason for the double eigenvalues is that it seems impossible to design a drum with frequencies 2:3:4 [47, 43, 48]). The idea in [46] was to use a conformal map from the circular domain to the domain occupied by the drum and to perform the eigenfrequency analysis on the former domain. Note that this idea is similar to IGA in the sense that a parametrization of the domain is utilized. Kane and Schoenauer [49] later attacked the problem by genetic algorithms, while in the present work we utilize gradient-based algorithms within the IGSO framework. We emphasize that we consider the problem as a model on which we can illustrate various re-parametrization strategies within IGSO context.

In the present work, the only generic requirement we place on a family of candidate feasible shapes in the shape optimization problems we consider is that they are diffeomorphic to each other. Whereas this requirement may be viewed as a restrictive one from the theoretical perspective, it is much more general than what is often considered within the shape optimization framework and leads to certain computational challenges. This is in a stark contrast with the situations when domain families parametrized by only a few variables are consedered (such as, for example, a circle of a varying radius [17, 18], or a family of super-elliptical shapes [19, 20]), or when only certain parts of the boundary are allowed to vary locally [21, 17, 11, 13]. Restrictions on the variations of the shape simplify significantly the task of remeshing in a FEM-based shape optimization, or the task of extending the parametrization from the boundary into the interior of the domain in IGSO-based shape optimization.

Owing to the richness of the family of shapes which we allow, constructing the expension of parametrization from the boundary into the interior of the domain becomes a non-trivial task in the present situation. We experiment with two linear methods for computing such an extension numerically: one is based on a spring model of the mesh and the other one is based on the idea of a quasi-conformal deformation. The former method is inspired by ideas coming from linear elasticity and works well for problems with convex domains. The strategy for the latter method is to find a well-behaving spline parametrization of an initial reference shape by solving auxiliary optimization problems, and then generate the inner control points by "quasi-conformally deforming" the reference shape into the resulting configuration. The procedure is repeated if an invalid parametrization appears at some shape optimization iteration.

The remainder of this paper is organized as follows. In Section 2, we briefly recall the equations governing vibrating membranes and their Galerkin discretization. The IGA model used in the present work and necessary techniques of handling a spline parametrization are presented in Section 3. In Section 4, we state the IGSO problem formulation and its sensitivity

analysis. Our numerical experiments with IGSO are reported in Section 5. We conclude the paper with a summary of the results.

3.2 Physical problem

In this section we briefly recall the partial differential equations governing harmonic oscillations of a membrane and their Galerkin discretization.

3.2.1 Governing equation

Let Ω be a membrane whose circumference Γ is constrained to be motionless. The out-of-plane displacement $U(\mathbf{x}, t)$ of a point $\mathbf{x} \in \Omega$ at time t obeys the wave equation with homogeneous Dirichlet boundary condition

$$\frac{\partial^2 U(\mathbf{x}, t)}{\partial t^2} = c^2 \Delta U(\mathbf{x}, t) \qquad \forall\, \mathbf{x} \in \Omega \tag{3.1}$$

$$U(\mathbf{x}, t) = 0 \qquad \forall\, \mathbf{x} \in \Gamma \tag{3.2}$$

where Δ is the spatial Laplacian operator and c is the wave speed, depending on the tension and the surface density of the membrane (c.f. [50]). Without losing generality, in what follows we assume that $c = 1$.

The time-harmonic solutions to (3.1) having the form

$$U(\mathbf{x}, t) = u(\mathbf{x}) e^{i\sqrt{\lambda} t}, \tag{3.3}$$

where $i^2 = -1$ and $\lambda = (2\pi f)^2$ with f being the vibration frequency, are the pure tones the membrane is capable of producing (c.f. [51, 46]).

Substituting (3.3) into (3.1) and (3.2) we recover Helmholtz equation with Dirichlet boundary condition

$$\Delta u + \lambda u = 0 \qquad \text{in } \Omega \tag{3.4}$$

$$u = 0 \qquad \text{on } \Gamma. \tag{3.5}$$

The eigenfunctions u are customarily normalized so that $\int\limits_{\Omega} u^2 \,\mathrm{d}V = 1$.

3.2.2 Weak form and discretization

Let $H_0^1(\Omega)$ be the subspace of the Sobolev space $H^1(\Omega)$ (c.f. [26]) containing functions which vanish on the boundary. In its weak form, the homogeneous boundary value problem (3.4), (3.5) can be stated as follows: find $u \in H_0^1(\Omega)$ such that for every $v \in H_0^1(\Omega)$ it holds that

$$\int\limits_{\Omega} \nabla u \cdot \nabla v \,\mathrm{d}V = \lambda \int\limits_{\Omega} uv \,\mathrm{d}V. \tag{3.6}$$

Applying the Galerkin method (c.f. [2]) to (3.6) by approximating $H_0^1(\Omega)$ with conforming finite-dimensional subspaces to be described in Section 3.3.1 one arrives at the following generalized eigenvalue problem:

$$\mathbf{K}\mathbf{u} = \lambda \mathbf{M}\mathbf{u} \tag{3.7}$$

where $\mathbf{K}$ and $\mathbf{M}$, are the stiffness and the mass matrices, respectively. The eigenvectors in (3.7) are customarily normalized as

$$\mathbf{u}^T \mathbf{M}\mathbf{u} = 1. \tag{3.8}$$

Later on, components of $\mathbf{u}$ will be referred to as the *state variables* to distinguish them from *design variables*.

3.3 Isogeometric Analysis

Isogeometric analysis (IGA) has recently been introduced by Hughes et al. [6] and has already found many applications in a variety of engineering disciplines [7]. The basic idea of IGA is to parametrize the domain, its boundary, and the solution space using B-splines defined by a single pair of knot vectors. For the purposes of isogeometric shape optimization this approach is modified, as described in the present section. We also discuss several approaches towards extending B-spline parametrizations from the boundary of the domain into its interior, validating the resulting parametrization, and improving its quality.

3.3.1 Isogeometric analysis model

Let us consider a simply connected domain $\Omega \subset \mathbb{R}^2$. In the present work, we use three different pairs of knot vectors for parametrizing the boundary $\Gamma = \partial\Omega$, the domain Ω, and the solution space for (3.6), see Fig. 3.1. Our starting point is the pair of knot vectors $\boldsymbol{\Xi}_u$ and $\boldsymbol{\Xi}_v$ parametriz-

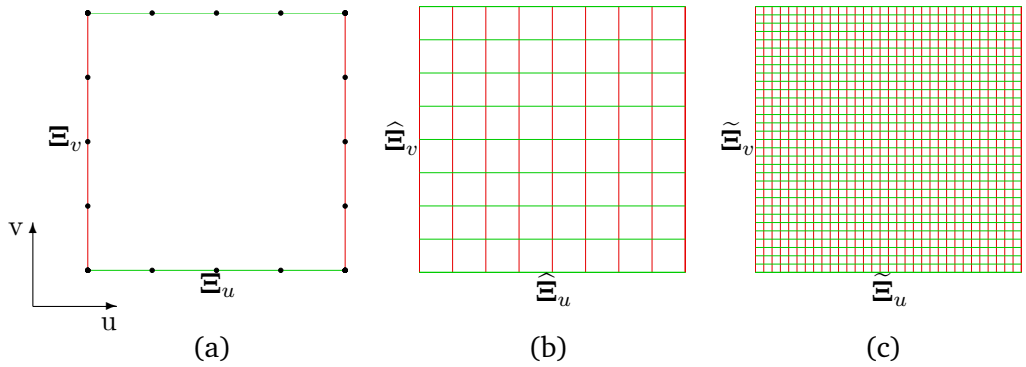

(a) (b) (c)

Figure 3.1: Three pairs of knot vectors of the IGA model used in the present work. (a): Knot vectors for the boundary parametrization; (b): knot vectors for the domain parametrization; (c): knot vectors for the solution space parametrization. The green and red lines correspond to horizontal and vertical parameter lines, respectively.

ing the domain boundary with B-splines of degrees p and q. Let $\boldsymbol{\rho}_b$ be the vector of the control point components of the boundary parametrization.

The second step is extending the boundary parametrization onto the interior of the domain Ω. Here we may use a "finer" pair of knot vectors $\widehat{\boldsymbol{\Xi}}_u$ and $\widehat{\boldsymbol{\Xi}}_v$, obtained by inserting new knots into the knot vectors $\boldsymbol{\Xi}_u$ and $\boldsymbol{\Xi}_v$ respectively. The vector $\widehat{\boldsymbol{\rho}}_b$ containing components of the resulting boundary control points is obtained as

$$\widehat{\boldsymbol{\rho}}_b = \mathbf{T}\,\boldsymbol{\rho}_b, \tag{3.9}$$

where $\mathbf{T}$ is a constant matrix depending only on the knot vectors [24]. Given the vector of the boundary control points $\widehat{\boldsymbol{\rho}}_b$ one may determine the inner control points $\widehat{\mathbf{d}}_{i,j}$, $i = 1, \ldots, \widehat{n}$, $j = 1, \ldots, \widehat{m}$ (the precise procedure will be discussed in Section 3.3.3). In turn, they parametrize the domain $\Omega = \{\, \mathbf{x} \in \mathbb{R}^2 \mid \mathbf{x} = \mathbf{F}(u,v),\ (u,v) \in [0,1]^2 \,\}$, where

$$\mathbf{F}(u,v) = \sum_{i=1}^{\widehat{m}} \sum_{j=1}^{\widehat{n}} \widehat{\mathbf{d}}_{i,j} \widehat{M}_i^p(u) \widehat{N}_j^q(v). \tag{3.10}$$

In (3.10), $\widehat{M}_i^p$ and $\widehat{N}_i^q$ are B-splines of degree p and q with the knot vectors $\widehat{\boldsymbol{\Xi}}_u$ and $\widehat{\boldsymbol{\Xi}}_v$, respectively.

Suppose that the map $\mathbf{F}$ in (3.10) is found to be a parametrization of Ω, that is, the determinant of its Jacobian is *positive* (or negative) everywhere. Let $\mathbf{F}^{-1} : \Omega \to [0,1]^2$ be the inverse of $\mathbf{F}$. The solution space $\mathcal{S}$ approximating $H_0^1(\Omega)$ will be defined in terms of functions $\widetilde{R}_k^{\widetilde{p},\widetilde{q}} : [0,1]^2 \to \mathbb{R}$, $k = 1,\dots,\widetilde{m}\widetilde{n}$ and $\mathbf{F}^{-1}$ as $\mathcal{S} = \operatorname{span}\{\widetilde{R}_k^{\widetilde{p},\widetilde{q}} \circ \mathbf{F}^{-1} |\, k = 1,\dots,\widetilde{m}\widetilde{n}\}$. To ensure that we can approximate any function in $H_0^1(\Omega)$ sufficiently well, we may want to use an even finer (when compared to $\widehat{\boldsymbol{\Xi}}_u$ and $\widehat{\boldsymbol{\Xi}}_v$) pair of knot vectors $\widetilde{\boldsymbol{\Xi}}_u$ and $\widetilde{\boldsymbol{\Xi}}_v$, see Fig. 3.1. Thus we define $\widetilde{M}_i^{\widetilde{p}}$, $i = 1,\dots,\widetilde{m}$ and $\widetilde{N}_j^{\widetilde{q}}$, $j = 1,\dots,\widetilde{n}$ as the B-splines of degree $\widetilde{p}$ and $\widetilde{q}$ (not neccesary equal to p and q) with the knot vector $\widetilde{\boldsymbol{\Xi}}_u$ and $\widetilde{\boldsymbol{\Xi}}_v$, respectively. Finally, the splines $\widetilde{R}_k^{\widetilde{p},\widetilde{q}}$ involved in the definition of $\mathcal{S}$ are defined as the tensor product splines $\widetilde{R}_k^{\widetilde{p},\widetilde{q}}(u,v) = \widetilde{M}_i^{\widetilde{p}}(u)\widetilde{N}_j^{\widetilde{q}}(v)$, $k = (\widetilde{n}-1)i + j$. Given the structure of $\mathcal{S}$, the entries of the stiffness and mass matrices in the discretized form (3.7) are computed as where $\mathbf{J}$ is the Jacobian of the parametrization $\mathbf{F}$ and $\mathbf{D}f(u,v) = \begin{bmatrix} \frac{\partial f}{\partial u}(u,v) & \frac{\partial f}{\partial v}(u,v) \end{bmatrix}$ is the differential of a real-valued function $f : [0,1]^2 \to \mathbb{R}$.

3.3.2 Validating a spline parametrization

In order to ensure that a given choice of inner control points $\widehat{\mathbf{d}}_{i,j}$, $i = 1,\dots,\widehat{n}$, $j = 1,\dots,\widehat{m}$ results in a valid spline parametrization of Ω we employ the following approach.

The determinant of a Jacobian of $\mathbf{F}$ given by (3.10) is computed as

$$\det(\mathbf{J}) = \sum_{i,j=1}^{\widehat{m},\widehat{n}} \sum_{k,\ell=1}^{\widehat{m},\widehat{n}} \det[\widehat{\mathbf{d}}_{i,j}, \widehat{\mathbf{d}}_{k,\ell}] \, \frac{\mathrm{d}\widehat{M}_i^p(u)}{\mathrm{d}u} \, \widehat{N}_j^q(v) \, \widehat{M}_k^p(u) \, \frac{\mathrm{d}\widehat{N}_\ell^q(v)}{\mathrm{d}v}, \tag{3.11}$$

where $\det[\widehat{\mathbf{d}}_{i,j}, \widehat{\mathbf{d}}_{k,\ell}]$ is the determinant of the 2×2 matrix with columns $\widehat{\mathbf{d}}_{i,j}$, $\widehat{\mathbf{d}}_{k,\ell}$. Equation (3.11) defines a piecewise polynomial of degree $2p-1$ in u and degree $2q-1$ in v, with the differentiability at a knot lower by 1 in u and also lower by 1 in v. Such a map can be written in terms of B-splines $\mathcal{M}_k^{2p-1}$ and $\mathcal{N}_\ell^{2q-1}$ of degree $2p-1$ and $2q-1$ with the knot vectors obtained from $\widehat{\boldsymbol{\Xi}}_u$ and $\widehat{\boldsymbol{\Xi}}_v$ by raising the multiplicities of the inner u-knots and v-knots by p and q, respectively [52]. That is

$$\det(\mathbf{J}) = \sum_{k,\ell=1}^{M,N} c_{k,\ell} \, \mathcal{M}_k^{2p-1}(u) \, \mathcal{N}_\ell^{2q-1}(v), \tag{3.12}$$

where the coefficients $c_{k,\ell}$ depend linearly on the quantities $\det[\widehat{\mathbf{d}}_{i,j}, \widehat{\mathbf{d}}_{k,\ell}]$. Equation (3.12) tells us that if all $c_{k,\ell}$ are positive, then so is the determinant.

3.3.3 Extending a spline parametrization from the boundary to the interior domain

The only part needed to complete our IGA model of the vibrating membrane is the computation of interior control points $\widehat{\mathbf{d}}_{i,j}$ defining $\mathbf{F}$ from the vector of boundary control points $\widehat{\boldsymbol{\rho}}_b$. Since we have to perform this calculation during every shape optimization iteration, we are looking for computationally inexpensive methods, which would preferably result in parametrizations (in the sense of Section 3.3.2) of the domain. Two methods described in the following subsections perform relatively well in both categories, in our computational experience. Both methods are linear, that is, they can be written as

$$\widehat{\boldsymbol{\rho}} = \mathbf{G} \, \widehat{\boldsymbol{\rho}}_b, \tag{3.13}$$

for some matrix $\mathbf{G}$, where $\widehat{\boldsymbol{\rho}}$ is the vector containing all components of all control points $\widehat{\mathbf{d}}_{i,j}$.

3.3.3.1 The spring model

Imagine that the edges of the control net are replaced by equally stiff linear elastic springs. Then the locations of the inner control boundary nodes $\widehat{\mathbf{d}}_{i,j}$ at the static force equilibrium, which are uniquely determined by the positions of the boundary control nodes, are the locations taken by this method. More precisely, $\widehat{\mathbf{d}}_{i,j}$ satisfy the equations

$$\widehat{\mathbf{d}}_{i,j} = (\widehat{\mathbf{d}}_{i,j-1} + \widehat{\mathbf{d}}_{i+1,j} + \widehat{\mathbf{d}}_{i,j+1} + \widehat{\mathbf{d}}_{i-1,j})/4, \tag{3.14}$$

where $\widehat{\mathbf{d}}_{i,j-1}$, $\widehat{\mathbf{d}}_{i+1,j}$, $\widehat{\mathbf{d}}_{i,j+1}$, and $\widehat{\mathbf{d}}_{i-1,j}$ are the neighbouring nodes attached to $\widehat{\mathbf{d}}_{i,j}$ with imaginary springs. Being diagonally dominant and irreducible, this system of linear equations admits a unique solution.

3.3.3.2 The quasi-conformal deformation

Assume we have found a reference control net with desirable properties, in particular of being a parametrization of the domain. Let $\widehat{\mathbf{v}}$ and $\widehat{\mathbf{w}}$ be two adjacent edges of the control net as depicted in Fig. 3.2. The rotation matrix $\mathbf{R}(\widehat{\theta})$, with $\widehat{\theta}$ being the angle between $\widehat{\mathbf{v}}$ and $\widehat{\mathbf{w}}$, enjoys

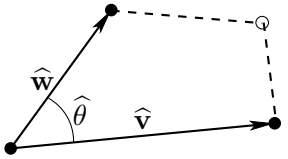

Figure 3.2: A local configuration in a reference control net

the identity

$$\|\widehat{\mathbf{w}}\|\mathbf{R}(\widehat{\theta})\widehat{\mathbf{v}} = \|\widehat{\mathbf{v}}\|\widehat{\mathbf{w}}. \tag{3.15}$$

Consider now a new control net with $\mathbf{v}$ and $\mathbf{w}$ being the adjacent edges corresponding to $\widehat{\mathbf{v}}$ and $\widehat{\mathbf{w}}$ of the reference control net. For each such pair of edges we consider linear equations

$$\|\widehat{\mathbf{w}}\|\mathbf{R}(\widehat{\theta})\mathbf{v} = \|\widehat{\mathbf{v}}\|\mathbf{w}. \tag{3.16}$$

The resulting linear system is overdetermined (there are $8(\widehat{m}-2)(\widehat{n}-2)$ equations with only $2(\widehat{m}-2)(\widehat{n}-2)$ unknown nodal positions) and is solved in the least squares sense.

3.3.4 Improving a spline parametrization

As none of the linear methods for extending the parametrization of the boundary into the interior of the domain can in general guarantee that the resulting map $\mathbf{F}$ will satisfy $\det(\mathbf{J}) > 0$ everywhere on $[0,1]^2$, sometimes we have to utilize a more expensive non-linear method for improving the distribution of the interior control points $\widehat{\mathbf{d}}_{i,j}$. One natural approach to ensure that $\det(\mathbf{J})$ is bounded away from zero is, by virtue of (3.12), to solve the following optimization problem:

$$\begin{aligned} &\underset{\widehat{\mathbf{d}}_{i,j},z}{\text{maximize}} && z, \\ &\text{subject to} && c_{k,\ell}\big(\widehat{\mathbf{d}}_{i,j}\big) \geq z, \end{aligned} \tag{3.17}$$

where $\widehat{\mathbf{d}}_{i,j}$ are inner control points as stated in (3.10), $c_{k,\ell}$ are given by (3.12), and z is an auxiliary optimization variable. If z resulting from approximately solving (3.17) to local optimality is positive then we are guaranteed to have a valid parametrization. Unfortunately, the quality of the parametrization obtained in this fashion needs not to be very high. We can further improve

the parametrization by trying to approximate a conformal map. That is, ideally we would like $\mathbf{g} = \mathbf{J}^T\mathbf{J}$ to be an identically diagonal matrix (e.g., see [32]).

Let λ_1 and λ_2 be the eigenvalues of the matrix $\mathbf{g}$. Then $\mathbf{g}$ satisfies the ideal condition if and only if $\lambda_1 = \lambda_2$. The identity

$$\frac{(\sqrt{\lambda_1} - \sqrt{\lambda_2})^2}{\sqrt{\lambda_1\lambda_2}} = \frac{\lambda_1 + \lambda_2}{\sqrt{\lambda_1\lambda_2}} - 2 \tag{3.18}$$

gives rise to *Winslow functional* [31]

$$W = \frac{\lambda_1 + \lambda_2}{\sqrt{\lambda_1\lambda_2}} = \frac{\operatorname{trace}(\mathbf{g})}{\sqrt{\det(\mathbf{g})}} = \frac{\|\mathbf{F}_u\|^2 + \|\mathbf{F}_v\|^2}{\det[\mathbf{F}_u, \mathbf{F}_v]}. \tag{3.19}$$

In order to make $\mathbf{g}$ "as identically diagonal as possible" we would like to minimize W; however, to ensure the positivity of the determinant we consider the following constrained optimization problem:

$$\begin{aligned} \underset{\widehat{\mathbf{d}}_{i,j}}{\text{minimize}} \quad & \int_0^1 \int_0^1 W\big(\widehat{\mathbf{d}}_{i,j}\big)\,\mathrm{d}u\,\mathrm{d}v, \\ \text{subject to} \quad & c_{k\ell}\big(\widehat{\mathbf{d}}_{i,j}\big) \geq \delta z_0. \end{aligned} \tag{3.20}$$

In (3.20), $z_0 > 0$ is computed by approximately solving (3.17) and $\delta \in [0, 1]$ is a fixed relaxation parameter. For further properties of the problem (3.20), we refer the interested reader to [**?**].

In our numerical experiments we utilize Matlab's optimization framework for solving optimization problems (3.17), (3.20) to approximate stationarity. Also, we set $\delta = 0$ in (3.20).

3.4 Isogeometric shape optimization problem

We consider the problem of finding a shape of a membrane where the first N eigenfrequencies (eigenvalues of the Laplacian) are prescribed. For simplicity we restrict ourselves to domains constituted by one patch. We first discuss different formulations of such a shape optimization problem, and then its sensitivity analysis is carried out.

3.4.1 Problem formulation

The shape of the membrane is fully determined given the parametrization of the boundary. Therefore we let boundary control points be our design variables. One may also require some regularity from the resulting shape; for example, one may be interested in membranes bounded with tangent continuous curves. The latter requirement can be easily fulfilled by enforcing simple constraints on the boundary control points, see [24]. Furthermore, "one can not hear the shape of a drum," that is, even if an (admissible) full spectrum is prescribed there could be more than one shape of a membrane that matches it [53]. Therefore, one may expect that there is more than one shape that matches the prescribed few eigenvalues. In order to further restrict the shapes generated by our optimization procedure, we search for a shape, which in addition to satisfying the eigenvalue constraints also has the shortest perimeter. Fig. 3.3 illustrates the issue. Using this regularization idea, we arrive at the following shape optimization problem:

$$\underset{\boldsymbol{\rho}_b, z}{\text{minimize}} \quad L(\boldsymbol{\rho}_b), \tag{3.21a}$$

$$\text{subject to} \quad \lambda_k(\boldsymbol{\rho}_b) = \lambda_k^0, \qquad \text{if } \lambda_k^0 \text{ has multiplicity one}, \tag{3.21b}$$

$$\begin{cases} \lambda_k(\boldsymbol{\rho}_b) + \lambda_{k+1}(\boldsymbol{\rho}_b) = \lambda_k^0 + \lambda_{k+1}^0 \\ \lambda_k(\boldsymbol{\rho}_b)\lambda_{k+1}(\boldsymbol{\rho}_b) = \lambda_k^0\lambda_{k+1}^0 \end{cases} \qquad \text{if } \lambda_k^0 = \lambda_{k+1}^0, \tag{3.21c}$$

$$\det[\mathbf{d}_2^j - \mathbf{d}_1^j, \mathbf{d}_2^j - \mathbf{d}_3^j] = 0, \qquad j = 1, \ldots, 4, \tag{3.21d}$$

$$\text{where} \quad \mathbf{K}(\boldsymbol{\rho}_b)\mathbf{u}_k = \lambda_k(\boldsymbol{\rho}_b)\mathbf{M}(\boldsymbol{\rho}_b)\mathbf{u}_k, \qquad \text{for some } \mathbf{u}_k \neq \mathbf{0}, k = 1, \ldots, N, \tag{3.21e}$$

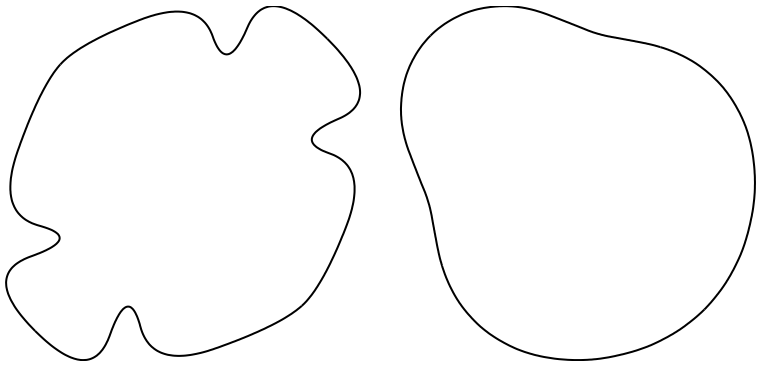

Figure 3.3: Membranes on the left and on the right have the same five lowest eigenfrequencies, prescribed to be $5.0122, 11.6349, 13.4102, 20.6025$ and 23.6877. The shape on the right (a "pear-shaped" region [46]) was obtained by minimizing the perimeter of the domain.

where, $L = L(\boldsymbol{\rho}_b)$ is the perimeter of the shape, λ_k^0, $k = 1, \ldots, N$, are prescribed values for the first N eigenvalues, and $\boldsymbol{\rho}_b$ are the boundary control points given by (3.9). The constraints (3.21c) are introduced to handle problems with double eigenvalues, c.f. [54]; and the constraints (3.21d) result from enforcing the continuous tangent condition of the boundary at four corners of $[0,1]^2$, in which $\mathbf{d}_1^j$, $\mathbf{d}_2^j$, $\mathbf{d}_3^j$ is the triple of boundary control points corresponding to the corners.

3.4.2 Sensitivity analysis

In order to utilize gradient-based optimization algorithms for solving (3.21) numerically, we need to compute derivatives of the constraints entering (3.21) with respect to changes in boundary control points. If the eigenvalues involved in a constraint have multiplicity one, then one may derive, using (3.7) and (3.8), that

$$\frac{\partial \lambda_k}{\partial \widehat{\rho}} = \mathbf{u}_k^T \left(\frac{\partial \mathbf{K}}{\partial \widehat{\rho}} - \lambda_k \frac{\partial \mathbf{M}}{\partial \widehat{\rho}} \right) \mathbf{u}, \tag{3.22}$$

where $\widehat{\rho}$ is an arbitrary component of the vector $\widehat{\boldsymbol{\rho}}$, and λ_k and $\mathbf{u}_k$ are an eigenvalue and an eigenvector of (3.7), (3.8). However, if the multiplicity of an eigenvalue λ_k may change during the optimization process, then the individual eigenvalues may not be differentiable functions of the design variables any longer. Nevertheless, it may still be possible to differentiate certain functions of the eigenvalues. It can be shown [54] that the sensitivities of the functions $\lambda_k + \lambda_{k+1}$ and $\lambda_k \lambda_{k+1}$ are given as

$$\frac{\partial(\lambda_k + \lambda_{k+1})}{\partial \widehat{\rho}} = \mathbf{u}_k^T (\frac{\partial \mathbf{K}}{\partial \widehat{\rho}} - \lambda_k \frac{\partial \mathbf{M}}{\partial \widehat{\rho}}) \mathbf{u}_k + \mathbf{u}_{k+1}^T (\frac{\partial \mathbf{K}}{\partial \widehat{\rho}} - \lambda_{k+1} \frac{\partial \mathbf{M}}{\partial \widehat{\rho}}) \mathbf{u}_{k+1}, \tag{3.23}$$

$$\frac{\partial(\lambda_k \lambda_{k+1})}{\partial \widehat{\rho}} = \lambda_{k+1} \mathbf{u}_k^T (\frac{\partial \mathbf{K}}{\partial \widehat{\rho}} - \lambda_k \frac{\partial \mathbf{M}}{\partial \widehat{\rho}}) \mathbf{u}_k + \lambda_k \mathbf{u}_{k+1}^T (\frac{\partial \mathbf{K}}{\partial \widehat{\rho}} - \lambda_{k+1} \frac{\partial \mathbf{M}}{\partial \widehat{\rho}}) \mathbf{u}_{k+1}. \tag{3.24}$$

From (3.9) and (3.13), it follows that if the partial derivative of a function f with respect to $\widehat{\rho}$ has been calculated as above, its sensitivities with respect to the design variables $\boldsymbol{\rho}_b$ are given by

$$\frac{\partial f}{\partial \boldsymbol{\rho}_b} = \frac{\partial f}{\partial \widehat{\boldsymbol{\rho}}_b} \mathbf{T} = \frac{\partial f}{\partial \widehat{\boldsymbol{\rho}}} \mathbf{G}\, \mathbf{T}. \tag{3.25}$$

Other methods of dealing with multiple eigenvalues are discussed in [55, 56, 57, 58].

3.5 Numerical examples

In this section, we discuss our strategy for solving (3.21), and then illustrate its practical performance by solving a few shape optimization problems for vibrating membranes.

3.5.1 Solution strategy

We use the following approach for solving (3.21):

1. *Preparing a good initial shape*: We want to find a good initial shape in a "cheap" way and use it for more expensive computational work. To this end, we use a small number of control points to approximately solve (3.21). The constraint tolerance T_{con} is set to be around 10^{-4}–10^{-6}. After a suitable shape is found, we disregard the perimeter, look only at the eigenvalues, and use a very small constraint tolerance T_{con} around 10^{-14}–10^{-16}. After a feasible initial shape is found, we refine the computational grid by inserting more knots into the knot vectors.

2. *Improving the initial parametrization*: If the quasi-conformal deformation method is chosen, the control net of the initial shape will be used as the reference configuration during the optimization iterations. Since the mesh regularity affects the accuracy of the numerical solution [40, 59], it is necessary to improve the parametrization of the reference configuration as discussed in Section 3.3.4. Fig. 3.10 demonstrates the necessity.

3. *Performing optimization*: We determine the knot vectors $\widetilde{\boldsymbol{\Xi}}_u$ and $\widetilde{\boldsymbol{\Xi}}_v$ by halving the knot intervals of the knot vectors $\widehat{\boldsymbol{\Xi}}_u$ and $\widehat{\boldsymbol{\Xi}}_v$ several times such that further halving does not change the calculated eigenvalues by more than a given tolerance T_{cv}. The optimization problem is then solved numerically with the obtained knot vectors and initial shape.

Throughout the present work, numerical integration is done by using standard Gaussian quadratures. The homogeneus Dirichlet boundary conditions are enforced by setting the corresponding boundary state variables to zero [6].

All the solutions presented in this section have been obtained with gradient based non-linear programming solver `fmincon`, which is a part of the optimization toolbox of `Matlab`, version 7.5.0 (R2007b) [33].

3.5.2 Pear-shaped region

We start with an example of a membrane with the lowest five eigenvalues prescribed to be 5.0122, 11.6349, 13.4102, 20.6025, and 23.6877. This numerical example has been considered in Hutchinson et al. [46]. The initial shape shown in Fig. 3.4 has been obtained by "rounding" the rectangle $[-3/\pi, 3/\pi] \times [-1, 1]$. This choice of the initial shape ensures that its first five eigenvalues, which are 5.2202, 12.7756, 13.4938, 21.3752, 26.0602, are close to the target ones and have multiplicity one. The latter allows us to avoid the issues with double eigenvalue discussed in Section 3.4. To compute a good initial shape as described in Step (1), Section 3.5.1, we use the same knot vectors for the geometry, parametrization and the solution space

$$\boldsymbol{\Xi}_s = \boldsymbol{\Xi}_t = \widehat{\boldsymbol{\Xi}}_s = \widehat{\boldsymbol{\Xi}}_t = \widetilde{\boldsymbol{\Xi}}_s = \widetilde{\boldsymbol{\Xi}}_t = \{0, 0, 0, 0.25, 0.5, 0.75, 1, 1, 1\}. \tag{3.26}$$

The spring model is used for extending the parametrization from boundary to the interior of the domain. The B-splines for representing the parametrization and solution space are quadratic. This setting yields a 6×6 control net, 16 elements and 16 degrees of freedom (dof). The optimization process with $T_{con} = 10^{-7}$ finishes after 290 iterations. The final shape is shown in Fig. 3.5; its overall features are fairly similar to that of [46].

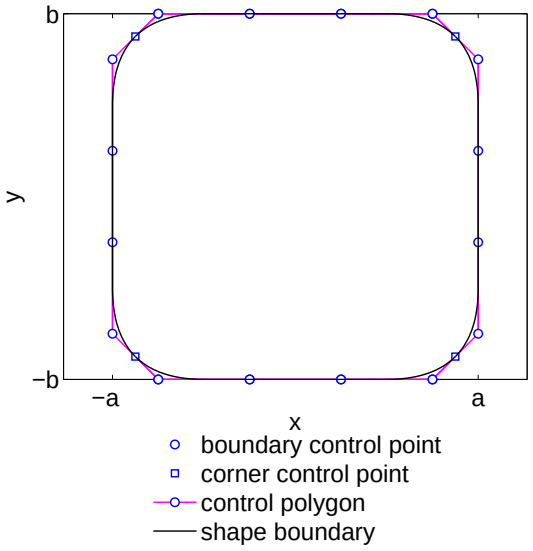

Figure 3.4: Initial shape

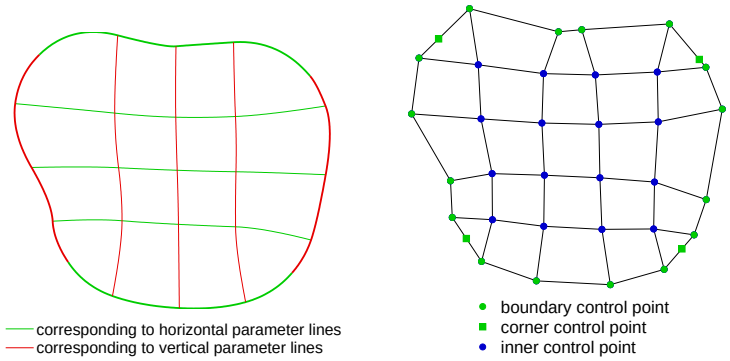

(a) (b)

Figure 3.5: (a): Optimized shape and (b): the corresponding control net of a pear-shape region.

The solution shown in Fig. 3.5 is further refined and is used a new initial design. The refinement is done by halving all knot intervals of all knot vectors. The new setting has 10×10 control points, 64 elements and 64 degrees of freedom. The optimal shape is depicted in Fig. 3.6 (a)–(b); this shape is closer to that of [46].

The optimized shape in Fig. 3.6 (a) is nearly symmetric about the straight line connecting its two opposite corner control points, see Fig. 3.6 (b). To investigate the robustness of the isogeometric shape optimization in preserving a line symmetry, we resolve the shape optimization problem this time explicitly imposing the shape to be symmetric about the line $x + y = 0$. This is done by imposing the boundary control points of the shape to be symmetric about the line. Repeating the same procedure as with the last design (with the same initial shape in Fig. 3.5), but with symmetry constraints, we obtain an optimized shape Fig. 3.6 (c)–(d). Both designs, with and without explicit symmetry constraints, agree very well both qualitatively (Fig. 3.6) and quantitatively (Tab. 3.1).

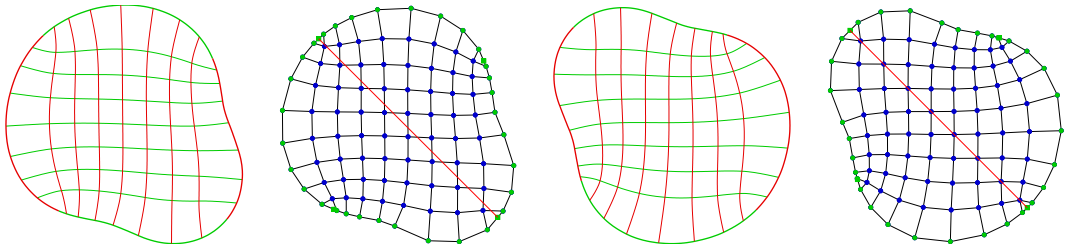

(a) (b) (c) (d)

Figure 3.6: (a), (c): optimized shapes and (b), (d): corresponding control nets for a pear-shaped region example. (a), (b): design computed without explicit symmetry constraints; (c), (d): design computed with explicit symmetry constraint.

Design	$\widetilde{p}$	# var.	dof	# iter.	relative error	perimeter	area
Initial (Fig. 3.6)	2	–	64	–	0.019	7.1592	3.8208
Without sym.	2	72	64	340	6.1×10^{-8}	7.0380	3.7686
With sym.	2	72	64	340	2.3×10^{-9}	7.0378	3.7686

Table 3.1: Quantitative comparison of the optimized pear-shaped membranes without and with explicit enforcing of symmetry. # var.: Number of design variables; # iter.: number of optimization iterations needed to achieve convergence.

3.5.3 Harmonic drums

Another interesting and more challenging example of shape optimization is the problem of finding a shape of a *harmonic drum* [46]. That is, we are looking for a membrane such that when "played" its lowest eigenfrequencies correspond to the notes C_1, G_1, and C_2 on the Pythagorean Scale, c.f. [51, Chapter 4]. Since repeating the second note should not change the sound, we look for a membrane with the first four eigenfrequencies constituting a ratio 2:3:3:4 (c.f. [46]).

3.5.3.1 One patch design

In this example, we start with an initial shape similar to that of the pear-shaped region case, see Fig. 3.5. The only difference is that the rectangle $[-3/\pi, 3/\pi] \times [-1, 1]$ is replaced by the square $[-1, 1]^2$. The first four eigenvalues of the shape are 4.9844, 12.5403, 12.6183 and 20.537. Choosing the second initial eigenvalue as a reference frequency, we calculate the prescribed eigenvalues as 5.5735, 12.5403, 12.5403, and 22.2939. Bi-quadratic B-spline parametrizations with respect to the knot vectors (3.26) are used for the initial design. The extension of a parametrization from the domain boundary to the interior is done by the quasi-conformal deformation method. The first reference configuration is depicted in Fig. 3.7 (a), where we have introduced a slight asymmetry. In our experience, this helps to accelerate the convergence of the optimization algorithm.

The optimized shape is shown in Fig. 3.7. For the resulting control net, we examine the validity of the corresponding parametrization. We compute the coefficients $c_{k,\ell}$ in the expansion of the determinant of its Jacobian, given by (3.12). Only three out of 28561 control points are negative, see Fig. 3.8 (a). Furthermore, after refining the grid, the new coefficients $c_{k,\ell}$ are all positive, see Fig. 3.8 (b).

After neglecting the perimeter and only optimizing eigenvalues, a very similar shape is ob-

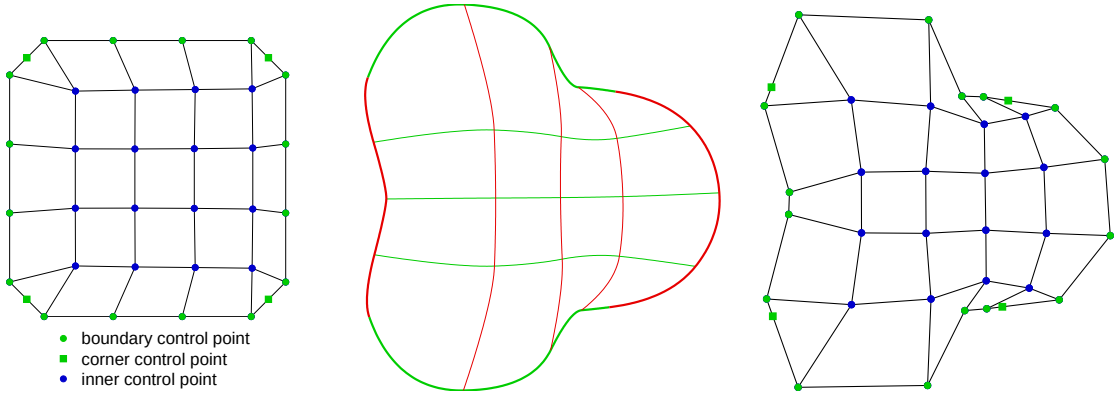

(a) (b) (c)

Figure 3.7: Optimized design of a harmonic drum. (a): Initial reference control net. (b): Optimized shape and (c): the corresponding control net.

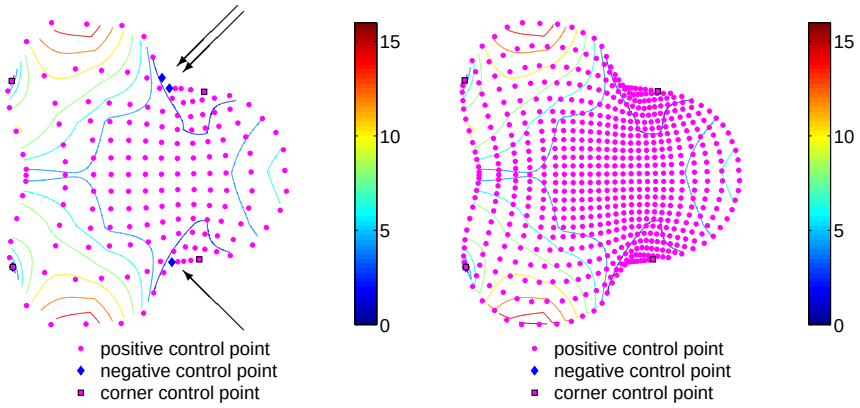

(a) (b)

Figure 3.8: Illustration of the validation of the B-spline parametrization shown in Fig. 3.7. (a): The expansion coefficients and contour lines of the Jacobian determinant corresponding to the original control net; (b): the same for the refined control net.

tained. Refining the grid and starting the optimization algorithm from the last obtained shape we get a drum shown in Fig. 3.9. When we use the control net in Fig. 3.9 as a reference net, we find that an invalid parametrization appeared after a few optimization iterations. Therefore, it is crucial to improve the resulting parametrization utilizing either the optimization problem (3.17) or (3.20). This leads to the different configurations shown in Fig. 3.10. The solution space is chosen by halving the knot intervals three times. Finally, resolving the optimization problem results in a shape shown in Fig. 3.11. The first four eigenmodes of the shape are depicted in Fig. 3.12. See Tab. 3.2 and 3.3 for more quantitative data on the design. Corners in the shapes in Fig. 3.11 (dof = 4096) are sharper than those in the one shown in Fig. 3.7 (dof = 16), meaning that the last refinement step was necessary.

3.5.3.2 Three patch design

The resulting shapes in Fig. 3.11 enjoy a nearly $120°$ symmetry. To further explore the problem, we impose the exact $120°$ symmetry by modeling the shape with three identical patches as shown

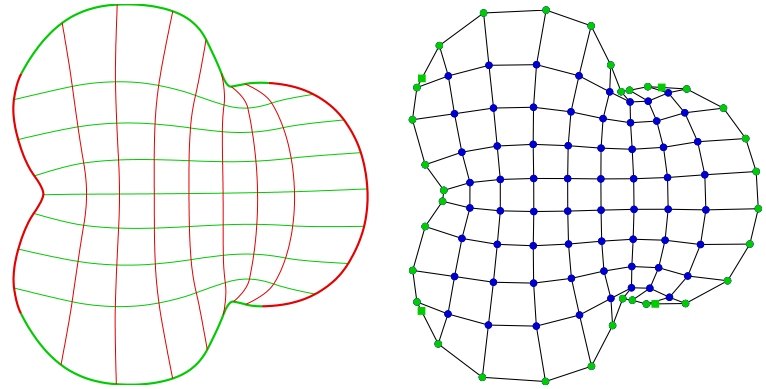

(a) (b)

Figure 3.9: (a): Optimized shape and (b): control net for a further refinement of a harmonic drum shape optimization problem.

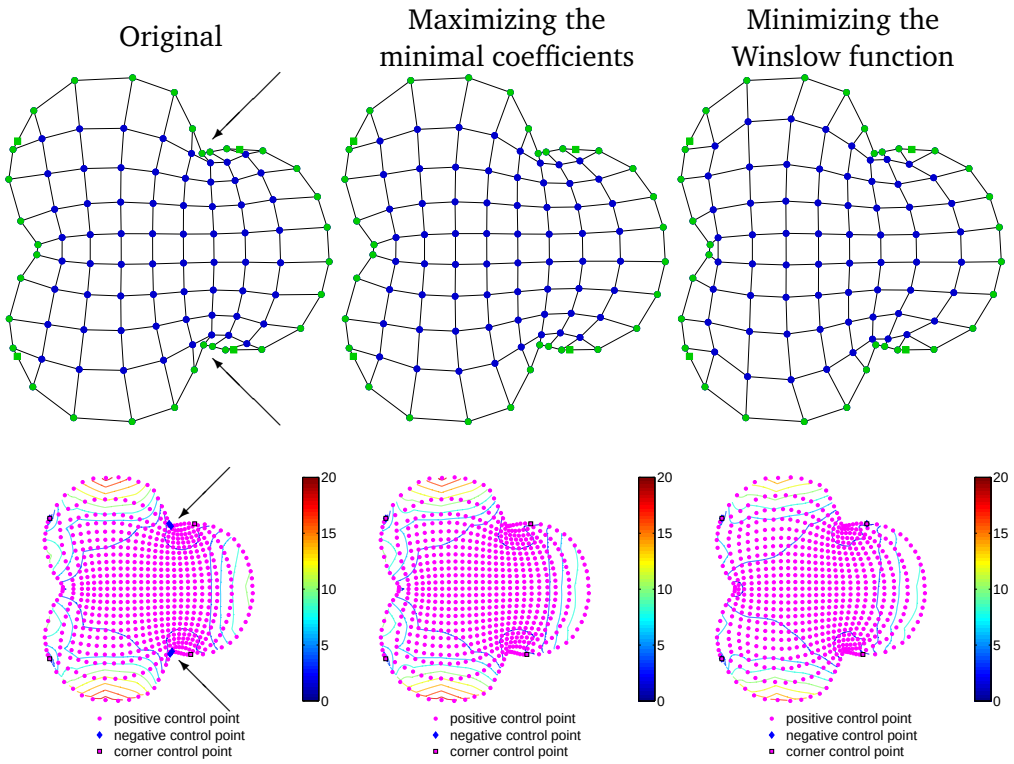

Figure 3.10: Various ways of improving the B-spline parametrization. Upper row: Control nets; lower row: corresponding expansion coefficients and contour lines of the Jacobian determinant.

in Fig. 3.13. The exact symmetry implies that $\lambda_2 = \lambda_3$ at all times, and therefore this double eigenvalue remains differentiable with respect to the design parameters. For the first design problem, we use bicubic B-splines with knot vectors

$$\Xi_s = \Xi_t = \widehat{\Xi}_s = \widehat{\Xi}_t = \widetilde{\Xi}_s = \widetilde{\Xi}_t = \{0, 0, 0, 0, 0.25, 0.5, 0.75, 1, 1, 1, 1\}. \tag{3.27}$$

The spring model is used to generate the inner control points. The initial shape of the design is shown in Fig. 3.13. We follow the scheme outlined in Section **??**. After performing the first step, we obtain a shape shown in Fig. 3.14. We continue by using the resulting shape as a new

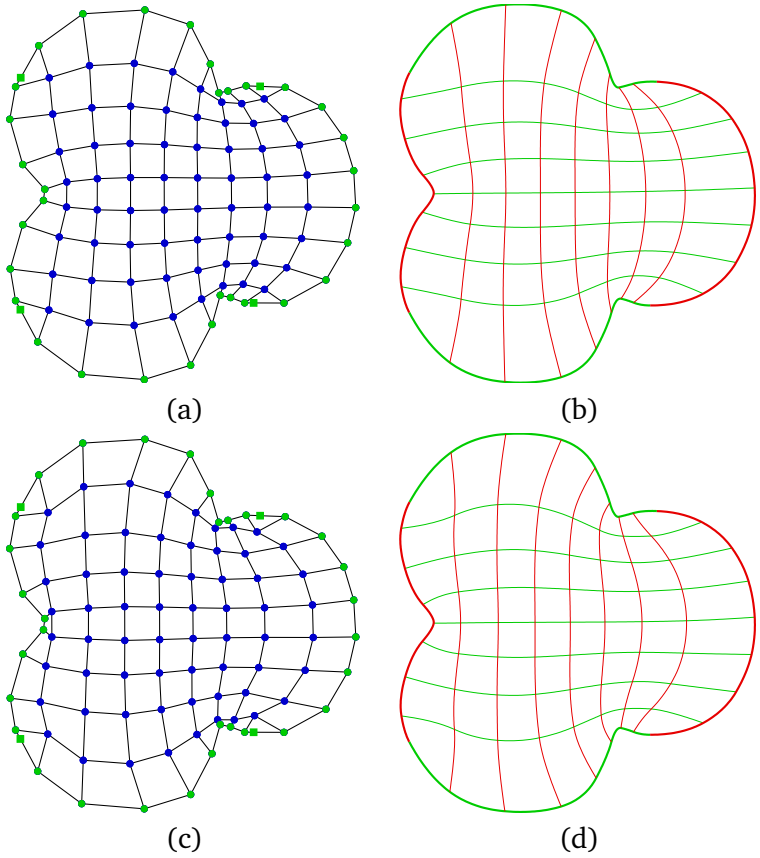

Figure 3.11: (a), (c): The final optimized shapes and (b), (d): the corresponding control nets of a harmonic drum. (a) & (b): results corresponding to the reference control net in Fig. 3.10 (b); (c) & (d): results corresponding to the reference control net in Fig. 3.10 (c).

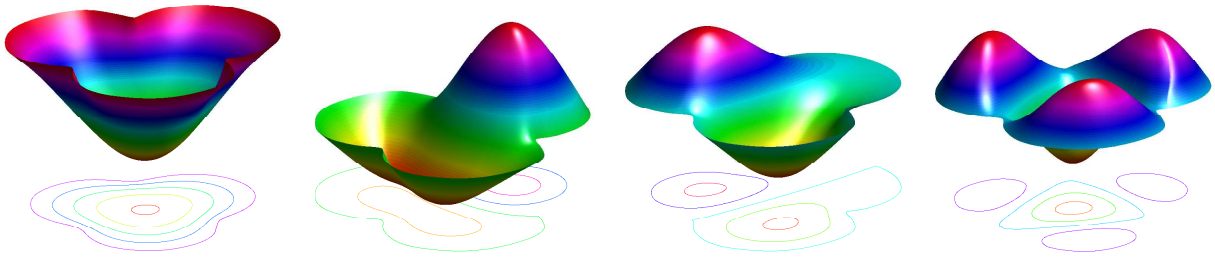

Figure 3.12: The first four eigenmodes and normalized frequencies of the optimized shape in Fig. 3.11 (d).

initial shape and halving the knot intervals three times. After performing the optimization on a refined geometry, we obtain a drum shown in Fig. 3.15. The resulting shape is symmetric about the line connecting the two opposite corner control points, see Fig. 3.15 (b), even though we did not explicitly impose the symmetry requirement. One also observes that the resulting parametrization is valid, see Fig. 3.15 (c).

We again investigate the effects on the results of the two optimization strategies, that is, just matching the eigenvalues (disregarding the perimeter) vs. minimizing the perimeter *in addition to* matching the eigenvalues (problem (3.21)). In this numerical experiment we use the knot

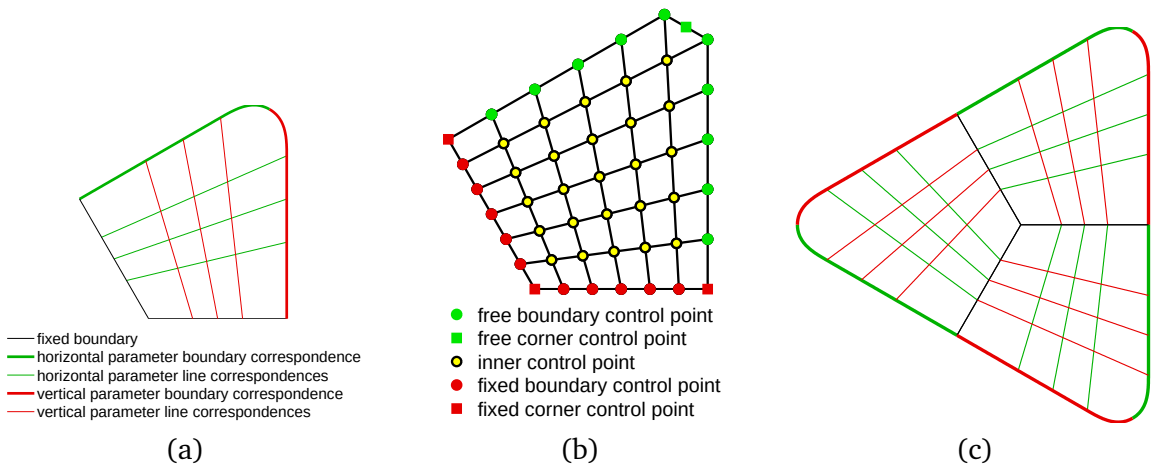

Figure 3.13: Initial shape for the three-patch design of the harmonic drum. (a): Generating patch and (b): the corresponding control net. (c): Entire domain consisting of the generating patch repeated three times.

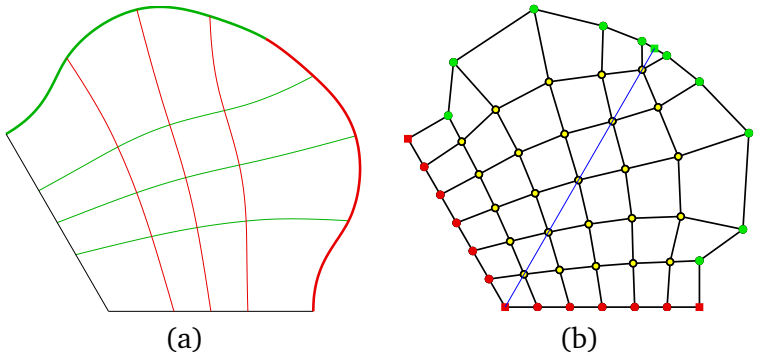

Figure 3.14: (a): Optimized shape and (b): the corresponding control net of a three-patch design of a harmonic drum.

vectors which are given by (3.27), the B-splines of degree three, resulting in dof = 91. The constraint tolerances are set to $T_{con} = 10^{-7}$. We start the optimization algorithm from two initial points, and obtain final shapes shown in Fig. 3.16. One may observe that the numerical solutions to the optimization problem where only eigenvalue matching is optimized are extremely sensitive with respect to the choice of the initial shapes, whereas this is not the case with the optimization problem (3.21).

We now measure the errors in eigenvalues achieved by the different designs. Let λ_i, $i = 1, 2, 3, 4$, be resulting eigenvalues of an optimized shape. We use $\lambda_2 = \lambda_2^0$ as the normalization factor to obtain the values λ_i^0, $i = 1, 2, 3, 4$. Then we compute the relative error corresponding to a given design as

$$\text{relative error} = \max_{i=1,2,3,4} \frac{|\lambda_i - \lambda_i^0|}{\lambda_i^0}.$$

The relative errors and the normalized first four frequencies of the designs presented above are summarized in Tab. 3.2 and 3.3, respectively. Tab. 3.2 shows that the designs computed using a three-patch approach achieve better accuracy with respect to the eigenvalues. This matches well the theoretical prediction that we have exact double eigenvalues due to the symmetry. It is also observed that the drum in Fig. 3.15 has gross features similar to those of [46] but with far more satisfactory frequencies ($120°$-symmetry is imposed in the both cases).

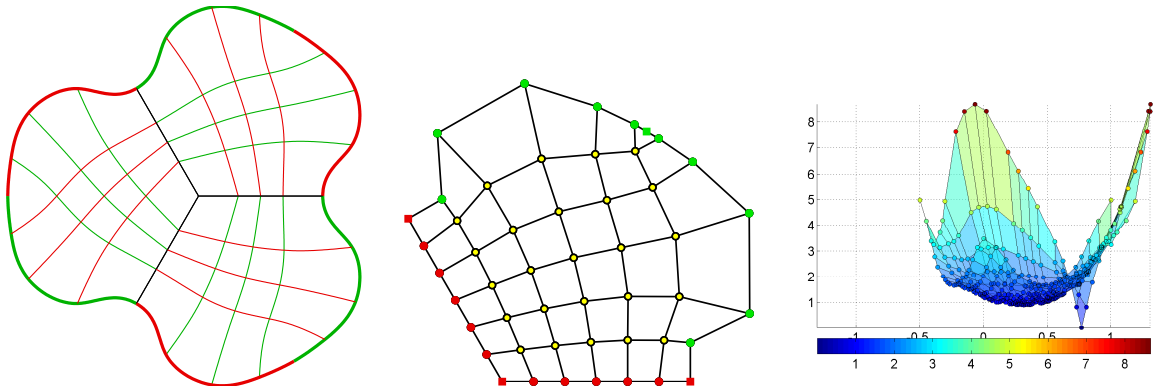

(a) (b) (c)

Figure 3.15: Refined and optimized shape of a three-patch design of a harmonic drum. (a): Optimal generating patch and (b): the corresponding control net. (c): Coefficients in the expansion of the determinant of the Jacobian. The non-positive (zero) coefficient is the corner control point where the smoothness constraints (3.21d) force a singularity.

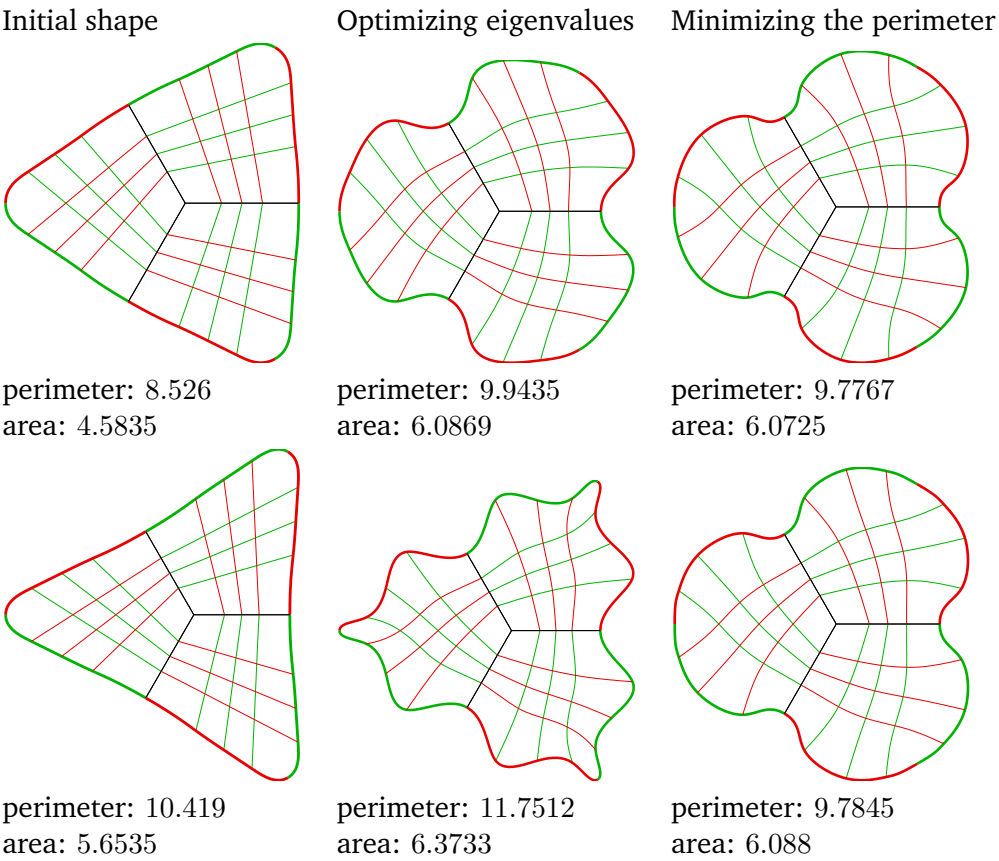

Figure 3.16: Comparison between different optimization strategies with different initial shapes.

3.5.4 CEG drums

Finally, we design a different kind of a harmonic drum. Namely, we seek a shape capable of "playing" the musical triad C-E-G (c.f. [51]), corresponding to the ratio 4:5:5:6 of the first four

Design	# refinements	$\widetilde{p}$	# var.	dof	# iter.	relative error
Fig. 3.4 (initial)	3	2	–	4096	–	0.1148
Fig. 3.11 (b) (1 patch)	3	2	72	4096	17	1.6×10^{-4}
Fig. 3.11 (d) (1 patch)	3	2	72	4096	16	1.6×10^{-4}
Fig. 3.13 (initial)	3	3	–	3367	–	0.0380
Fig. 3.15 (3 patches)	3	3	22	3367	31	1.5×10^{-13}
Harmonic drum of [46]	–	–	14	60	–	0.7×10^{-4}

Table 3.2: Quantitative data for various designs of the harmonic drum. # refinements: Number of halving the knot intervals; $\widetilde{p}$: degrees of the B-splines used for forming the solution space; # var.: number of design variables; # iter.: number of optimization iterations needed to achieve convergence.

Design	f_1	f_2	f_3	f_4	perimeter	area
Fig. 3.4 (initial)	1.89426	3.00000	3.00024	3.82078	7.2465	3.8333
Fig. 3.11b (1 patch)	2.00008	3.00000	3.00024	4.00016	7.6232	4.0255
Fig. 3.11d (1 patch)	2.00007	3.00000	3.00023	4.00015	7.6232	4.0276
Fig. 3.13 (initial)	1.96351	3.00000	3.00000	3.93126	9.3460	5.0617
Fig. 3.15 (3 patches)	2.00000	3.00000	3.00000	4.00000	9.8592	6.0686
Harmonic drum of [46]	2.00011	3.00000	3.00000	3.99972	–	–

Table 3.3: The first four normalized eigenfrequencies, the length of the perimeter, and the area of the different computed optimal shapes for the harmonic drum example.

natural frequencies. We start by using the same initial shape and knot vectors as in the last example. The B-splines for geometry and solution space are quadratic. Following the optimization scheme outlined in Section 3.5.1 we obtain the shapes shown in Fig. 3.17. In this example refined the geometry by halving the knot intervals two times, which leads to a problem with 817 degrees of freedom. The first four normalized frequencies of the found optimized shape are 3.99999, 5.00000, 5.00000, and 5.99999, as required.

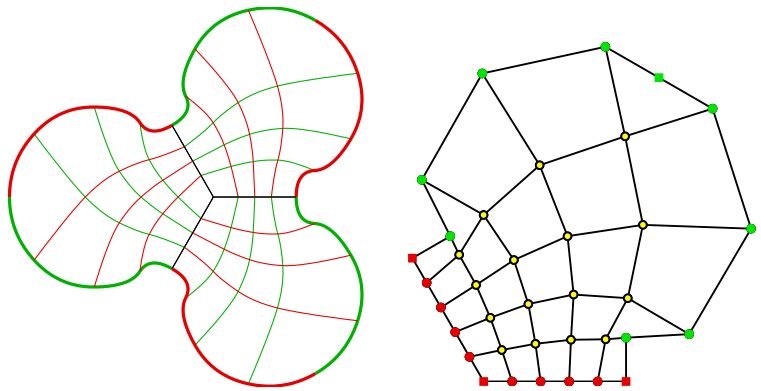

(a) (b)

Figure 3.17: (a): Optimized shape of a CEG drum; (b): control net corresponding to the generating patch.

3.6 Conclusions

We have applied isogeometric analysis towards shape optimization problems of vibrating membranes, where we allow the shape of the domain to experience very large deformations. We have used three different spline parametrizations for the boundary and the interior of the domains, as well as for the approximate solution space for the governing boundary value problem. This allows us to independently vary the number of control points for the shape parametrization and the approximation properties of the discretization of the governing equations.

We have carried out numerical studies of several techniques for extending the domain parametrization from the boundary to the interior and improving the quality of the domain parametrization. As a result, we have presented solutions to several eigenvalue optimization problems for the Laplace equation. Due to the properties of B-splines, some nice shapes have been obtained with a relatively small number of design variables. The problems have been solved numerically in a number of different ways (for example, without and with explicit constraints ensuring certain symmetries) yet they yielded the same optimal solutions, thus supporting the robustness of our approach.

Chapter 4

On the sensitivities of multiple eigenvalues

J. Gravesen, A. Evgrafov, Nguyen D. M., On the sensitivities of multiple eigenvalues, *Structural and Multidisciplinary Optimization*, vol. 44, pp. 583-587, 2011.

Abstract. We consider the generalized symmetric eigenvalue problem where matrices depend smoothly on a parameter. It is well known that in general individual eigenvalues, when sorted in accordance with the usual ordering on the real line, do not depend smoothly on the parameter. Nevertheless, symmetric polynomials of a number of eigenvalues, regardless of their multiplicity, which are known to be isolated from the rest depend smoothly on the parameter. We present explicit readily computable expressions for their first derivatives. Finally, we demonstrate the utility of our approach on a problem of finding a shape of a vibrating membrane with a smallest perimeter and with prescribed four lowest eigenvalues, only two of which are have algebraic multiplicity one.

Keywords: Multiple eigenvalues; sensitivity analysis.

4.1 Introduction

Consider a function $\mathbf{A} : \mathbb{R} \to \mathbb{S}^2$ mapping a parameter t into a set of 2×2 symmetric matrices. Even when entries $a_{ij}(t)$, $i, j = 1, 2$ depend smoothly on the parameter, the eigenvalues $\lambda_1(t) \leq \lambda_2(t)$ may be non-smooth functions at points where their multiplicity changes. Nevertheless, both their sum $\lambda_1(t) + \lambda_2(t) = \operatorname{trace} \mathbf{A}(t) = a_{11}(t) + a_{22}(t)$ and their product $\lambda_1(t)\,\lambda_2(t) = \det \mathbf{A}(t) = a_{11}(t)\,a_{22}(t) - a_{12}(t)\,a_{21}(t)$ clearly remain smooth functions. This knowledge may be used to, for example, replace potentially non-smooth pair of constraints $\lambda_1(t) = \hat{\lambda}_1$, $\lambda_2(t) = \hat{\lambda}_2$, with a pair of smooth ones: $\operatorname{trace} \mathbf{A}(t) = \hat{\lambda}_1 + \hat{\lambda}_2$, $\det \mathbf{A}(t) = \hat{\lambda}_1\,\hat{\lambda}_2$, see [9].

For 2×2 matrices explicit expressions for $[\operatorname{trace} \mathbf{A}(t)]'$ and $[\det \mathbf{A}(t)]'$, where with prime throughout the paper we denote differentiation with respect to t, may be easily obtained in terms of $a_{ij}(t)$, $i, j = 1, 2$, and their derivatives. However, we seek an alternative representation of these quantities, which remain valid for higher-dimensional problems. To this end, let $\mathbf{u}_1 : \mathbb{R} \to \mathbb{R}^2$, $\mathbf{u}_2 : \mathbb{R} \to \mathbb{R}^2$ be the normalized eigenvectors corresponding to $\lambda_1(t)$, $\lambda_2(t)$. We assume a computationally realistic situation, when the vectors $\mathbf{u}_1(t)$ and $\mathbf{u}_2(t)$ are *not necessarily continuous* for $t \in \mathbb{R}$ such that $\lambda_1(t) = \lambda_2(t)$. (Indeed, in our simple two-dimensional example an *arbitrary* pair of non-zero vectors $\mathbf{u}_1(t)$ and $\mathbf{u}_2(t)$ constitutes a pair of eigenvectors for $t \in \mathbb{R}$ such that $\lambda_1(t) = \lambda_2(t)$.) However, we do assume that these vectors are chosen to be orthonormal for all $t \in \mathbb{R}$. Whenever the function $\lambda_i(t)$, $i = 1, 2$, is differentiable at a point $t_0 \in \mathbb{R}$, its derivative

is known to satisfy the equation $\lambda_i'(t_0) = \mathbf{u}_i^{\mathrm{T}}(t_0)\mathbf{A}'(t_0)\mathbf{u}_i(t_0)$, $i = 1, 2$, see for example [60]. As a result, we get

$$\begin{aligned}[\operatorname{trace}\mathbf{A}(t_0)]' &= \sum_{i=1}^{2} \mathbf{u}_i^{\mathrm{T}}(t_0)\mathbf{A}'(t_0)\mathbf{u}_i(t_0),\\ [\det\mathbf{A}(t_0)]' &= \sum_{i=1}^{2} \mathbf{u}_i^{\mathrm{T}}(t_0)\mathbf{A}'(t_0)\mathbf{u}_i(t_0)\prod_{j\neq i}\lambda_j(t_0).\end{aligned} \tag{4.1}$$

Interestingly enough, these formulas remain valid even when the eigenvalues are not smooth any longer, as well as in higher-dimensional cases. We start by illustrating this phenomenon on a concrete 2×2 example and then proceed to presenting a general theory.

Example 1. *Consider the symmetric 2×2 symmetric matrix*

$$\mathbf{A}(t) = \begin{pmatrix} \cos(t) & \sin(t) \\ \sin(t) & \cos(t) \end{pmatrix}.$$

Its eigenvalues are

$$\begin{aligned}\lambda_1(t) &= \cos(t) - |\sin(t)|,\\ \lambda_2(t) &= \cos(t) + |\sin(t)|,\end{aligned}$$

which are smooth functions of $t \in \mathbb{R}$ except at points $t_k = \pi k$, $k = 0, \pm1, \pm2, \ldots$. The corresponding eigenvectors are

$$\begin{aligned}\mathbf{u}_1(t) &= 2^{-1/2}(-|\sin(t)|/\sin(t), 1)^{\mathrm{T}},\\ \mathbf{u}_2(t) &= 2^{-1/2}(|\sin(t)|/\sin(t), 1)^{\mathrm{T}},\end{aligned}$$

for $t \neq t_k$, and an arbitrary pair of orthonormal vectors for $t = t_k$, $k = 0, \pm1, \pm2, \ldots$. A direct computation shows that

$$\begin{aligned}\operatorname{trace}\mathbf{A}(t) &= 2\cos(t), & \det\mathbf{A}(t) &= \cos(2t),\\ [\operatorname{trace}\mathbf{A}(t)]' &= -2\sin(t), & [\det\mathbf{A}(t)]' &= -2\sin(2t).\end{aligned}$$

For $t \neq t_k$, $k = 0, \pm1, \pm2, \ldots$, we have

$$\begin{aligned}\mathbf{u}_1^{\mathrm{T}}(t)\mathbf{A}'(t)\mathbf{u}_1(t) + \mathbf{u}_2^{\mathrm{T}}(t)\mathbf{A}'(t)\mathbf{u}_2(t) &= -2\sin(t),\\ \lambda_1(t)\mathbf{u}_2^{\mathrm{T}}(t)\mathbf{A}'(t)\mathbf{u}_2(t) + \lambda_2(t)\mathbf{u}_1^{\mathrm{T}}(t)\mathbf{A}'(t)\mathbf{u}_1(t) &= -2\sin(2t).\end{aligned}$$

Finally, when $t = t_k$ we can for example put

$$\begin{aligned}\mathbf{u}_1(t_k) &= (\sin(\phi), \cos(\phi))^{\mathrm{T}},\\ \mathbf{u}_2(t_k) &= (\cos(\phi), -\sin(\phi))^{\mathrm{T}},\end{aligned}$$

$\phi \in [0, 2\pi)$. Then

$$\mathbf{u}_1^{\mathrm{T}}(t_k)\mathbf{A}'(t_k)\mathbf{u}_1(t_k) + \mathbf{u}_2^{\mathrm{T}}(t_k)\mathbf{A}'(t_k)\mathbf{u}_2(t_k) = 0,$$

as well as

$$\lambda_1(t_k)\mathbf{u}_2^{\mathrm{T}}(t_k)\mathbf{A}'(t_k)\mathbf{u}_2(t_k) + \lambda_2(t_k)\mathbf{u}_1^{\mathrm{T}}(t_k)\mathbf{A}'(t_k)\mathbf{u}_1(t_k) = 0,$$

which is consistent with (4.1).

Remark 6. Theoretically, for symmetric matrices it is always possible to choose eigenvalue branches, which depend on the parameter in a differentiable manner [61]. In our Example 1 we can of course choose

$$\widetilde{\lambda}_1(t) = \cos(t) - \sin(t),$$
$$\widetilde{\lambda}_2(t) = \cos(t) + \sin(t),$$

which are smooth functions of $t \in \mathbb{R}$ with the corresponding smooth eigenvectors

$$\widetilde{\mathbf{u}}_1(t) = 2^{-1/2}(-1, 1)^{\mathrm{T}},$$
$$\widetilde{\mathbf{u}}_2(t) = 2^{-1/2}(1, 1)^{\mathrm{T}}.$$

However, computing the "smooth" eigenvectors, such as $\widetilde{\mathbf{u}}_1(t)$, $\widetilde{\mathbf{u}}_2(t)$, may be prohibitively expensive at points where algebraic multiplicity of eigenvalues changes for realistic large scale eigenvalue problems, which depend on many parameters (t in our case). At the same time, the formulas $\widetilde{\lambda}_i'(t) = \mathbf{u}_i^{\mathrm{T}}(t)\mathbf{A}'(t)\mathbf{u}_i(t)$, $i = 1, 2$ do not hold any longer if an arbitrary eigenvector $\mathbf{u}_i(t)$ is used in place of the smooth one, $\widetilde{\mathbf{u}}_i(t)$, $i = 1, 2$. Indeed, as in Example 1 above, we put at $t = t_k$, $k = 0, \pm 1, \pm 2, \ldots$

$$\mathbf{u}_1(t_k) = (\sin(\phi), \cos(\phi))^{\mathrm{T}},$$
$$\mathbf{u}_2(t_k) = (\cos(\phi), -\sin(\phi))^{\mathrm{T}},$$

$\phi \in [0, 2\pi)$. Then, unless $\phi = 3\pi/4$ or $\phi = 7\pi/4$,

$$(-1)^{k+1} = \widetilde{\lambda}_1'(t_k) \neq \mathbf{u}_1^{\mathrm{T}}(t_k)\mathbf{A}'(t_k)\mathbf{u}_1(t_k) = (-1)^k \sin(2\phi),$$
$$(-1)^{k} = \widetilde{\lambda}_2'(t_k) \neq \mathbf{u}_2^{\mathrm{T}}(t_k)\mathbf{A}'(t_k)\mathbf{u}_2(t_k) = (-1)^{k+1} \sin(2\phi).$$

Thus formulas (4.1) *agree with* but *do not follow from* the well-known expressions for the derivatives of the individual eigenvalues of algebraic multiplicity one, particularly in higher-dimensional cases.

In this note we establish generalizations (4.1) for higher-dimensional cases, where in place of $\operatorname{trace} \mathbf{A}(t)$ and $\det \mathbf{A}(t)$ we have general symmetric polynomials of the eigenvalues. We conclude the introduction by noting that sensitivity analysis in the presence of multiple eigenvalues is a well known and well studied issue. For alternative approaches to the problem we refer to the two review papers [62, 63] and references therein. The main advantage of the present approach is its exactness yet computational simplicity; indeed, it only requires computing the same information as one would need for the case without eigenvalue multiplicity, that is: eigenvalues, corresponding eigenvectors, and derivatives of the matrices with respect to the parameter. Of course this comes at the cost of only providing sensitivity information about the symmetric polynomials of the eigenvalues and not individual eigenvalues, which may not be sufficient for certain applications.

4.2 Sensitivity of symmetric polynomials of eigenvalues

To simplify the notation, we consider the case of real symmetric matrices $\mathbb{S}^m$, but all results hold true for complex self-adjoint matrices as well. For a pair of smooth matrix functions $\mathbf{K}, \mathbf{M} : \mathbb{R} \to \mathbb{S}^m$ such that $\mathbf{M}(t)$ is positive definite for every $t \in \mathbb{R}$ we consider a parametric generalized eigenvalue problem:

$$\mathbf{K}(t)\mathbf{v}(t) = \lambda(t)\mathbf{M}(t)\mathbf{v}(t). \tag{4.2}$$

We assume that (4.2) admits n eigenvalues isolated from the rest. That is, the eigenvalues satisfy

$$\cdots \leq \lambda_0(t) < \lambda_1(t) \leq \cdots \leq \lambda_n(t) < \lambda_{n+1}(t) \leq \cdots . \tag{4.3}$$

We let $E_i(t)$ denote the eigenspace corresponding to the eigenvalue $\lambda_i(t)$; that is, $E_i(t) = \{\, \mathbf{v} \in \mathbb{R}^m \mid \mathbf{K}(t)\mathbf{v} = \lambda_i(t)\mathbf{M}(t)\mathbf{v} \,\}$. We furthermore let $E(t) = E_1(t)+\cdots+E_n(t)$ be the joint eigenspace of the eigenvalues $\lambda_1(t), \ldots, \lambda_n(t)$. A crucial fact going back to Rellich 1953 is that this space depends smoothly on the parameter t, see [61]. In particular, there exists a basis $\mathbf{v}_1(t), \ldots, \mathbf{v}_n(t)$ for $E(t)$ that depends smoothly on t. We will prove that there is another basis for $E(t)$ satisfying certain additional requirements.

Lemma 2. *Let $\mathbf{K}, \mathbf{M} : \mathbb{R} \to \mathbb{S}^m$ be a smooth family of symmetric matrices as described above with n generalized eigenvalues satisfying* (4.3)*. Assume furthermore that $\mathbf{u}_1, \ldots, \mathbf{u}_n \in \mathbb{R}^m$ is an $\mathbf{M}(0)$-orthonormal set of eigenvectors for* (4.2) *at $t = 0$ corresponding to eigenvalues $\lambda_1(0), \ldots, \lambda_n(0)$. Then we can find another basis $\mathbf{w}_1(t), \ldots, \mathbf{w}_n(t) \in \mathbb{R}^m$ for $E(t)$ such that, for all $k, \ell = 1, \ldots, n$, $t \in \mathbb{R}$:*

1. *$\mathbf{w}_k(t)$ is a smooth function of t;*
2. *$\mathbf{w}_k(t)$ and $\mathbf{w}_\ell(t)$ are $\mathbf{M}(t)$-orthogonal, that is, $\mathbf{w}_k^{\mathrm{T}}(t)\mathbf{M}(t)\mathbf{w}_\ell(t) = \delta_{k\ell}$, where $\delta_{k\ell}$ is Kronecker's delta;*
3. *$\mathbf{w}_k(0) = \mathbf{u}_k$.*

Proof. Applying Gram–Schmidt orthogonalization process to the basis $\mathbf{v}_k(t)$, $k = 1, \ldots, n$ we obtain a $\mathbf{M}(t)$-orthonormal basis for $E(t)$ smoothly depending on the parameter; we denote this basis again with $\mathbf{v}_k(t)$, $k = 1, \ldots, n$. Let us write $(\mathbf{u}_1, \ldots, \mathbf{u}_n)$ in terms of the latter basis as $(\mathbf{v}_1(0), \ldots, \mathbf{v}_n(0))\mathbf{U}$, where $\mathbf{U} \in O(n)$ is a $n \times n$ orthogonal matrix. We now define out new basis as $(\mathbf{w}_1(t), \ldots, \mathbf{w}_n(t)) := (\mathbf{v}_1(t), \ldots, \mathbf{v}_n(t))\mathbf{U}$ and obtain a basis for $E(t)$ which satisfies conditions 1, 2, and 3. □ □

Theorem 4. *Let $\mathbf{K}, \mathbf{M} : \mathbb{R} \to \mathbb{S}^m$ be a smooth family of symmetric matrices as described above with n generalized eigenvalues satisfying* (4.3)*. Then the symmetric polynomials*

$$s_k(t) = \sum_{1 \le i_1 < \cdots < i_k \le n} \lambda_{i_1}(t) \cdots \lambda_{i_k}(t), \tag{4.4}$$

$k = 1, \ldots, n$ are smooth functions and their derivatives at $t = 0$ are given by

$$\begin{aligned} s_k'(0) = \sum_{1 \le i_1 < \cdots i_k \le n} \sum_{\ell=1}^{k} \lambda_{i_1}(0) \cdots \lambda_{i_{\ell-1}}(0) \times \\ \times \mathbf{u}_{i_\ell}^{\mathrm{T}} [\mathbf{K}'(0) - \lambda_{i_\ell}(0)\mathbf{M}'(0)] \mathbf{u}_{i_\ell} \cdot \lambda_{i_{\ell+1}}(0) \cdots \lambda_{i_k}(0), \end{aligned} \tag{4.5}$$

where $\mathbf{u}_1, \ldots, \mathbf{u}_n \in \mathbb{R}^m$ is an $\mathbf{M}(0)$-orthonormal set of eigenvectors for (4.2) *at $t = 0$ corresponding to eigenvalues $\lambda_1(0), \ldots, \lambda_n(0)$.*

Proof. Choose the basis $\mathbf{w}_1(t), \ldots, \mathbf{w}_n(t)$ for $E(t)$ secured by Lemma 2. We now define the matrix families $\hat{\mathbf{K}}, \hat{\mathbf{M}} : \mathbb{R} \to \mathbb{S}^n$ with elements

$$\begin{aligned} \hat{k}_{k\ell}(t) &= \mathbf{w}_k^{\mathrm{T}}(t)\mathbf{K}(t)\mathbf{w}_\ell(t), \\ \hat{m}_{k\ell}(t) &= \mathbf{w}_k^{\mathrm{T}}(t)\mathbf{M}(t)\mathbf{w}_\ell(t), \end{aligned}$$

$k, \ell = 1, \ldots, n$. That is, $\hat{\mathbf{K}}(t)$, $\hat{\mathbf{M}}(t)$ are restrictions of $\mathbf{K}(t)$, $\mathbf{M}(t)$ to $E(t)$ expressed in the basis $\mathbf{w}_k(t)$, $k = 1, \ldots, n$. As this is an $\mathbf{M}(t)$-orthonormal basis we have that $\hat{\mathbf{M}}(t) \equiv \mathbf{I}$ or equivalently that $\hat{m}_{k\ell}(t) = \delta_{k\ell}$, $k, \ell = 1, \ldots, n$. It is easy to verify that the eigenvalue problem $\hat{\mathbf{K}}(t)\mathbf{v} = \lambda(t)\hat{\mathbf{M}}(t)\mathbf{v} = \lambda(t)\mathbf{v}$ shares its n eigenvalues with the problem (4.2), namely $\lambda_1(t), \ldots, \lambda_n(t)$.

Let us now consider the characteristic polynomial $p_t(\lambda) = \det[\hat{\mathbf{K}}(t) - \lambda\mathbf{I}]$. The matrix $\hat{\mathbf{K}}(t) - \lambda\mathbf{I}$ has components $\hat{k}_{k\ell}(t) - \lambda\delta_{k\ell}$ and the characteristic polynomial can be written as

$$p_t(\lambda) = \sum_{\text{permutations } \sigma} \operatorname{sgn}\sigma \prod_{k=1}^{n} [\hat{k}_{k,\sigma(k)}(t) - \lambda\delta_{k,\sigma(k)}].$$

Differentiating the product above with respect to t and evaluating the derivative at $t = 0$ we get:

$$\frac{\mathrm{d}}{\mathrm{d}t} \prod_{k=1}^{n} [\hat{k}_{k,\sigma(k)}(t) - \lambda\delta_{k,\sigma(k)}]\Big|_{t=0} = \sum_{k=1}^{n} \left\{ \hat{k}'_{k,\sigma(k)}(0) \cdot \prod_{\ell\neq k} [\hat{k}_{\ell,\sigma(\ell)}(0) - \lambda\delta_{\ell,\sigma(\ell)}] \right\}. \quad (4.6)$$

Since $\hat{\mathbf{K}}(0) = \operatorname{diag}[\lambda_1(0), \ldots, \lambda_n(0)]$ owing to condition 3 of Lemma 2, we immediately infer that the right hand side sum in (4.6) is zero unless σ is identity. As a result, we get the equality

$$\frac{\mathrm{d}}{\mathrm{d}t} p_t(\lambda)\big|_{t=0} = \sum_{k=1}^{n} \hat{k}'_{kk}(0) \cdot \prod_{\ell\neq k} [\lambda_\ell(0) - \lambda]. \quad (4.7)$$

Owing to the symmetry of $\mathbf{M}(t)$ we have

$$\begin{aligned} 0 = \hat{m}'_{kk}(0) &= \mathbf{w}'_k(0)^T \mathbf{M}(0)\mathbf{w}_k(0) + \mathbf{w}_k(0)^T \mathbf{M}'(0)\mathbf{w}_k(0) \\ &\quad + \mathbf{w}_k(0)^T \mathbf{M}(0)\mathbf{w}'_k(0) \\ &= \mathbf{u}_k^T \mathbf{M}'(0)\mathbf{u}_k + 2\mathbf{w}'_k(0)^T \mathbf{M}(0)\mathbf{u}_k. \end{aligned}$$

Similarly, utilizing the fact that $\mathbf{u}_k$ is a generalized eigenvector corresponding to $\lambda_k(0)$ we get

$$\begin{aligned} \hat{k}'_{kk}(0) &= \mathbf{u}_k^T \mathbf{K}'(0)\mathbf{u}_k + 2\mathbf{w}'_k(0)^T \mathbf{K}(0)\mathbf{u}_k \\ &= \mathbf{u}_k^T \mathbf{K}'(0)\mathbf{u}_k + 2\lambda_k(0)\mathbf{w}'_k(0)^T \mathbf{M}(0)\mathbf{u}_k \\ &= \mathbf{u}_k^T \mathbf{K}'(0)\mathbf{u}_k - \lambda_k(0)\mathbf{u}_k^T \mathbf{M}'(0)\mathbf{u}_k. \end{aligned} \quad (4.8)$$

Substituting (4.8) into (4.7) results in:

$$\frac{\mathrm{d}}{\mathrm{d}t} p_t(\lambda)\big|_{t=0} = \sum_{k=1}^{n} \left\{ \mathbf{u}_k^{\mathrm{T}} [\mathbf{K}'(0) - \lambda_k(0)\mathbf{M}'(0)]\mathbf{u}_k \cdot \prod_{\ell\neq k} [\lambda_\ell(0) - \lambda] \right\}. \quad (4.9)$$

Let us denote by $a_k(t)$, $k = 0, \ldots, n$, the coefficient of the characteristic polynomial in front of λ^{n-k}. They are related to the symmetric polynomials (4.4) as $s_k(t) = (-1)^{n-k} a_k(t)$, $k = 1, \ldots, n$. As a result, $s_k(t)$, $k = 1, \ldots, n$ are smooth functions of t. Finally, from (4.9) we obtain (4.5). □ □

Remark 7. Of course, there is nothing special about $t = 0$ and, with obvious modifications, formulas (4.5) allow us to evaluate $s'_k(t)$, $k = 1, \ldots, n$ for an arbitrary $t \in \mathbb{R}$.

4.3 Application to shape optimization

In this section we briefly describe a problem where we have successfully used the presented approach to multiple eigenvalues; the interested reader is referred to [9] for more details. The

problem concerns finding a shape of a drum, or a vibrating membrane, where the first four frequencies of the spectrum are given. These frequencies should be in the proportion $2:3:3:4$, and as a result the eigenvalues of the Laplace operator have to be in the proportion $4:9:9:16$. Therefore, for the final shape we want $\lambda_2 = \lambda_3 = \frac{9}{4}\lambda_1$, and $\lambda_4 = 4\lambda_1$. These requirements on the eigenvalues are far from determining the shape of the drum, so we employ them as constraints and minimize the perimeter of the drum for regularization purposes. Numerically, we discretize the problem using the isogeometric analysis approach; the boundary is parametrized using B-splines with 40 control (design) variables.

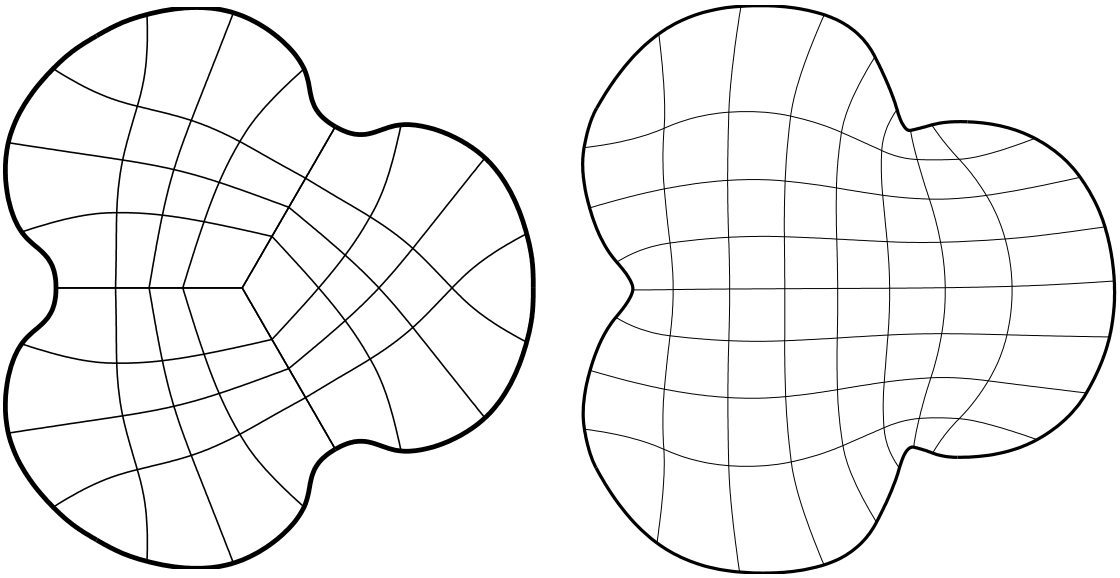

Figure 4.1: Left: membrane shape found by imposing the exact 120° symmetry implying only smooth eigenvalues. Right: the result obtained without imposing symmetry; non-smooth eigenvalues are handled by the method described in this note.

When we impose the exact 120° symmetry on the family of admissible shapes, see Fig. 4.1, then the constraint $\lambda_2 = \lambda_3$ is automatically satisfied at all times and as a result all four eigenvalues become smooth functions of the parameters, defining the symmetric shape. However, without explicitly imposing the exact symmetry the desired double eigenvalue $\lambda_2 = \lambda_3$ causes problems for the optimization. Each time λ_2 and λ_3 "cross" during the optimization process, the employed non-linear programming algorithm finds itself at a non-differentiable point in the space of parameters, defining the shape. As a result, the non-linear algorithm gets "thrown off" and in fact we never obtained convergence in this setting, see Fig. 4.2. However, when we replace the non-smooth constraints $\lambda_2 = \mu$ and $\lambda_3 = \mu$ with the equivalent smooth constraints $\lambda_2 + \lambda_3 = 2\mu$ and $\lambda_2\,\lambda_3 = \mu^2$ with derivatives evaluated on the basis of (4.5), the optimization succeeds, see the right hand side of Fig. 4.1 and Fig. 4.3.

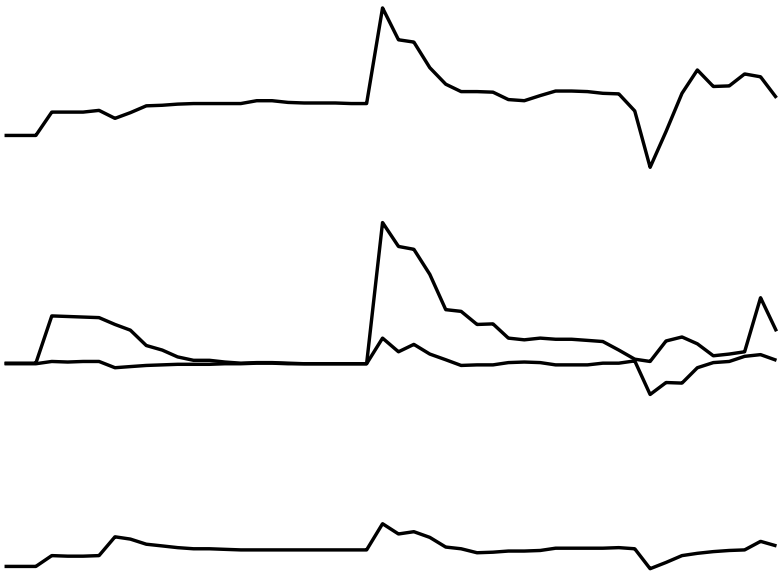

Figure 4.2: Behaviour of (normalized) eigenvalues as functions of the optimization iteration: ignoring the non-smoothness of the eigenvalues results in large "jumps" at non-smooth points when λ_2 and λ_3 cross. In the end, optimization fails to converge to a desired precision.

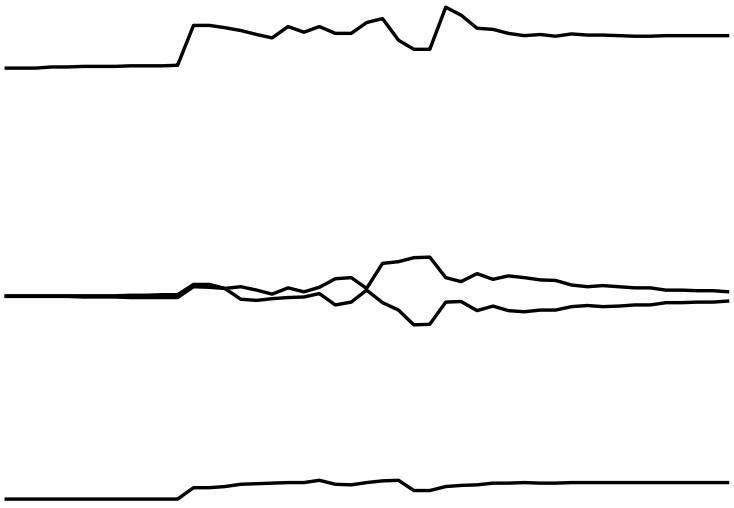

Figure 4.3: Behaviour of (normalized) eigenvalues as functions of the optimization iteration: replacing the non-smooth double-eigenvalue constraints with their smooth equivalents based on evaluating symmetric polynomials allows us to successfully compute the desired shape.

Part III

Shape optimization of sub-wavelength antennas

Chapter 5

Shape optimization of sub-wavelength antennas using isogeometric analysis

Nguyen D. M., A. Evgrafov, J. Gravesen, Shape optimization of sub-wavelength antenna using isogeometric analysis, *International Journal for Numerical Methods in Engineering*, submitted, August, 2011.

Abstract. We consider a problem of designing an antenna that concentrates the magnetic energy of an incoming electromagnetic wave in a small spatial region, having in mind potential applications for wireless energy transfer. For this purpose we utilize shape optimization and isogeometric analysis. In order to make such a combination of methods work successfully for this problem, we propose an inexpensive linear method for re-parametrizing the computational domain after each shape update by the optimization algorithm. Our method is based on a quadratic programming approximation of a minimization problem of Winslow functional. This simple idea works rather well in our numerical tests. Indeed, we benchmark our shape optimization algorithm against earlier attempts of antenna design based on topology optimization, and quite remarkably, our design improves the performance by a factor of one million.

Keywords: shape optimization; isogeometric analysis; spline parametrization; wireless energy transfer; sub-wavelength antennas.

5.1 Introduction

Shape optimization has been a subject of a great interest in the past decades, see for example [17, 34, 35], and the references therein. Such an interest is fueled by many important and direct applications of shape optimization in various engineering disciplines, and the subject has seen many advances during these years. In this paper, we concentrate on utilizing shape optimization techniques to facilitate optimal design of sub-wavelength antennas. As a model problem we consider that of focusing the incoming electromagnetic energy into a given small spatial area, which has immediate applications for wireless energy transfer [64, 65]. Due to a variety of potential industrial applications, such as wireless charging of portable electronic devices [66] and electric commuter vehicles [67], the problem has attracted a lot of attention. One of the major issues remaining to be resolved is improving the efficiency of the process [68, 69, 70, 71, 72, 73]. The idea of employing a systematic design procedure such as shape optimization for this purpose arises quite naturally.

Many shape optimization approaches continue to rely on polygonal grids inherited from the underlying numerical methods used for numerical approximation of partial differential equa-

tions (PDEs) governing a given physical system under consideration, Maxwell's equations in our case. This creates a disparity between a computer aided design (CAD)-like geometric representation of the shape, which is most often utilized for manufacturing purposes, and a polygonal representation utilized for the numerical computations [21, 17, 74]. Additionally, the need for automatic remeshing often imposes artificial limits on the admissible variations of shapes, in turn limiting the possible improvements of the performance, see for example [17, 30] and references therein for a discussion.

The arrival of isogeometric analysis (IGA) [1] provided the subject of shape optimization with a new direction of development. Potential benefits of shape optimization based on IGA have been indicated in the original paper [1], and have later been further developed in [11, 12, 14, 13, 75, 30]. In particular, shapes are often represented very well with relatively few variables using splines, and for PDE problems with smooth solutions the availability of k-refinement in IGA demonstrates improved accuracy per degree of freedom (dof) when compared with traditional finite element method (FEM), see [3, 4, 5, 59]. Since IGA framework eliminates the disagreement between the CAD and the analysis representations, optimized designs may be easily imported back to a CAD system for manufacturing [1, 7].

The issue of remeshing (reparametrization) is left unresolved within IGA-based shape optimization: a robust and inexpensive method for re-parametrizing the physical domain during shape optimization iterations is still required. The need for such a reparametrization has been recognized in Nguyen et al. [30], and two inexpensive linear methods have been utilized for this purpose. In this paper, we utilize an observation that minima of Winslow functional [31] correspond to high quality (nearly-conformal) parametrizations [28, 29]. However, solving an auxiliary non-linear mathematical programming problem at every shape optimization iteration is computationally too expensive. Therefore, as a simplification we work with quadratic optimization problems (whose optimality conditions are linear systems) based on second order Taylor series expansion of the original non-linear Winslow functional. Further, to prevent self-intersection of the boundaries of the domain, which we encounter while solving the antenna design problem, we formulate a set of easily computable sufficient conditions guaranteeing non-self-intersecting boundaries without greatly restricting the family of considered antenna shapes.

With application to antenna design for the wireless energy transfer, shape optimization based on IGA is a very natural choice. Indeed, in this situation we are interested in the behaviour of the electromagnetic fields near the antenna (near field models). It is well known, both theoretically and experimentally, that the fields are rather sensitive with respect to the location and the shape of the air-antenna interface. Utilizing the same geometric representation for the analysis and manufacturing seems to be an essential advantage in this case.

We remark that the systematic optimal design of antennas for wireless energy transfer has been attempted previously [71] utilizing techniques of topology optimization. Within the framework of topology optimization (see, for example, [76, 37]), also known as control in the coefficients or shape optimization through homogenization, one approaches the shape optimization problem from an entirely different angle. For example, in the present case the geometry of the antenna may be encoded in the coefficients of Maxwell's equations, which remain valid both outside of the antenna (dielectric or air phase) and inside of the antenna (conductor phase). Interpolating between the two phases/values of the coefficients, one casts the shape optimization problem into a problem of finding the coefficients of Maxwell's equations assuming only two extreme values (dielectric/conductor phase), which maximize a given performance functional. In the present case, things get slightly more complicated by the fast variation of the fields near the interface ("skindepth problem"), which requires either a computationally infeasibly fine mesh, or some special computational treatment, see [71]. The results obtained in [71] are shown in Fig. 5.1. Note that owing to the chosen way of representing the geometry, the boundary of the

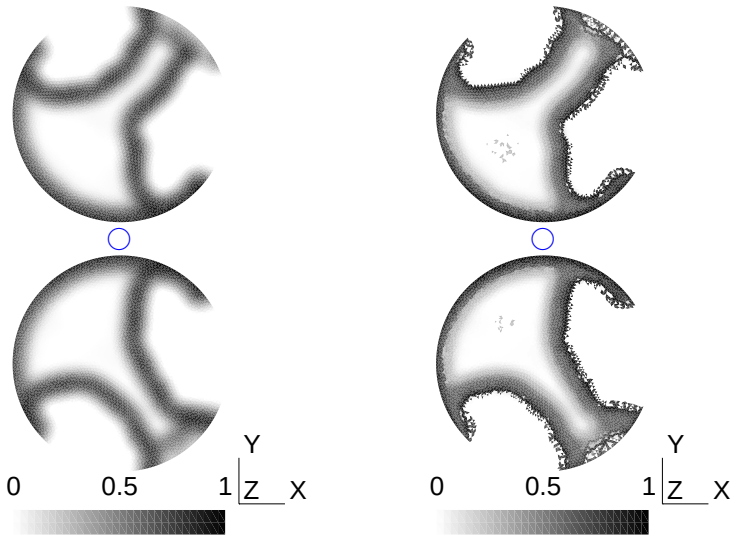

$\log_{10} W_\circ = -0.204$ $\log_{10} W_\circ = -0.076$

Figure 5.1: Two topology optimization results taken from Aage et al. [71]. $W_\circ$ is proportional to the magnetic energy calculated in a small circular domain between the two antennas.

optimized model is very "rough," see Fig. 5.1 (right), which might be unfavourable from the manufacturing point of view.

Throughout this paper we utilize Fig. 5.1 as a benchmark result for our IGA-based shape optimization algorithm. By maintaining an explicit representation of the interface throughout the iterations of the optimization algorithm we automatically avoid the need for special treatment of the skindepth problem through the use of the appropriate (transmission) boundary conditions. Additionally, we automatically maintain the regularity of the boundary by representing it with B-splines. Compared with the topology optimization result, we obtain an antenna that performs by a factor of 10^6 better in terms of guiding the incoming energy to a prescribed area.

The paper is organized as follows. In section 5.2, we briefly sketch the numerical model used in the present work for solving for electromagnetic fields and state the optimization problem associated with antenna design. We then, in section **??**, recall the basic isogeometric analysis and discuss several approaches for handling B-spline parametrizations within the shape optimization context. In section 5.4, the optimization problem stated in section 5.2 is considered in an isogeometric analysis context; sensitivity analysis and shape optimization strategy are then indicated. Numerical experiments on shape optimizations of the antenna are presented in section 5.5. We then summarize the results in section **??**. Finally, in appendix 5.7 we describe a method of approximating a circular arc by a B-spline curve which is used several times in the numerical experiments.

5.2 Physical problem

In this section, we briefly describe the models used in the present work to simulate a 2D electromangetic scattering problem. We then discuss various aspects of the antenna shape optimization problem.

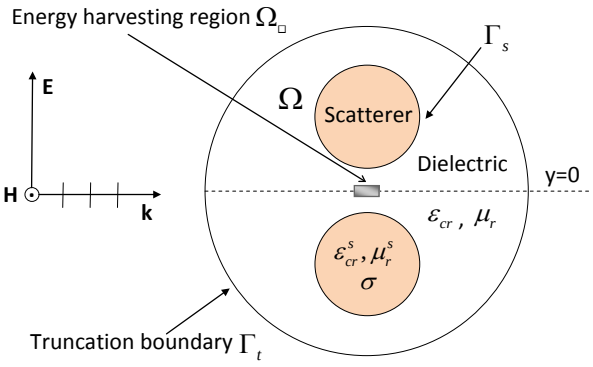

Figure 5.2: Model scattering problem considered in this framework. Due to the symmetry, only the upper half of the truncated domain is considered.

5.2.1 Electromagnetic scattering problem

We consider a two-dimensional electromagnetic (EM) TE_z model, that is, the situation when z-component of the electric field intensity vanishes. In particular, we look at a scattering problem in which a uniform plane wave with a frequency f travels in a linear and isotropic dielectric in the presence of conducting scatterers with high electric conductivity σ. The incident magnetic field intensity is given as $\mathbf{H} = (0, 0, H_z^i)$. We denote the relative complex permittivity and permeability of the dielectric by ε_{cr} and μ_r, and those of the scatterer by ε_{cr}^s and μ_r^s. Note that $\varepsilon_{cr}^s = \varepsilon_r^s - j\dfrac{\sigma}{\omega\varepsilon_0}$, where $j^2 = -1$ and $\omega = 2\pi f$. All EM fields in this paper are assumed to be time-harmonic with an $e^{j\omega t}$ time dependence.

The infinite domain outside the scatterers is truncated by a circle with radius r_t, as shown in Fig. 5.2. The equations modelling such a problem, c.f. [77], are

$$\boldsymbol{\nabla} \cdot \big(\frac{1}{\varepsilon_{cr}} \boldsymbol{\nabla} H_z\big) + k_0^2 \mu_r H_z = 0 \qquad \text{in } \Omega, \tag{5.1a}$$

$$\frac{1}{\varepsilon_{cr}} \frac{\partial H_z}{\partial \mathbf{n}} - jk_0 \sqrt{\frac{\mu_r^{\mathrm{s}}}{\varepsilon_{cr}^{\mathrm{s}}}}\, H_z = 0 \qquad \text{on } \Gamma_s, \tag{5.1b}$$

$$\frac{\partial (H_z - H_z^i)}{\partial \mathbf{n}} + (jk_0 + \frac{1}{2r_t})(H_z - H_z^i) = 0 \qquad \text{on } \Gamma_t, \tag{5.1c}$$

where $k_0 = 2\pi f\sqrt{\varepsilon_0 \mu_0}$, ε_0 and μ_0 are the wavenumber, the permittivity and the permeability of free space, respectively; $\mathbf{n}$ is the outward unit normal vector to Γ_t. The equations (5.1b) and (5.1c) are referred to as impedance and first order absorbing boundary conditions [77], respectively. Note that the equations entering (5.1) are invariant under simultaneous scaling of the frequency and size of the domain except for the frequency dependence of the complex permittivity of the scatterer.

A variational statement of (5.1) may be written as follows: find $H_z \in H^1(\Omega)$ (see [26]) such that for every $\phi \in H^1(\Omega)$ we have the equality:

$$\int_\Omega \frac{1}{\varepsilon_{cr}} \boldsymbol{\nabla} H_z \cdot \boldsymbol{\nabla} \phi \,\mathrm{d}V - k_0^2 \int_\Omega \mu_r H_z \,\phi \,\mathrm{d}V - jk_0 \int_{\Gamma_s} \sqrt{\frac{\mu_r^{\mathrm{s}}}{\varepsilon_{cr}^{\mathrm{s}}}} H_z \,\phi \,\mathrm{d}\Gamma$$
$$+ \big(jk_0 + \frac{1}{2r_t}\big) \int_{\Gamma_t} \frac{1}{\varepsilon_{cr}} H_z \,\phi \,\mathrm{d}\Gamma = \int_{\Gamma_t} \frac{1}{\varepsilon_{cr}} \left(\frac{\partial H_z^i}{\partial \mathbf{n}} + \big(jk_0 + \frac{1}{2r_t}\big) H_z^i \right) \phi \,\mathrm{d}\Gamma. \tag{5.2}$$

We assume that the incident field is a plane wave, that is $H_z^i = e^{-jk_0\sqrt{\varepsilon_{cr}\mu_{cr}}x}$, and consider two scatterers which are symmetric about the x-axis. As a result, H_z is also symmetric about the x-

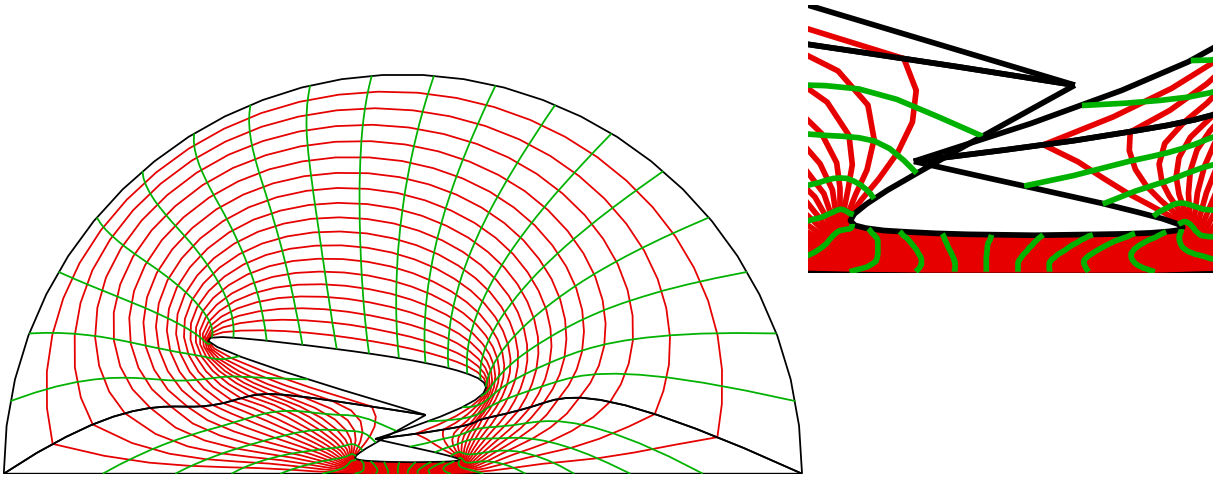

Figure 5.3: An optimization result in which no regularity conditions are imposed. Note that the boundary of the antenna approaches the truncation boundaries and also self-intersects.

axis. Thus we can solve the problem in half the domain with the following boundary condition:

$$\frac{\partial H_z}{\partial y} = 0 \quad \text{if} \quad y = 0. \tag{5.3}$$

5.2.2 Shape optimization problem

We consider the problem of finding shapes of antennas depicted in Fig. 5.2 in order to maximize the following quantity, which is proportional to the magnetic energy

$$W_{\square} = 2 \int_{\Omega_{\square}} |H_z|^2 \, \mathrm{d}V \tag{5.4}$$

where H_z is the solution to the equations (5.1). The domain $\Omega_{\square}$ in (5.4) is a relatively small region of space between the two antennas, see in Fig. 5.2. In (5.4), the factor 2 accounts for the fact that we integrate only over a half of a symmetric domain. The only difference between the problem studied in Aage et al. [71] and the one studied in this paper is that we maximize magnetic energy in a small rectangular region and not in a small circular region. However, in order to compare the efficiency of our antenna design with the one found in Aage et al. [71] we later evaluate the magnetic energy in the circular region as well.

We now look at whether and which regularization conditions and/or constraints are needed for this problem. Having applications for wireless energy transfers in mind, a space between the two antennas is needed for placing an energy harvesting device. Therefore, it is necessary to introduce a lower bound on the position of the antenna guaranteeing the existence of such a space. We also observe that, unless prevented from doing so the resonator tends to grow without bound and its boundary tends to self-intersect, see Fig. 5.3. Therefore, we also introduce an upper bound on resonator's volume and a set of conditions to prevent the shape from self-intersecting.

5.3 Isogeometric analysis

In this section we recall the basic two-dimensional B-spline based isogeometric analysis (IGA). Similarly to the standard FEM, the underlying principle of IGA is the use of the Galerkin

method [2]. Thus we approximate a weak solution to a given boundary value problem associated with Maxwell's equations in a finite-dimensional space spanned by certain basis (shape) functions. In the present case, the basis functions are defined indirectly via a spline parametrization of the physical domain and bivariate B-spline tensor products in the parameter domain $[0,1]^2$.

5.3.1 B-splines

B-splines are piecewise polynomials of a certain degree p, typically differentiable up to the degree $p-1$, which are non-negative and compactly supported, see Fig. 5.4 (left). They are completely defined by specifying certain parameter values, called *knots*, $\xi_1 \leq \ldots \leq \xi_{n+p+1}$. More precisely, B-splines may be defined recursively as follows: for $i = 1, \ldots, n$ we put

$$N_i^0(\xi) = \begin{cases} 1 & \text{if} \quad \xi \in [\xi_i, \xi_{i+1}[, \\ 0 & \text{otherwise}, \end{cases} \qquad N_i^p(\xi) = \frac{\xi - \xi_i}{\xi_{i+p} - \xi_i} N_i^{p-1}(\xi) + \frac{\xi_{i+p+1} - \xi}{\xi_{i+p+1} - \xi_{i+1}} N_{i+1}^{p-1}(\xi).$$

In the context of IGA, the *knot vector* $\boldsymbol{\Xi} = \{\xi_1, \ldots, \xi_{n+p+1}\}$ typically has its first and last knots set to 0 and 1, respectively, and repeated $p+1$ times. That is, we have $\xi_1 = \ldots = \xi_{p+1} = 0$ and $\xi_{n+1} = \ldots = \xi_{n+p+1} = 1$, see Fig. 5.4 (right). Such B-splines form a partition of unity. Further properties of B-splines can be found in, e.g., [22, 24].

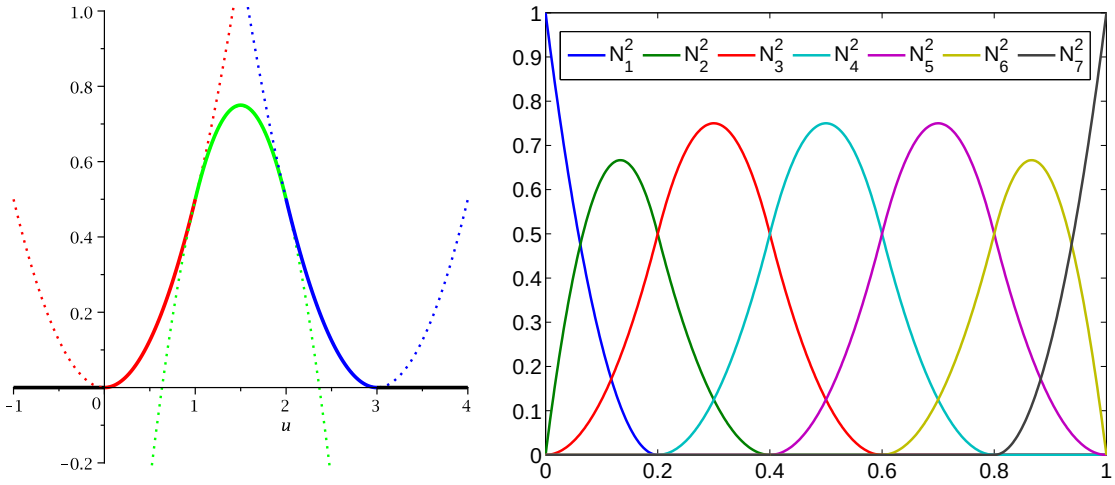

Figure 5.4: To the left: a quadratic B-spline composed of polynomial "pieces" (shown in different colors). The alignments of the dashed-straight lines show that the B-spline is C^1-continuous at the joint points. To the right: quadratic B-splines with the knot vector $\{0,0,0,0.2,0.4,0.6,0.8,1,1,1\}$.

5.3.2 Basis functions for analysis

Let us consider a simply connected open domain $\Omega \subset \mathbb{R}^2$. We are looking for a spline parametrization of Ω, that is, for a *bijective* map $\mathbf{F} : [0,1]^2 \to \Omega$ of the form

$$\mathbf{F}(u,v) = \big(x(u,v), y(u,v)\big) = \sum_{i=1}^{\widehat{m}} \sum_{j=1}^{\widehat{n}} \widehat{\mathbf{d}}_{i,j} \widehat{M}_i^p(u) \widehat{N}_j^q(v), \tag{5.5}$$

where $\widehat{M}_i^p$ and $\widehat{N}_i^q$ are B-splines of degree p and q with knot vectors $\widehat{\boldsymbol{\Xi}}_u$ and $\widehat{\boldsymbol{\Xi}}_v$, respectively. By composing the inverse $\mathbf{F}^{-1}$ with some basis functions on the parameter (reference) domain

$]0,1[^2$ we obtain basis functions defined on the physical domain Ω. We let $\widetilde{M}_i^{\widetilde{p}}$, $i = 1, \ldots, \widetilde{m}$ and $\widetilde{N}_j^{\widetilde{q}}$, $j = 1, \ldots, \widetilde{n}$ be B-splines of degree $\widetilde{p}$ and $\widetilde{q}$ (not necessary equal to p and q) with knot vector $\widetilde{\boldsymbol{\Xi}}_u$ and $\widetilde{\boldsymbol{\Xi}}_v$, respectively. The basis functions on the parameter domain are defined as the tensor product splines $\widetilde{R}_k^{\widetilde{p},\widetilde{q}}(u,v) = \widetilde{M}_i^{\widetilde{p}}(u)\widetilde{N}_j^{\widetilde{q}}(v)$, $k = (\widetilde{n}-1)i + j$. Thus, the basis functions on the physical domain Ω are given as $\widetilde{R}_k^{\widetilde{p},\widetilde{q}} \circ \mathbf{F}^{-1}$. An integral over Ω can be now transformed to an integral over $]0,1[^2$ as

$$\iint_{\Omega} f(x,y)\,\mathrm{d}x\,\mathrm{d}y = \iint_{]0,1[^2} f(x(u,v),y(u,v))\,\det(\mathbf{J})\,\mathrm{d}u\,\mathrm{d}v, \tag{5.6}$$

where $\mathbf{J}$ is the Jacobian of the variable transformation $\mathbf{F}$, and we have assumed that $\det(\mathbf{J}) > 0$. Note that the knot vectors $\widehat{\boldsymbol{\Xi}}_u$ and $\widehat{\boldsymbol{\Xi}}_v$ used for for the parametrization of Ω may be "finer" than the four knot vectors $\boldsymbol{\Xi}_\ell$ ($\ell = 1, \ldots, 4$) used in the parametrization of the domain boundary $\partial\Omega$. The "refinement" is achieved by inserting new knots into the two pairs of knot vectors $(\boldsymbol{\Xi}_1, \boldsymbol{\Xi}_3)$ and $(\boldsymbol{\Xi}_2, \boldsymbol{\Xi}_4)$ respectively. Furthermore, to ensure that we can approximate any function in $H^1(\Omega)$ [26] sufficiently well, we may want to use an even finer (when compared to $\widehat{\boldsymbol{\Xi}}_u$ and $\widehat{\boldsymbol{\Xi}}_v$) pair of knot vectors $\widetilde{\boldsymbol{\Xi}}_u$ and $\widetilde{\boldsymbol{\Xi}}_v$ for the analysis, see Fig. 5.5.

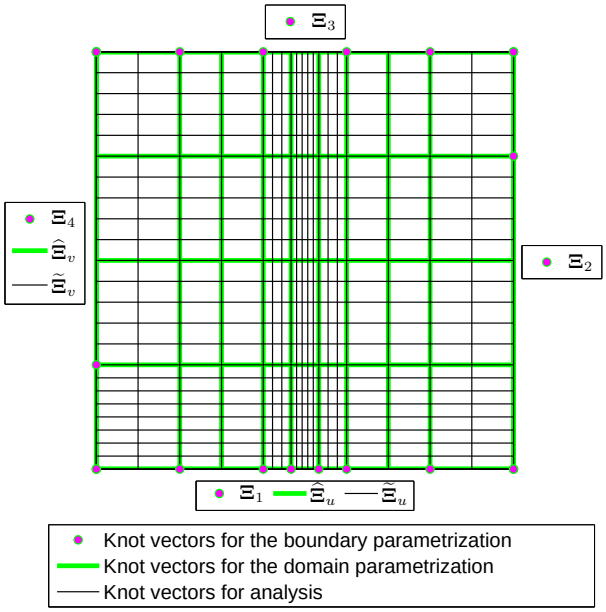

Figure 5.5: The three types of knot vectors of an IGA model used in the present work.

Remark 8. As a consequence of the formula (5.6), one may evaluate integrals over Ω entering a variational form of a given boundary value problem by computing the integrals over the parameter domain instead. Thus an "IGA assembly routine" may be implemented as a loop over elements defined by the knot vectors $\widetilde{\boldsymbol{\Xi}}_u$ and $\widetilde{\boldsymbol{\Xi}}_v$, see Fig. 5.5.

5.3.3 spline parametrization

In this section, we recall techniques for handling B-spline parametrizations in IGA. For more details, see [28, 29, 30].

5.3.3.1 Validating a spline parametrization.

In order to ensure that a given choice of inner control points $\widehat{\mathbf{d}}_{i,j}$, $i = 1, \ldots, \widehat{n}$, $j = 1, \ldots, \widehat{m}$ results in a valid spline parametrization of Ω we employ the following approach. The determinant of the Jacobian of $\mathbf{F}$ given by (5.5) is computed as

$$\det(\mathbf{J}) = \sum_{i,j=1}^{\widehat{m},\widehat{n}} \sum_{k,\ell=1}^{\widehat{m},\widehat{n}} \det[\widehat{\mathbf{d}}_{i,j}, \widehat{\mathbf{d}}_{k,\ell}] \, \frac{\mathrm{d}\widehat{M}_i^p(u)}{\mathrm{d}u} \, \widehat{N}_j^q(v) \, \widehat{M}_k^p(u) \, \frac{\mathrm{d}\widehat{N}_\ell^q(v)}{\mathrm{d}v}, \tag{5.7}$$

where $\det[\widehat{\mathbf{d}}_{i,j}, \widehat{\mathbf{d}}_{k,\ell}]$ is the determinant of the 2×2 matrix with columns $\widehat{\mathbf{d}}_{i,j}$, $\widehat{\mathbf{d}}_{k,\ell}$. Equation (5.7) defines a piecewise polynomial of degree $2p-1$ in u and degree $2q-1$ in v, with the differentiability at a knot lower by 1 in u and also lower by 1 in v. Such a map can be written in terms of B-splines $\mathcal{M}_k^{2p-1}$ and $\mathcal{N}_\ell^{2q-1}$ of degree $2p-1$ and $2q-1$ with the knot vectors obtained from $\widehat{\boldsymbol{\Xi}}_u$ and $\widehat{\boldsymbol{\Xi}}_v$ by raising the multiplicities of the inner u-knots and v-knots by p and q, respectively [52]. That is

$$\det(\mathbf{J}) = \sum_{k,\ell=1}^{M,N} c_{k,\ell} \, \mathcal{M}_k^{2p-1}(u) \, \mathcal{N}_\ell^{2q-1}(v), \tag{5.8}$$

where the coefficients $c_{k,\ell}$ depend linearly on the quantities $\det[\widehat{\mathbf{d}}_{i,j}, \widehat{\mathbf{d}}_{k,\ell}]$. As B-splines are non-negative, we conclude that whenever all the coefficients $c_{k,\ell}$ are positive (or negative), then so is the determinant.

5.3.3.2 Obtaining a spline parametrization.

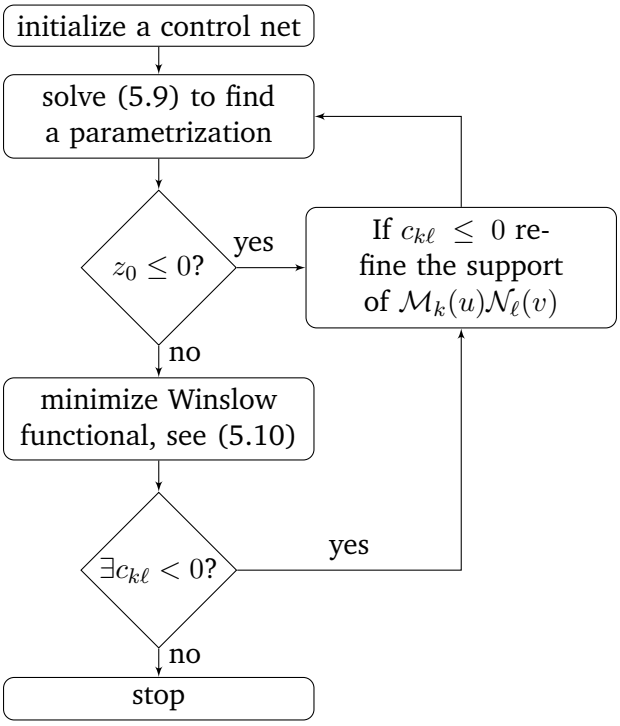

Figure 5.6: The algorithm for extending a boundary parametrization to the interior.

None of the linear methods presented in [29, 30] for extending the parametrization of the boundary into the interior of the domain can in general guarantee that the resulting map $\mathbf{F}$ will

satisfy $\det(\mathbf{J}) > 0$ everywhere on $[0,1]^2$. Therefore, during some shape optimization iterations we have to utilize a more expensive non-linear method for improving the distribution of the interior control points $\widehat{\mathbf{d}}_{i,j}$. In a view of (5.8), a natural approach to ensure that $\det(\mathbf{J})$ is bounded away from zero is to solve the following optimization problem:

$$\begin{aligned} &\underset{\widehat{\mathbf{d}}_{i,j},z}{\text{maximize}} && z, \\ &\text{subject to} && c_{k,\ell}\big(\widehat{\mathbf{d}}_{i,j}\big) \geq z, \end{aligned} \tag{5.9}$$

where $\widehat{\mathbf{d}}_{i,j}$ are inner control points as stated in (5.5), $c_{k,\ell}$ are given by (5.8), and z is an auxiliary optimization variable. If z resulting from approximately solving (5.9) to local optimality is positive then we are guaranteed to have a valid parametrization. Unfortunately, the quality of the parametrization obtained in this fashion needs not to be very high. Thus, we improve the parametrization by looking at the following constrained optimization problem:

$$\begin{aligned} &\underset{\text{inner control points } \widehat{\mathbf{d}}_{i,j}}{\text{minimize}} && \int_0^1 \int_0^1 W(\widehat{\mathbf{d}}_{i,j})\,\mathrm{d}u\,\mathrm{d}v, \\ &\text{subject to} && c_{k\ell}\big(\widehat{\mathbf{d}}_{i,j}\big) \geq \delta z_0 \end{aligned} \tag{5.10}$$

where $W(\widehat{\mathbf{d}}_{i,j}) = (\|\mathbf{F}_u\|^2 + \|\mathbf{F}_v\|^2)/\det[\mathbf{F}_u, \mathbf{F}_v]$ is referred to as the Winslow functional [31]. In (5.10), $z_0 > 0$ is computed by approximately solving (5.9) and $\delta \in [0,1]$ is a fixed relaxation parameter.

In our numerical experiments we utilize the interior point algorithm constituting a part of Optimization Framework in Matlab [33] for solving the optimization problems (5.9) and (5.10) to approximate stationarity. Also, we set $\delta = 0$ in (5.10). The whole process is outlined in Fig. 5.6.

5.3.3.3 Linearized Winslow functional.

The algorithm for finding a valid domain parametrization described above has to be carried out at every iteration of an "outer" shape optimization algorithm. Firstly, this process is rather computationally expensive, as it requires solving two non-linear programming problems at every shape optimization iteration. Secondly, as we solve the said optimization problems only approximately, it is not possible to find the derivatives of the inner control points with respect to changes of boundary control points. The latter does not allow us to use gradient based optimization algorithms for the "outer" shape optimization problem.

To avoid this difficulty, we linearize the process of computing a domain parametrization. Namely, we can Taylor-expand the Winslow functional as

$$\mathcal{W}(\widehat{\mathbf{d}}) = \iint_\Omega W(\widehat{\mathbf{d}})\,\mathrm{d}u\,\mathrm{d}v \approx \mathcal{W}(\widehat{\mathbf{d}}_0) + (\widehat{\mathbf{d}} - \widehat{\mathbf{d}}_0)^T\,\mathbf{G}(\widehat{\mathbf{d}}_0) + \frac{1}{2}(\widehat{\mathbf{d}} - \widehat{\mathbf{d}}_0)^T\,\mathbf{H}(\widehat{\mathbf{d}}_0)\,(\widehat{\mathbf{d}} - \widehat{\mathbf{d}}_0), \tag{5.11}$$

where $\widehat{\mathbf{d}}$ is a vector with all control points $\widehat{\mathbf{d}}_{i,j}$, $\widehat{\mathbf{d}}_0$ is the control points for a reference parametrization obtained by solving (5.10), and $\mathbf{G}$ and $\mathbf{H}$ are the gradient and Hessian of $\mathcal{W}$ respectively. If we split the control points $\widehat{\mathbf{d}} = (\widehat{\mathbf{d}}_1\ \widehat{\mathbf{d}}_2)^T$ into the part $\widehat{\mathbf{d}}_2$ that is given (typically the boundary control points) and the part $\widehat{\mathbf{d}}_1$ that has to be determined (typically the inner control points), then we can write (5.11) as

$$\begin{aligned} \mathcal{W}(\widehat{\mathbf{d}}) \approx \mathcal{W}(\widehat{\mathbf{d}}_0) &+ \begin{pmatrix} \widehat{\mathbf{d}}_1 - \widehat{\mathbf{d}}_{1,0} & \widehat{\mathbf{d}}_2 - \widehat{\mathbf{d}}_{2,0} \end{pmatrix} \begin{pmatrix} \mathbf{G}_1 \\ \mathbf{G}_2 \end{pmatrix} \\ &+ \frac{1}{2} \begin{pmatrix} \widehat{\mathbf{d}}_1 - \widehat{\mathbf{d}}_{1,0} & \widehat{\mathbf{d}}_2 - \widehat{\mathbf{d}}_{2,0} \end{pmatrix} \begin{pmatrix} \mathbf{H}_{11} & \mathbf{H}_{12} \\ \mathbf{H}_{21} & \mathbf{H}_{22} \end{pmatrix} \begin{pmatrix} \widehat{\mathbf{d}}_1 - \widehat{\mathbf{d}}_{1,0} \\ \widehat{\mathbf{d}}_2 - \widehat{\mathbf{d}}_{2,0} \end{pmatrix}. \end{aligned} \tag{5.12}$$

The minimum of the right hand side of (5.12) is obtained when $\widehat{\mathbf{d}}_1$ satisfies the *linear equation*

$$\mathbf{H}_{11}(\widehat{\mathbf{d}}_1 - \widehat{\mathbf{d}}_{1,0}) = -\mathbf{G}_1 - \mathbf{H}_{12}(\widehat{\mathbf{d}}_2 - \widehat{\mathbf{d}}_{2,0}). \tag{5.13}$$

This gives us a fast method for computing the domain parametrization and its derivatives with respect to the boundary control points. We use this method as long as we obtain a valid parametrization, but if the parametrization at some point fails the test described in Section 5.3.3.1 then we restart the "outer" shape optimization algorithm with a new reference parametrization $\widehat{\mathbf{d}}_0$ found by the method described in Section 5.3.3.2.

The given control points $\widehat{\mathbf{d}}_2$ can further be split into the set of fixed control points $\widehat{\mathbf{d}}_f$ and control points $\mathbf{R}\mathbf{d}$ obtained from the design variables (control points) $\mathbf{d}$ by knot insertion (refinement).

5.3.3.4 Multiple patches.

The need for configuring a physical domain by several patches arises naturally when the (connected) domain is not simple, that is when there is at least one "hole" in the domain (see Fig. 5.9), or when avoiding singularities, that is when the IGA-mapping is not bijective at some corner (see [30, 7]). In any case, the parametrization of the domain boundary is given. Thus, the task of extending the parametrization into the interior is the same as in the one patch case except the parametrizations of inner patch boundaries are unknown. For such a domain, the optimization problems (5.9), (5.10), and the linear system (5.13) should account for the control points with respect to the inner boundaries as design variables while maintaining C^0-continuities across the boundaries by linear constraints on the control points. The constraints are obtained by the usual refinement rule. For implementing details see [29].

5.4 Isogeometric shape optimization modeling

In this section, we formulate the optimization problem stated in the section 5.2.2 in an isogeometric analysis context. We then derive differentiable constraints to prevent the shape of the antenna from self-intersecting. Finally sensitivity analysis is derived explicitly and the strategy for performing shape optimization using isogeometric analysis is presented.

We parametrize the physical domain by the 2-patch model shown in Fig. 5.10. The circular truncation boundary of the numerical model in Fig. 5.2 is approximated by a B-spline curve. The approximation is done by the method presented in appendix 5.7. Let $\mathbf{F}$ be the parametrization of the physical domain given by (5.5). The energy $W_\square$ given by (5.4) now becomes

$$W_\square = 2\int_{\Omega_\square} |H_z|^2 \,\mathrm{d}V = 2\iint_{\mathbf{F}^{-1}(\Omega_\square)} |H_z \circ \mathbf{F}|^2 \,\det(\mathbf{J})\,\mathrm{d}u\,\mathrm{d}v. \tag{5.14}$$

To simplify the procedure for computing the above integral we chose the region $\Omega_\square$ equivalent to one knot span, see Fig. 5.10. We keep the parametrization of this region fixed during shape optimization iterations, that is, the region does not depend on design variables. Finally, we choose the corresponding control points so that the region is a rectangle, see Fig. 5.2, 5.9 and 5.10.

Let us now examine the regularities and constraints discussed in section 5.2.2. First, to enforce a lower bound on the vertical placement of the antenna we impose a lower bound on the y-coordinates of design control points, see Fig. 5.9. Furthermore, the volume constraint described in section 5.2.2 now reads

$$\text{Vol.} = \frac{1}{2}\oint_{\partial D} \det[\mathbf{r}, \dot{\mathbf{r}}]\,\mathrm{d}\Gamma \leq V_0, \tag{5.15}$$

where D is the domain inside the resonator, $\mathbf{r}$ is a parametrization of (one component of) the boundary ∂D of D, V_0 is a volume limit, and $\det[\mathbf{r}, \dot{\mathbf{r}}]$ is the determinant of the matrix with

columns $\mathbf{r}$ and $\dot{\mathbf{r}}$. The positive orientation of the line integral in (5.15) is counterclockwise. If $\mathbf{r}(\xi) = \sum_i \mathbf{c}_i N_i(\xi)$, where $N_i(\xi)$ $(i = 1, \ldots, n)$ are B-splines of degree p with a knot vector $\boldsymbol{\Xi}$, the integral in (5.15) becomes

$$\oint_{\mathbf{r}([0,1])} \det[\mathbf{r}, \dot{\mathbf{r}}]\, \mathrm{d}\Gamma = \sum_{i,j} \det[\mathbf{c}_i, \mathbf{c}_j] \int_0^1 N_i(\xi)\, \dot{N}_j(\xi)\, \mathrm{d}\xi. \tag{5.16}$$

We now investigate the remaining constraints.

5.4.1 Non self-intersection constraint

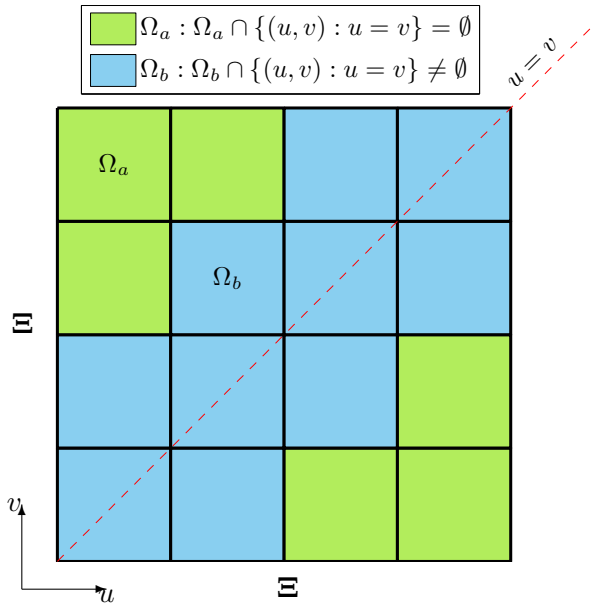

Figure 5.7: A knot vector $\boldsymbol{\Xi}$ partitions the unit square $[0,1]^2$ into products of knot spans. We classify the rectangles according to whether they intersect the diagonal or not.

Let $N_i(\xi)$ $(i = 1, \ldots, n)$ be B-splines of degree p with a knot vector $\boldsymbol{\Xi}$. Consider a B-spline curve $\mathbf{r}(\xi) = \sum_i \mathbf{c}_i N_i(\xi)$, where $\mathbf{c}_i$ are design control points. To ensure that $\mathbf{r}$ does not intersect itself, we look at the square distance between every pair of points on the curve, $(\mathbf{r}(u), \mathbf{r}(v))$, $(u, v) \in \boldsymbol{\Xi} \times \boldsymbol{\Xi}$. That is

$$d^2_{\mathbf{r}}(u,v) = \|\mathbf{r}(u) - \mathbf{r}(v)\|^2 = \sum_{i,j} \mathbf{c}_i \cdot \mathbf{c}_j \big(N_i(u) - N_j(v)\big)^2. \tag{5.17}$$

Clearly, the curve is simple if and only if $d^2_{\mathbf{r}}(u,v) > 0$ for every $u \neq v$, $u, v \in [0,1]^2$. To ensure that this condition is fulfilled, we look at rectangles in $[0,1]^2$ formed by the products of knot spans, see Fig. 5.7. First, consider a rectangle Ω_a that does not intersect the diagonal $\{(u,v) : u = v\}$. In Ω_a, $d^2_{\mathbf{r}}(u,v)$ can be expressed in terms of Bernstein polynomials [24] of degree $2p$, $B^{2p}_k(u) B^{2p}_\ell(v)$ $(k, \ell = 1, \ldots, 2p+1)$, defined within the element. That is

$$d^2_{\mathbf{r}}(u,v) = \sum_{k,\ell} a_{k,\ell} B^{2p}_k(u) B^{2p}_\ell(v), \quad (u,v) \in \Omega_a. \tag{5.18}$$

Clearly, if all control points $a_{k,\ell}$ are nonnegative and the corner points are strictly positive, then $d^2_{\mathbf{r}}$ is strictly positive. Next we consider a rectangle Ω_b that does intersect the diagonal. Here

$(u-v)^2$ is a factor of $d_{\mathbf{r}}^2$ and we can write

$$d_{\mathbf{r}}^2(u,v) = (u-v)^2 \sum_{\alpha,\beta} b_{\alpha,\beta} B_\alpha^{2p-2}(u) B_\beta^{2p-2}(v) \quad (u,v) \in \Omega_b \tag{5.19}$$

In (5.19), $B_\alpha^{2p-2}(u) B_\beta^{2p-2}(v)$ $(\alpha,\beta = 1,\ldots,2p-1)$ are Bernstein polynomials of degree $2p-2$ defined within Ω_b. Once again, if all control points $a_{k,\ell}$ are non negative and the corner points are strictly positive, then $d_{\mathbf{r}}$ is strictly positive. So we arrive at the sufficient conditions.

Proposition 1. *Let* $\mathbf{r}$ *be a B-spline curve and* $d_{\mathbf{r}}^2$ *be its associated function given by* (5.17)*. Furthermore, let* $a_{k,\ell}$ $(k,\ell = 1,\ldots,2p+1)$ *and* $b_{\alpha,\beta}$ $(\alpha,\beta = 1,\ldots,2p-1)$ *be the control points of* $d_{\mathbf{r}}^2$ *given by* (5.18) *and* (5.19)*, respectively. Then* $\mathbf{r}$ *is a simple curve if the following conditions are satisfied*

(i) $a_{k,\ell} \geq 0$ *for all* $k,\ell = 1,\ldots,2p+1$*,*

(ii) $b_{\alpha,\beta} \geq 0$ *for all* $\alpha,\beta = 1,\ldots,2p-1$*,*

(iii) $d_{\mathbf{r}}^2(\xi_i,\xi_j) \geq \delta$*,* $i,j = 1,\ldots,n$*, for some positive* δ*.*

Note that utilizing the symmetry in (5.17) about the line $u = v$, only one half of the conditions are needed. Also, similarly to (5.31), the coefficients $a_{k,\ell}$ in (5.18) and $b_{\alpha,\beta}$ in (5.19) may be explicitly represented as quadratic forms of the design control points $\mathbf{c}_i$. For the current optimization problem, the antenna boundary is composed of two B-spline curves. Proposition 1 can be straightforwardly extended to a piecewise B-spline curve. Finally, knot insertions may be needed in order to obtain tighter conditions for the sufficiency.

5.4.2 Discretization

An approximation to the solution H_z to (5.1) is expanded in terms of the basis functions (see Section 5.3.2) as $H_z = \sum_k h_k \,(\widetilde{R}_k^{\widetilde{p},\widetilde{q}} \circ \mathbf{F}^{-1}) = \big[\widetilde{R}_1^{\widetilde{p},\widetilde{q}} \circ \mathbf{F}^{-1}, \ldots, \widetilde{R}_{\widetilde{m}\widetilde{n}}^{\widetilde{p},\widetilde{q}} \circ \mathbf{F}^{-1}\big]\mathbf{h}$, where $\mathbf{h}$ contains all the coordinates of H_z with respect to the selected basis. Substituting this expression into the weak form (**??**) and utilizing the basis functions as the test functions, we arrive at the following set of linear algebraic equations:

$$(\mathbf{K} + \mathbf{M} + \mathbf{S} + \mathbf{T})\,\mathbf{h} = \mathbf{f}. \tag{5.20}$$

Entries of the matrices entering (5.20) are with the help of (5.6) calculated as:

$$\mathbf{K}_{k\ell} = \iint\limits_{[0,1]^2} \frac{1}{\varepsilon_{cr}} \left(\mathbf{D}\widetilde{R}_k^{\widetilde{p},\widetilde{q}}(u,v)\,\mathbf{J}^{-1}\right)^T \mathbf{D}\widetilde{R}_\ell^{\widetilde{p},\widetilde{q}}(u,v)\,\mathbf{J}^{-1}\,\det(\mathbf{J})\,\mathrm{d}u\,\mathrm{d}v, \tag{5.21a}$$

$$\mathbf{M}_{k\ell} = -k_0^2 \iint\limits_{[0,1]^2} \mu_r\,\widetilde{R}_k^{\widetilde{p},\widetilde{q}}(u,v)\,\widetilde{R}_\ell^{\widetilde{p},\widetilde{q}}(u,v)\,\det(\mathbf{J})\,\mathrm{d}u\,\mathrm{d}v, \tag{5.21b}$$

$$\mathbf{S}_{k\ell} = -jk_0 \int\limits_{\mathbf{F}^{-1}(\Gamma_s)} \frac{\mu_r^s}{\varepsilon_{cr}^s}\,\widetilde{R}_k^{\widetilde{p},\widetilde{q}}(u,v)\,\widetilde{R}_\ell^{\widetilde{p},\widetilde{q}}(u,v)\,\mathrm{d}s, \tag{5.21c}$$

$$\mathbf{T}_{k\ell} = \big(jk_0 + \frac{1}{2r_t}\big) \int\limits_{\mathbf{F}^{-1}(\Gamma_t)} \frac{1}{\varepsilon_{cr}}\,\widetilde{R}_k^{\widetilde{p},\widetilde{q}}(u,v)\,\widetilde{R}_\ell^{\widetilde{p},\widetilde{q}}(u,v)\,\mathrm{d}s, \tag{5.21d}$$

$$\mathbf{f}_\ell = \int\limits_{\mathbf{F}^{-1}(\Gamma_t)} \frac{1}{\varepsilon_{cr}} \left(\frac{\partial H_z^i}{\partial \mathbf{n}} + \big(jk_0 + \frac{1}{2r_t}\big) H_z^i\right) \widetilde{R}_\ell^{\widetilde{p},\widetilde{q}}(u,v)\,\mathrm{d}s, \tag{5.21e}$$

$k,\ell = 1,\ldots,\widetilde{m}\widetilde{n}$. In the equations (5.21), $\mathbf{J}$ is the Jacobian of the parametrization $\mathbf{F}$ and $\mathbf{D}f(u,v) = \left[\frac{\partial f}{\partial u}(u,v) \quad \frac{\partial f}{\partial v}(u,v)\right]$ is the differential of a real-valued function $f : [0,1]^2 \to \mathbb{R}$.

5.4.3 Formulation of the optimization problem and sensitivity analysis

Recall that $\mathbf{d}$ is the vector containing components of design control points, see Fig. 5.9. Taking the constraints discussed above into account and noting that in (5.14), $H_z \circ \mathbf{F} = \big[\widetilde{R}_1^{\widetilde{p},\widetilde{q}}, \ldots, \widetilde{R}_{\widetilde{m}\widetilde{n}}^{\widetilde{p},\widetilde{q}}\big]\mathbf{h}$, we arrive at the following shape optimization problem:

$$\underset{\mathbf{d}\in\mathbb{R}^N}{\text{maximize}} \quad \log_{10}(W_\square) = \log_{10}\left(2\iint_{\mathbf{F}^{-1}(\Omega_\square)} \left|\big[\widetilde{R}_1^{\widetilde{p},\widetilde{q}}, \ldots, \widetilde{R}_{\widetilde{m}\widetilde{n}}^{\widetilde{p},\widetilde{q}}\big]\mathbf{h}\right|^2 \det(\mathbf{J})\,\mathrm{d}u\,\mathrm{d}v\right), \tag{5.22a}$$

$$\text{such that} \quad y_{\mathbf{d}} \geq y_0, \tag{5.22b}$$

$$\text{Vol.} = \frac{1}{2}\oint_{\partial D} \det(\mathbf{r}, \dot{\mathbf{r}})\,\mathrm{d}\Gamma \leq V_0, \tag{5.22c}$$

$$a_{k,\ell} \geq 0,\ b_{\alpha,\beta} \geq 0,\ d_{\mathbf{r}}^2(\xi_i, \xi_j) \geq \delta,\ \text{(c.f. proposition 1)} \tag{5.22d}$$

$$(\mathbf{K} + \mathbf{M} + \mathbf{S} + \mathbf{T})\,\mathbf{h} = \mathbf{f}, \tag{5.22e}$$

where $y_{\mathbf{d}}$ are the y-coordinates of the design control points, and y_0 is a lower bound.

Let us now find first order derivatives of functions involved in (5.22). First, consider the constraints (5.22d). As noted in subsection 5.4.1 the quantities $a_{k,\ell}$, $b_{\alpha,\beta}$, and $d_{\mathbf{r}}(\xi_i, \xi_j)$ in $(i-iii)$ of Proposition 1 are quadratic forms of the design control point vector $\mathbf{d}$, therefore evaluating their gradients with respect to $\mathbf{d}$ is a straightforward calculation. The same holds for (5.22c) owing to (5.16). On the other hand, the objective function in (5.22) depends implicitly on $\mathbf{d}$ through the discretized Maxwell's equations (5.22e). Consider the partial derivative of $W_\square$ with respect to a component $\widehat{d}_i$ of $\widehat{\mathbf{d}}$. Rewriting (5.14) as $W_\square = 2\iint_{\mathbf{F}^{-1}(\Omega_\square)} H_z \circ \mathbf{F}\,\overline{H_z \circ \mathbf{F}}\,\det(\mathbf{J})\,\mathrm{d}u\,\mathrm{d}v$, and noting that $\mathbf{F}^{-1}(\Omega_\square)$ and consequently $\mathbf{J}\big|_{\mathbf{F}^{-1}(\Omega_\square)}$ is independent from $\widehat{d}_i$, we have

$$\frac{\partial W_\square}{\partial \widehat{d}_i} = 4\iint_{\mathbf{F}^{-1}(\Omega_\square)} \mathrm{Re}\left(\frac{\partial(H_z \circ \mathbf{F})}{\hat{d}_i}\,\overline{H_z \circ \mathbf{F}}\right)\det(\mathbf{J})\,\mathrm{d}u\,\mathrm{d}v. \tag{5.23}$$

Since we clearly have

$$\frac{\partial(H_z \circ \mathbf{F})}{\hat{d}_i} = \big[\widetilde{R}_1^{\widetilde{p},\widetilde{q}}, \ldots, \widetilde{R}_{\widetilde{m}\widetilde{n}}^{\widetilde{p},\widetilde{q}}\big]\frac{\partial \mathbf{h}}{\hat{d}_i}, \tag{5.24}$$

it remains to determine $\frac{\partial \mathbf{h}}{\hat{d}_i}$. Differentiating the two sides of (5.20) and utilizing the fact that $\frac{\partial \mathbf{T}}{\hat{d}_i} = \frac{\partial \mathbf{f}}{\hat{d}_i} = \mathbf{0}$, the partial derivative is in turn the solution to the following linear system

$$(\mathbf{K} + \mathbf{M} + \mathbf{S} + \mathbf{T})\frac{\partial \mathbf{h}}{\hat{d}_i} = -\frac{\partial(\mathbf{K} + \mathbf{M} + \mathbf{S})}{\hat{d}_i}\mathbf{h}. \tag{5.25}$$

In (5.25), the partial derivatives of $\mathbf{K}$, $\mathbf{M}$, and $\mathbf{S}$ are calculated straightforwardly by differentiating (5.21). Finally, as we employ a linear parametrization method discussed in Subsection 5.3.3.3, $\widehat{\mathbf{d}}$ is an affine function of $\mathbf{d}$. That is

$$\widehat{\mathbf{d}} = \mathbf{A}\mathbf{d} + \mathbf{B}, \tag{5.26}$$

where the matrices $\mathbf{A}$ and $\mathbf{B}$ can be explicitly determined from (2.13). Note that the refinement matrices [24] obtained when inserting knots into the boundary knot vectors to have parametrization knot vectors are already taken into account in $\mathbf{A}$. Therefore, the desired sensitivities are

$$\frac{\partial W_\square}{\partial \mathbf{d}} = \mathbf{A}^{\mathrm{T}}\frac{\partial W_\square}{\partial \widehat{\mathbf{d}}}. \tag{5.27}$$

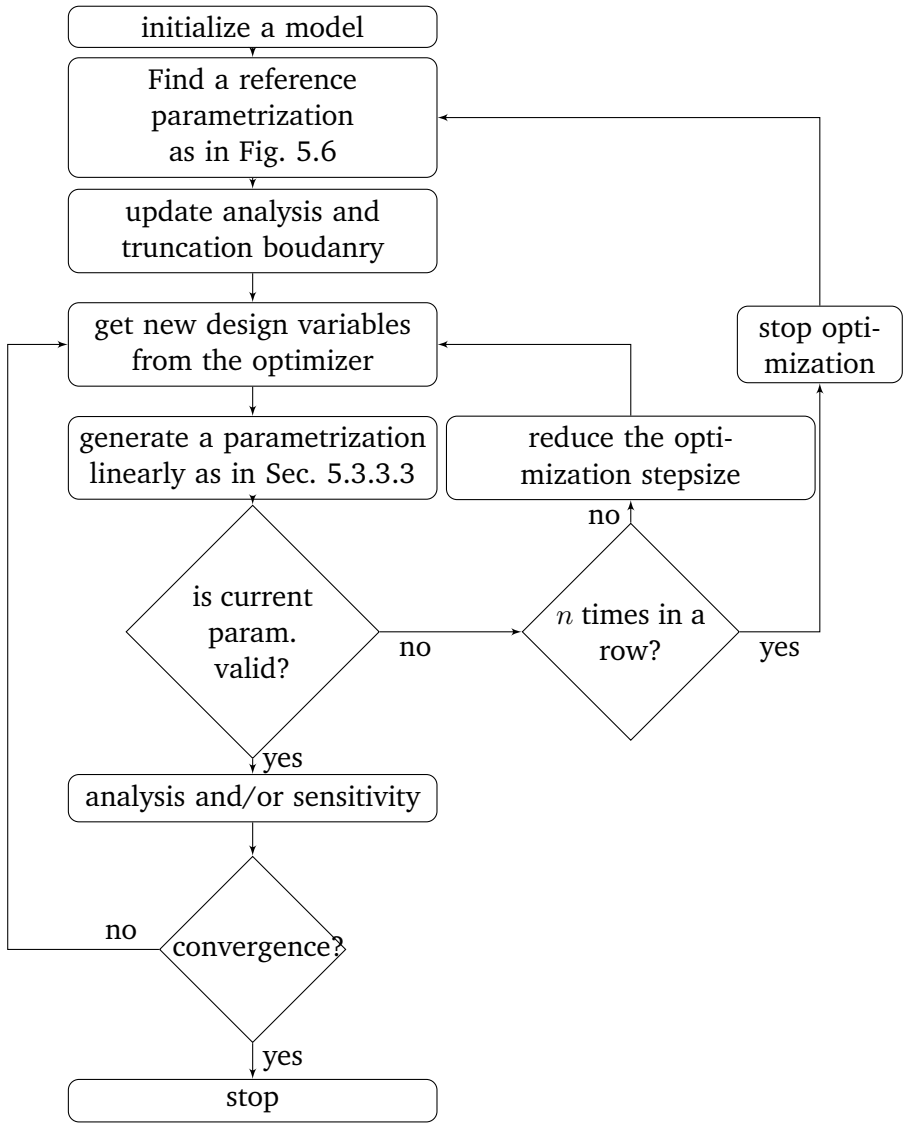

Figure 5.8: Isogeometric shape optimization algorithm used in the current work.

5.4.4 Shape optimization strategy

The optimization strategy is outlined in Fig. 5.8. It should be noted that the step "make smaller optimization step" is inefficient if the number of design variables is relatively large. Nevertheless, within isogeometric shape optimization we usually have relatively small number of design variables, and consequently the relative computational cost of such a step is tolerable. Also, by the step "update analysis and truncation boundar" the correctness of solution as well as truncation boundary approximation is improved towards the end of optimization.

Let us now elaborate on a few steps in the diagram in Fig. 5.8. Verifying whether "the current parametrization is valid" is done by dividing every knot interval of the parametrization knot vectors uniformly N times. The parametrization is valid if all the control points in (5.8) satisfy the inequalities $c_{k,\ell} \geq \delta_c$, and $\det(\mathbf{J})(\text{at Gaussian net}) \geq \delta_{\mathbf{J}}$, where δ_c and $\delta_{\mathbf{J}}$ are small numbers relatively to the volume of the checked patch. Finally, in the step "n times in a row," one could alternatively check whether the magnitude of the stepsize from the current design variables to that of the reference parametrization exceeds a given parameter.

electromagnetic constants of air	electromagnetic constants of copper
$\varepsilon_r = 1$	$\varepsilon_r^s = 1$
$\mu_r = 1$	$\mu_r^s = 1$
$-$	$\sigma = 10^6$ [S/m]

Table 5.1: Electromagnetic constants used in this work.

property	value
Lower bound on the y-coordinates of the design control points in (5.22)	$y_0 = 0.1$ [m]
Upper bound on the volume of the antenna, c.f. (5.22)	$V_0 = \pi 0.65^2$ [m^2]
Number of knot insertions in section 5.4.4	$N = 2$
Minimum allowed value of $c_{k,\ell}$, c.f. section 5.4.4	$\delta_c = 10^{-4}$
Minimum allowed value of $\det(\mathbf{J})$(at Gaussian net), c.f. section 5.4.4	$\delta_{\mathbf{J}} = 10^{-3}$
Maximum allowed number of failing updates, c.f. section 5.4.4	$n = 10$

Table 5.2: Specification of optimization parameters used in this work.

5.5 Numerical examples

We begin this section by specifying physical and optimization parameters used in the present numerical experiments. We then present the results of shape optimization of antennas with the IGA-based shape optimization algorithm described earlier. Different fineness levels of analysis (meshing) for computing a model response numerically in each optimization iteration are carefully chosen for different stages of the optimization problem.

5.5.1 Technical remarks and optimization parameters

We list here a few technical remarks. For the sake of computational efficiency, the matrices of the quadratic forms in (5.8), (5.16), (5.18), and (5.19) as well as the fixed matrices $\mathbf{T}$, $\mathbf{f}$ in (5.20) are pre-computed and stored before the optimization process starts. We use standard Gaussian quadratures [25] for numerical integration. All the solutions presented in this section have been obtained with gradient based non-linear programming solver *fmincon* from Optimization Framework of Matlab, version 7.9 (R2009b) [33].

In tables 5.1 and 5.2 we list the physical and optimization parameters needed by the present numerical experiments. In the former table, we take all parameters, including the conductivity of copper, from Aage et al. [71] in order to be able to compare optimal designs.

5.5.2 Initial shape and its parametrization

We start the present optimization using the following set of knot vectors in the notation of Fig. 5.5: $\Xi_1 = \{0,0,0,1/5,2/5,7/15,8/15,3/5,4/5,1,1,1\}$, $\Xi_3 = \{0,0,0,1/5,2/5,3/5,4/5,1,1,1\}$, $\Xi_2 = \Xi_4 = \{0,0,0,1/2,1,1,1\}$, and $\widehat{\Xi}_u = \Xi_1$, $\widehat{\Xi}_v = \Xi_2$ for parametrizing the two patches. Unless explicitly stated otherwise, all B-splines used in the present experiment are quadratic. For the initial shape, we choose (a piecewise B-spline approximation, see Sec. 5.7) the circle with center at $(0, 0.75)$ and radius $r = 0.65$ [m], as in Aage et al. [71]. For the truncation boundary, we utilize the B-spline approximation of the upper half of the circle with center at $(0,0)$ and radius $r_t = 4$ [m] depicted in Fig. 5.17. Note that the electrical condition [78] at the truncation boundary is fulfilled because $k\, r_t = 9.6438 \gg 1$, where k is the wavenumber of the incoming wave in air.

Having the parametrization of the initial antenna and the truncation boundary, we extend it to a parametrization of the entire domain using a spring model [29, 30]. Feeding the resulting parametrization, see Fig. 5.9(a),(b), to the parametrization routine in Fig. 5.6, we obtain the parametrization shown in Fig. 5.9(c),(d). Importantly, new knots have been inserted to the domain parametrization knot vectors of patch 2. The new knots could be seen as the differences between the two sets of knot vectors in Fig. 5.10. Note that for a multiple patch model, the usual refinement constraints along common boundary components are required to have a *continuous* parametrization of the entire domain.

If we during the optimization need to refine the knot vectors for the parametrization we may also need to refine the knot vectors for the analysis, see Fig. 5.6. The insertion rule we apply is illustrated in Fig. 5.10. Moreover, in order to accurately approximate the numerical solution in the energy harvesting region $\Omega_{\square}$ we would like to refine the parametrization locally around this region. Fortunately the special "horizontally dominant" geometry of the patch 1 allows us to easily fulfill this requirement. Indeed, the local refinement is carried out by inserting many knots in the area whose image is near $\Omega_{\square}$, and using a finer analysis knot vector for the patch 1 than for the patch 2, see Fig. 5.10. Given the *continuous* parametrization of the physical domain, we maintain C^0-continuity of the numerical solution in a quite simple way. We replace the B-splines of the analysis knot vectors along every common boundary components by those of the corresponding "maximum common" knot vector, that is the knot vector whose inner knots are the common inner knots of two knot vectors.

5.5.3 The first shape optimization result

We now feed the initial setting discussed in subsection 5.5.2 to the optimization routine outlined in Fig. 5.8. The optimization algorithm terminates succesfully after 143 iterations. Throughut this process, there are four times when fmincon is terminated so that we can update the reference parametrization. Knot insertions during the updates result in the following parametrization knot vectors for the final model:

$$\begin{aligned}
\widehat{\boldsymbol{\Xi}}_u^1 &= \{0,0,0,\tfrac{1}{5},\tfrac{3}{10},\tfrac{2}{5},\tfrac{7}{15},\tfrac{8}{15},\tfrac{3}{5},\tfrac{13}{20},\tfrac{7}{10},\tfrac{4}{5},1,1,1\},\\
\widehat{\boldsymbol{\Xi}}_v^1 &= \{0,0,0,\tfrac{1}{2},\tfrac{5}{8},\tfrac{3}{4},\tfrac{7}{8},1,1,1\},\\
\widehat{\boldsymbol{\Xi}}_u^2 &= \{0,0,0,\tfrac{1}{10},\tfrac{1}{5},\tfrac{2}{5},\tfrac{7}{15},\tfrac{8}{15},\tfrac{3}{5},\tfrac{4}{5},\tfrac{17}{20},\tfrac{9}{10},1,1,1\},\\
\widehat{\boldsymbol{\Xi}}_v^2 &= \{0,0,0,\tfrac{1}{2},\tfrac{3}{4},\tfrac{7}{8},\tfrac{15}{16},1,1,1\},
\end{aligned}$$

for patch 1 and 2 respectively. The number of dofs in the corresponding analysis is 5096. In Fig. 5.11 we show the antennas where the parametrization needs to be updated, as well as the final optimized antenna and the optimization history.

Let us now take a closer look at the result by performing a frequency sweep with analyses on two different meshes: the final optimization mesh and a refined one. Utilizing the notation of Fig. 5.10, the later analysis corresponds to the following refinement indicators: $(k_1,k_2,k_3,k_4,k_5) = (49,29,13,13,13)$, $(\ell_1,\ell_2,\ell_3,\ell_4,\ell_5) = (3,31,19,19,19)$ for patch 1, and $k = 19$, $(\ell_1,\ell_2,\ell_3,\ell_4,\ell_5) = (1,11,7,7,7)$ for patch 2 and results in 38780 dofs. The sweep is shown in Fig. 5.13. Clearly the sweep with respect to the finer analysis is shifted from the prescribed driving frequency and also has a smaller peak. However, the frequency shift is only $1.4 \times 10^{-4}\%$ from the driving frequency, which is much smaller than the 4% shift of a post-processed antenna in Aage et al. [71]. Also, the resulting energy in the harvesting region is still very large, $\log_{10}(W_\circ) \approx 2.76$ compared to $\log_{10}(W_\circ) \approx -0.075$ for the result from [71]. The energy distribution and magnetic field intensity in the resulting physical domain are shown in Fig. 5.12.

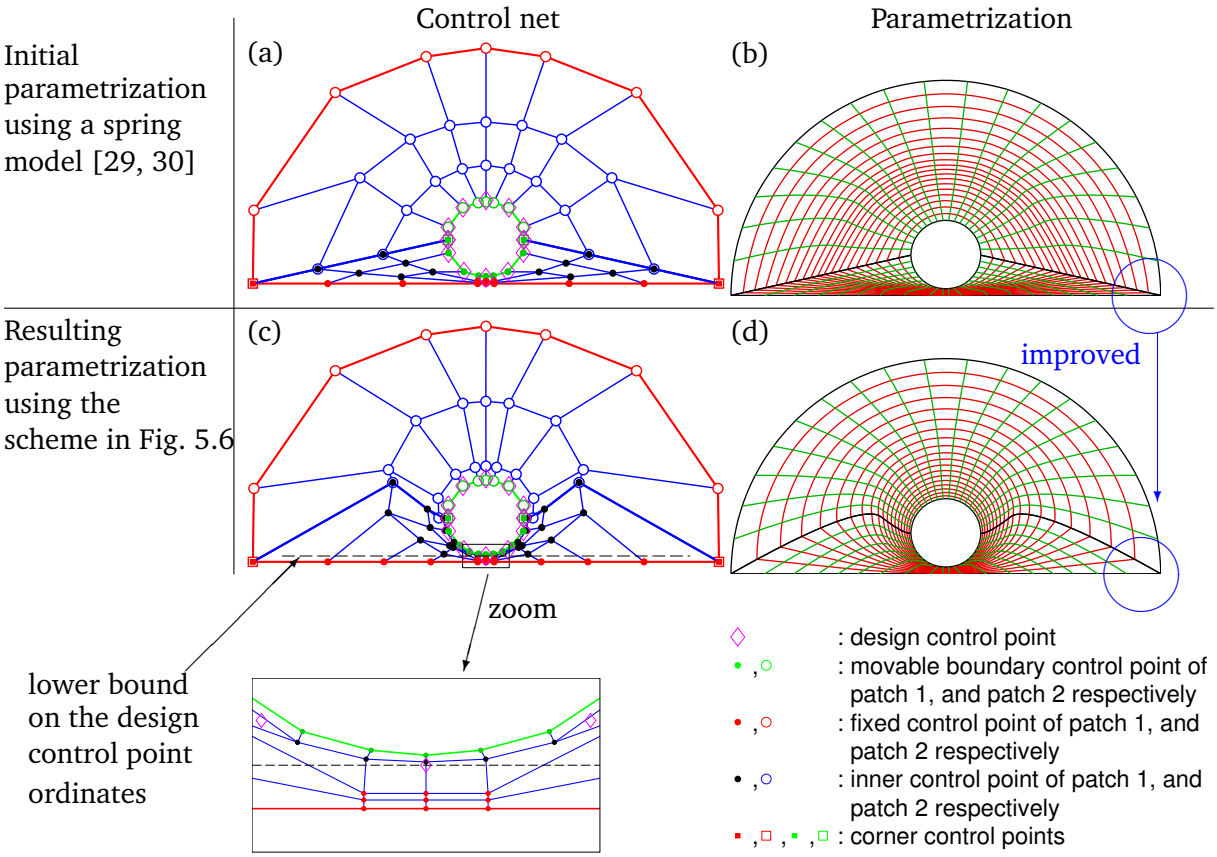

Figure 5.9: Initial shape used for the optimization, and a comparison between two parametrizations of this domain. Interestingly enough, the excessively acute angle in one corner of patch 1 shown in (b) is improved in (d). The agreements of parameter lines in (b) and (d) illustrate the C^0-continuity of the parametrization, despite possible disagreements of knot vectors. Below (c), a zoom near the energy harvesting region shows a set of fixed control points (in red). The parametrization is frozen in this area thereby simplifying the task of evaluating the objective function and its sensitivity.

5.5.4 Optimization with a finer mesh

In order to alleviate the small frequency shift observed in our numerical experiment, see Fig. 5.13, we continue the last optimization on finer mesh. In the notation of Fig. 5.10 the analysis mesh for the present run is given by $(k_1, k_2, k_3, k_4, k_5) = (49, 29, 13, 13, 13)$, $(\ell_1, \ell_2, \ell_3, \ell_4, \ell_5) = (1, 15, 9, 9, 9)$ for patch 1, and $k = 9$, $(\ell_1, \ell_2, \ell_3, \ell_4, \ell_5) = (0, 5, 3, 3, 3)$ for patch 2. Such an analysis requires 15600 dofs. The optimization algorithm converges in 68 iterations without updating reference parametrizations. The frequency sweep corresponding to the new antenna looks similarly to the one obtained previously, except the new peak is lower: $\log_{10}(W_\square) \approx 16.6$. On a fine mesh (which is the same as in subsection 5.5.3) we can observe that the frequency shift has also become smaller than in the previous case, see Fig. 5.13. When compared with the design from subsection 5.5.3, the new antenna is slightly "shifted to the right," see Fig. 5.14 to compensate for the shift of the region of the maximal field intensity relative to the energy harvesting region observed previously, see Fig. 5.12.

We now compare the last antenna with the topology optimization result from [71]. To this end, we need to compute the energy given by (**??**) in the circular domain $\Omega_\circ$: $x^2+y^2 \leq 0.08$ [m]. Since it is inefficient to find the partition of $\Omega_\circ$ specified by the images of the analysis knot lines

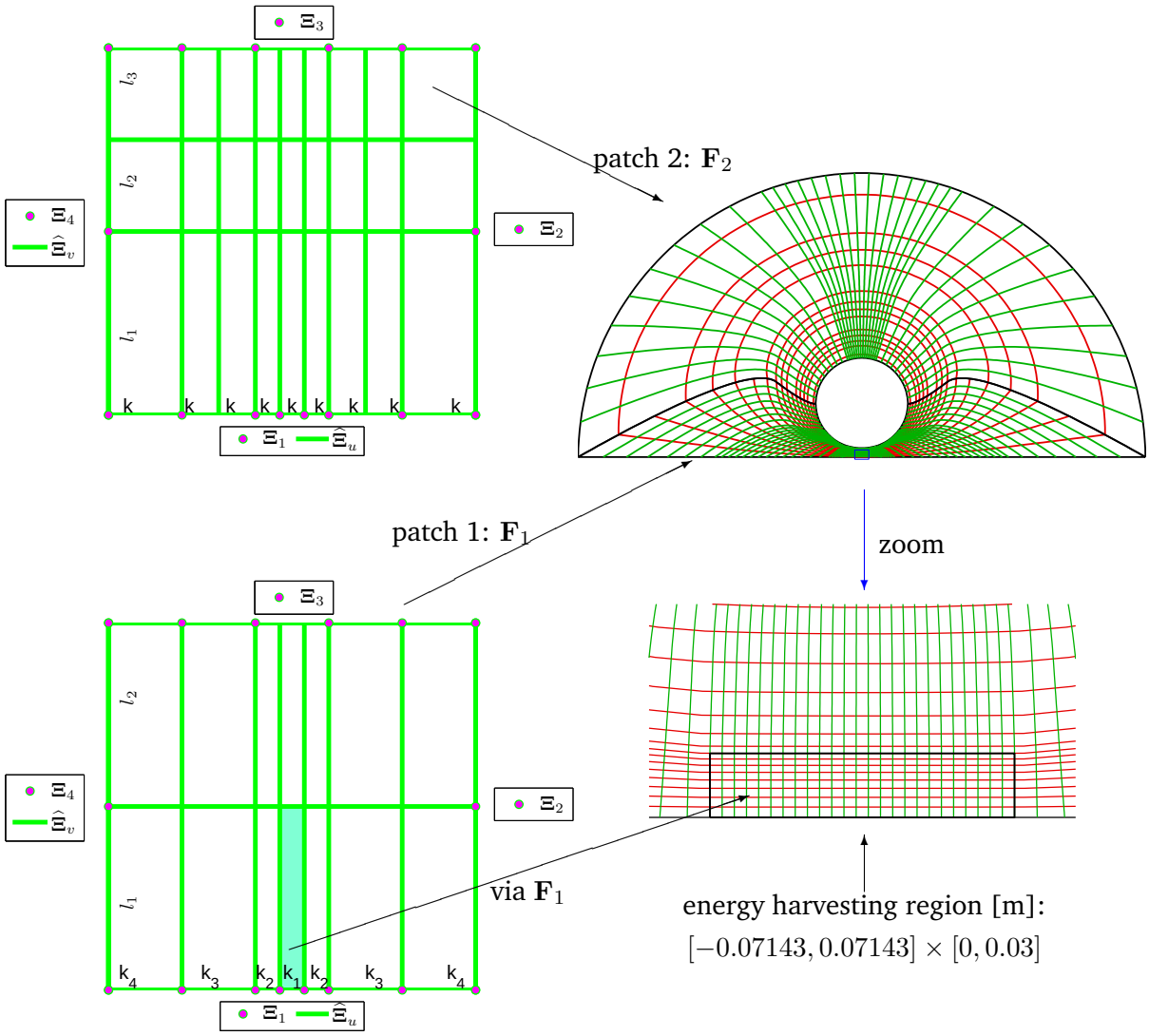

Figure 5.10: The initial analysis model of the present optimization. Two different sets of knot vectors are employed to parametrize the two patches comprising of the physical domain. The knot vector notations are given by Fig. 5.5. The numbers $k_1, \ldots, k_4, k$ and ℓ_1, ℓ_2 indicate the numbers of additional knots uniformly inserted into the corresponding knot spans to generate analysis knot vectors. For the initial (or a general) model, we use $(k_1, \ldots, k_4[, k_5, \ldots]) = (24, 14, 6, 6[, 6, \ldots])$, $(\ell_1, \ell_2[, \ell_3, \ldots]) = (0, 7[, 4, \ldots])$ for patch 1, and $k = 4$, $(\ell_1, \ell_2, \ell_3[, \ell_4 \ldots]) = (0, 5, 3[, 3, \ldots])$ for the other. The analysis configuration results in a model with 2612 degrees of freedom.

when employing the standard Gaussian quadratures, we use the following extended trapezoidal rule [25]:

$$\int_{x_0}^{x_m} f(x)\mathrm{d}x = h[\frac{f(x_0)}{2} + f(x_1) + \ldots + f(x_{m-1}) + \frac{f(x_m)}{2}] - \frac{mh^3}{12} f''(\xi), \tag{5.28}$$

where $x_0, \ldots, x_m$ form a uniform partition of $[x_0, x_m]$ and h is the partition's size. Given $\mathbf{x}_k$, integration points from the rule, their preimages via the domain parametrization (5.5) can be com-

puted via the inverse problem: Find u_k, v_k such that $\mathbf{F}(u_k, v_k) = \sum_{i,j} \widehat{\mathbf{d}}_{i,j} M_i(u_k) N_j(v_k) = \mathbf{x}_k$. We utilize a Matlab's implementation of Newton's algorithm *fsolve* [33] for solving this problem. We then carry out the frequency sweep for the new energy harvesting domain and compare it with the one found in [71] see Fig. 5.15. When comparing note that in [71], the two antennas are (arbitrarily) constrained to be in the circular domains only, while in the present situation the antennas have more freedom to vary. Having the approximately invariant properties of the problem (**??**) under simultaneous scaling of the frequency and size, we can easily scale the geometry to obtain the peak at the driving frequency. Our scaled antenna concentrates 10^6 times more energy in the harvesting region compared to the one computed in [71]. The *quality factor* [79, chapter 9] of the model is $Q \approx 1.95 \times 10^5$. We note that recently Aage [80] has computed an updated version of the topology optimized antenna using the bounding box of Fig. 5.12 as a design domain. This resulted in an improved design with the performance of $\log_{10}(W_\square) = 1.4$. Finally, note that the scaling described above has resolved the frequency shift issue observed in Fig. 5.15, also in [71].

To provide some physical insight into the performance of the antenna, we solve the eigenvalue problem corresponding to (5.1a) with homogeneous Dirichlet boundary condition on the truncation boundary Γ_t and the homogeneous Neumann boundary condition on the scatterer's interface Γ_s, see Fig. 5.2. The later boundary condition corresponds to assuming that the antenna is made from a perfect electric conductor. Interestingly enough, one of the modes, u_{13}, looks strikingly similar to the solution $u = H_z$ shown in Fig. 5.16 (left), and the corresponding eigenfrequency $f_{13} = 1.1499 \times 10^8$ [Hz] is very close to the frequency of the incident wave $f = 1.15 \times 10^8$ [Hz]. By calculating the L^2-projection of the solution u on the eigenfunctions u_i

$$c_i = \langle u, u_i \rangle = \int_\Omega u\, u_i \, \mathrm{d}V, \tag{5.29}$$

we find that 98% of the L^2-energy of the solution is contained in the mode u_{13}, that is $|c_{13}|^2 / \|u\|_{L^2}^2 \approx 0.98$. Thus, the high energy concentration happens owing to a resonance-type phenomenon.

5.6 Conclusions

We have utilized shape optimization and isogeometric analysis to attack the problem of optimal design of sub-wavelength electromagnetic antennas. We have designed an antenna that focuses the magnetic energy of an incident electromagnetic wave in a desired region of space. The resulting antenna has increased the energy concentration by a factor of one million compared to the topology optimization result of Aage et al. [71]. It also has a very high quality factor and thus is very promising for realistic industrial applications despite the 2-dimensional idealization.

In addition, we have devised an inexpensive method based on minimizing a second order approximation to a Winslow functional for extending a B-spline parametrization of the boundary of a domain to its interior on the main optimization problem. As shown in the paper, the resulting algorithm works satisfactorily well. Finally, we have implemented a routine that executes our oprimization strategy in an automated way. This is promising and important for the future development of the code into engineering software.

5.7 Appendix: spline approximation of a circular arc

In this section, we describe the method used in the present work for approximating circular arcs using B-splines. We employ this method for approximating the truncation boundary and the initial shape of the antenna.

Let $N_i(\xi)$, $i = 1, \ldots, n$, be B-splines of degree p with a knot vector $\boldsymbol{\Xi}$. Consider a B-spline curve $\mathbf{r}(\xi) = \sum_i \mathbf{c}_i N_i(\xi)$ with unknown control points $\mathbf{c}_i$, with which we would like to approximate a given circular arc. Assuming that arc's center is at the origin, we want to maintain the equality $\mathbf{r} \cdot \dot{\mathbf{r}} = 0$, where $\dot{\mathbf{r}}$ denotes the derivative of $\mathbf{r}$ with respect to ξ. Similarly to (5.8) we write

$$\mathbf{r} \cdot \dot{\mathbf{r}} = \sum_{i,j} \mathbf{c}_i \cdot \mathbf{c}_j N_i \dot{N}_j = \sum_{\alpha} d_\alpha \widetilde{N}_\alpha, \tag{5.30}$$

where $\widetilde{N}_\alpha$, $\alpha = 1, \ldots, \widetilde{n}$, are B-splines of degree $2p-1$ with multiplicities of inner knots raised by p. If all $d_\alpha = 0$ in (5.30), then so is the quantity $\mathbf{r} \cdot \dot{\mathbf{r}}$.

We now derive explicit expressions for d_α in terms of the vector of control variables $\widehat{\mathbf{d}} = [x_{\mathbf{c}_1}, y_{\mathbf{c}_1}, \ldots, x_{\mathbf{c}_n}, y_{\mathbf{c}_n}]^T$. To this end, consider $\widetilde{N}^*_\alpha$, the dual functions of $\widetilde{N}_\alpha$ in $\mathrm{span}\{\widetilde{N}_\alpha\} \subset L^2([0,1])$ which are defined by the constitutive relations $\langle \widetilde{N}^*_\alpha, \widetilde{N}_\beta \rangle = \delta_{\alpha,\beta}$. Taking the inner product of (5.30) with $\widetilde{N}^*_\alpha$ we obtain the equality

$$d_\alpha = \langle \widetilde{N}^*_\alpha, \mathbf{r} \cdot \dot{\mathbf{r}} \rangle = \sum_{i,j} \mathbf{c}_i \cdot \mathbf{c}_j \langle \widetilde{N}^*_\alpha, N_i \dot{N}_j \rangle = \widehat{\mathbf{d}}^T \mathbf{Q}_\alpha \widehat{\mathbf{d}}. \tag{5.31}$$

The equation (5.31) implies that d_α are quadratic forms of the vector of control variables $\widehat{\mathbf{d}}$. Naturally we arrive at the following optimization problem

$$\min_{\widehat{\mathbf{d}}} \max_{\alpha} d_\alpha^2, \tag{5.32}$$

which can be numerically solved to approximate stationarity using the same approach as the optimization problem (5.9). Utilizing (5.32), we obtain a good approximation for the circular truncation boundary, see Fig. 5.17.

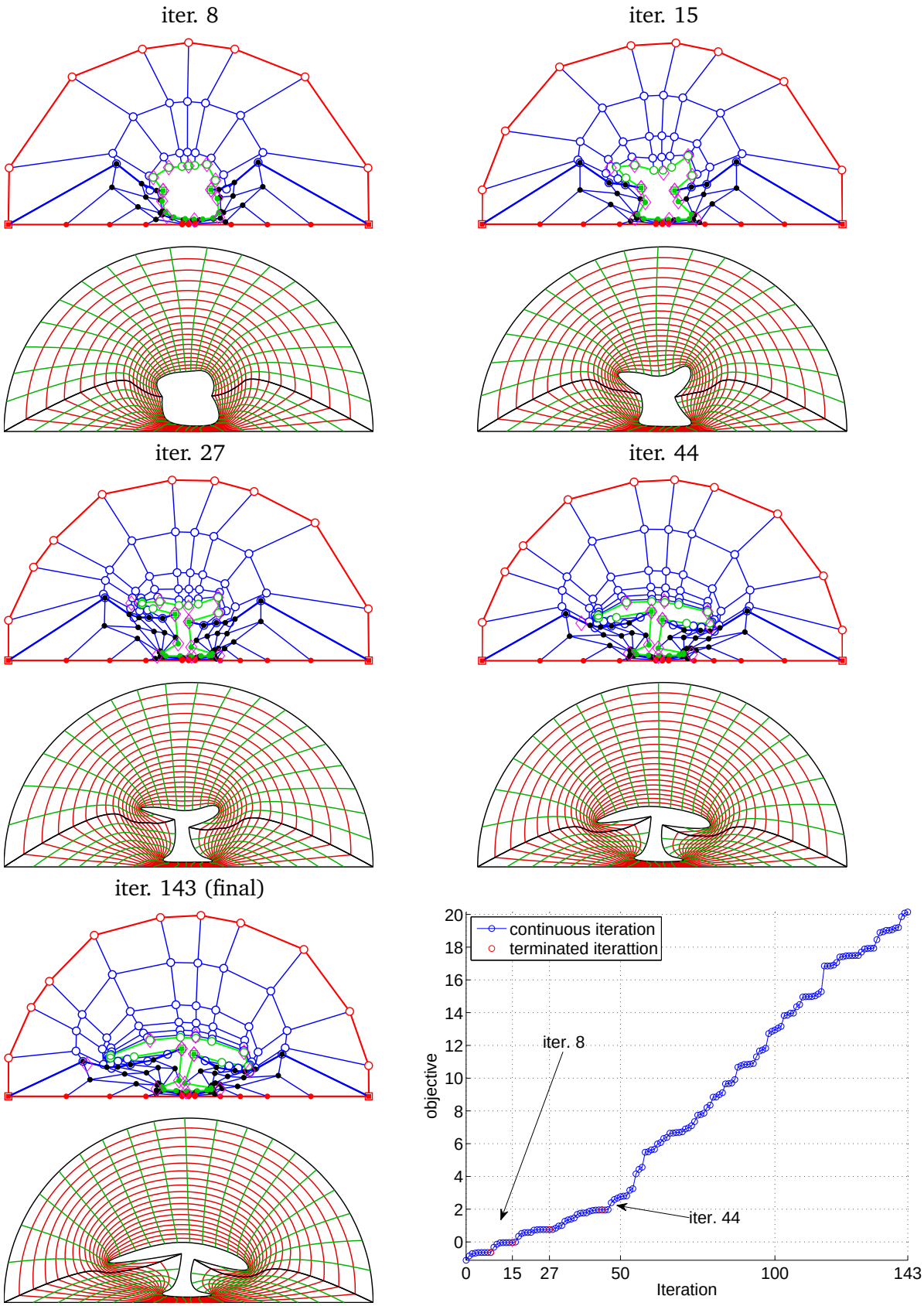

Figure 5.11: Snapshots of the control nets and parametrizations at the iterations where the outer optimization algorithm is stopped in order to update the reference parametrization (see Fig. 5.6). In the bottom right corner we show the values of the objective function during the iterations.

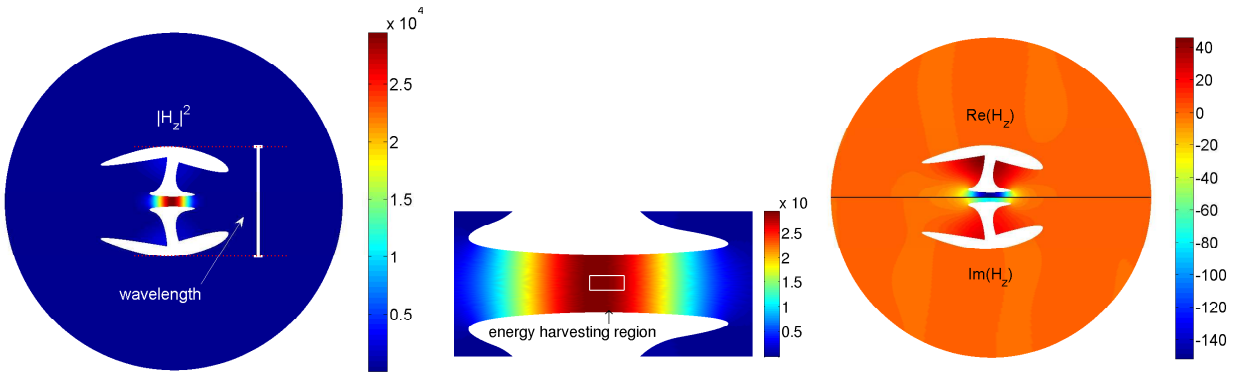

Figure 5.12: To the left: the energy (square L^2-norm) of the magnetic field around the optimized antenna (see Subsection 5.5.3), in the middle: a zoom near the region where the energy is maximized, and to the right: the real and imaginary parts of the field. The field is calculated using a higher accuracy than that used during the optimization. That explains why the maximum field intensity is shifted slightly from the energy harvesting region.

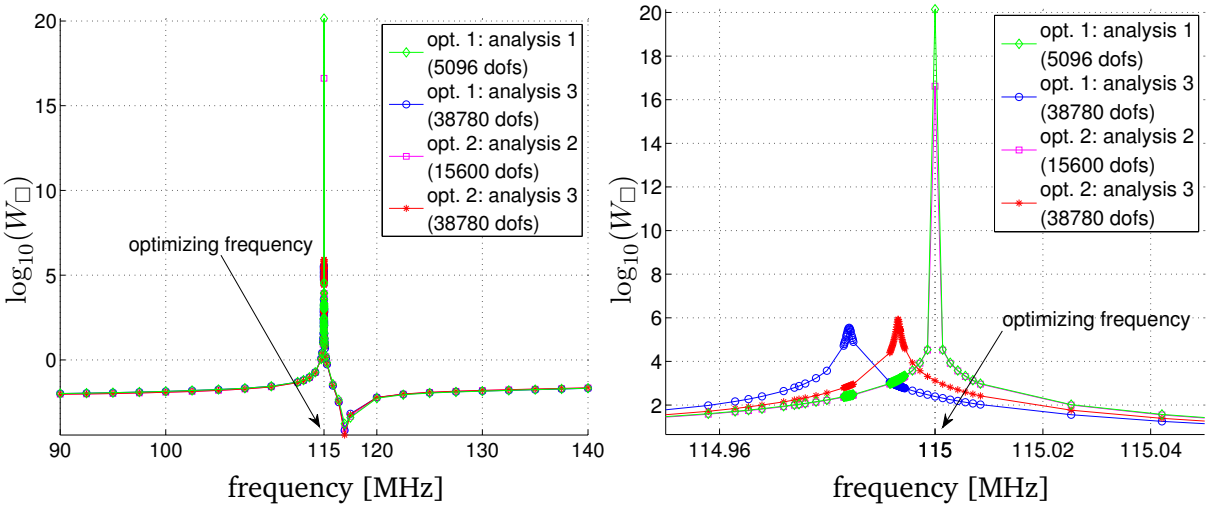

Figure 5.13: To the left: the frequency sweep of optimized antennas, and to the right: a zoom near the optimizing frequency. The frequency sweep of the first optimization result discussed in subsection 5.5.3 is calculated twice: one time using the same analysis as used in the optimization (the green curve) and a second time using refined knot vectors (finer mesh) and consequently with higher accuracy (the blue curve). The later analysis is used once again for evaluating the frequency sweep of the optimization result presented in subsection 5.5.4 (the red curve).

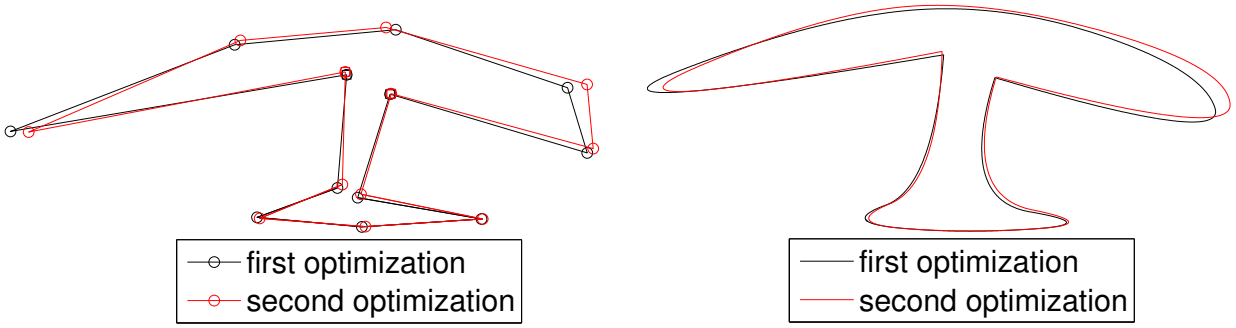

Figure 5.14: To the left: design control nets and to the right: the shapes of the first optimization presented in subsection 5.5.3 and of the second optimization with a finer mesh presented in subsection 5.5.4.

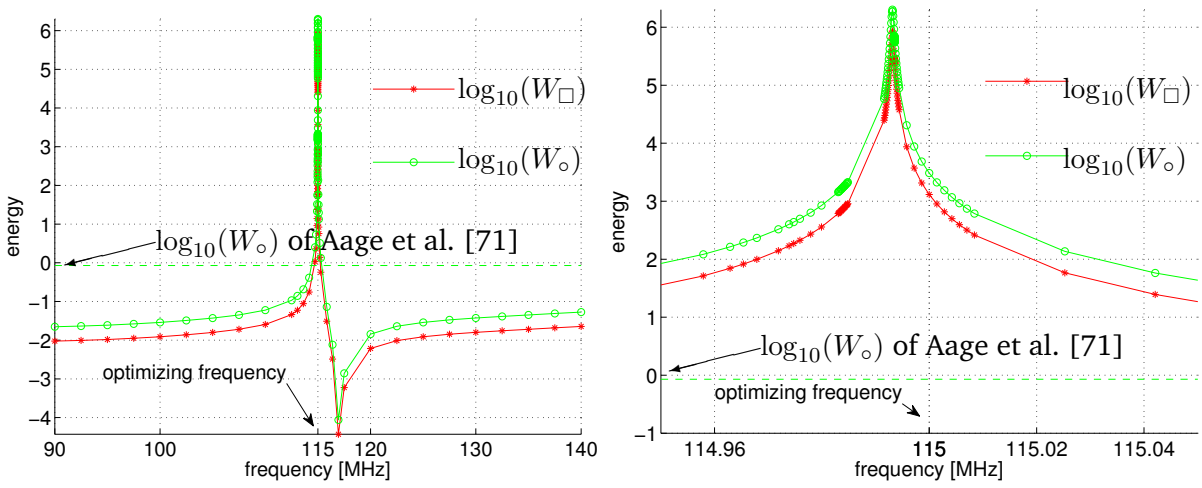

Figure 5.15: To the left: the frequency sweep of the final optimization result and to the right: a zoom near the optimizing frequency. The energy is also calculated in the circular domain $\Omega_\circ$ to compare results with those from Aage et al. [71].

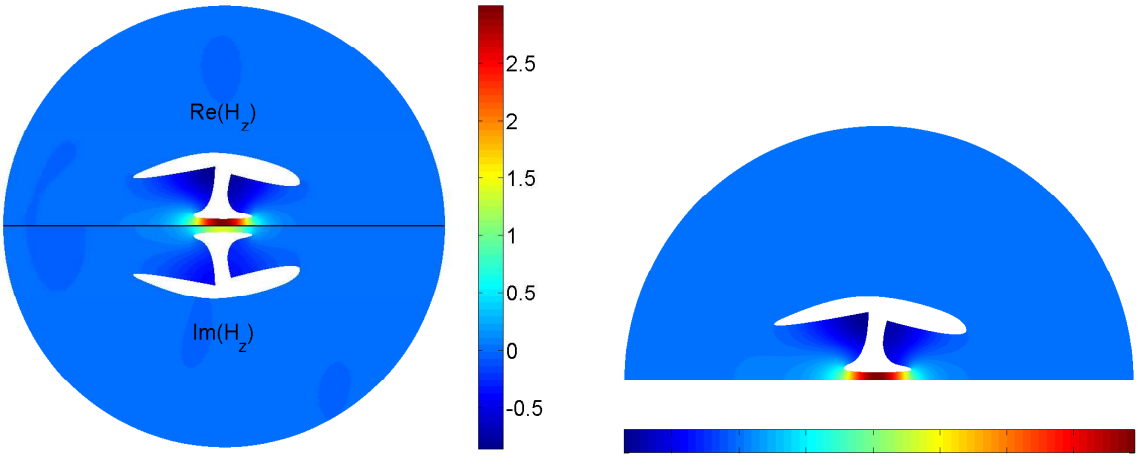

$f = 1.15 \times 10^8$ [Hz] $f_{13} = 1.499 \times 10^8$ [Hz]

Figure 5.16: To the left: the normalized real and imaginary parts of H_z of the last resulting antenna; f is the frequency of the incoming wave. To the right: the thirteenth eigenmode of the eigenproblem described in section 5.5.4; f_{13} is the corresponding eigenfrequency.

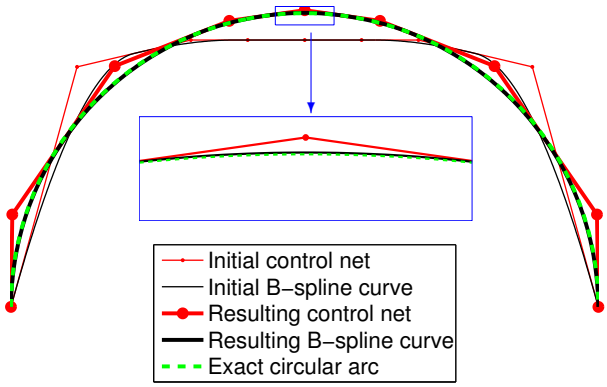

Figure 5.17: Approximation of the circular arc $x^2 + y^2 = 4^2$, $y \geq 0$ by a quadratic spline curve with the knot vector $\boldsymbol{\Xi} = \{0, 0, 0, 1/5, 2/5, 7/15, 8/15, 3/5, 4/5, 1, 1, 1\}$, using the optimization problem (5.32). The spline curve is used as the truncation boundary in the model in Fig. 5.2.

Chapter 6

Isogeometric shape optimization of nano-antennas for field enhancement

In collaboration with Sergey I. Bozhevolnyi, Morten Willatzen and their research group at University of Southern Denmark.

The study of shape optimization of micro-antennas using isogeometric analysis presented in Chapter 5 clearly shows a great potential of the methodology for antenna design. The observations, indeed, motivated this work. We now look for nano-antennas that have a strong field concentration in a specific region of space. The potential results may find its utilization in nano-applications [81, 82, 83, 84].

6.1 Physical problem

In this section, we briefly recall the numerical models used in this work to simulate a 2D electromangetic scattering problem. The antenna shape optimization is then addressed.

6.1.1 Numerical modeling

We consider a two-dimensional electromagnetic (EM) TE_z model, that is, the situation when z-component of the electric field intensity vanishes. In particular, we look at a scattering problem in which a uniform plane wave with a frequency f travels in a linear and isotropic dielectric in the presence of conducting scatterers. The incident magnetic field intensity is given as $\mathbf{H}^i = (0, 0, H_z^i)$. We denote the relative complex permittivity and permeability of a material by ε_{cr} and μ_r, respectively. All EM fields in this paper are assumed to be time-harmonic with an $e^{j\omega t}$ time dependence.

The infinite domain outside the scatterers is truncated by a circle with radius r_t, as shown in Fig. 6.1. The equations modelling such a problem, c.f. [77], are

$$\boldsymbol{\nabla} \cdot \big(\frac{1}{\varepsilon_{cr}} \boldsymbol{\nabla} H_z\big) + k_0^2 \mu_r H_z = 0 \qquad \text{in } \Omega, \tag{6.1a}$$

$$\frac{\partial (H_z - H_z^i)}{\partial \mathbf{n}} + (jk_0 + \frac{1}{2r_t})(H_z - H_z^i) = 0 \qquad \text{on } \Gamma_t, \tag{6.1b}$$

where $k_0 = 2\pi f \sqrt{\varepsilon_0 \mu_0}$, ε_0 and μ_0 are the wavenumber, the permittivity and the permeability of free space, respectively; $\mathbf{n}$ is the outward unit normal vector to Γ_t. The equation (6.1b) is referred to as first order absorbing boundary condition [77].

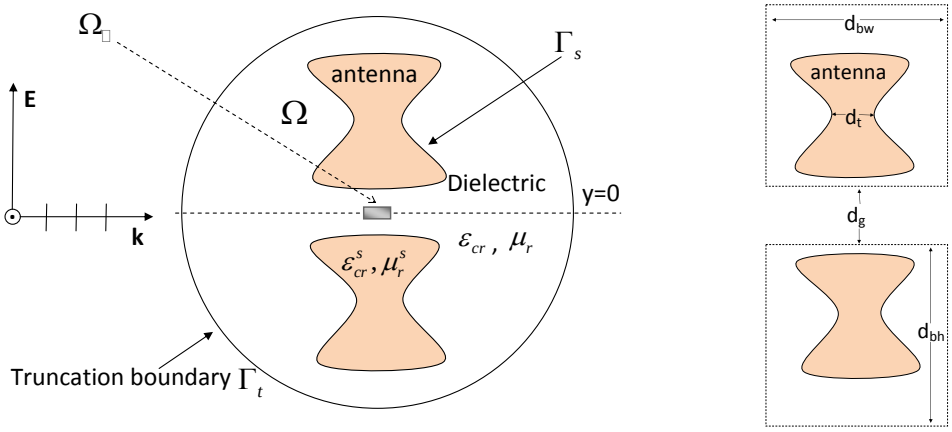

Figure 6.1: To the left, model scattering problem considered in this framework; to the right, design parameters for constraining the antennas: the minimum allowed gap d_g between the two antennas, the minimum allowed "thickness" d_t of each antenna, and the bounding box of the antennas with width d_{bw} and height d_{bh}. The concept *thickness* of an antenna is defined precisely in Section 6.2.1. Due to the symmetry, only the upper half of the truncated domain is considered.

Remark 9. Note that the equations entering (6.1) are invariant under simultaneous scaling of the frequency and size of the domain except for the frequency dependence of the complex permittivity of the scatterer.

A variational statement of (6.1) may be written as follows: find $H_z \in H^1(\Omega)$ (see [26]) such that for every $\phi \in H^1(\Omega)$ we have the equality:

$$\int_\Omega \frac{1}{\varepsilon_{cr}} \boldsymbol{\nabla} H_z \cdot \boldsymbol{\nabla}\phi \,\mathrm{d}V \;-\; k_0^2 \int_\Omega \mu_r H_z \,\phi \,\mathrm{d}V \;=\; \int_{\Gamma_t} \frac{1}{\varepsilon_{cr}} \left(\frac{\partial H_z^i}{\partial \mathbf{n}} \;+\; \left(jk_0 \;+\; \frac{1}{2r_t} \right) H_z^i \right) \phi \,\mathrm{d}\Gamma. \quad (6.2)$$

We assume that the incident field is a plane wave, that is $H_z^i = e^{-jk_0\sqrt{\varepsilon_{cr}\mu_{cr}}x}$, and consider two scatterers which are symmetric about the x-axis. As a result, H_z is also symmetric about the x-axis. Thus we can solve the problem in half the domain with the following boundary condition:

$$\frac{\partial H_z}{\partial y} = 0 \quad \text{if} \quad y = 0. \quad (6.3)$$

6.1.2 Shape optimization problem for field enhancement

Toward applications in nano-technology [81], the magnitude of either of the total EM fields in a specific spatial region is expected to be much larger than that of the incident wave. In order to design nano-antennas having such a capability, we consider the problem of finding shapes of antennas depicted in Fig. 6.1 in order to maximize the following quantity

$$W_\square = 2 \int_{\Omega_\square} |H_z|^2 \,\mathrm{d}V \quad (6.4)$$

where H_z is the solution to the equations (6.1). The domain $\Omega_\square$ in (6.4) is a relatively small region of space between the two antennas, see in Fig. 6.1. In (6.4), the factor 2 accounts for the fact that we integrate only over a half of a symmetric domain. The optimization problem

stated above is to maximize the magnitude of the magnetic field intensity in the domain $\Omega_{\square}$. See Fig. 6.1(right) for the design constraints on the antennas.

6.2 Isogeometric shape optimization setting

In this section, we describe the isogeometric analysis modeling of the shape optimization problem stated in Section 6.1.

For convenience, we consider the problem in a dimensionless fashion. Utilizing Remark 9, we normalize the geometry by a factor $L_f = \dfrac{f}{f_r}$, where f is the considered frequency and f_r is a reference frequency. In this work, we use $f_r = 1.15 \times 10^8$ [Hz], the optimizing frequency of an earlier work presented in Chapter 5. Moreover, we discretize the computational domain Ω, see Fig. 6.1(left), by 5 spline patches. The model is depicted in Fig. 6.2.

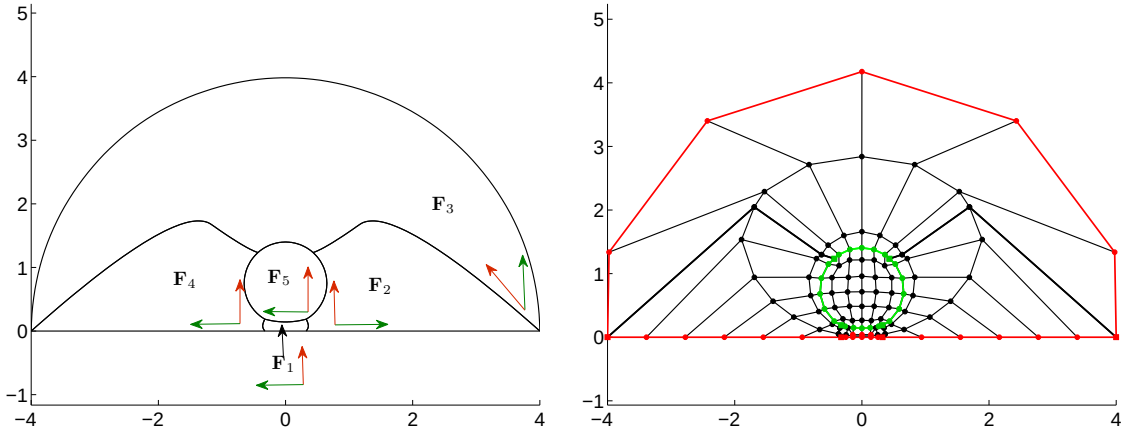

Figure 6.2: To the left, the layout of the patches used to discretize the domain Ω depicted in Fig. 6.1; to the right, a control net corresponds to the patches on the left. In the picture on the left, $\mathbf{F}_i(u, v)$ denotes the parametrization of patch i, $i = 1, \ldots, 5$, $(u, v) \in [0, 1]^2$; within each patch i, the *green* arrow represents the one-sided derivative $\dfrac{\partial_+ \mathbf{F}_i}{\partial u}(0, 0)$, while the *red* arrow represents $\dfrac{\partial_+ \mathbf{F}_i}{\partial v}(0, 0)$.

Remark 10. It should be noted that when a patch is parametrized in the clockwise fashion, i.e., a valid parametrization of this patch has negative Jacobian determinant everywhere, the parametrization optimization problems presented in Section 2.1.2 of Chapter 2 should be modified. The modification is straightforward.

Let us now consider the constraints mentioned in Section 6.1.2 and in Fig. 6.1, and in particular pay attention to the minimum allowed "thickness" d_t of the antenna. To constrain the "thickness", we utilize the smooth constraints for preventing a spline curve from self-intersection [10] as follows.

6.2.1 Constraining the thickness of an antenna

Let us define the concept *thickness* of an antenna in a precise way.

***Definition* 5.** Let $\mathbf{r}(t)$ be a smooth parametrized curve in $\mathbb{R}^d$ with $t \in [a, b]$. Assume that $\mathbf{r}$ is unit-speed, i.e., $\dfrac{\mathrm{d}\mathbf{r}}{\mathrm{d}t}(t) = 1$ for all $t \in (a, b)$. If the curve $\mathbf{r}$ is simple and closed, i.e., $\mathbf{r}(a) = \mathbf{r}(b)$, then the *thickness* $\tau_{\mathbf{r},T}$ with respect to a number $0 < T < b - a$ of the domain enclosed by $\mathbf{r}$ is defined by the following expression

$$\tau_{\mathbf{r},T} = \min\{\|\mathbf{r}(t_1) - \mathbf{r}(t_2)\|,\ |t_1 - t_2| \geq T,\ t_1, t_2 \in [a, b]\}. \tag{6.5}$$

That is, the thickness $\tau_{\mathbf{r},T}$ of the curve $\mathbf{r}$ is the minimal distance between any pair of points on $\mathbf{r}$ for which in order to reach one point from the other, one has to go along the curve $\mathbf{r}$ for at least a distance T .

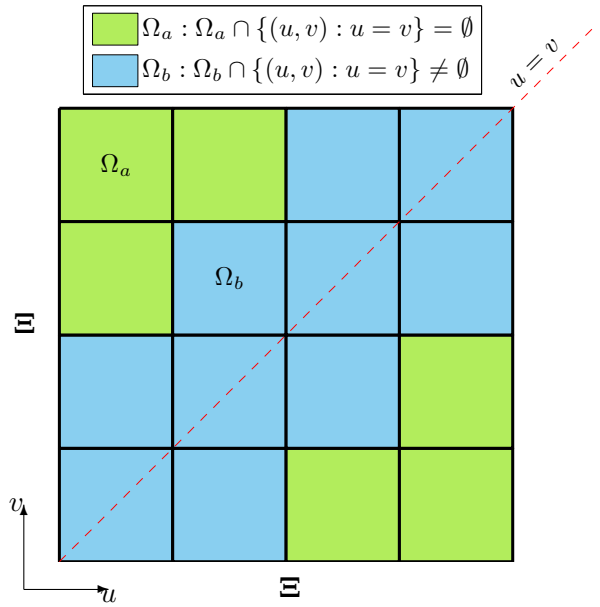

Figure 6.3: A knot vector Ξ partitions the unit square $[0, 1]^2$ into products of knot spans. We classify the rectangles according to whether they intersect the diagonal or not.

Let $N_i(\xi)$ $(i = 1, \ldots, n)$ be B-splines of degree p with a knot vector $\Xi = \{\xi_1, \ldots, \xi_{n+p+1}\}$. Consider a spline curve $\mathbf{r}(\xi) = \sum_i \mathbf{c}_i N_i(\xi)$, where $\mathbf{c}_i$ are design control points. To ensure that $\mathbf{r}$ does not intersect itself, we look at the square distance between every pair of points on the curve, $(\mathbf{r}(u), \mathbf{r}(v))$, $(u, v) \in \Xi \times \Xi$. That is

$$d^2_{\mathbf{r}}(u, v) = \|\mathbf{r}(u) - \mathbf{r}(v)\|^2 = \sum_{i,j} \mathbf{c}_i \cdot \mathbf{c}_j \big(N_i(u) - N_j(v)\big)^2. \tag{6.6}$$

Clearly, the curve is simple if and only if $d^2_{\mathbf{r}}(u, v) > 0$ for every $u \neq v$, $u, v \in [0, 1]^2$. To ensure that this condition is fulfilled, we look at rectangles in $[0, 1]^2$ formed by the products of knot spans, see Fig. 6.3. First, consider a rectangle Ω_a that does not intersect the diagonal $\{(u, v) : u = v\}$. In Ω_a, $d^2_{\mathbf{r}}(u, v)$ can be expressed in terms of Bernstein polynomials [24] of degree $2p$, $B^{2p}_k(u)B^{2p}_\ell(v)$ $(k, \ell = 1, \ldots, 2p + 1)$, defined within the element. That is

$$d^2_{\mathbf{r}}(u, v) = \sum_{k,\ell} a_{k,\ell} B^{2p}_k(u) B^{2p}_\ell(v), \quad (u, v) \in \Omega_a. \tag{6.7}$$

Clearly, if all control points $a_{k,\ell}$ are nonnegative and the corner points are strictly positive, then $d^2_{\mathbf{r}}$ is strictly positive. Next we consider a rectangle Ω_b that does intersect the diagonal. Here

$(u-v)^2$ is a factor of $d_{\mathbf{r}}^2$ and we can write

$$d_{\mathbf{r}}^2(u,v) = (u-v)^2 \sum_{\alpha,\beta} b_{\alpha,\beta} B_\alpha^{2p-2}(u) B_\beta^{2p-2}(v) \quad (u,v) \in \Omega_b \tag{6.8}$$

In (6.8), $B_\alpha^{2p-2}(u)B_\beta^{2p-2}(v)$ $(\alpha,\beta = 1,\ldots,2p-1)$ are Bernstein polynomials of degree $2p-2$ defined within Ω_b. Once again, if all control points $a_{k,\ell}$ are non negative and the corner points are strictly positive, then $d_{\mathbf{r}}$ is strictly positive. So we arrive at the sufficient conditions: The curve $\mathbf{r}$ is a simple curve if the following conditions are satisfied

(i) $a_{k,\ell} \geq 0$ for all $k,\ell = 1,\ldots,2p+1$,

(ii) $b_{\alpha,\beta} \geq 0$ for all $\alpha,\beta = 1,\ldots,2p-1$,

(iii) $d_{\mathbf{r}}^2(\xi_i,\xi_j) \geq \delta$, $i,j = 1,\ldots,n$, for some positive δ.

To further constrain the minimum allowed thickness d_t of the antenna, inspired by Definition 6.5, we replace the constraints (i) above with the following

(i-1) $a_{k_1,\ell_1} \geq 0$ for all $k_1,\ell_1 = 1,\ldots,2p+1$, if the corresponding supporting domain $\Omega_a = [\xi_r,\xi_{r+1}] \times [\xi_s,\xi_{s+1}]$ are with $|r-s| < n_k$,

(i-2) $a_{k_2,\ell_2} \geq d_t^2$ for all $k_2,\ell_2 = 1,\ldots,2p+1$,if the corresponding supporting domain $\Omega_a = [\xi_r,\xi_{r+1}] \times [\xi_s,\xi_{s+1}]$ are with $|r-s| \geq n_k$,

where $n_k \in \mathbb{N}$ is the difference in the ordering of the knot intervals $[\xi_r,\xi_{r+1}]$ and $[\xi_s,\xi_{s+1}]$ in all knot intervals with respect to the knot vector $\boldsymbol{\Xi}$. In this work, we use $n_k = 3$.

Note that utilizing the symmetry in (6.6) about the line $u = v$, only one half of the conditions are needed. Also, similarly to (2.6), the coefficients $a_{k,\ell}$ in (6.7) and $b_{\alpha,\beta}$ in (6.8) may be explicitly represented as quadratic forms of the design control points $\mathbf{c}_i$. For the current optimization problem, the antenna boundary is composed of two spline curves. Proposition 1 can be straightforwardly extended to a piecewise spline curve. Finally, knot insertions may be needed in order to obtain tighter conditions for the sufficiency.

6.2.2 Parametrization of a given domain

In an optimization problem using IGA, often the objective function is given by the integral over a given domain in the physical space. To simplify the implementation of IGA when the standard Gaussian quadratures [25] are used for numerical integrations, we would like the boundary of the domain to be the images of knot lines in the parameter space via a parametrization of the physical space. This leads to the standard interpolation problem [23] and can be solved as follows.

Let $\mathbf{r}(u) = \mathbf{c}_1 N_1(u) + \ldots + \mathbf{c}_n N_n(u)$ be a B-spline curve of degree p, where N_k are B-spline with knot vector $\boldsymbol{\Xi} = \{u_1,\ldots,u_N\}$ and $\mathbf{c}_k \in \mathbb{R}^d$, $k = 1,\ldots,n$. For simplicity, assume that all inner knots of $\boldsymbol{\Xi}$ have multiplicity 1. Note that the image of any knot u_k via $\mathbf{r}$ is a convex combination of the control points whose corresponding B-splines do not vanish at the knot. Indeed, if we repeat inserting u_k into $\boldsymbol{\Xi}$ in $p-1$ times, then the resulting control point with respect to the B-spline defined by the knots

$$u_{k-1}, \underbrace{u_k,\ldots,u_k}_{p \text{ times}}, u_{k+1}$$

must be $\mathbf{r}(u_k)$. By that way, we can formulate explicitly the weights of the convex combination. For instance if $p = 2$ we have

$$\mathbf{r}(u_k) = (1-\alpha_k)\mathbf{c}_{k-2} + \alpha_k \mathbf{c}_{k-1}, \quad k = p+1,\ldots,n+1, \tag{6.9}$$

where $\alpha_k = \dfrac{u_k - u_{k-1}}{u_{k+1} - u_{k-1}}$. If $\mathbf{r}(u_k)$, $k = p+1, \ldots, n+1$, are given, then (6.9) are a system of $d(n-p+1)$ linear equations of dn unknowns, the coordinates of the control points $\mathbf{c}_k$. Thus the curve $\mathbf{r}$ is completely defined if $\mathbf{r}(u_k)$, $k = p+1, \ldots, n+1$ are given together with other $d(p-1)$ linear equations. In this work, the remaining conditions are chosen to be $p-1$ predefined control points $\mathbf{c}_2, \ldots, \mathbf{c}_p$.

6.2.3 Discretization

An approximation to the solution H_z to (6.1) is expanded in terms of the basis functions (see Section 1.2.1) as $H_z = \sum_k h_k \, (\widetilde{R}_k^{\widetilde{p},\widetilde{q}} \circ \mathbf{F}^{-1}) = \big[\widetilde{R}_1^{\widetilde{p},\widetilde{q}} \circ \mathbf{F}^{-1}, \ldots, \widetilde{R}_{\widetilde{m}\widetilde{n}}^{\widetilde{p},\widetilde{q}} \circ \mathbf{F}^{-1}\big]\mathbf{h}$, where $\mathbf{h}$ contains all the coordinates of H_z with respect to the selected basis. Substituting this expression into the weak form (6.2) and utilizing the basis functions as the test functions, we arrive at the following set of linear algebraic equations:

$$(\mathbf{K} + \mathbf{M} + \mathbf{T})\,\mathbf{h} = \mathbf{f}. \tag{6.10}$$

Entries of the matrices entering (6.10) are calculated as:

$$\mathbf{K}_{k\ell} = \iint\limits_{[0,1]^2} \frac{1}{\varepsilon_{cr}} \left(\mathbf{D}\widetilde{R}_k^{\widetilde{p},\widetilde{q}}(u,v)\,\mathbf{J}^{-1}\right)^T \mathbf{D}\widetilde{R}_\ell^{\widetilde{p},\widetilde{q}}(u,v)\,\mathbf{J}^{-1}\,\det(\mathbf{J})\,\mathrm{d}u\,\mathrm{d}v, \tag{6.11a}$$

$$\mathbf{M}_{k\ell} = -k_0^2 \iint\limits_{[0,1]^2} \mu_r\,\widetilde{R}_k^{\widetilde{p},\widetilde{q}}(u,v)\,\widetilde{R}_\ell^{\widetilde{p},\widetilde{q}}(u,v)\,\det(\mathbf{J})\,\mathrm{d}u\,\mathrm{d}v, \tag{6.11b}$$

$$\mathbf{T}_{k\ell} = \big(jk_0 + \frac{1}{2r_t}\big) \int\limits_{\mathbf{F}^{-1}(\Gamma_t)} \frac{1}{\varepsilon_{cr}}\,\widetilde{R}_k^{\widetilde{p},\widetilde{q}}(u,v)\,\widetilde{R}_\ell^{\widetilde{p},\widetilde{q}}(u,v)\,\mathrm{d}s, \tag{6.11c}$$

$$\mathbf{f}_\ell = \int\limits_{\mathbf{F}^{-1}(\Gamma_t)} \frac{1}{\varepsilon_{cr}} \left(\frac{\partial H_z^i}{\partial \mathbf{n}} + \big(jk_0 + \frac{1}{2r_t}\big) H_z^i\right) \widetilde{R}_\ell^{\widetilde{p},\widetilde{q}}(u,v)\,\mathrm{d}s, \tag{6.11d}$$

$k, \ell = 1, \ldots, \widetilde{m}\widetilde{n}$. In the equations (6.11), $\mathbf{J}$ is the Jacobian of the parametrization $\mathbf{F}$ and $\mathbf{D}f(u,v) = \begin{bmatrix} \frac{\partial f}{\partial u}(u,v) & \frac{\partial f}{\partial v}(u,v) \end{bmatrix}$ is the differential of a real-valued function $f : [0,1]^2 \to \mathbb{R}$.

6.2.4 Formulation of the optimization problem and sensitivity analysis

Recall that $\mathbf{d}$ is the vector containing components of design control points, see Fig. 6.4. Taking the constraints discussed above into account and noting that in (6.4), $H_z \circ \mathbf{F} = \big[\widetilde{R}_1^{\widetilde{p},\widetilde{q}}, \ldots, \widetilde{R}_{\widetilde{m}\widetilde{n}}^{\widetilde{p},\widetilde{q}}\big]\mathbf{h}$, we arrive at the following shape optimization problem:

$$\underset{\mathbf{d}\in\mathbb{R}^N}{\text{maximize}} \quad \log_{10}(W_\square) = \log_{10}\left(2 \iint_{\mathbf{F}^{-1}(\Omega_\square)} \left|\big[\widetilde{R}_1^{\widetilde{p},\widetilde{q}}, \ldots, \widetilde{R}_{\widetilde{m}\widetilde{n}}^{\widetilde{p},\widetilde{q}}\big]\mathbf{h}\right|^2 \det(\mathbf{J})\,\mathrm{d}u\,\mathrm{d}v\right), \tag{6.12a}$$

$$\text{such that} \quad y_{\mathbf{d}} \geq y_0, \tag{6.12b}$$

$$a_{k_1,\ell_1} \geq 0,\ a_{k_2,\ell_2} \geq d_t^2,\ b_{\alpha,\beta} \geq 0,\ d_{\mathbf{r}}^2(\xi_i,\xi_j) \geq \delta, \text{ (c.f. Section 6.2.1)} \tag{6.12c}$$

$$(\mathbf{K} + \mathbf{M} + \mathbf{T})\,\mathbf{h} = \mathbf{f}, \tag{6.12d}$$

where $y_{\mathbf{d}}$ are the y-coordinates of the design control points, and y_0 is a lower bound.

Let us now find first order derivatives of functions involved in (6.12). First, consider the constraints (6.12c). As noted in subsection 6.2.1 the quantities $a_{k,\ell}$, $b_{\alpha,\beta}$, and $d_{\mathbf{r}}(\xi_i,\xi_j)$ in $(i-iii)$ of Proposition 1 are quadratic forms of the design control point vector $\mathbf{d}$, therefore evaluating their gradients with respect to $\mathbf{d}$ is a straightforward calculation. On the other hand, the objective function in (6.12) depends implicitly on $\mathbf{d}$ through the discretized Maxwell's equations (6.12d).

Consider the partial derivative of $W_\square$ with respect to a component $\widehat{d}_i$ of $\widehat{\mathbf{d}}$. To facilitate the sensitivity analysis, we keep the parametrization of the objective domain $\Omega_\square$ stay fixed during optimization, see Fig. 6.4. Rewriting (6.4) as $W_\square = 2\iint_{\mathbf{F}^{-1}(\Omega_\square)} H_z \circ \mathbf{F}\, \overline{H_z \circ \mathbf{F}}\, \det(\mathbf{J})\, \mathrm{d}u\, \mathrm{d}v$, and

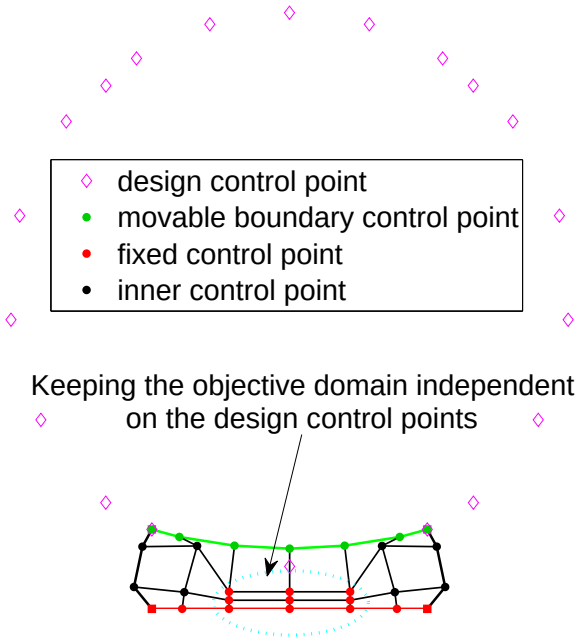

Figure 6.4: Graphical specification of different types of control points and the fixed parametrization of the objective domain $\Omega_\square$. The control points of patch 1 are chosen such that the fixed domain are $\Omega_\square = [-0.07143, 0.07143] \times [0, 0.03]$.

noting that $\mathbf{F}^{-1}(\Omega_\square)$ and consequently $\mathbf{J}\big|_{\mathbf{F}^{-1}(\Omega_\square)}$ is independent from $\widehat{d}_i$, we have

$$\frac{\partial W_\square}{\partial \widehat{d}_i} = 4 \iint_{\mathbf{F}^{-1}(\Omega_\square)} \mathrm{Re}\left(\frac{\partial (H_z \circ \mathbf{F})}{\hat{d}_i}\, \overline{H_z \circ \mathbf{F}} \right) \det(\mathbf{J})\, \mathrm{d}u\, \mathrm{d}v. \tag{6.13}$$

Since we clearly have

$$\frac{\partial (H_z \circ \mathbf{F})}{\hat{d}_i} = \left[\widetilde{R}_1^{\widetilde{p},\widetilde{q}}, \ldots, \widetilde{R}_{\widetilde{m}\widetilde{n}}^{\widetilde{p},\widetilde{q}} \right] \frac{\partial \mathbf{h}}{\hat{d}_i}, \tag{6.14}$$

it remains to determine $\frac{\partial \mathbf{h}}{\hat{d}_i}$. Differentiating the two sides of (6.10) and utilizing the fact that $\frac{\partial \mathbf{T}}{\hat{d}_i} = \frac{\partial \mathbf{f}}{\hat{d}_i} = \mathbf{0}$, the partial derivative is in turn the solution to the following linear system

$$(\mathbf{K} + \mathbf{M} + \mathbf{T}) \frac{\partial \mathbf{h}}{\hat{d}_i} = -\frac{\partial (\mathbf{K} + \mathbf{M})}{\hat{d}_i} \mathbf{h}. \tag{6.15}$$

In (6.15), the partial derivatives of $\mathbf{K}$, and $\mathbf{M}$ are calculated straightforwardly by differentiating (6.11). Finally, as we employ a linear parametrization method discussed in Subsection 2.1.3, $\widehat{\mathbf{d}}$ is an affine function of $\mathbf{d}$. That is

$$\widehat{\mathbf{d}} = \mathbf{A}\mathbf{d} + \mathbf{B}, \tag{6.16}$$

where the matrices $\mathbf{A}$ and $\mathbf{B}$ can be explicitly determined from (2.13). Note that the refinement matrices [24] obtained when inserting knots into the boundary knot vectors to have parametrization knot vectors are already taken into account in $\mathbf{A}$. Therefore, the desired sensitivities are

$$\frac{\partial W_\square}{\partial \mathbf{d}} = \mathbf{A}^{\mathrm{T}} \frac{\partial W_\square}{\partial \widehat{\mathbf{d}}}. \tag{6.17}$$

electromagnetic constants of air	electromagnetic constants of gold w.r.t $f = 4 \times 10^{14}$ [Hz]
$\varepsilon_r = 1$	$\varepsilon_r^s \approx -20.198689873114411 + 1.382706392375553j$
$\mu_r = 1$	$\mu_r^s = 1$

Table 6.1: Electromagnetic constants used in this work.

Property	required value	used value
minimum allowed gap between the 2 antennas	$d_g = 25$ [nm]	$d_g = 57.5$ [nm]
minimal thickness	$d_t = 25$ [nm]	$d_t = 25$ [nm]
width of the bounding box	$d_{bw} = 2000$ [nm]	$d_{bw} = 776.25$ [nm]
height of the bounding box	$d_{bh} = 2000$ [nm]	$d_{bh} = 546.25$ [nm]

Table 6.2: Specification of optimization parameters used in this work when the frequency under consideration is $f = 4 \times 10^{14}$ [Hz].

6.3 Numerical results

In this section, after listing a few technical remarks, we present a first shape optimization result which is based on the use of the impedance boundary condition (IBC). We then present the main results using the setting described in Section 6.2. All experiments in this section correspond to the frequency $f = 4 \times 10^{14}$ [Hz] with respect to which the wavelength is approximately 750 [nm].

6.3.1 Technical remarks

We note that the present optimization results have been obtained using the shape optimization method presented in Chapter 5. Moreover, we use standard Gaussian quadratures [25] for numerical integration. All the solutions presented in this section have been obtained with gradient based non-linear programming solver *fmincon* from Optimization Framework of Matlab, version 7.9 (R2009b) [33].

For electromagnetic constants, Table 6.1 lists the values used in the present experiments. In this table, the complex relative permittivity ε_r^s of gold is chosen in accordance with A. Vial et al. [85]. Finally, the design parameters illustrated in Fig. 6.1(right) are listed in Table 6.2.

6.3.2 Using the impedance boundary condition

As a first direct application of the previous work presented in Chapter 5, we disregard the EM fields inside the antennas and impose the following impedance boundary condition (IBC) on the boundary of the antennas, c.f. Fig. 6.1(left),

$$\frac{1}{\varepsilon_{cr}} \frac{\partial H_z}{\partial \mathbf{n}} - jk_0 \sqrt{\frac{\mu_r^{\mathrm{s}}}{\varepsilon_{cr}^{\mathrm{s}}}} H_z = 0 \quad \text{on } \Gamma_s. \tag{6.18}$$

Using the same modeling for isogeometric analysis and shape optimization as that in Chapter 5, we obtain the resulting model depicted in Fig. 6.5. Note that the result depicted in Fig. 6.5 relies on the IBC. Thus we investigate the reliability of the IBC for the resulting antenna by comparing the numerical solution obtained using the IBC with that obtained when solving the EM fields inside the antennas. To perform the computations, we use FEM implemented by COMSOL [86] and obtain the comparison depicted in Fig. 6.6. The comparison shows that there is a remarkable discrepancy between the two numerical methods: using the IBC and solving

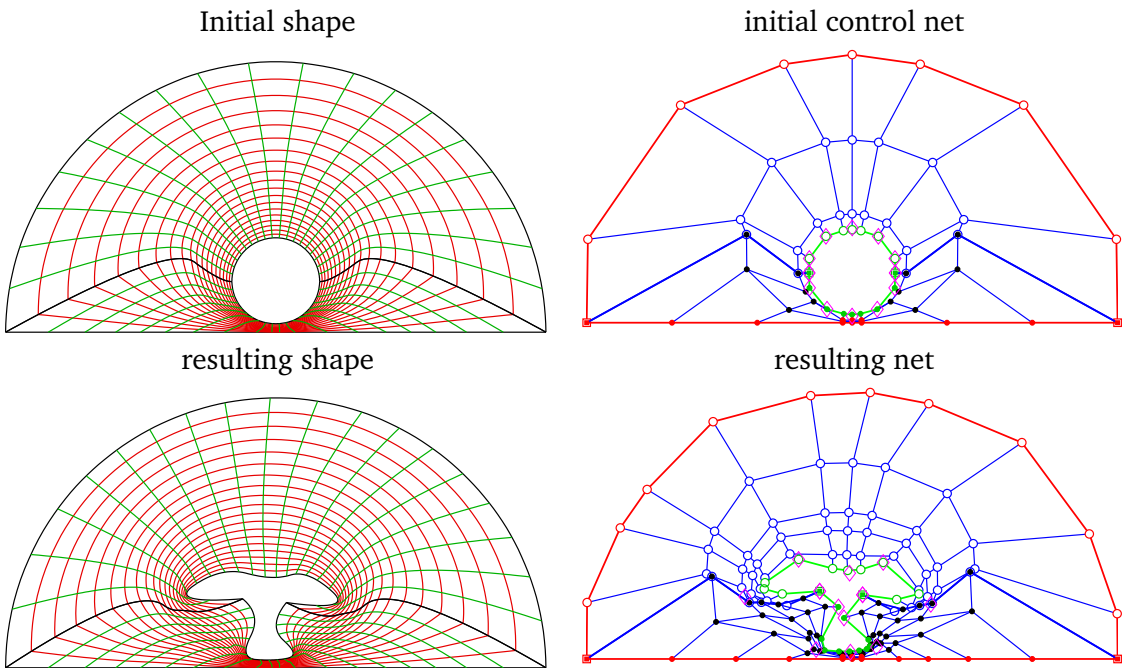

Figure 6.5: An optimization result for the optimization problem **??** using the IBC given by (6.18). In the present example, the computational domain is comprised of two spline patches and the objective domain is: $\Omega_{\square} = [-0.07143, 0.07143] \times [0, 0.03]$.

the numerical solution also inside the antenna interior. Quantitatively, the numerical magnetic energy $W_{\square}$ obtained by using the former is nearly 1000 times larger than the numerical magnetic energy obtained by sing the later. Therefore, we will solve the EM fields inside the antennas and perform optimization for that numerical configuration.

6.3.3 Inclusion of the antenna interior in the computational domain

We now use the 5-patch model depicted in Fig. 6.2 for calculating a numerical solution also in the antenna interior. Considering the resulting antenna in Section 6.3.2 as a reference design, we enforce the objective domain $\Omega_{\square}$ with respect to the 5-patch model to be the same as that in Section 6.3.2: $\Omega_{\square} = [-0.07143, 0.07143] \times [0, 0.03]$. This is done by the approach described in Section 6.2.2, see Fig. 6.7 for the resulting control points.

The optimization problem with the new numerical configuration results in an optima depicted in Fig. 6.7. We again use COMSOL to calculate the EM fields of the new resulting antenna. The numerical resulting EM fields for, depicted in Fig. 6.9, indicate that the resulting antenna is capable of creating a very strong field enhancement. This conclusion is again confirmed by looking at the frequency sweep for the resulting antenna in Fig. 6.8. However, if we extrude the 2D resulting antenna with a thickness either 100 [nm] or 750 [nm], c.f. Fig. 6.10, the resulting 3D models seem resonant but with a rather weak field enhancement.

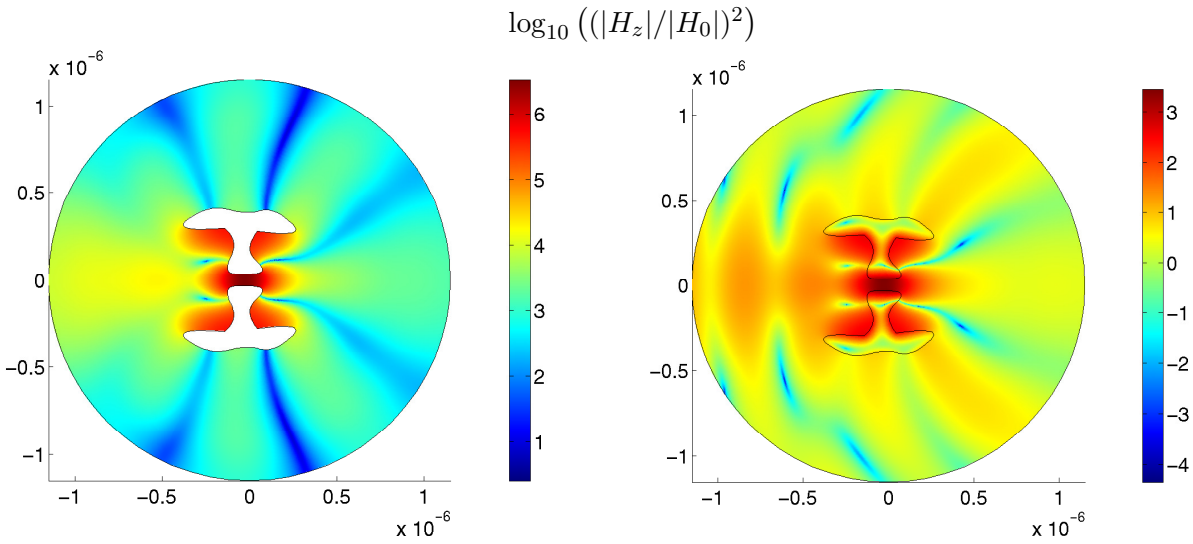

in the upper half and the lower half of the following circular domains: $\mathrm{Re}(H_z/H_0)$ and $\mathrm{Im}(H_z/H_0)$

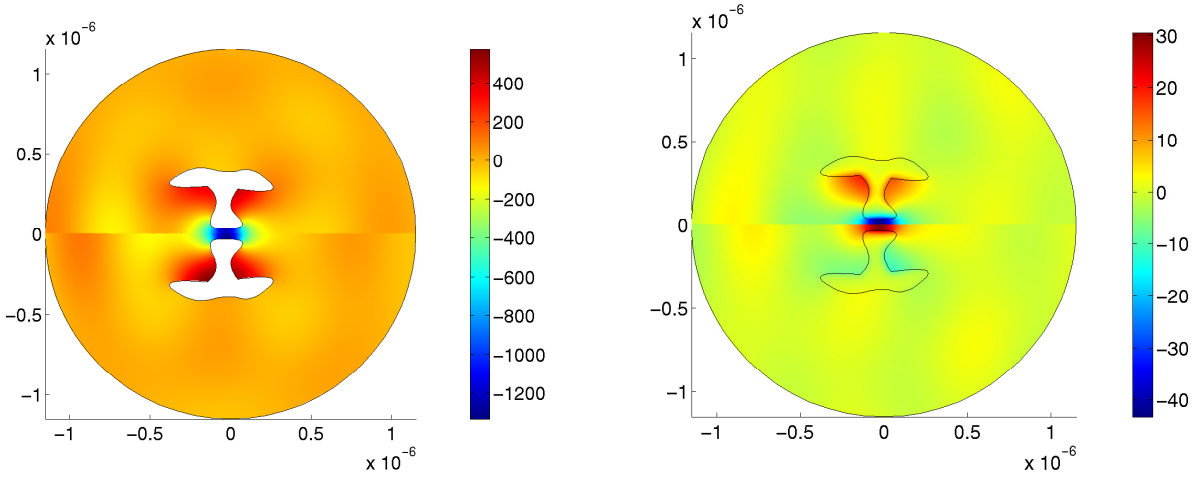

$\log_{10}(W_\square) = 4.9964$ $\log_{10}(W_\square) = 2.0568$

Figure 6.6: The comparison of the EM fields with respect to the resulting model in Fig. 6.5 when using (on the left) and not using the IBC (on the right). In the picture, H_0 is the magnitude of the incident magnetic field intensity. The numerical results for the both cases are computed in the real dimensions of the nano-antennas using the FEM with the same mesh, and the same shape functions of the third order Lagrange polynomial type.

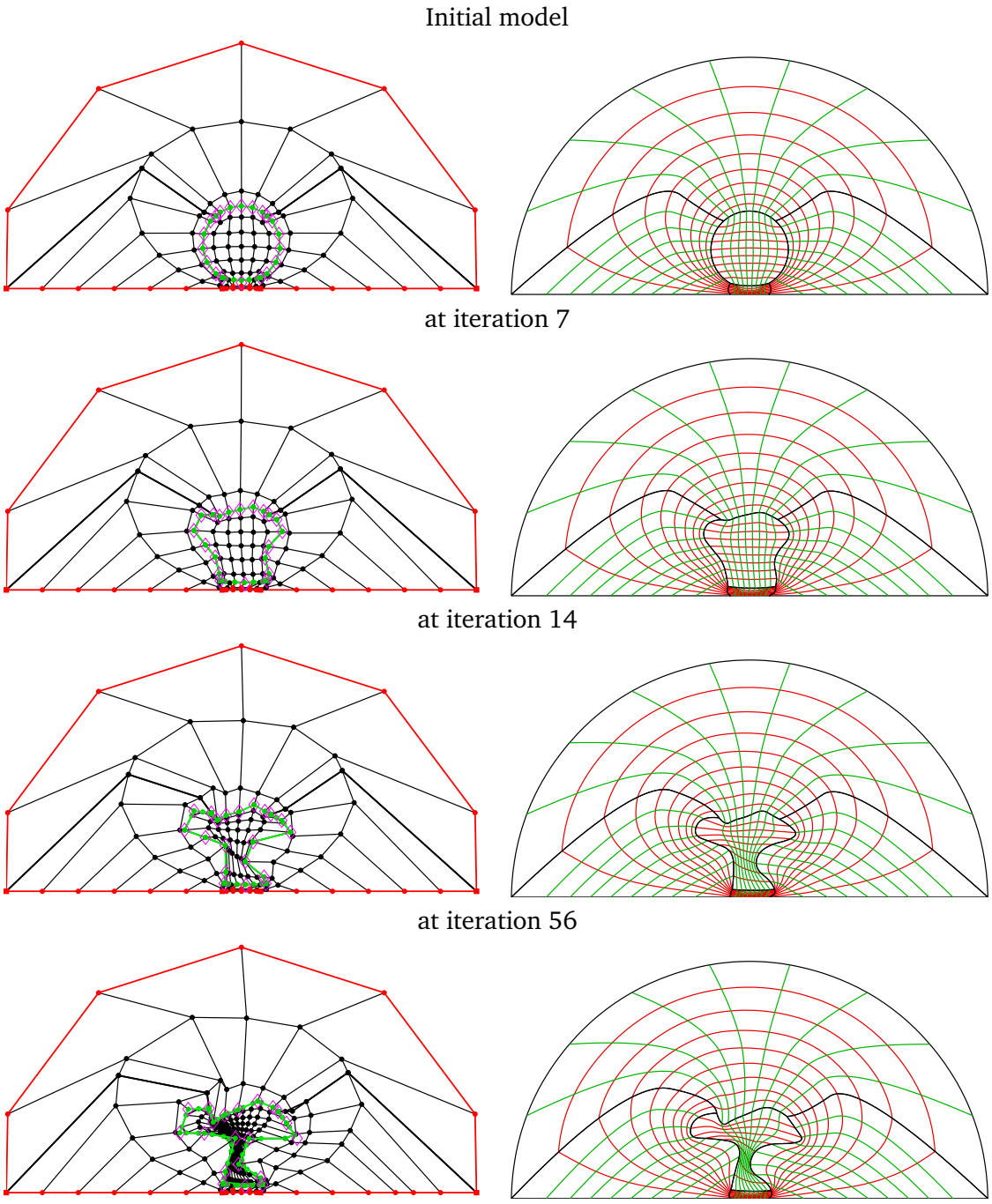

Figure 6.7: Intermediate models during the shape optimization process each of which is represented by a control net (on the left) and a shape (on the right) at a specific iteration.

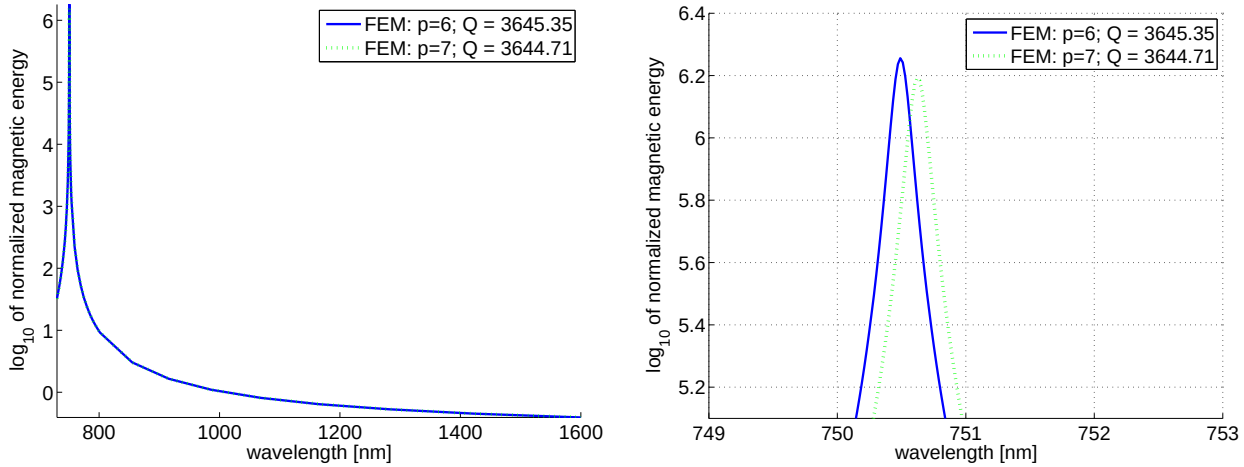

Figure 6.8: To the left, the frequency sweep of the antenna in Fig.6.7 in the vicinity of the wavelength $\lambda = 750$ [nm], and to the right the same frequency sweep but in an even smaller vicinity of the wavelength $\lambda = 750$ [nm].

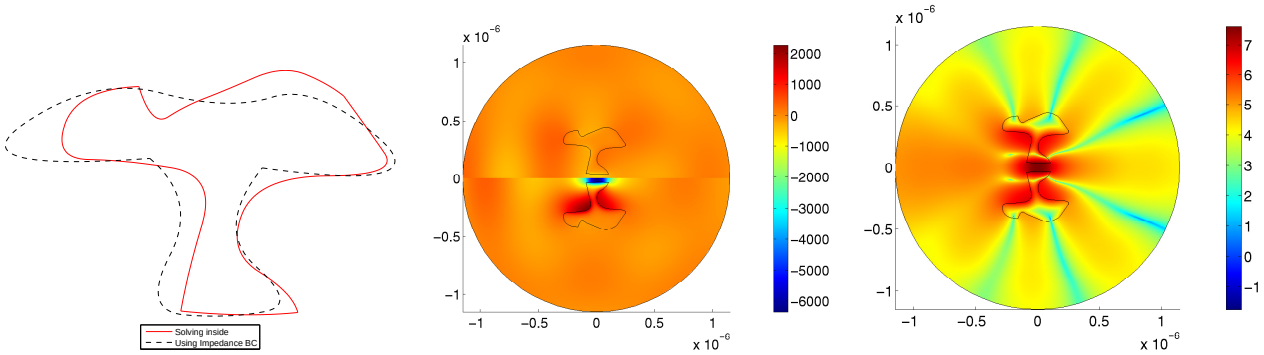

upper half: $\mathrm{Re}(H_z/H_0)$
lower half: $\mathrm{Im}(H_z/H_0)$

$\log_{10}\left((|H_z/H_0|)^2\right)$

Figure 6.9: To the left, the comparison of the resulting shapes when using the IBC (dashed curve) and when solving the numerical solution in the domain containing the antenna interior (the solid curve); in the middle, the real part and imaginary part of H_z with respect to the peak of the frequency sweep in Fig. 6.8; and to the right, $\log_{10}$ of the normalized magnetic energy with respect to the peak of the frequency sweep in Fig. 6.8. The computations are calculated using the FEM with shape functions of the 6^{th} order Lagrange polynomial type.

3D extruded antenna from the antenna in Fig.6.7 with thickness 100 [nm]

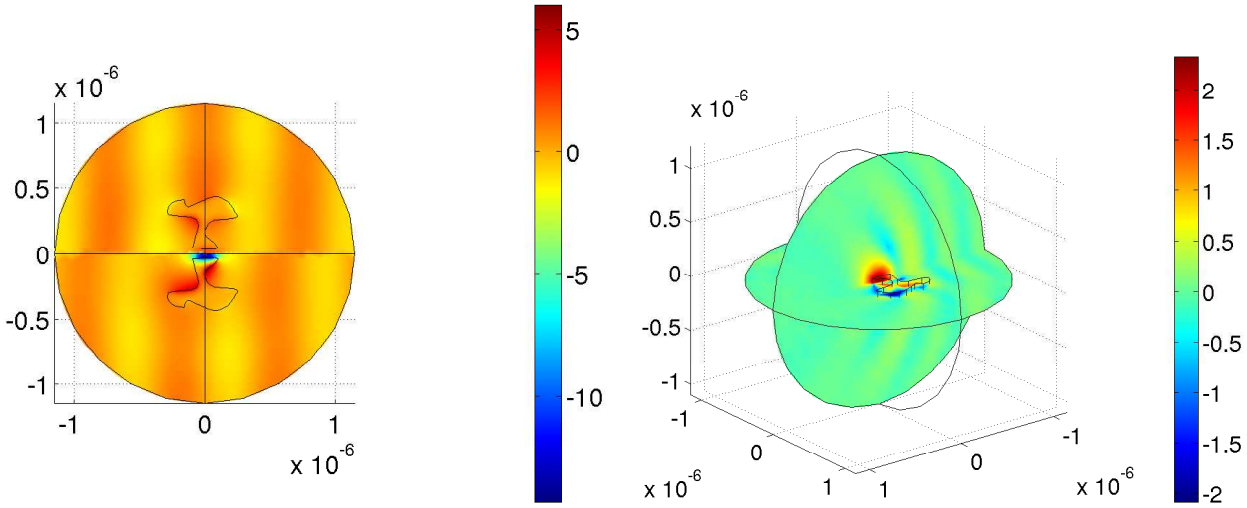

3D extruded antenna from the antenna in Fig.6.7 with thickness 750 [nm]

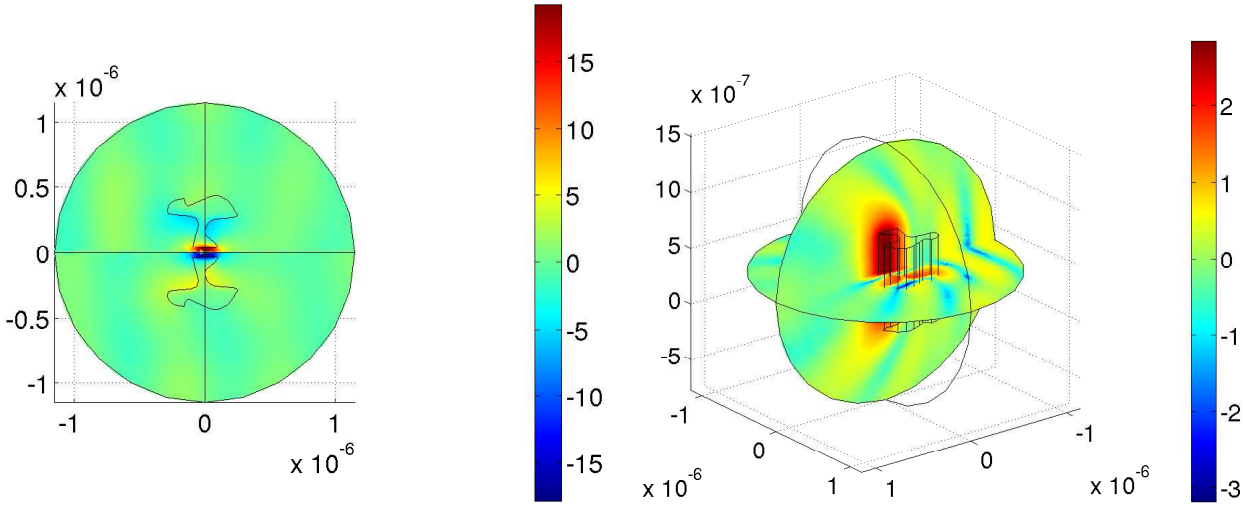

upper half: $\mathrm{Re}(H_z/H_0)$
lower half: $\mathrm{Im}(H_z/H_0)$

$\log_{10}\left((|H_z/H_0|)^2\right)$

Figure 6.10: Three-dimensional antennas resulting from extruding the antenna in Fig. 6.7 in the direction of the z-axis with different thicknesses.

Part IV

Economical designs of magnetic density separators

Chapter 7

Economical designs of magnetic density separators using isogeometric analysis and shape optimization

Nguyen D. M., A. Evgrafov, J. Gravesen, D. Lahaye, Economical designs of magnetic density separators using isogeometric analysis and shape optimization, *Structural and Multidisciplinary Optimization*, to be submitted, 2012.

Abstract. We study the use of isogeometric analysis-based shape optimization for improving an emerging magnetic density separation device. In particular, we look at a recently proposed design of such a device, which reduces the number of used electromagnets by a factor of two or three compared to conventional designs. The use of a systematic design approach based on shape optimization allows us to further improve the performance of a known analytical design. The obtained results also show that the shapes of iron components have a very pronounced effect on the magnetic fields inside the device, which can be effectively utilized in different engineering applications as well.

Keywords: Magnetic density separator; waste separator; shape optimization; isogeometric analysis.

In collaboration with Domenico Lahaye, Delft Institute for Applied Mathematics, Delft University of Technology, Mekelweg 4, 2628 CD Delft, The Netherlands.

7.1 Introduction

In recent years, isogeometric analysis-based shape optimization (IGSO) has witnessed intensive developments and has been applied in various engineering disciplines [11, 12, 9, 15, 16, 10]. Such an interest is fueled by the fact that the incorporation of isogeometric analysis (IGA) into a shape optimization workflow allows one to represent complicated shapes with spline boundaries exactly and with relatively few parameters (control points), and perhaps even more importantly, import the optimized shapes back into a CAD system for manufacturing purposes [6, 7]. The involvement of CAD systems also allows the utilizations of several well-studied and powerful tools for regularizing the shape parametrization and the geometries under consideration [8, 9, 10].

Unfortunately, the incorporation of IGA into a shape optimization framework is not trivial due to the fact that the parametrization control points need to be determined as smooth functions of the design control points in such a way, that they form a valid parametrization of the physical domain. This problem has been partially addressed in Nguyen et al. [9, 10]. In this paper, we take a slightly different approach, which leads to an improved algorithmic performance when compared with the previous results. Namely, we utilize the fact that the Jacobian determinant of a 2D spline parametrization is also a spline function, and that the coefficients of the spline function are quadratic forms of the parametrization control points. Having computed these coefficients, we require them to be positive thereby enforcing the validity of the domain parametrization. In addition, the algorithm also includes constraints on the local regularity of the domain boundary and on the "validity" of each angle of one spline patch, that is, forcing the angle to be less than π. The mentioned regularities are discussed in J. Gravesen et al. [28].

Our study is motivated by a design problem for an emerging magnetic density separation technology [87]. To describe the underlying principle of the technology, let us first recall from Murariu et al. [88] that a particle of radius b (small enough) with volume V_p and density ρ_p moving with a velocity $\mathbf{v}_v$ in a magnetic liquid of density ρ_f, dynamic viscosity η and saturation magnetization M_f in the presence of an external magnetic flux density $\mathbf{B}$ will experience the following forces

(i) Force of gravity: $\mathbf{F}_G = \rho_p V_p \mathbf{g}$;

(ii) Buoyancy force: $\mathbf{F}_B = -\rho_f V_p \mathbf{g}$;

(iii) Magnetically induced buoyancy force: $\mathbf{F}_{BM} = V_p M_f \boldsymbol{\nabla} \|\mathbf{B}\|$;

(iv) Drag force: $\mathbf{F}_D = 6\pi\eta b \mathbf{v}_p$,

where $\mathbf{g}$ is the gravitational acceleration. Let us consider a (x, y, z)-Cartesian coordinate system such that $-\mathbf{g}$ and the unit vector $(0, 1, 0)$ are co-directional vectors. (We have assumed that $\mathbf{g}$ is uniform over the space under consideration). In equilibrium, the total force on the particle vanishes, thereby leading to the following so-called an apparent density

$$\rho_{app} = \rho_f + M_f \frac{\partial \|\mathbf{B}\|}{\partial y} \frac{1}{g}. \tag{7.1}$$

It is proven by Murariu et al. [89] that a particle with density not lower than ρ_{app} will sink, whereas a particle with density lower than ρ_{app} will float. In 2009, E.J. Bakker et al. [90] proposed that the use of an array of alternating magnetic poles in the, e.g., (z, x)-plane may create a magnetic flux density with constant magnitude in the x-direction (that is, $\frac{\partial}{\partial x}\|\mathbf{B}\| = 0$) and varies exponentially in the y-direction. The array of alternating magnetic poles is called a magnetic density separator (MDS) and illustrated in Fig. 7.1(left). Such a device can segregate mixed materials into layers of different materials, see Fig. 7.1(right), with each material floating on a distance from the device according to its density and the apparent density of the liquid. There are two problems related to the design of MDSs. Firstly, for harvesting the classified materials, the apparent density should be uniform in the horizontal direction. Secondly, it would be desirable to use less permanent magnets for designing the MDS. This is because, c.f. [91], the permanent magnets are made from FENdB, a compound containing the rare earth metal Neodymium (expected to become less available in the near future). Due to that fact, D. Lahaye et al. [91] proposed MDSs consisting of alternating ferromagnetic and permanent magnet poles, see Fig. 7.2. According to Fig. 7.2, while the design with infinitely many poles performs well, the design with finitely many poles faces end effects. Thus we use shape optimization using IGA to improve the later design by varying the shapes of the iron poles. This is also motivated by the increasing importance of MDSs in industrial applications. Indeed, MDS is one of the two main technologies in the W2Plastics project [87] for economically recovering high-purity polyolefin's

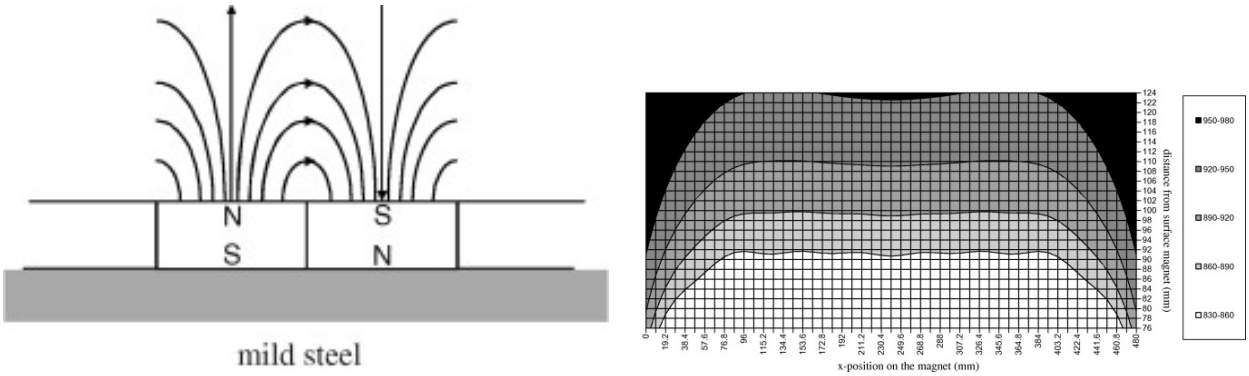

Figure 7.1: To the left, the magnet configuration of the original MDS proposed by E.J. Bakker et al. [90]. And to the right, effective medium density in the magnetic liquid below the magnet (the magnet is at the bottom in this figure); gravitation is in the upper direction; the colours are indicating the density in kg/m^3. These pictures are also taken from [90].

from complex wastes. Moreover, due to its great potential for material separation, MDS has intensively been pushed forward in various industrial applications [92, 93, 94, 95, 96].

This paper is structured as follows. Some numerical aspects of the physical problem is presented in 7.2. Section 7.3 recalls basis 2D isogeometric analysis. Section 7.4 then describes how isogeometric analysis is incorporated into shape optimization. The isogeometric analysis modeling of the shape optimization problem stated in Section 7.2 is now presented in Section 7.5. Numerical results are reported in Section 7.6. Section 7.7 complete the paper with a few remarks.

7.2 Physical problem

In this section, we first recall numerical approaches for solving a computational domain with the presence of iron parts and electromagnets. We then formulate the shape optimization problem in a mathematically precise fashion.

7.2.1 Magnetic density separator: Governing equation

A magnetic density separator (MDS) considered in this work is a device comprised of permanent electromagnets and iron components, c.f. Fig. 7.3. Provided that the length in the z-direction of the MDS is large relative to that in the x-direction and y-direction, it suffices to consider the problem in 2D [97]. We then look at the magnetic vector potential $\mathbf{A} = (0, 0, A_z)$ which will then be used to calculate the magnetic flux density $\mathbf{B}$ as $\mathbf{B} = \boldsymbol{\nabla} \times \mathbf{A}$. Let $\mathbf{M} = M_0(0, \mathbf{1}_{\Omega_m}, 0)$ represent the magnetizations of magnets, where M_0 is a constant reflecting the magnitude of $\mathbf{M}$, Ω_m is the domain with the presence of the magnets, and $\mathbf{1}_{\Omega_m}$ is the indicator function of Ω_m (i.e., $\mathbf{1}_{\Omega_m}(x, y) = 1$ if $(x, y) \in \Omega_m$ and $\mathbf{1}_{\Omega_m}(x, y) = 0$ otherwise). The fundamental equations of magnetostatics, see [79], applied for the 2D model result in the following equation in the weak sense

$$\boldsymbol{\nabla} \cdot \frac{1}{\mu} \boldsymbol{\nabla} A_z = -M_0 \frac{\partial \mathbf{1}_{\Omega_m}}{\partial x}, \tag{7.2}$$

where μ is the material permeability. In particular, if the shapes of the magnets are rectangles with edges parallel to the x and y axes, i.e., Ω_m can be written as $\Omega_m = [a_1, b_1] \times [c_1, d_1] \cup \ldots \cup$

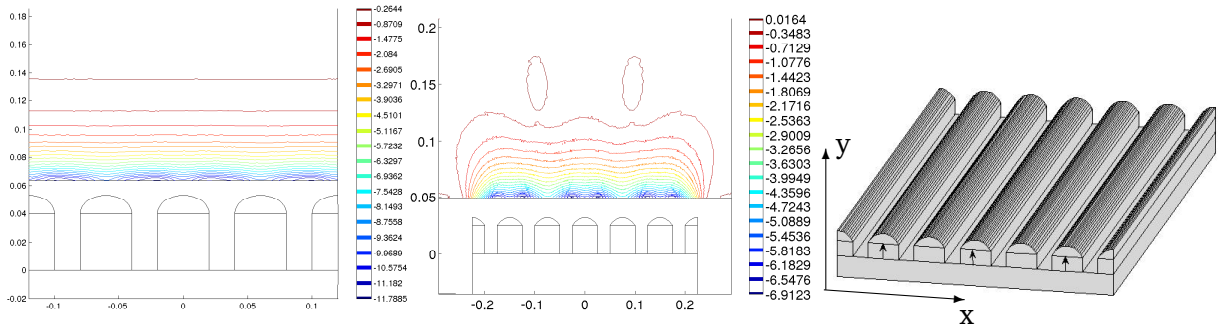

Figure 7.2: Designs of MDSs by D. Lahaye et al. [91]. On the left: contour lines of $\frac{\partial\|\mathbf{B}\|}{\partial y}$ with respect to an infinitely many alternating magnetic poles; at the middle: contour lines of $\frac{\partial\|\mathbf{B}\|}{\partial y}$ with respect to an induced finitely many poles; on the right: 3D view of the design with finite poles in which an arrow represent the presence of a magnet. The pictures are by courtesy of Domenico Lahaye.

$[a_m, b_m] \times [c_m, d_m]$, we can express $\mathbf{1}_{\Omega_m}$ as follows: for $(x, y) \in \mathbb{R}^2$

$$\mathbf{1}_{\Omega_m}(x, y) = (\theta_{a_1} - \theta_{b_1}) \otimes (\theta_{c_1} - \theta_{d_1}) + \ldots + (\theta_{a_m} - \theta_{b_m}) \otimes (\theta_{c_m} - \theta_{d_m}), \tag{7.3}$$

for $(x, y) \in \mathbb{R}^2$, where θ is the Heaviside step function, c.f. [26], and the $\otimes$ operator is defined as $(f \otimes g)(x, y) = f(x)g(y)$ for real functions f and g of one variable. Since in a distributional sense [26], $\partial\theta_a/\partial x = \delta_a$, the equation (7.2) can be reformulated in the weak sense as

$$\boldsymbol{\nabla} \cdot \frac{1}{\mu}\boldsymbol{\nabla} A_z = -M_0\big((\delta_{a_1} - \delta_{b_1}) \otimes (\theta_{c_1} - \theta_{d_1}) + \ldots + (\delta_{a_m} - \delta_{b_m}) \otimes (\theta_{c_m} - \theta_{d_m})\big). \tag{7.4}$$

7.2.2 Numerical modeling

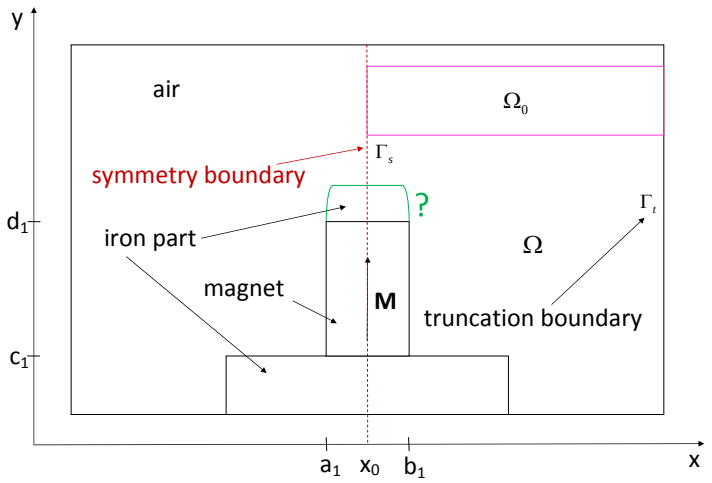

Figure 7.3: A simplified magnetic density separator, in which a magnet is placed in the box $[a_1, b_1] \times [c_1, d_1]$.

For simplicity, we restrict ourself to the case where the distribution of magnets and iron components are symmetric about a vertical line $x = x_0$. We then truncate the surrounding space

of the device by a closed curve. Let Ω denote the intersection of the half-plane $x \geq x_0$ and the domain enclosed by the truncation curve, c.f. Fig. 7.3. The boundary of Ω thus contains two parts: Γ_s, a segment in the symmetry line $x = x_0$, and Γ_t, the part belonging to the truncation curve, c.f. Fig. 7.3. We now look at the following classical magnetic vector potential [78]

$$\mathbf{A}(u,v,w) = \mu_0 \int_D \mathbf{J}_e(x,y,z) \frac{1}{4\pi\sqrt{(u-x)^2+(v-y)^2+(w-z)^2}} \,\mathrm{d}V, \tag{7.5}$$

where $\mathbf{J}_e$ is the (equivalent) electric current, D is the domain where the electric current exists, and μ_0 is the permeability of free space. As the symmetric distribution of magnets and iron components result in a skew-symmetric distribution of the equivalent (free and bound) electric current $\mathbf{J}_e = \nabla \times \mathbf{M}$, c.f. [78], from equations (7.5) it follows

$$A_z = 0 \quad \text{on}\, \Gamma_s. \tag{7.6}$$

For the boundary condition on the truncation boundary Γ_t, it is well-known [77] that

$$A_z = 0 \quad \text{on}\, \Gamma_t. \tag{7.7}$$

Thus, the boundary value problem given by (7.4), (7.6), (7.7) can, in the weak sense, be stated as follows: find $A_z \in H_0^1(\Omega)$, c.f. [26], such that for every $\phi \in H_0^1(\Omega)$ the following equality holds

$$\begin{aligned} \int_\Omega \frac{1}{\mu} \nabla A_z \cdot \nabla \phi \,\mathrm{d}V &= M_0 \sum_{k=1}^{m} \int_\Omega \left((\delta_{a_k} - \delta_{b_k}) \otimes (\theta_{c_k} - \theta_{d_k}) \right) \phi \,\mathrm{d}V \\ &= M_0 \sum_{k=1}^{m} \int_{c_k}^{d_k} \big(\phi(a_k, y) - \phi(b_k, y) \big) \mathrm{d}y. \end{aligned} \tag{7.8}$$

7.2.3 Optimization problem

First, we note that if $\|\mathbf{B}\| \in C^2(\mathrm{int}(\Omega))$ then we have the identity

$$\frac{\partial}{\partial x} \frac{\partial \|\mathbf{B}\|}{\partial y} = \frac{\partial}{\partial y} \frac{\partial \|\mathbf{B}\|}{\partial x}. \tag{7.9}$$

From (7.1), it follows that the apparent density ρ_{app} is uniform in the x-direction if $\frac{\partial^2 \|\mathbf{B}\|}{\partial x \partial y} = 0$. This condition is satisfied, according to (7.9), if $\frac{\partial \|\mathbf{B}\|}{\partial x} = 0$. Even though minimizing the quantity $|\frac{\partial \|\mathbf{B}\|}{\partial x}|$ is not identical to minimizing the quantity $|\frac{\partial^2 \|\mathbf{B}\|}{\partial x \partial y}|$, we have observed that the former produces good results. Thus, our optimization problem then reads: find the shapes of iron components of a MDS, c.f. Fig. 7.3, such that the following quantity is minimized

$$I = \int_{\Omega_o} \left(\frac{\partial \|\mathbf{B}\|^2}{\partial x} \right)^2 \mathrm{d}V = 4 \int_{\Omega_o} \left(\boldsymbol{\nabla} Az \cdot \frac{\partial}{\partial x} \boldsymbol{\nabla} Az \right)^2 \mathrm{d}V, \tag{7.10}$$

where Ω_0 is a specific region above the physical components of the MDS, c.f. Fig. 7.3. As known in the classical analysis that the vanishing of the integral in (7.10) strongly leads to the vanishing of its continuous integrand, and thus the optimization problem is theoretically well-defined.

7.3 Isogeometric analysis

In this section we recall the basic two-dimensional B-spline based isogeometric analysis (IGA). Similarly to the standard FEM, the underlying principle of IGA is the use of the Galerkin method [2]. Thus we approximate a weak solution to a given boundary value problem associated with Poisson's equations in a finite-dimensional space spanned by certain basis (shape) functions. In the present case, the basis functions are defined indirectly via a B-spline parametrization of the physical domain and bivariate B-spline tensor products in the parameter domain $[0,1]^2$.

7.3.1 B-splines

B-splines are piecewise polynomials of a certain degree p and typically differentiable up to the degree $p-1$. They are non-negative and compactly supported, see Fig. 7.4 (left). They are completely defined by specifying certain parameter values, called *knots*, $\xi_1 \leq \ldots \leq \xi_{n+p+1}$. More precisely, B-splines may be defined recursively as follows: for $i = 1, \ldots, n$ we put

$$N_i^0(\xi) = \begin{cases} 1 & \text{if} \quad \xi \in [\xi_i, \xi_{i+1}[, \\ 0 & \text{otherwise,} \end{cases} \qquad N_i^p(\xi) = \frac{\xi - \xi_i}{\xi_{i+p} - \xi_i} N_i^{p-1}(\xi) + \frac{\xi_{i+p+1} - \xi}{\xi_{i+p+1} - \xi_{i+1}} N_{i+1}^{p-1}(\xi).$$

In the context of IGA, the *knot vector* $\boldsymbol{\Xi} = \{\xi_1, \ldots, \xi_{n+p+1}\}$ typically has its first and last knots set to 0 and 1, respectively, and repeated $p+1$ times. That is, we have $\xi_1 = \ldots = \xi_{p+1} = 0$ and $\xi_{n+1} = \ldots = \xi_{n+p+1} = 1$, see Fig. 7.4 (right). Such B-splines form a partition of unity on the interval $[0, 1[$. Further properties of B-splines can be found in, e.g., [22, 24].

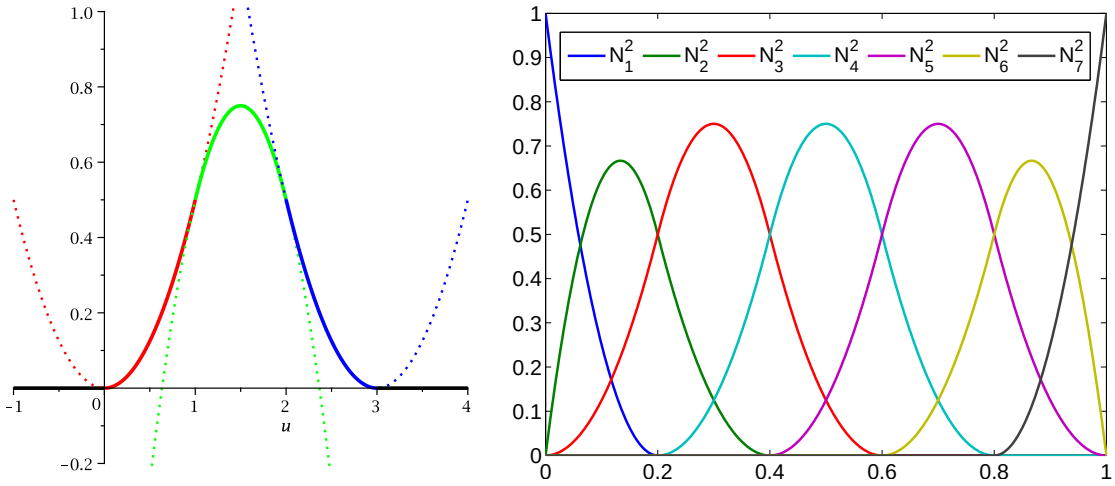

Figure 7.4: To the left: a quadratic B-spline composed of polynomial "pieces" (shown in different colors). The alignments of the dashed-straight lines show that the B-spline is C^1-continuous at the joint points. To the right: quadratic B-splines with the knot vector $\{0, 0, 0, 0.2, 0.4, 0.6, 0.8, 1, 1, 1\}$.

7.3.2 Basis functions for analysis

Let us consider a simply connected open domain $\Omega \subset \mathbb{R}^2$. We are looking for a spline parametrization of Ω, that is, for a *bijective* map $\mathbf{F} : [0, 1]^2 \to \Omega$ of the form

$$\mathbf{F}(u, v) = \big(x(u, v), y(u, v)\big) = \sum_{i=1}^{\widehat{m}} \sum_{j=1}^{\widehat{n}} \widehat{\mathbf{d}}_{i,j} \widehat{M}_i^p(u) \widehat{N}_j^q(v), \tag{7.11}$$

where $\widehat{M}_i^p$ and $\widehat{N}_i^q$ are B-splines of degree p and q with knot vectors $\widehat{\boldsymbol{\Xi}}_u$ and $\widehat{\boldsymbol{\Xi}}_v$, respectively. By composing the inverse $\mathbf{F}^{-1}$ with some basis functions on the parameter (reference) domain $]0, 1[^2$ we obtain basis functions defined on the physical domain Ω. We let $\widetilde{M}_i^{\widetilde{p}}$, $i = 1, \ldots, \widetilde{m}$ and $\widetilde{N}_j^{\widetilde{q}}$, $j = 1, \ldots, \widetilde{n}$ be B-splines of degree $\widetilde{p}$ and $\widetilde{q}$ (not necessary equal to p and q) with knot vector $\widetilde{\boldsymbol{\Xi}}_u$ and $\widetilde{\boldsymbol{\Xi}}_v$, respectively. The basis functions on the parameter domain are defined as the tensor product splines $\widetilde{R}_k^{\widetilde{p},\widetilde{q}}(u, v) = \widetilde{M}_i^{\widetilde{p}}(u) \widetilde{N}_j^{\widetilde{q}}(v)$, $k = (\widetilde{n} - 1)i + j$. Thus, the basis functions on the

physical domain Ω are given as $\widetilde{R}_k^{\widetilde{p},\widetilde{q}} \circ \mathbf{F}^{-1}$. An integral over Ω can be now transformed to an integral over $]0,1[^2$ as

$$\iint_{\Omega} f(x,y)\,\mathrm{d}x\,\mathrm{d}y = \iint_{[0,1]^2} f(x(u,v),y(u,v))\,\det(\mathbf{J})\,\mathrm{d}u\,\mathrm{d}v, \tag{7.12}$$

where $\mathbf{J}$ is the Jacobian of the variable transformation $\mathbf{F}$, and we have assumed that $\det(\mathbf{J}) > 0$. Note that the knot vectors $\widehat{\boldsymbol{\Xi}}_u$ and $\widehat{\boldsymbol{\Xi}}_v$ used for for the parametrization of Ω may be "finer" than the four knot vectors $\boldsymbol{\Xi}_\ell$ ($\ell = 1,\ldots,4$) used in the parametrization of the domain boundary $\partial\Omega$. The "refinement" is achieved by inserting new knots into the two pairs of knot vectors $(\boldsymbol{\Xi}_1, \boldsymbol{\Xi}_3)$ and $(\boldsymbol{\Xi}_2, \boldsymbol{\Xi}_4)$ respectively. Furthermore, to ensure that we can approximate any function in $H^1(\Omega)$ [26] sufficiently well, we may want to use an even finer (when compared to $\widehat{\boldsymbol{\Xi}}_u$ and $\widehat{\boldsymbol{\Xi}}_v$) pair of knot vectors $\widetilde{\boldsymbol{\Xi}}_u$ and $\widetilde{\boldsymbol{\Xi}}_v$ for the analysis, see Fig. 7.5.

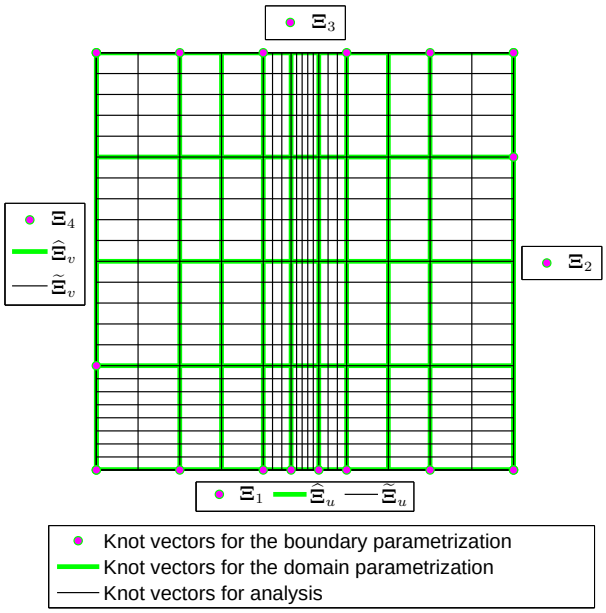

Figure 7.5: The three types of knot vectors of an IGA model used in the present work.

Remark 11. Often, it is convenient or even necessary to consider domains subdivided into several patches. Examples include non-simply connected domains or physical models involving several materials. For enforcing the C^0-continuity of the numerical solution across patch boundaries, we need the following property of spline curves.

Lemma 3. *Let* $\mathbf{r}$ *be a spline curve of degree* p *with knot vector* $\boldsymbol{\Xi} = \{t_1,\ldots,t_{n+p+1}\}$ *and control points* $\mathbf{c}_1,\ldots,\mathbf{c}_n$. *Then the following curve*

$$[0,1] \ni t \mapsto \mathbf{r}(a(1-t)+bt) \in \mathbb{R}^d, \quad t_{p+1} \le b < a \le t_{n+1},$$

is a spline curve with the knot vector

$$\boldsymbol{\Xi}_{a,b} = \{\frac{a-t_{n+p+1}}{a-b},\ldots,\frac{a-t_1}{a-b}\} \tag{7.13}$$

and with the control points $\mathbf{c}_n,\ldots,\mathbf{c}_1$.

Proof. Let $\boldsymbol{\gamma}_{a,b}$ be the spline curve of degree p with knot vector $\boldsymbol{\Xi}_{a,b}$ given by (7.13) and the control points $\mathbf{c}_n, \ldots, \mathbf{c}_1$. Furthermore, let f_r be the polar form, c.f. [22, 23], of $\mathbf{r}$ in the knot interval $[t_r, t_{r+1}]$ with $t_r < t_{r+1}$, and let f_r^* be the polar form of $\boldsymbol{\gamma}_{a,b}$ in the knot interval $[\frac{a-t_{r+1}}{a-b}, \frac{a-t_r}{a-b}]$. From the de Boor's algorithm [22, 23] it follows that

$$f_r^*(\frac{a-s_1}{a-b}, \ldots, \frac{a-s_p}{a-b}) = f_r(s_1, \ldots, s_p), \quad s_1, \ldots, s_p \in \mathbb{R}. \tag{7.14}$$

Substituting $s_1 = \ldots = s_p = a(1-t) + bt$ to (7.14), we arrive at the expected equality. □

The C^0-continuity of the numerical solution across boundaries between patches can be enforced as follows

- We parametrize all patches in the counter-clockwise fashion, i.e., a valid parametrization of this type has positive Jacobian determinant everywhere.
- *At a boundary* Γ *between two patches*, let spline curves $\mathbf{r}_i$ with knot vectors $\boldsymbol{\Xi}_i = \{t_1^{(i)}, \ldots, t_{n_i+p+1}^{(i)}\}$ and control points $\mathbf{c}_1^i, \ldots, \mathbf{c}_{n_i}^i$, $i = 1, 2$, be the induced parametrizations of the two parametrizations of the two patches of Γ, respectively. According to the direction of increasing parameter of the induced parametrizations, there are two cases, see Fig. 7.6 for illustrations,

  (i) $\mathbf{r}_1'(t) \cdot \mathbf{r}_2'(t) > 0$ for all $0 < t < 1$, i.e., $\mathbf{r}_1$ and $\mathbf{r}_2$ have co-directional tangent vectors. The criteria for the numerical solution to be continuous across Γ are

  1. *The two parametrizations are continuous across* Γ, i.e., $\mathbf{r}_1(t) = \mathbf{r}_2(t)$ for all $t \in \mathbf{F}^{-1}{}_i(\Gamma)$. This criterion is formulated as follows. First we find the "union" knot vector $\boldsymbol{\Xi}$ of $\boldsymbol{\Xi}_1$ and $\boldsymbol{\Xi}_2$, i.e., the knot vector whose inner knots are all inner knots of both knot vectors with maximum multiplicity. Let $\mathbf{R}_i$ be the refinement matrices [24] obtained when inserting knots into $\boldsymbol{\Xi}_i$ to have $\boldsymbol{\Xi}$, $i = 1, 2$. The C^0-continuity of the parametrizations now can be enforced by the following linear constraints on the control points

  $$\mathbf{R}_1[x_1^1, \ldots, x_{n_1}^1]^T = \mathbf{R}_2[x_1^2, \ldots, x_{n_2}^2]^T, \tag{7.15}$$

  where x_j^i is one of the coordinates of the control points $\mathbf{c}_j^i$.
  2. The same conditions as in (7.15) are enforced for the *state variables*, i.e., the coefficients of the representation of the numerical solution in terms of the basis functions defined in Section (7.3.2).

  (ii) $\mathbf{r}_1'(t) \cdot \mathbf{r}_2'(t) < 0$ for all $0 < t < 1$, i.e., the tangent vectors of $\mathbf{r}_1$ and $\mathbf{r}_2$ are the vectors with opposite directions. The criteria for the numerical solution to be continuous across Γ are

  1. *The two parametrizations are "continuous" across* Γ, i.e., $\mathbf{r}_1(1-t) = \mathbf{r}_2(t)$ for all $t \in \mathbf{F}_i^{-1}(\Gamma)$. This criterion is formulated as follows. Applying Lemma 3 with $a = 1$ and $b = 0$ for $\mathbf{r}_1$ to get the new knot vector $\boldsymbol{\Xi}_{1,1,0} = \{1 - t_{n_i+p+1}^{(1)}, \ldots, 1 - t_1^{(1)}\}$. Then similar to the previous case, we find the "union" knot vector $\boldsymbol{\Xi}$ of $\boldsymbol{\Xi}_{1,1,0}$ and $\boldsymbol{\Xi}_2$. Let $\mathbf{R}_1$ and $\mathbf{R}_2$ be the refinement matrices obtained when inserting knots into $\boldsymbol{\Xi}_{1,1,0}$ and $\boldsymbol{\Xi}_i$ to have $\boldsymbol{\Xi}$, respectively. The linear constraints for the "C^0-continuity" of the parametrizations are

  $$\mathbf{R}_1[x_{n_1}^1, \ldots, x_1^1]^T = \mathbf{R}_2[x_1^2, \ldots, x_{n_2}^2]^T, \tag{7.16}$$

  where x_j^i is one of the coordinates of the control points $\mathbf{c}_j^i$.

2. The same conditions as in (7.16) are enforced for the *state variables*.

- Let $\mathbf{Ch} = \mathbf{c}$ be the constraints, discussed above, on state variables $\mathbf{h}$. Let $\mathbf{Kh} = \mathbf{f}$ be the global discretization of the linear system, resulting from assembling matrices from all patches. Then $\mathbf{h}$ can be determined via the stationary point of the following Lagrange function with Lagrange multipliers $\boldsymbol{\lambda}$ [27]

$$\Lambda(\mathbf{h}, \boldsymbol{\lambda}) = \frac{1}{2}\mathbf{h}^T\mathbf{K}\mathbf{h} - \mathbf{h}^T\mathbf{f} + \boldsymbol{\lambda}^T(\mathbf{C}\mathbf{h} - \mathbf{c}). \tag{7.17}$$

That is,

$$\begin{bmatrix} \mathbf{K} & \mathbf{C}^T \\ \mathbf{C} & \mathbf{0} \end{bmatrix} \begin{bmatrix} \mathbf{h} \\ \boldsymbol{\lambda} \end{bmatrix} = \begin{bmatrix} \mathbf{f} \\ \mathbf{c} \end{bmatrix}. \tag{7.18}$$

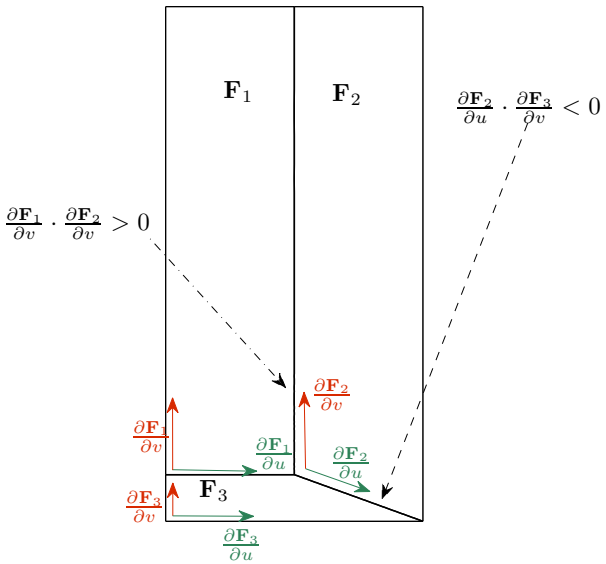

Figure 7.6: The first three patches of the multiple patch model depicted in Fig. 7.10. This is an example where the two cases (i) and (ii) in Remark 11 both occur. In the picture, $\mathbf{F}_i(u, v)$ denotes the parametrization of the patch i, $i = 1, 2, 3$, $(u, v) \in [0, 1]^2$.

7.3.3 Parametrization of a given domain

In an optimization problem using IGA, the objective function is often given by the integral over a given domain in the physical space. To simplify the implementation of IGA when the standard Gaussian quadratures [25] are used for numerical integrations, we would like the boundary of the domain to be the images of knot lines in the parameter space via a parametrization of the physical space. This leads to the standard interpolation problem [23] and can be solved as follows.

Let $\mathbf{r}(u) = \mathbf{c}_1 N_1(u) + \ldots + \mathbf{c}_n N_n(u)$ be a B-spline curve of degree p, where N_k are B-spline with knot vector $\boldsymbol{\Xi} = \{u_1, \ldots, u_N\}$ and $\mathbf{c}_k \in \mathbb{R}^d$, $k = 1, \ldots, n$. For simplicity, assume that all inner knots of $\boldsymbol{\Xi}$ have multiplicity 1. Note that the image of any knot u_k via $\mathbf{r}$ is a convex combination of the control points whose corresponding B-splines do not vanish at the knot.

Indeed, if we repeat inserting u_k into $\boldsymbol{\Xi}$ in $p-1$ times, then the resulting control point with respect to the B-spline defined by the knots

$$u_{k-1}, \underbrace{u_k, \ldots, u_k}_{p \text{ times}}, u_{k+1}$$

must be $\mathbf{r}(u_k)$. By that way, we can formulate explicitly the weights of the convex combination. For instance if $p = 3$ we have

$$\mathbf{r}(u_k) = \alpha_k \mathbf{c}_{k-p-1} + \beta_k \mathbf{c}_{k-p} + \gamma_k \mathbf{c}_{k-p+1}, \quad k = p+1, \ldots, n+1, \tag{7.19}$$

where α_k, β_k and γ_k are given by the following expressions

$$\alpha_k = (1-a_{k-2})(1-b_{k-1}),\ \beta_k = a_{k-2}(1-b_{k-1}) + (1-a_{k-1})b_{k-1},\ \gamma_k = a_{k-1}b_{k-1}, \tag{7.20}$$

$$a_{k-2} = \frac{u_k - u_{k-2}}{u_{k+1} - u_{k-2}},\ a_{k-1} = \frac{u_k - u_{k-1}}{u_{k+2} - u_{k-1}},\ b_{k-1} = \frac{u_k - u_{k-1}}{u_{k+1} - u_{k-1}}. \tag{7.21}$$

As expected $\alpha_k > 0, \beta_k > 0, \gamma_k > 0$ and $\alpha_k + \beta_k + \gamma_k = 1$, for all $k = p+1, \ldots, n+1$. If $\mathbf{r}(u_k)$, $k = p+1, \ldots, n+1$, are given, then (7.19) are a system of $d(n-p+1)$ linear equations of dn unknowns, the coordinates of the control points $\mathbf{c}_k$. Thus the curve $\mathbf{r}$ is completely defined if $\mathbf{r}(u_k)$, $k = p+1, \ldots, n+1$ are given together with other $d(p-1)$ linear equations. In this work, the remaining conditions are chosen to be $p-1$ predefined control points $\mathbf{c}_2, \ldots, \mathbf{c}_p$.

7.4 Shape optimization using isogeometric analysis

In this section, we first recall some parametrization techniques. The techniques are then combined into an iterative algorithm for shape optimization using isogeometric analysis. We also discuss the possibilities of using different methods of extending a parametrization from the boundary to the interior of the domain under consideration.

7.4.1 Spline parametrization

In this section, we recall techniques for handling spline parametrizations in isogeometric analysis while having their utilizations for shape optimization in mind. For more details, see [28, 29, 30, 10].

7.4.1.1 Jacobian determinant of a parametrization as a spline.

In order to constrain the validity of a parametrization of Ω when some of the control points $\widehat{\mathbf{d}}_{i,j}$, $i = 1, \ldots, \widehat{n}$, $j = 1, \ldots, \widehat{m}$ are design variables, we employ the following approach. The determinant of the Jacobian of $\mathbf{F}$ given by (7.11) is computed as

$$\det(\mathbf{J}) = \sum_{i,j=1}^{\widehat{m},\widehat{n}} \sum_{k,\ell=1}^{\widehat{m},\widehat{n}} \det[\widehat{\mathbf{d}}_{i,j}, \widehat{\mathbf{d}}_{k,\ell}] \frac{\mathrm{d}\widehat{M}_i^p(u)}{\mathrm{d}u} \widehat{N}_j^q(v) \widehat{M}_k^p(u) \frac{\mathrm{d}\widehat{N}_\ell^q(v)}{\mathrm{d}v}, \tag{7.22}$$

where $\det[\widehat{\mathbf{d}}_{i,j}, \widehat{\mathbf{d}}_{k,\ell}]$ is the determinant of the 2×2 matrix with columns $\widehat{\mathbf{d}}_{i,j}$, $\widehat{\mathbf{d}}_{k,\ell}$. Equation (7.22) defines a piecewise polynomial of degree $2p-1$ in u and degree $2q-1$ in v, with the differentiability at a knot lower by 1 in u and also lower by 1 in v. Such a map can be written in terms of B-splines $\mathcal{M}_k^{2p-1}$ and $\mathcal{N}_\ell^{2q-1}$ of degree $2p-1$ and $2q-1$ with the knot vectors

obtained from $\widehat{\Xi}_u$ and $\widehat{\Xi}_v$ by raising the multiplicities of the inner u-knots and v-knots by p and q, respectively. That is

$$\det(\mathbf{J}) = \sum_{k,\ell=1}^{M,N} c_{k,\ell}\, \mathcal{M}_k^{2p-1}(u)\, \mathcal{N}_\ell^{2q-1}(v). \tag{7.23}$$

As B-splines are non-negative, the positivity of the determinant can be ensured by the positivity of the coefficients $c_{k,\ell}$. Let $(\mathcal{N}_\ell^{2q-1})^*$ be a function having the following form

$$(\mathcal{N}_\ell^{2q-1})^* = \alpha_1 \mathcal{N}_1^{2q-1} + \ldots \alpha_N \mathcal{N}_N^{2q-1}, \tag{7.24}$$

and satisfy the conditions

$$\langle (\mathcal{N}_\ell^{2q-1})^*, \mathcal{N}_j^{2q-1} \rangle = \sum_{i=1}^{N} \alpha_k \int_0^1 \mathcal{N}_i^{2q-1}(v)\, \mathcal{N}_j^{2q-1}(v)\, \mathrm{d}v = \delta_{\ell,j}, \quad j = 1, \ldots, N. \tag{7.25}$$

$(\mathcal{N}_\ell^{2q-1})^*$ is called the *dual functional* of $\mathcal{N}_\ell^{2q-1}$, and may be determined via the system of linear equations (7.25) of unknowns $\alpha_1, \ldots, \alpha_N$. Utilizing the fact that $(\mathcal{M}_k^{2p-1}\mathcal{N}_\ell^{2q-1})^* = (\mathcal{M}_k^{2p-1})^*(\mathcal{N}_\ell^{2q-1})^*$, and substituting (7.22) to the relation $c_{k,\ell} = \langle (\mathcal{M}_k^{2p-1}\mathcal{N}_\ell^{2q-1})^*, \det(\mathbf{J}) \rangle$ we arrive at the following

$$c_{k,\ell} = \sum_{i,j=1}^{\widehat{m},\widehat{n}} \sum_{\alpha,\beta=1}^{\widehat{m},\widehat{n}} \det[\widehat{\mathbf{d}}_{i,j}, \widehat{\mathbf{d}}_{\alpha,\beta}] \, \langle\, (\mathcal{M}_k^{2p-1})^*\,,\, \frac{\mathrm{d}\widehat{M}_i^p}{\mathrm{d}u}\, \widehat{M}_\alpha^p \,\rangle \, \langle\, (\mathcal{N}_\ell^{2q-1})^*\,,\, \widehat{N}_j^q \frac{\mathrm{d}\widehat{N}_\beta^q}{\mathrm{d}v} \,\rangle. \tag{7.26}$$

If we let $\widehat{\mathbf{d}}$ denote the vector containing coordinates of the control points $\widehat{\mathbf{d}}_{i,j}$, then (7.26) shows that $c_{k,\ell}$ are quadratic forms of $\widehat{\mathbf{d}}$. The equation (7.26) also specifies coefficients of the matrices, denoted by $\mathbf{Q}_{k,\ell}$, of the quadratic forms. Thus we can write

$$c_{k,\ell} = \widehat{\mathbf{d}}^T \mathbf{Q}_{k,\ell} \widehat{\mathbf{d}}. \tag{7.27}$$

We now look for a linear method for extending a spline parametrization of the boundary of the physical domain onto the domain interior. By the term *linear*, we mean that that the resulting inner control points from the method are *affine* mappings of boundary control points. The linear method used in this work does not only depend on the knot vectors for the domain parametrization Ξ_u and Ξ_v but also depends on a reference parametrization of the domain. We obtain the reference parametrization by a minimization problem related to a so-called the Winslow functional [31]. We then "linearize" the Winslow functional to obtain the linear method. The approach for obtaining a reference parametrization of the domain and the derivation of the linear method are presented as follows.

7.4.1.2 Obtaining a (reference) spline parametrization.

None of the linear methods presented in [29, 30] for extending the parametrization of the boundary into the interior of the domain can in general guarantee that the resulting map $\mathbf{F}$ will satisfy $\det(\mathbf{J}) > 0$ everywhere on $[0,1]^2$. Therefore, during some shape optimization iterations we have to utilize a more expensive non-linear method for improving the distribution of the interior control points $\widehat{\mathbf{d}}_{i,j}$. In a view of (7.23), a natural approach to ensure that $\det(\mathbf{J})$ is bounded away from zero is to solve the following optimization problem:

$$\begin{aligned} &\underset{\widehat{\mathbf{d}}_{i,j},z}{\text{maximize}} \quad z, \\ &\text{subject to} \quad c_{k,\ell}\big(\widehat{\mathbf{d}}_{i,j}\big) \geq z, \end{aligned} \tag{7.28}$$

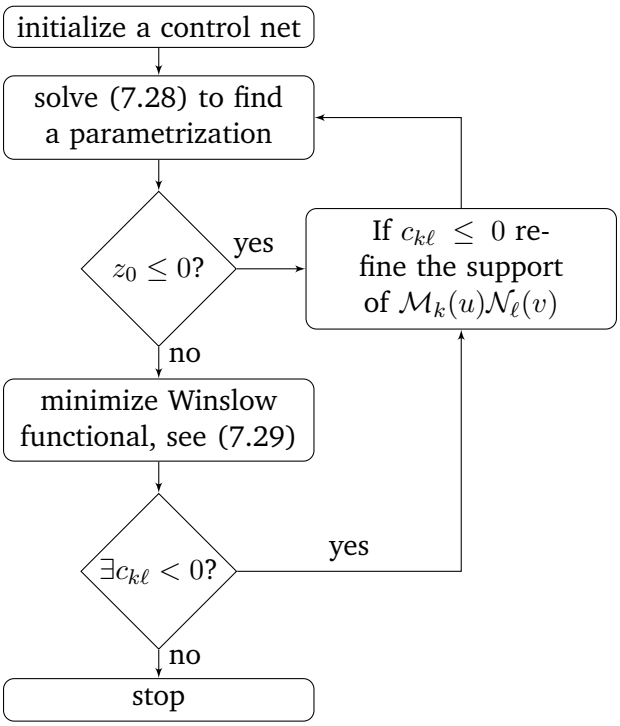

Figure 7.7: The algorithm for extending a boundary parametrization to the interior.

where $\widehat{\mathbf{d}}_{i,j}$ are inner control points as stated in (7.11), $c_{k,\ell}$ are given by (7.23), and z is an auxiliary optimization variable. If z resulting from approximately solving (7.28) to local optimality is positive then we are guaranteed to have a valid parametrization. Unfortunately, the quality of the parametrization obtained in this fashion needs not to be very high. Thus, we improve the parametrization by looking at the following constrained optimization problem:

$$\begin{aligned} \underset{\text{inner control points } \widehat{\mathbf{d}}_{i,j}}{\text{minimize}} \quad & \int_0^1 \int_0^1 W(\widehat{\mathbf{d}}_{i,j})\,\mathrm{d}u\,\mathrm{d}v, \\ \text{subject to} \quad & c_{k\ell}\big(\widehat{\mathbf{d}}_{i,j}\big) \geq \delta z_0 \end{aligned} \tag{7.29}$$

where $W(\widehat{\mathbf{d}}_{i,j}) = (\|\mathbf{F}_u\|^2 + \|\mathbf{F}_v\|^2)/\det[\mathbf{F}_u, \mathbf{F}_v]$ is referred to as the Winslow functional [31]. In (7.29), $z_0 > 0$ is computed by approximately solving (7.28) and $\delta \in [0, 1]$ is a fixed relaxation parameter.

In our numerical experiments we utilize the interior point algorithm constituting a part of Optimization Framework in Matlab [33] for solving the optimization problems (7.28) and (7.29) to approximate stationarity. Also, we set $\delta = 0$ in (7.29). The whole process is outlined in Fig. 7.7.

7.4.1.3 Linearized Winslow functional.

The algorithm for finding a valid domain parametrization described above has to be executed at every iteration of an "outer" shape optimization algorithm. Firstly, this process is rather computationally expensive, as it requires solving two non-linear programming problems at every shape optimization iteration. Secondly, as we solve the said optimization problems only approximately, it is not possible to find the derivatives of the inner control points with respect to changes of boundary control points. The latter does not allow us to use gradient based optimization algorithms for the "outer" shape optimization problem.

To avoid this difficulty, we linearize the process of computing a domain parametrization. Namely, we can Taylor-expand the Winslow functional as

$$\mathcal{W}(\widehat{\mathbf{d}}) = \iint_{\Omega} W(\widehat{\mathbf{d}})\,\mathrm{d}u\,\mathrm{d}v \approx \mathcal{W}(\widehat{\mathbf{d}}_0) + (\widehat{\mathbf{d}} - \widehat{\mathbf{d}}_0)^T\,\mathbf{G}(\widehat{\mathbf{d}}_0) + \frac{1}{2}(\widehat{\mathbf{d}} - \widehat{\mathbf{d}}_0)^T\,\mathbf{H}(\widehat{\mathbf{d}}_0)\,(\widehat{\mathbf{d}} - \widehat{\mathbf{d}}_0), \quad (7.30)$$

where $\widehat{\mathbf{d}}$ is a vector with all control points $\widehat{\mathbf{d}}_{i,j}$, $\widehat{\mathbf{d}}_0$ is the control points for a reference parametrization obtained by solving (7.29), and $\mathbf{G}$ and $\mathbf{H}$ are the gradient and Hessian of $\mathcal{W}$ respectively. If we split the control points $\widehat{\mathbf{d}} = (\widehat{\mathbf{d}}_1\,\widehat{\mathbf{d}}_2)^T$ into the part $\widehat{\mathbf{d}}_2$ that is given (typically the boundary control points) and the part $\widehat{\mathbf{d}}_1$ that has to be determined (typically the inner control points), then we can write (7.30) as

$$\begin{aligned}\mathcal{W}(\widehat{\mathbf{d}}) \approx \mathcal{W}(\widehat{\mathbf{d}}_0) &+ \begin{pmatrix}\widehat{\mathbf{d}}_1 - \widehat{\mathbf{d}}_{1,0} & \widehat{\mathbf{d}}_2 - \widehat{\mathbf{d}}_{2,0}\end{pmatrix}\begin{pmatrix}\mathbf{G}_1\\ \mathbf{G}_2\end{pmatrix}\\ &+ \frac{1}{2}\begin{pmatrix}\widehat{\mathbf{d}}_1 - \widehat{\mathbf{d}}_{1,0} & \widehat{\mathbf{d}}_2 - \widehat{\mathbf{d}}_{2,0}\end{pmatrix}\begin{pmatrix}\mathbf{H}_{11} & \mathbf{H}_{12}\\ \mathbf{H}_{21} & \mathbf{H}_{22}\end{pmatrix}\begin{pmatrix}\widehat{\mathbf{d}}_1 - \widehat{\mathbf{d}}_{1,0}\\ \widehat{\mathbf{d}}_2 - \widehat{\mathbf{d}}_{2,0}\end{pmatrix}. \quad (7.31)\end{aligned}$$

The minimum of the right hand side of (7.31) is obtained when $\widehat{\mathbf{d}}_1$ satisfies the *linear equation*

$$\mathbf{H}_{11}(\widehat{\mathbf{d}}_1 - \widehat{\mathbf{d}}_{1,0}) = -\mathbf{G}_1 - \mathbf{H}_{12}(\widehat{\mathbf{d}}_2 - \widehat{\mathbf{d}}_{2,0}). \quad (7.32)$$

This gives us a fast method for computing the domain parametrization and its derivatives with respect to the boundary control points. We use this method as long as we obtain a valid parametrization, but if the parametrization at some point fails the test described in Section 7.4.1.1 then we restart the "outer" shape optimization algorithm with a new reference parametrization $\widehat{\mathbf{d}}_0$ found by the method described in Section 7.4.1.2.

The given control points $\widehat{\mathbf{d}}_2$ can further be split into the set of fixed control points $\widehat{\mathbf{d}}_f$ and control points $\mathbf{R}\mathbf{d}$ obtained from the design variables (control points) $\mathbf{d}$ by knot insertion (refinement).

7.4.2 Shape optimization algorithm

Let us consider the following shape optimization problem using isogeometric analysis

$$\underset{\mathbf{d}\in\Omega_{\mathbf{d}}}{\text{minimize}} \quad f(\mathbf{d}) \quad (7.33)$$

where $\Omega_{\mathbf{d}} \subset \mathbb{R}^n$ is the space of design variables, and $\mathbf{d}$ are typically coordinates of boundary control points of spline patches. We solve the problem by the following iterative algorithm

- Start the algorithm with a guess $\mathbf{d}_0 \in \mathrm{int}(\Omega_{\mathbf{d}})$.
- Let $\mathbf{A}_{\mathbf{d}_0}$ and $\mathbf{B}_{\mathbf{d}_0}$ be the matrices of an affine mapping that represent a linear method of extending the parametrization from the boundary to the interior of the physical domain, i.e., it generates all control points $\widehat{\mathbf{d}}$ from $\mathbf{d}$ by the following relation

  $$\widehat{\mathbf{d}}(\mathbf{d}) = \mathbf{A}_{\mathbf{d}_0}\mathbf{d} + \mathbf{B}_{\mathbf{d}_0}, \quad \mathbf{d} \in \Omega_{\mathbf{d}}. \quad (7.34)$$

  Assume $\mathbf{A}_{\mathbf{d}_0}$ and $\mathbf{B}_{\mathbf{d}_0}$ satisfy the condition that $\widehat{\mathbf{d}}(\mathbf{d}_0) = \mathbf{A}_{\mathbf{d}_0}\mathbf{d}_0 + \mathbf{B}_{\mathbf{d}_0}$ corresponds to a valid parametrization. Thus with a sufficient subdivision of the Jacobian determinant surface, c.f. (7.22), its representing control points $c_{k,\ell}$ given by (7.23) are positive. For simplicity let us assume that without further refinement, the control points $c_{k,\ell}$ are positive. According to (7.27)

  $$c_{k,\ell}(\mathbf{d}) = (\mathbf{A}_{\mathbf{d}_0}\mathbf{d} + \mathbf{B}_{\mathbf{d}_0})^T\mathbf{Q}_{k,\ell}(\mathbf{A}_{\mathbf{d}_0}\mathbf{d} + \mathbf{B}_{\mathbf{d}_0}). \quad (7.35)$$

  The control points $c_{k,\ell}$ are obviously continuous functions of $\mathbf{d}$, thus there exists a neighborhood $B_{\mathbf{d}_0} \subset \Omega_{\mathbf{d}_0}$ of $\mathbf{d}_0$ such that

  $$c_{k,\ell}(\mathbf{d}) > 0 \quad \forall \mathbf{d} \in B_{\mathbf{d}_0},\ \forall k, \ell. \quad (7.36)$$

- We then would like to solve the following sub-optimization problem

$$\mathbf{d}_1 = \underset{\mathbf{d}\in B_{\mathbf{d}_0}}{\operatorname{argmin}} \quad f(\mathbf{d}), \tag{7.37}$$

where argmin denotes the argument of the minimum of a function. In practice, it is difficult to determine $B_{\mathbf{d}_0}$, especially the "maximal" one, i.e., the largest neighborhood satisfying (7.36). Instead, we find $\mathbf{d}_1$ as the solution to the following problem

$$\underset{\mathbf{d}\in\Omega_{\mathbf{d}}}{\text{minimize}} \quad f(\mathbf{d}), \tag{7.38a}$$

$$\text{such that} \quad c_{k,\ell}(\mathbf{d}) \geq \varepsilon, \tag{7.38b}$$

where ε is some positive constant. Note that the values and sensitivities of the constraints (7.38b) are very easy to compute using (7.35).

- Repeat the steps above by replacing $\mathbf{d}_0$ with $\mathbf{d}_1$, and stop when convergence.

Remark 12. We note that

(i) The linearized Winslow functional presented in Section 7.4.1.3 and the quasi-conformal deformation [30] are among the methods that fulfill the condition related to (7.34).

(ii) In J. Gravesen et al. [28], any parametrization of a 2D B-spline patch with a corner having angle more than π is invalid. Therefore, it is necessary to constrain the angles. Fortunately, they are already included in the constraints (7.38b) as those on the corner control points of the Jacobian determinant ensure the "validity" of the corresponding angles.

(iii) One problem of shape optimization using isogeometric analysis has been encountered in fluid mechanics is the clustering of control points [28]. This requires some special treatment [28]. Interestingly, without extra efforts the algorithm above avoids this issue. Indeed, since the the boundary control points of the Jacobian determinant are constrained to be positive, the boundary parametrization must be locally regular.

7.4.3 Multiple methods of extending parametrization from boundary to interior

For some problems, there are regions which can be parametrized in a simple and effective way. For such a case, it is not necessary to employ more complicated and expensive methods to extend the parametrization from the boundaries to the interiors of those regions. Thus in general we can have different linear parametrization extension methods for different regions. See Fig. 7.10 and Fig. 7.13 for illustrations of the argument.

For the sake of deriving sensitivity later on and implementation, let us formulate the general configuration. Let Ω be a connected domain. Assume that according to parametrization extension, Ω can be partitioned into N sub-domains Ω_k, $k = 1, \ldots, N$. Each sub-domains are comprised of several B-spline patches. Let $\mathbf{d}$ be the design variable vector and $\mathbf{d}_k$ be the control point vector of $\partial\Omega_k$. The first task for the algorithm is to determine affine maps that sending $\mathbf{d}$ to $\mathbf{d}_k$ as

$$\mathbf{d}_k = \mathbf{a}_k\mathbf{d} + \mathbf{b}_k. \tag{7.39}$$

The next task will be to derive affine transformations that map $\mathbf{d}_k$ to unknown inner control points of Ω_k, and therefore to the control point vector $\mathbf{d}_k$ of Ω_k

$$\widehat{\mathbf{d}}_k = \mathbf{A}_k\mathbf{d}_k + \mathbf{B}_k = \mathbf{A}_k\mathbf{a}_k\mathbf{d} + \mathbf{A}_k\mathbf{b}_k + \mathbf{B}_k. \tag{7.40}$$

Note that the refinement matrices [24] obtained when inserting knots into the boundary knot vectors to have parametrization knot vectors are already taken into account in $\mathbf{A}_k$. If for some sub-domain Ω_k, the parametrization extension method used in this domain is guaranteed to result in a valid parametrization then the constraints (7.38b) with respect to this domain should be removed to reduce computational time consume.

7.5 Discretization and sensitivity analysis

Formulation of the discretization using isogeometric analysis are first presented. The sensitivity analysis are then derived precisely.

7.5.1 Discretization

An approximation to the solution A_z to the boundary value problem given by (7.4), (7.6), (7.7) is expanded in terms of the basis functions (see Section 7.3.2) as

$$A_z = \sum_k h_k \, (\widetilde{R}_k^{\widetilde{p},\widetilde{q}} \circ \mathbf{F}^{-1}) = \big[\widetilde{R}_1^{\widetilde{p},\widetilde{q}} \circ \mathbf{F}^{-1}, \ldots, \widetilde{R}_{\widetilde{m}\widetilde{n}}^{\widetilde{p},\widetilde{q}} \circ \mathbf{F}^{-1}\big]\mathbf{h}, \tag{7.41}$$

where $\mathbf{h}$ contains all the coordinates of A_z with respect to the selected basis. Substituting this expression into the weak form (7.8) and utilizing the basis functions as the test functions, we arrive at the following set of linear algebraic equations:

$$\mathbf{K}\,\mathbf{h} = \mathbf{f}. \tag{7.42}$$

Entries of the matrices entering (7.42) are with the help of (7.12) calculated as:

$$\mathbf{K}_{k\ell} = \iint\limits_{[0,1]^2} \frac{1}{\mu} \left(\boldsymbol{\nabla} \widetilde{R}_k^{\widetilde{p},\widetilde{q}}(u,v)\, \mathbf{J}^{-1}\right)^T \boldsymbol{\nabla} \widetilde{R}_\ell^{\widetilde{p},\widetilde{q}}(u,v)\, \mathbf{J}^{-1}\, \det(\mathbf{J})\, \mathrm{d}u\, \mathrm{d}v, \tag{7.43a}$$

$$\mathbf{f}_\ell = M_0 \sum_{i=1}^{m} \left(\int_{\mathbf{F}^{-1}(a_i \times [c_i,d_i])} \widetilde{R}_\ell^{\widetilde{p},\widetilde{q}}\, \mathrm{d}s - \int_{\mathbf{F}^{-1}(b_i \times [c_i,d_i])} \widetilde{R}_\ell^{\widetilde{p},\widetilde{q}}\, \mathrm{d}s \right), \tag{7.43b}$$

$k, \ell = 1, \ldots, \widetilde{m}\widetilde{n}$. In (7.43), $\mathbf{J}$ denotes the Jacobian of the parametrization $\mathbf{F}$.

7.5.2 Sensitivity analysis

For convenience, let us first introduce the basis notations: $\mathbf{F}(u,v) = (x(u,v), y(u,v))$ and $\mathbf{F}^{-1}(x,y) = (u(x,y), v(x,y))$. Let us now formulate the objective function given by (7.10). Differentiation of (7.41) gives

$$\boldsymbol{\nabla} A_z = \big[\mathbf{J}^{-1}\, (\boldsymbol{\nabla} \widetilde{R}_1^{\widetilde{p},\widetilde{q}} \circ \mathbf{F}^{-1}), \ldots, \mathbf{J}^{-1}\, (\boldsymbol{\nabla} \widetilde{R}_{\widetilde{m}\widetilde{n}}^{\widetilde{p},\widetilde{q}} \circ \mathbf{F}^{-1})\big]\mathbf{h}. \tag{7.44}$$

Furthermore, note that by differentiating the identity $\mathbf{J}^{-1}\mathbf{J} = \mathbf{I}$, where $\mathbf{I}$ is the 2-by-2 identity matrix, we get

$$\frac{\partial}{\partial x}\mathbf{J}^{-1} = -\mathbf{J}^{-1}\big(\frac{\partial \mathbf{J}}{\partial u} u_x + \frac{\partial \mathbf{J}}{\partial v} v_x\big)\mathbf{J}^{-1}. \tag{7.45}$$

Thus again from differentiating (7.44) with respect to x, it follows

$$\frac{\partial}{\partial x}\boldsymbol{\nabla} A_z = \big[\mathbf{g}_1 \circ \mathbf{F}^{-1}, \ldots, \mathbf{g}_{\widetilde{m}\widetilde{n}} \circ \mathbf{F}^{-1}\big]\mathbf{h}, \tag{7.46}$$

where

$$\mathbf{g}_k = \frac{\mathbf{J}^{-1}}{\det(\mathbf{J})} \left(\mathbf{H}(\widetilde{R}_k^{\widetilde{p},\widetilde{q}}) \begin{bmatrix} y_v \\ -y_u \end{bmatrix} - \mathbf{J}^{-1}\big(\frac{\partial \mathbf{J}}{\partial u} y_v - \frac{\partial \mathbf{J}}{\partial v} y_u\big)\mathbf{J}^{-1} \boldsymbol{\nabla} \widetilde{R}_k^{\widetilde{p},\widetilde{q}} \right). \tag{7.47}$$

In (7.47), $\mathbf{H}(f)$ is the Hessian of a real-valued function $f : [0,1]^2 \mapsto \mathbb{R}$. The objective function now can be written as

$$I = 4 \iint\limits_{\mathbf{F}^{-1}(\Omega_0)} \left(\big[\mathbf{J}^{-1}\boldsymbol{\nabla} \widetilde{R}_1^{\widetilde{p},\widetilde{q}}, \ldots, \mathbf{J}^{-1}\boldsymbol{\nabla} \widetilde{R}_{\widetilde{m}\widetilde{n}}^{\widetilde{p},\widetilde{q}}\big]\mathbf{h} \cdot \big[\mathbf{g}_1, \ldots, \mathbf{g}_{\widetilde{m}\widetilde{n}}\big]\mathbf{h} \right)^2 \det(\mathbf{J})\, \mathrm{d}u\, \mathrm{d}v. \tag{7.48}$$

To facilitate sensitivity analysis, we keep the parametrization of Ω_0 fixed, i.e., independent from changes of design control points, see Fig. 7.11. Thus to calculate the sensitivity $\frac{\partial I}{\partial \hat{d}_i}$ of I, given by (7.48), with respect to a design control point coordinate $\hat{d}_i$, we only need to determine $\frac{\partial \mathbf{h}}{\partial \hat{d}_i}$. Differentiating both sides of (7.42) and utilizing the fact that $\frac{\partial \mathbf{f}}{\partial \hat{d}_i} = \mathbf{0}$, the partial derivative is in turn the solution to the following linear system

$$\mathbf{K}\frac{\partial \mathbf{h}}{\hat{d}_i} = -\frac{\partial \mathbf{K}}{\hat{d}_i}\mathbf{h}. \tag{7.49}$$

In (7.49), the partial derivatives of $\mathbf{K}$ are calculated straightforwardly by differentiating (7.43). Finally, as we employ linear parametrization methods formulated in (7.40), the desired sensitivities are

$$\frac{\partial I}{\partial \mathbf{d}} = \mathbf{a}_1^T\mathbf{A}_1^T\frac{\partial I}{\partial \widehat{\mathbf{d}}_1} + \ldots + \mathbf{a}_N^T\mathbf{A}_N^T\frac{\partial I}{\partial \widehat{\mathbf{d}}_N}. \tag{7.50}$$

7.6 Numerical experiments

It has been noted in [91] that complex geometries of the design iron components make it difficult to remove magnetic contaminants attracted to the device. We therefore only consider the ordinates of the control points of the iron poles as design variables. Furthermore, as a standard in engineering, we consider $\log_{10}(I)$ as the objective function for the shape optimization instead of I given by (7.10). The relative permeabilities of air and iron are 1 and 1000, respectively. The magnitude of the magnetization of the magnets is $M_0 = 10^6$ [A/m].

For the content of this section, we first test all numerical settings including the shape optimization algorithm presented in Section 7.4.2, the choice of the fixed domain for optimization and the choice of the objective function given by (7.10) in an example with known analytical solution. Then then perform shape optimization on different configurations.

7.6.1 A test problem

In this section we consider a simple shape optimization problem that inspired by D. Lahaye et al. [91]. For this, let us first look at the following harmonic function

$$u(x,y) = u_0\cos(\frac{\pi x}{\lambda})e^{\frac{-\pi y}{\lambda}}, \quad u_0 > 0, \lambda > 0. \tag{7.51}$$

The geometry that adapts the above function to its solution should be the optimum of the optimization problem (7.10) since

$$\frac{\partial}{\partial x}\|\mathbf{B}\| = \frac{\partial}{\partial x}\|(\frac{\partial u}{\partial y}, -\frac{\partial u}{\partial y}, 0)\| = \frac{\partial}{\partial x}\big(u_0\frac{\pi}{\lambda}e^{\frac{-\pi y}{\lambda}}\big) = 0. \tag{7.52}$$

Interestingly, the geometry can be derived analytically by observing that we can write the explicit formula for the level set of u with respect to a positive constant c, $u(x,y) = c$ as

$$y = \frac{\lambda}{\pi}\ln\cos(\frac{\pi x}{\lambda}) + \frac{\lambda}{\pi}\ln\frac{u_0}{c}, \quad -\frac{\lambda}{2} < -(\frac{\lambda}{2} - \varepsilon) \le x < \frac{\lambda}{2} - \varepsilon \le \frac{\lambda}{2}. \tag{7.53}$$

In (7.53), as x approaches $-\frac{\lambda}{2}$ or $\frac{\lambda}{2}$, y approaches $-\infty$, a positive constant ε is introduced to truncate the two singularities. That is, $u(x,y)$ given by (7.51) is the solution to the following Dirichlet boundary value problem on a domain D with boundary components Γ_b, Γ_r, Γ_t, and Γ_l as depicted in Fig. 7.8

$$\Delta u = 0 \qquad \text{in } D \tag{7.54a}$$

$$u = c \qquad \text{on } \Gamma_b \tag{7.54b}$$

$$u = u_0\cos(\frac{\pi x}{\lambda})e^{\frac{-\pi y}{\lambda}} \qquad \text{on } \Gamma_l, \Gamma_r, \text{ and } \Gamma_t \tag{7.54c}$$

if Γ_b is given by (7.53).

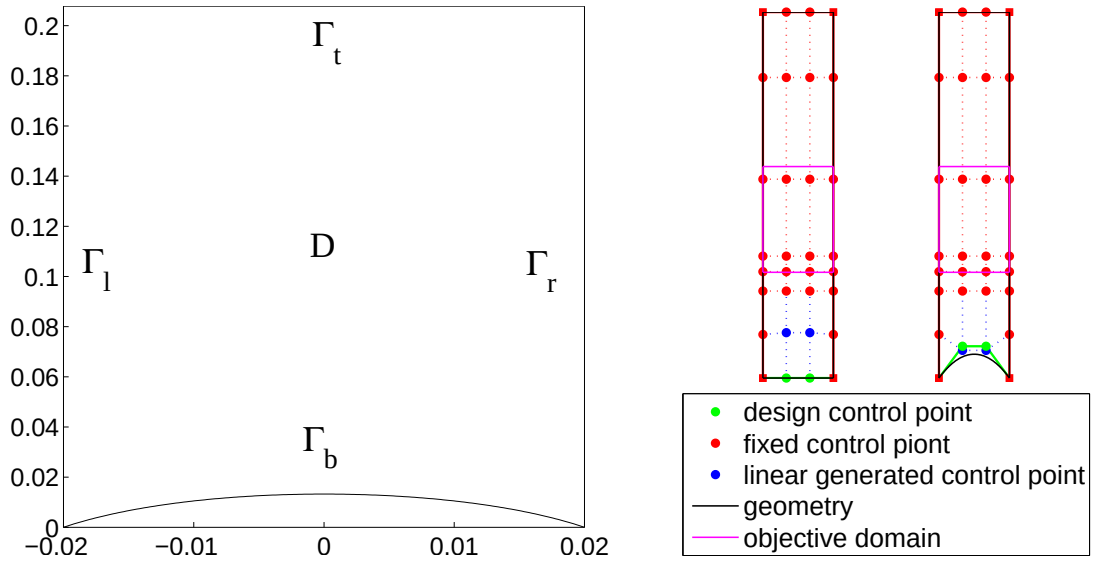

Figure 7.8: To the left, the computational domain for the equations (7.54). To the right the shape and control net of the initial and resulting models.

We will now investigate whether the shape defined by (7.53) can be rediscovered by shape optimization. To this end, we model the domain D by one cubic patch with knot vectors

$$\widehat{\Xi}_u = \widehat{\Xi}_v = \{0,0,0,0,\tfrac{1}{5},\tfrac{2}{5},\tfrac{3}{5},\tfrac{4}{5},1,1,1,1\}. \tag{7.55}$$

The ordinates of the inner control points with respect the boundary Γ_b are design variables, see Fig. 7.8(right). For the ordinates of the inner unknown control points (the blue points in Fig. 7.8(right)), they are generated using the linearized Winslow function method presented in Section 7.4.1.3. The objective domain is the images via the parametrization of the knot span $[\frac{2}{5},\frac{4}{5}]\times[0,1]$. To enforce the domain to be $[-0.02,0.02]\times[0.06,0.12]$ we employ the approach discussed in Section 7.3.3 with the predefined knot image vector $\{0,0.045,0.06,0.075,0.12,0.2078\}$. The optimization converges in 18 iterations and results in the shape depicted in Fig. 7.8(right). The objective function reduces from -4.41631 to -8.5188, and $\|\mathbf{B}\|$ of the optimum indeed behaves very well, c.f. Fig. 7.9(left). The resulting shape also looks similar to the analytical one, c.f. Fig. 7.9(right). However, there is still a remarkable discrepancy between them (the red and green curves). This can be well understood by calculating the L^2-projection of the analytical shape onto the space of the B-splines used for design control points. Having the calculation, it can be observed from Fig. 7.9(right) that the resulting shape has indeed nearly reached the best L^2-approximation of the analytical shape. This demonstrates the success of the shape optimization algorithm presented in Section 7.4.2, and the appropriation of the choices of the objective functions (7.10) and the objective domain described in this section.

7.6.2 Main results

7.6.2.1 Magnetic density separator: A first configuration

We now consider the magnetic density separator suggested by D. Lahaye et al. [91], see Fig. 7.2 and Fig. 7.10(left). Let us first discuss the isogeometric analysis design for this configuration. To discretize the computational domain, we use 35 cubic patches, c.f. Fig. 7.10(right). For the objective domain Ω_0, we choose it to be $[0,b]\times[0.06,0.11]$ [m $\times$ m], $b>0$. While the horizontal interval $[0,b]$ [m] is simply chosen according to the extremities of involved

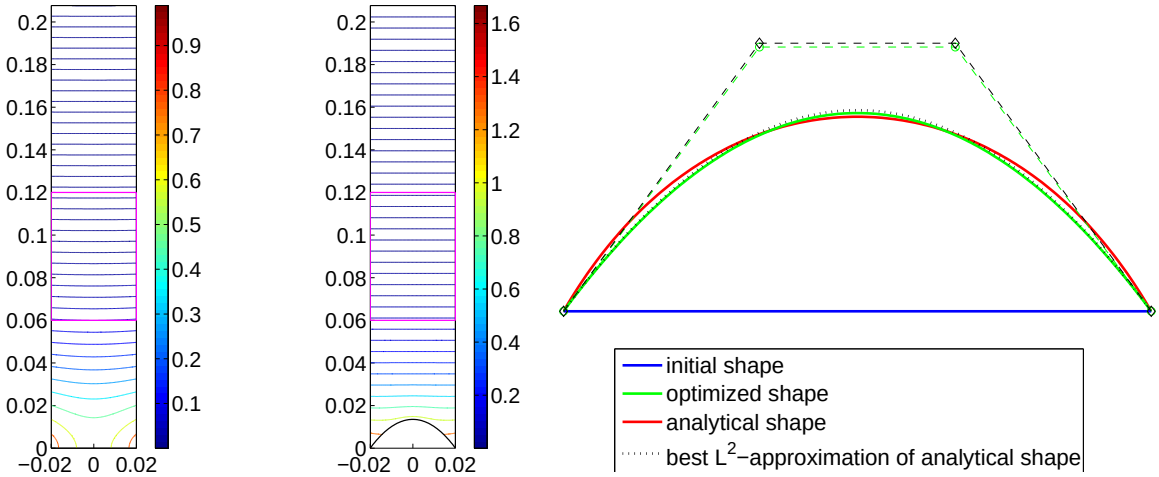

Figure 7.9: To the left, the contour lines of $\|\mathbf{B}\| = u_0 \frac{\pi}{\lambda} e^{\frac{-\pi y}{\lambda}}$, $\lambda = 0.06$, $\varepsilon = 0.01$, $c = \lambda/\pi$, with respect to the initial shape and resulting shape in Fig. 7.8; as $\|\mathbf{B}\|$ decays exponentially, the contour lines are chosen in accordance with an exponential scale too. To the right comparison of various shapes of the bottom boundary of the domain D, c.f. Fig. 7.8; the black dashed line is the L^2-projection of the analytical shape on the space of B-splines used for modeling the optimized shape.

patches, c.f. Fig. 7.11, the vertical interval $[0.06, 0.11]$ [m] is enforced in accordance with Section 7.3.3 using the vertical parametrization of patch 1 with the predefined knot images $\{0.0416, 0.05, 0.06, 0.075, 0.11, 0.2078\}$ [m].

Naturally, we first choose the objective domain Ω_0 to be the one that, in horizontal direction, exactly covers the space above the iron and magnet poles, see Fig. 7.11. The optimization stops after 33 iterations and results in a model depicted in Fig. 7.11. The behavior of the contour lines of $\|\mathbf{B}\|$ placed at the bottom of Fig. 7.11 shows the clear improvement of the resulting model. Though, there is yet remarkable variation in the horizontal direction of $\|\mathbf{B}\|$ in the right end of Ω_0. In practice, this issue has been noted and solved by reducing the width of the considered region above the device [98]. Thus it is worth investigating whether performing shape optimization for such a situation can improve the quality of the remaining region.

To this end, we repeat the experiment with different smaller objective domains. The resulting models with respect to these changes, depicted in Fig. 7.12, show that neglecting the spaces at the two ends indeed leads to more satisfactory designs.

7.6.2.2 Magnetic density separator: A second configuration

As we can observe from Fig. 7.11 and Fig. 7.12 that for the last separator even with different geometries, there always exists a minimum of $\|\mathbf{B}\|$ in the region above the devices. Such kind of points is obviously not expected. Fortunately, this phenomenon seems to be avoided if we interchange the order of the magnet and iron poles. The precise description of this configuration is presented in Fig. 7.13(left). Indeed, having simulated the mentioned configuration using the same patch layout as in the last section, the above observation can be recognized in Fig. 7.14(right). Furthermore, keeping in mind that for 2D problems, the distance with respect to normal direction between contour lines of A_z reflects the strength of the magnetic flux density, the better uniformity of the equipotential lines of the new configuration in Fig. 7.14 also shows clear improvement compared to the last separator.

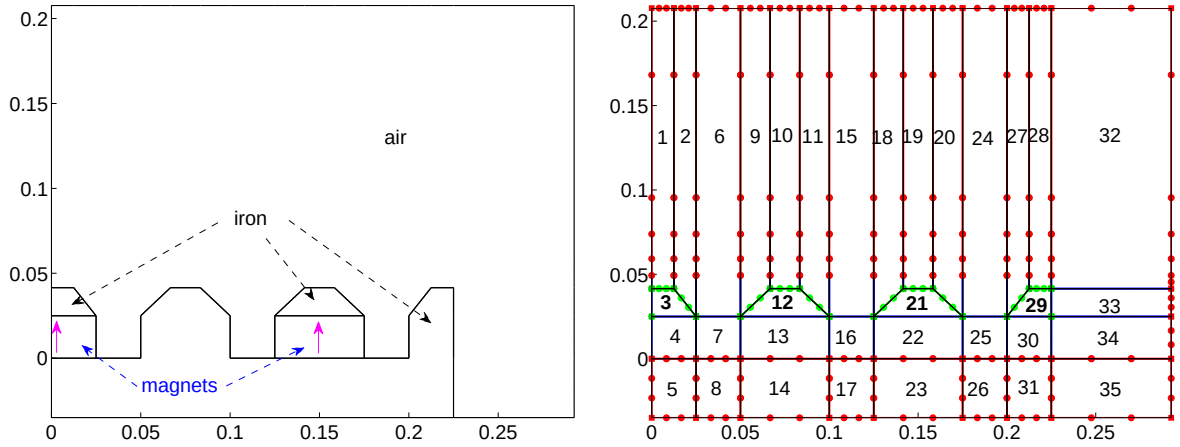

Figure 7.10: To the left the physical configuration of a magnetic density separator; the solid arrows represent the directions of magnetizations of the corresponding magnets. To the right its isogeometric analysis-based modeling with 35 B-spline patches. Note that the plots above represent the right half of the full symmetric model about the line $x = 0$. In connection to Section 7.4.3, this computational domain is partitioned into 35 sub-domains with respect to each patch. The parametrization extension method used for the patches **3**, **12**, **21** and **29** below the optimized curves is the linearized Winslow functional, c.f. Section 7.4.1.3, whereas that of the remaining patches is the simple uniformly and vertically linear scaling of boundary control points (in green and red) in the vertical direction. See Fig. 7.11 for the resulting inner control points.

Let us now perform shape optimization on the second configuration. To have better regularization for parametrization, we reconstruct the patch layout into a discretization using 30 patches, c.f. Fig. 7.13(right). We also utilize the observation from the last section that neglecting a relatively small spatial region at the boundary of the device to enhance the remaining area. The optimization finishes after 92 iterations and results in a more satisfactory model depicted in Fig. 7.15, according to the table 7.1.

7.6.3 Comparison with a reference design

We now compare the resulting designs with an analytical design by D. Lahaye et al. [91] by looking at $\|\mathbf{B}\|$ at three horizontal lines $y = 5.5$ [cm], $y = 6.5$ [cm], and $y = 8.5$ [cm]. For also the purpose of validating the current implementing code, we use COMSOL [86] to calculate the comparison. The comparison is depicted in Fig. 7.16 and shows that any of the new designs are better than the reference design.

7.7 Conclusions

We have used isogeometric analysis-based shape optimization for improving the uniformity of the magnitude of magnetic flux density in a region of space above a magnetic density separator by optimizing the shapes of iron components of the separator. In addition, we have also examined an iterative algorithm that enforces the validity of the domain parametrizations, thus also the regularity of the parametrizations of the domain boundaries, during the optimization iterations. For future work, local refinement should be used to save computational efficiency

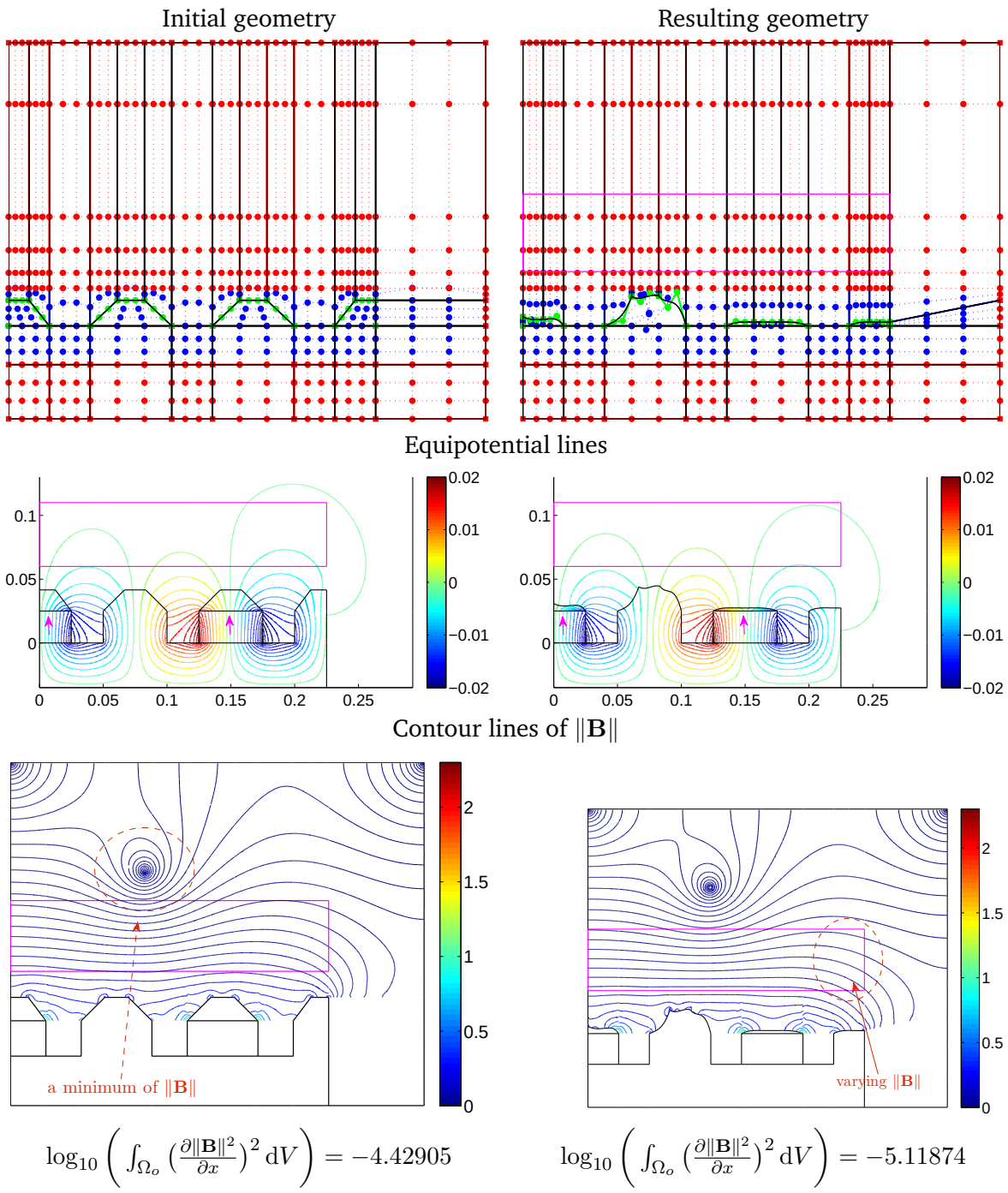

Figure 7.11: To the left, the initial model of the magnetic density separator described in Fig. 7.10, and to the right, the resulting model. The domain enclosed by the magenta curve is the objective domain Ω_0. In the present experiment, $\Omega_0 = [0, 0.225] \times [0.06, 0.11]$ [m × m]. To facilitate sensitivity analysis, the control points related to the parametrization of Ω_0 are kept fixed. In this picture, they are the *red* points of the patches 1, 2, 6, 9, 10, 11, 15, 18, 19, 20, 24, 27, 28, 32. The magenta arrows show the presence of magnets.

by setting up a coarser mesh for the region in air outside the objective domain above the mag-

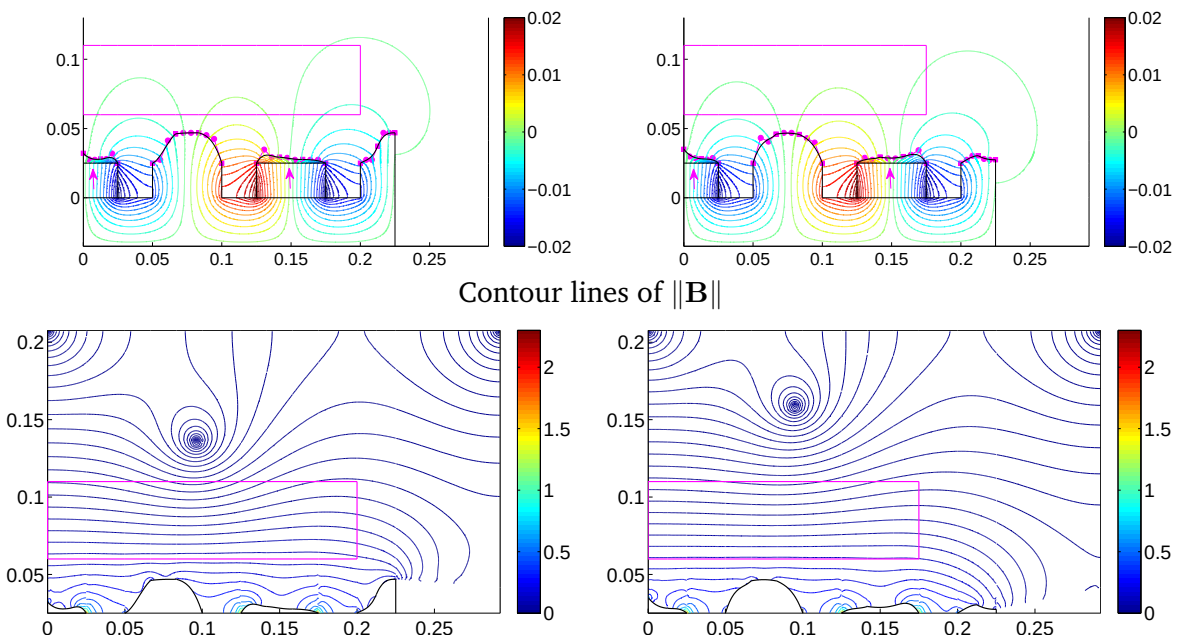

Figure 7.12: Resulting models using a similar shape optimization design as the one in Fig. 7.11 except with smaller objective domains. To the left, the result relates to the objective domain $\Omega_0 = [0, 0.2] \times [0.06, 0.11]$ [m $\times$ m], and to the right the result relates to the objective domain $\Omega_0 = [0, 0.175] \times [0.06, 0.11]$ [m $\times$ m].

netic density separator under consideration. Experiments on the obtained models will hopefully confirm the results so they can be used for industrial applications.

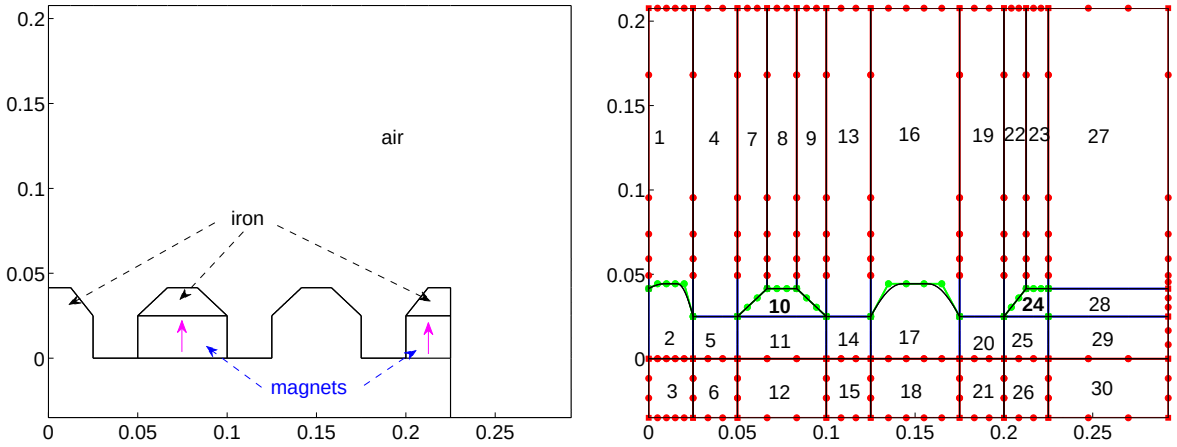

Figure 7.13: To the left, another physical configuration of a magnetic density separator; compared to the one in Fig. 7.10, the order of iron poles and magnet poles has been interchanged. To the right, the 30 B-spline patch model of the separator on the left. Similar to the last separator, the physical domain is subdivided into 30 sub-domains with respect to each patch. The bottom boundaries of the patches 4, 13, 19 and the top ones of the patches 5, 14, 20 are generated by a linear scaling of the corresponding design control points (in green). For deriving sensitivities, the scaling should be formulated as in (7.39). Only patch **10** and patch **24** below the optimized curves use the linearized Winslow functional to extend parametrization from boundary to interior, the rest uses the simple uniformly and vertically linear scaling of boundary control points (in green and red).

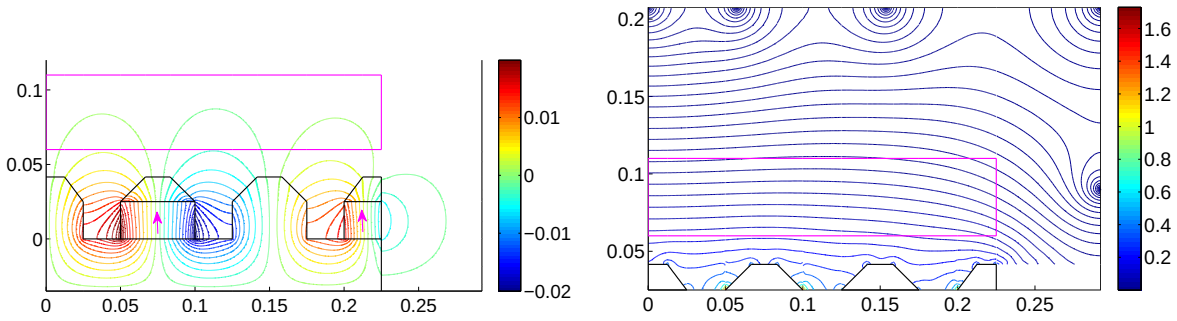

Figure 7.14: Simulation of the second configuration for a magnetic density separator described in Fig. 7.13(left).

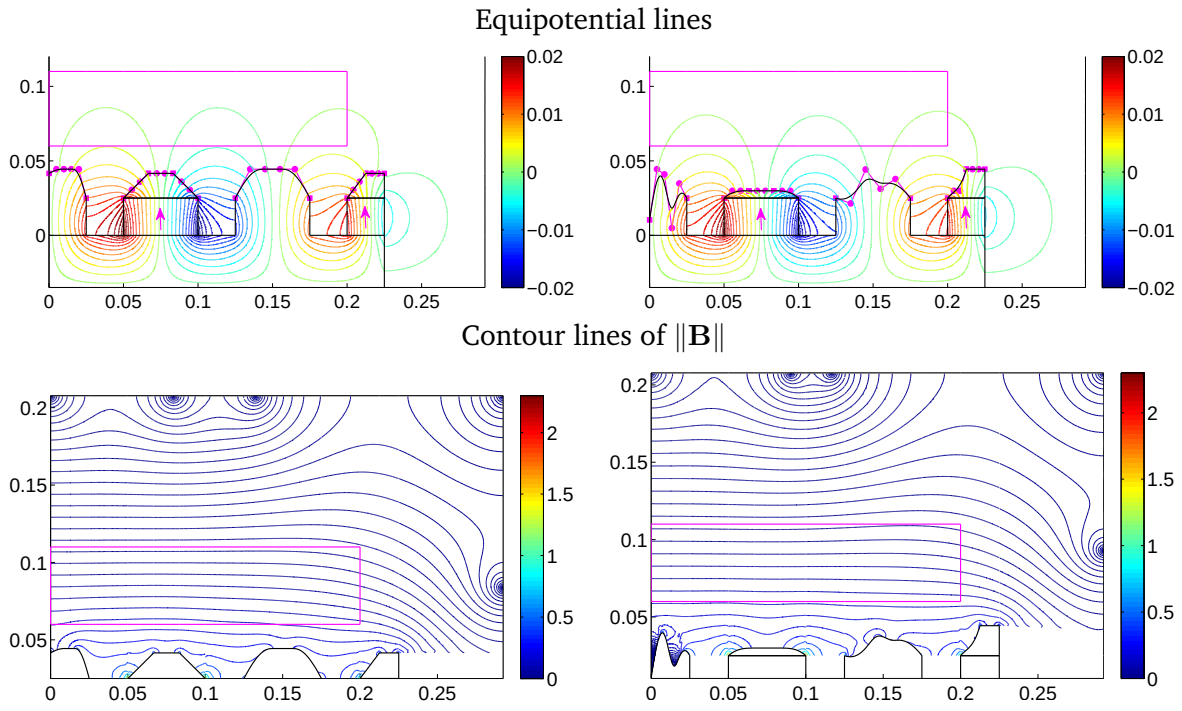

Figure 7.15: Designs of magnetic density separators using the configuration in Fig. 7.13. To the left the initial design and to the right the optimized. The objective domain of the optimization is $\Omega_0 = [0, 0.2] \times [0.06, 0.11]$ [m $\times$ m].

Model	# iteration	$\log_{10}\left(\iint_{[0,0.2]\times[0.06,0.11]} \left(\frac{\partial\|\mathbf{B}\|^2}{\partial x}\right)^2 \mathrm{d}x\mathrm{d}y\right)$
in Fig. 7.11/left	–	-4.6888
in Fig. 7.11/right	31	-5.4329
in Fig. 7.12/left	46	-5.5967
in Fig. 7.12/right	38	-5.3242
in Fig. 7.14	–	-5.2394
in Fig. 7.15/left	–	-5.1193
in Fig. 7.15/right	95	-6.3482

Table 7.1: Quantitative comparison of various designs of magnetic density separators. This is done by evaluating the objective function (7.10) over a common domain $\Omega_0 = [0, 0.2] \times [0.06, 0.11]$ [m $\times$ m].

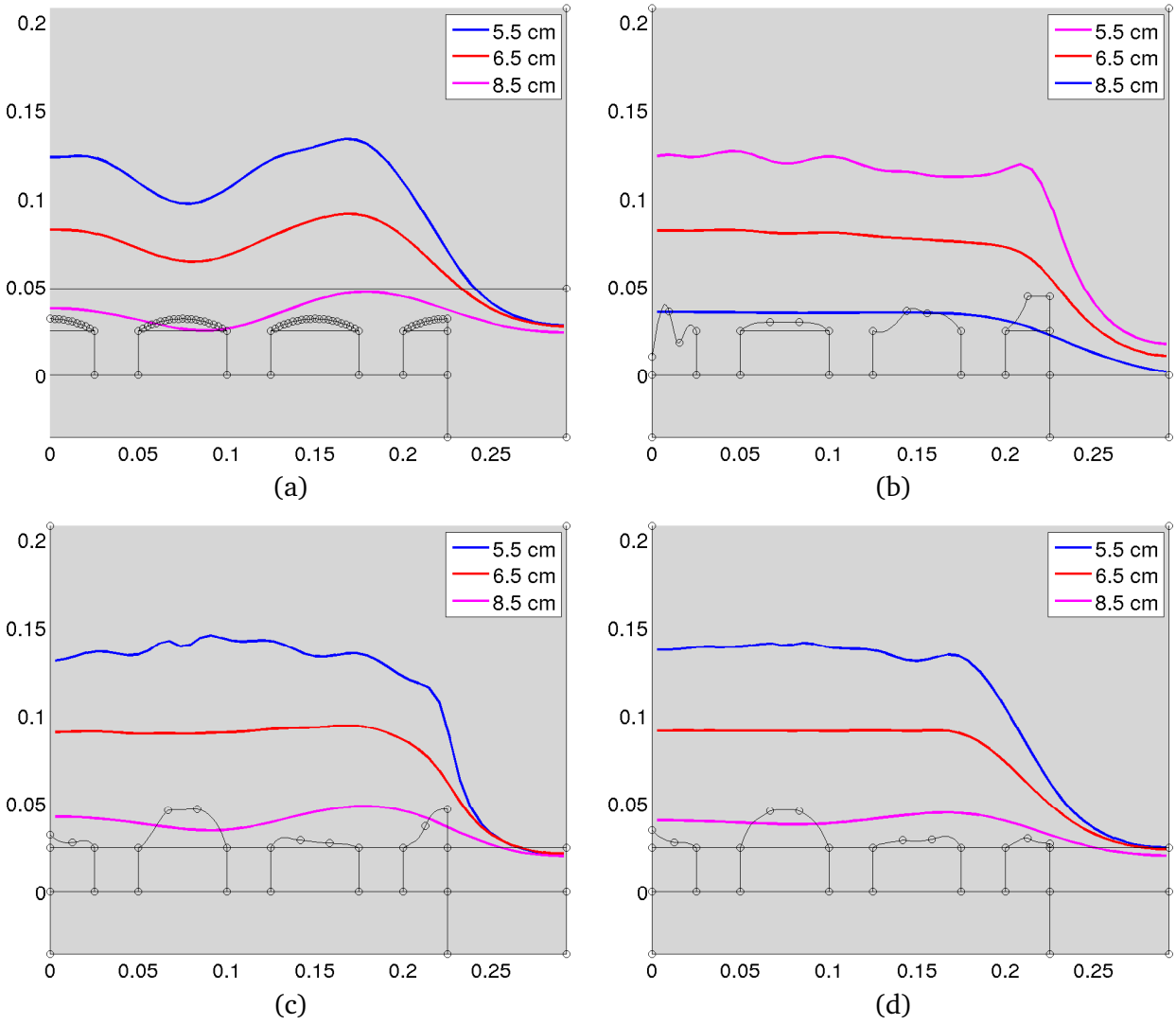

Figure 7.16: The magnitude of the magnetic flux density $\|\mathbf{B}\|$ at three horizontal lines $y = 5.5$ [cm], $y = 6.5$ [cm], and $y = 8.5$ [cm] for various designs of magnetic density separators. (a): Reference design D. Lahaye et al. [91]. (b): The design in 7.13(right). (c): The design in 7.12(left). (d): The design in 7.12(right). The pictures are by courtesy of Domenico Lahaye.

Conclusions and future work

In this thesis, we have investigated the utilization of isogeometric analysis for shape optimization for several two dimensional electromagnetic problems. Within the problems, we have observed that, when unphysical restrictions on the variation of the shape under consideration are avoided as much as possible, a resulting design often outperforms an existing design. Thus they are worth considering for real engineering applications. Inspired by this observation:

- The resulting *nano-antennas* presented in Chapter 6 are being built and experimented. This is done by Sergey I. Bozhevolnyi, Morten Willatzen and their research group at University of Southern Denmark.
- The resulting *magnetic density separators* presented in Chapter 7 are potentially built and experimentally measured by Domenico Lahaye and his research group at Delft University of Technology.

Further potential future work are

1. *Utilization of a local refinement method*: It is important in many parts of the work presented in this thesis to call in the utilization of a local refinement method. First, in the minimization problem of the Winslow functional presented in Fig. 2.1, each time there is a need to refine a knot interval tensor product $[u_i, u_{i+1}] \times [v_j, v_{j+1}]$, the present code will insert a new knot to each dimension and the insertion will effect all other knot interval. Thus a local refinement method would certainly improve the computational efficiency of the code. Moreover, for the design problem of antennas discussed in Part III, in particular, when the size of the antennas are equivalent to several wavelength, it is very computational beneficial or even necessary to use a local refinement along the interfaces of the antennas to capture the skindepth. Also in the space where the magnetic energy is concentrated. Finally, for the design of magnetic density separators described in Part IV, a local refinement is also important to save computational efficiency for a relatively large air region above the objective domain.

2. *Three-dimensional shape optimization of nano-antennas for field enhancement*: It has been pointed out in Fig. 6.10 that the 2D assumption for the design problem of nano-antennas presented in Chapter 6 is insufficient for designing realistic 3D nano-antennas. Due to the importance of such nano-antennas in nano-applications [81], it is very meaningful for investigating shape optimization of 3D nano-antennas. It may suffice to consider a cylindrical antenna and perform shape optimization on its 2D cross-section while solving the numerical solution in 3D. Again, as the size of the antenna may be equivalent to several wavelengths, a local refinement method is very important to save computational efficiency when dealing with 3D analysis.

3. *Utilization of the manifold mapping method [99, 100, 101]*: In the shape optimization problem of antennas in Part III, we have observed that the optimal shape with respect to a mesh and that with respect to a finer mesh are remarkably different, c.f. Fig. 5.14. Especially, an analysis with very fine mesh and basis functions of high order is required to gain sufficient

accuracy for the numerical solution with respect to an optimal shape, c.f. Fig. 6.8. Thus it is too computational expensive to use such an analysis to calculate numerical values in a complete optimization process. Meanwhile, the manifold mapping method is capable of finding the optimum with respect to a finer mesh while mostly using the computational effort in evaluating numerical values with respect to a coarser mesh. Therefore, the utilization of the manifold method, also with possibly a combination with a local refinement method, for the shape optimization problem of antennas is worth investigating.

References

[1] T.J.R. Hughes, J.A. Cottrell, and Y. Bazilevs. Isogeometric analysis: CAD, finite elements, NURBS, exact geometry and mesh refinement. *Comput. Methods Appl. Mech. Engrg.*, 194(39-41):4135–4195, 2005.

[2] O.C. Zienkiewicz and R.L. Taylor. *The finite element method. Vol. 1. The basis*. Butterworth-Heinemann, Oxford, fifth edition, 2000.

[3] J.A. Cottrell, A. Reali, Y. Bazilevs, and T.J.R. Hughes. Isogeometric analysis of structural vibrations. *Comput. Methods Appl. Mech. Engrg.*, 195(41-43):5257–5296, 2006.

[4] Y. Bazilevs, L. Beirão da Veiga, J.A. Cottrell, T.J.R. Hughes, and G. Sangalli. Isogeometric analysis: approximation, stability and error estimates for h-refined meshes. *Math. Models Methods Appl. Sci.*, 16(7):1031–1090, 2006.

[5] T.J.R. Hughes, A. Reali, and G. Sangalli. Duality and unified analysis of discrete approximations in structural dynamics and wave propagation: comparison of p-method finite elements with k-method NURBS. *Comput. Methods Appl. Mech. Engrg.*, 197(49-50):4104–4124, 2008.

[6] T.J.R. Hughes, J.A. Cottrell, and Y. Bazilevs. Isogeometric analysis: CAD, finite elements, NURBS, exact geometry and mesh refinement. *Comput. Methods Appl. Mech. Engrg.*, 194(39-41):4135–4195, 2005.

[7] Yuri Bazilevs J.A. Cottrell, T.J.R. Hughes. *Isogeometric Analysis: Toward Integration of CAD and FEA*. J. Wiley., West Sussex, 2009.

[8] Les Piegl and Wayne Tiller. *The $NURBS$ book*. Monographs in Visual Communication. Berlin: Springer-Verlag. xiv, 646 p. DM 129.00; öS 941.70; sFr 124.00 , 1995.

[9] D.M. Nguyen, A. Evgrafov, A.R. Gersborg, and J. Gravesen. Isogeometric shape optimization of vibrating membranes. *Computer Methods in Applied Mechanics and Engineering*, 200(13-16):1343 – 1353, 2011.

[10] D.M. Nguyen, A. Evgrafov, and J. Gravesen. Shape optimization of sub-wavelength antennas using isogeometric analysis. *International Journal for numerical methods in engineering*, submitted, 2011.

[11] W.A. Wall, M.A. Frenzel, and C. Cyron. Isogeometric structural shape optimization. *Comput. Methods Appl. Mech. Engrg.*, 197(33-40):2976–2988, 2008.

[12] Seonho Cho and Seung-Hyun Ha. Isogeometric shape design optimization: exact geometry and enhanced sensitivity. *Struct. Multidiscip. Optim.*, 38(1):53–70, 2009.

[13] Xiaoping Qian. Full analytical sensitivities in nurbs based isogeometric shape optimization. *Computer Methods in Applied Mechanics and Engineering*, 199(29-32):2059 – 2071, 2010.

[14] A.P. Nagy, M.M. Abdalla, and Z. Gurdal. Isogeometric sizing and shape optimisation of beam structures. *Comput. Methods Appl. Mech. Engrg.*, 199(17-20):1216–1230, 2010.

[15] Attila P. Nagy, Mostafa M. Abdalla, and Zafer Gurdal. Isogeometric design of elastic arches for maximum fundamental frequency. *Structural and Multidisciplinary Optimization*, 43(1):135–149, 2011.

[16] Xiaoping Qian and Ole Sigmund. Isogeometric shape optimization of photonic crystals via Coons patches. *Computer Methods in Applied Mechanics and Engineering*, 200(25-28):2237–2255, 2011.

[17] Y. Ding. Shape optimization of structures: a literature survey. *Computers & Structures*, 24(6):985 – 1004, 1986.

[18] Seonho Cho and Seung-Hyun Ha. Isogeometric shape design optimization: exact geometry and enhanced sensitivity. *Struct. Multidiscip. Optim.*, 38(1):53–70, 2009.

[19] N.L. Pedersen. Optimization of holes in plates for control of eigenfrequencies. *Struct. Multidiscip. Optim.*, 28(1):1–10, AUG 2004.

[20] N.L. Pedersen. On simultaneous shape and orientational design for eigenfrequency optimization. *Struct. Multidiscip. Optim.*, 33(4-5):387–399, APR 2007.

[21] V. Braibant and C. Fleury. Shape optimal design using B-splines. *Comput. Methods Appl. Mech. Engrg.*, 44(3):247 – 267, 1984.

[22] Jens Gravesen. *Differential Geometry and Design of Shape and Motion*. Department of Mathematics, Technical University of Denmark, 2002.

[23] Hartmut Prautzsch, Wolfgang Boehm, and Marco Paluszny. *Bézier and B-spline techniques*. Mathematics and Visualization. Springer-Verlag, Berlin, 2002.

[24] Les Piegl and Wayne Tiller. *The $NURBS$ book*. Monographs in Visual Communication. Berlin: Springer-Verlag. xiv, 646 p. DM 129.00; öS 941.70; sFr 124.00 , 1995.

[25] Milton Abramowitz and Irene A. Stegun. *Handbook of Mathematical Functions with Formulas, Graphs, and Mathematical Tables*. Dover, New York, 1964.

[26] R.A. Adams. *Sobolev spaces. Pure and Applied Mathematics, Vol. 65*. Academic Press, New York-London, 1975.

[27] R. D. Cook, D. S. Malkus, M. E. Plesha, and R. J. Witt. *Concepts and applications of finite element analysis*. John Wiley and Sons. Inc., fourth edition, 2002.

[28] J. Gravesen, A. Evgrafov, A.R. Gersborg, D.M. Nguyen, and P.N. Nielsen. Isogeometric analysis and shape optimisation. *Proceedings of NSCM-23: the 23rd Nordic Seminar on Computational Mechanics*, 23:14–17, 2010.

[29] J. Gravesen, A. Evgrafov, and D. M. Nguyen. Parametrisation in 2-dimensional isogeometric analysis. *in preparation*.

[30] D.M. Nguyen, A. Evgrafov, A.R. Gersborg, and J. Gravesen. Isogeometric shape optimization of vibrating membranes. *Computer Methods in Applied Mechanics and Engineering*, 200(13-16):1343 – 1353, 2011.

[31] P. Knupp and S. Steinberg. *Fundamentals of Grid Generation*. CRC Press, Boca Ranton, 1993.

[32] L.V. Ahlfors. *Complex analysis. An introduction to the theory of analytic functions of one complex variable, International Series in Pure and Applied Mathematics*. McGraw-Hill Book Co., New York, third edition, 1978.

[33] MathWorks Inc.

[34] M.C. Delfour and J.P. Zolésio. *Shapes and geometries. Analysis, differential calculus, and optimization*, volume 4 of *Advances in Design and Control*. Society for Industrial and Applied Mathematics (SIAM), Philadelphia, PA, 2001.

[35] B. Mohammadi and O. Pironneau. *Applied Shape Optimization for Fluids*. Oxford University Press, 2001.

[36] Grégoire Allaire. *Shape optimization by the homogenization method*, volume 146 of *Applied Mathematical Sciences*. Springer-Verlag, New York, 2002.

[37] M.P. Bendsøe and O. Sigmund. *Topology optimization. Theory, methods and applications*. Springer-Verlag, Berlin, 2003.

[38] J.A. Sethian. *Level Set Methods and Fast Marching Methods : Evolving Interfaces in Computational Geometry, Fluid Mechanics, Computer Vision, and Materials Science*. Cambridge University Press, 1999.

[39] J.A. Cottrell, A. Reali, Y. Bazilevs, and T.J.R. Hughes. Isogeometric analysis of structural vibrations. *Comput. Methods Appl. Mech. Engrg.*, 195(41-43):5257–5296, 2006.

[40] Y. Bazilevs, L. Beirão da Veiga, J.A. Cottrell, T.J.R. Hughes, and G. Sangalli. Isogeometric analysis: approximation, stability and error estimates for h-refined meshes. *Math. Models Methods Appl. Sci.*, 16(7):1031–1090, 2006.

[41] T.J.R. Hughes, A. Reali, and G. Sangalli. Duality and unified analysis of discrete approximations in structural dynamics and wave propagation: comparison of p-method finite elements with k-method NURBS. *Comput. Methods Appl. Mech. Engrg.*, 197(49-50):4104–4124, 2008.

[42] A.P. Nagy, M.M. Abdalla, and Z. Gurdal. Isogeometric sizing and shape optimisation of beam structures. *Comput. Methods Appl. Mech. Engrg.*, 199(17-20):1216–1230, 2010.

[43] Antoine Henrot. Minimization problems for eigenvalues of the Laplacian. *J. Evol. Equ.*, 3(3):443–461, 2003.

[44] Zakaria Belhachmi, Dorin Bucur, Giuseppe Buttazzo, and Jean-Marc Sac-Epée. Shape optimization problems for eigenvalues of elliptic operators. *ZAMM Z. Angew. Math. Mech.*, 86(3):171–184, 2006.

[45] Zhixue Wu. Optimal hole shape for minimum stress concentration using parameterized geometry models. *Struct. Multidiscip. Optim.*, 37(6):625–634, FEB 2009.

[46] J.W. Hutchinson and F.I. Niordson. Designing vibrating membranes. In *Continuum mechanics and related problems of analysis (Russian)*, pages 581–590. Izdat. "Nauka", Moscow, 1972.

[47] S.A. Wolf and J.B. Keller. Range of the first two eigenvalues of the laplacian. *Proceedings: Mathematical and Physical Sciences*, 447(1930):397–412, 1994.

[48] Dorin Bucur. Do optimal shapes exist? *Milan J. Math.*, 75:379–398, 2007.

[49] Couro Kane and Marc Schoenauer. A drum shape optimisation by genetic algorithms. *Complexity International*, 2, 1995.

[50] L.E. Kinsler, A.R. Frey, A.B. Coppens, and J.V. Sanders. *Fundamentals of Acoustics*. John Wiley & Sons, Singapore, 1982.

[51] D.R. Lapp. *The Physics of Music and Musical Instruments*. Wright Center for Innovative Science Education, Tufts University, Medford, Massachusetts, 2003.

[52] C. de Boor and G.J. Fix. Spline approximation by quasiinterpolants. *J. Approximation Theory*, 8:19–45, 1973.

[53] C. Gordon, D.L. Webb, and S. Wolpert. One cannot hear the shape of a drum. *Bull. Amer. Math. Soc. (N.S.)*, 27(1):134–138, 1992.

[54] Jens Gravesen, Anton Evgrafov, and Nguyen Dang Manh. On the sensitivities of multiple eigenvalues. *Structural and Multidisciplinary Optimization*, 44(4):583–587, 2011.

[55] A.P. Seyranian, E. Lund, and N. Olhoff. Multiple eigenvalues in structural optimization problems. *Structural Optimization*, 8:207–227, 1994.

[56] N.L. Pedersen and A.K. Nielsen. Optimization of practical trusses with constraints on eigenfrequencies, displacements, stresses, and buckling. *Struct. Multidiscip. Optim.*, 25(5-6):436–445, DEC 2003.

[57] J.S. Jensen and N.L. Pedersen. On maximal eigenfrequency separation in two-material structures: the 1D and 2D scalar cases. *J. of Sound and Vibration*, 289(4-5):967–986, FEB 7 2006.

[58] Jianbin Du and Niels Olhoff. Topological design of freely vibrating continuum structures for maximum values of simple and multiple eigenfrequencies and frequency gaps. *Struct. Multidiscip. Optim.*, 34(2):91–110, AUG 2007.

[59] A. Buffa, G. Sangalli, and R. Vazquez. Isogeometric analysis in electromagnetics: B-splines approximation. *Comput. Methods Appl. Mech. Engrg.*, 199(17-20):1143–1152, 2010.

[60] M.P. Bendsøe and O. Sigmund. *Topology optimization. Theory, methods and applications*. Springer-Verlag, Berlin, 2003.

[61] Tosio Kato. *Perturbation for Linear Operators*. Springer, Germany, 1995.

[62] F. van Keulen, R.T. Haftka, and N.H. Kim. Review of options for structural design sensitivity analysis. part 1: Linear systems. *Computer Methods in Applied Mechanics and Engineering*, 194:3213–3243, 2005.

[63] A.P. Seyranian, E. Lund, and N. Olhoff. Multiple eigenvalues in structural optimization problems. *Structural Optimization*, 8:207–227, 1994.

[64] Andre Kurs, Aristeidis Karalis, Robert Moffatt, J. D. Joannopoulos, Peter Fisher, and Marin Soljačić. Wireless power transfer via strongly coupled magnetic resonances. *Science*, 317(5834):83–86, 2007.

[65] Aristeidis Karalis, J. D. Joannopoulos, and Marin Soljacic. Efficient wireless non-radiative mid-range energy transfer. *Annals of Physics*, 323(1):34–48, 2008.

[66] Witricity corp.

[67] Bombardier corp.

[68] Leixiang Bian, Yumei Wen, Ping Li, Qiuling Gao, and Min Zheng. Magnetoelectric transducer with high quality factor for wireless power receiving. *Sensors and Actuators A: Physical*, 150(2):207 – 211, 2009.

[69] B.L. Cannon, J.F. Hoburg, D.D. Stancil, and S.C. Goldstein. Magnetic resonant coupling as a potential means for wireless power transfer to multiple small receivers. *Power Electronics, IEEE Transactions on*, 24(7):1819 –1825, july 2009.

[70] J. Choi and C. Seo. High-efficiency wireless energy transmission using magnetic resonance based on metamaterial with relative permeability equal to -1. *Progress in electromagnetics research-pier*, 106:33–47, 2010.

[71] N. Aage, N.A. Mortensen, and O. Sigmund. Topology optimization of metallic devices for microwave applications. *International Journal for numerical methods in engineering*, 83(2):228–248, 2010.

[72] L. Peng, O. Breinbjerg, and N.A. Mortensen. Wireless energy transfer through non-resonant magnetic coupling. *Journal of Electromagnetic Waves and Applications*, 24:1587–1598(12), July 2010.

[73] Aycan Erentok and Ole Sigmund. Topology Optimization of Sub-Wavelength Antennas. *IEEE transactions on antennas and propagation*, 59(1):58–69, 2011.

[74] N. Olhoff, M. P. Bendsøe, and J. Rasmussen. CAD-integrated structural topology and design optimization. In *Shape and layout optimization of structural systems and optimality criteria methods*, volume 325 of *CISM Courses and Lectures*, pages 171–197. Springer, Vienna, 1992.

[75] Yu-Deok Seo, Hyun-Jung Kim, and Sung-Kie Youn. Shape optimization and its extension to topological design based on isogeometric analysis. *International Journal of Solids and Structures*, 47(11-12):1618 – 1640, 2010.

[76] G. Allaire. *Conception optimale de structures*, volume 58 of *Mathématiques et Applications*. Springer, 2007.

[77] Jianming Jin. *The finite element method in electromagnetics*. John Wiley & Sons, New York, 2002.

[78] Constantine A. Balanis. *Advanced engineering electromagnetics*. Wiley, New York, 2005.

[79] David K. Cheng. *Fundamentals of engineering electromagnetics*. Addison-Wesley, Reading, Massachusetts, 1993.

[80] N. Aage. Personal communication, 2011.

[81] G. Della Valle, T. Søndergaard, and S. I. Bozhevolnyi. High-q plasmonic resonators based on metal split nanocylinders. *Phys. Rev. B*, 80:235405, 2009.

[82] Seungchul Kim, Jonghan Jin, Young-Jin Kim, In-Yong Park, Yunseok Kim, and Seung-Woo Kim. High-harmonic generation by resonant plasmon field enhancement. *Nature*, 453:757–760, 2008.

[83] Daniel R. Ward, Falco Huser, Fabian Pauly, and Douglas Cuevas, Juan Carlos Natelson. Optical rectification and field enhancement in a plasmonic nanogap. *Nat Nature*, 5:732–736, 2010.

[84] Alexandre Aubry, Dang Yuan Lei, Antonio I. Fernandez-Domnguez, Yannick Sonnefraud, Stefan A. Maier, and J. B. Pendry. Plasmonic light-harvesting devices over the whole visible spectrum. *Nano Letters*, 10(7):2574–2579, 2010.

[85] Alexandre Vial, Anne-Sophie Grimault, Demetrio Macías, Dominique Barchiesi, and Marc Lamy de la Chapelle. Improved analytical fit of gold dispersion: application to the modeling of extinction spectra with a finite-difference time-domain method. *Phys. Rev. B*, 71, 2005.

[86] COMSOL Inc.

[87] F. Di Maio, P. Rem, S. Serranti, and G. Bonifazi. The W2Plastics Project: Exploring the Limits of Polymer Separation. *The Open Waste Management Journal*, 3:90–98, 2010.

[88] V. Murariu, J. Svoboda, and P. Sergeant. The modelling of the separation process in a ferrohydrostatic separator. *Minerals Engineering*, 18(4):449–457, 2005.

[89] V. Murariu and J. Svoboda. The effect of magnetic susceptibility on the motion of particles in a ferrohydrostatic separator. *Magnetic and Electrical Separation*, 11:51–61, 2002.

[90] E. J. Bakker, P. C. Rem, and N. Fraunholcz. Upgrading mixed polyolefin waste with magnetic density separation. *Waste Management*, 29(5):1712–1717, 2009.

[91] D. Lahaye, H. Polinder, and P. Rem. Magnet designs for magnetic density separation of polymers. *The Journal of Solid Waste Technology and Management*, 26:977–983, 2011.

[92] F. Weijmans, E. Bakker, and P.C. Rem. Magnetic density separation of diamonds from gangue. *Environmental Engineering and Management Journal*, 8(4):981–984, 2009.

[93] L. Muchova and P. Rem. Precious metals in municipal solid waste incineration bottom ash. *Magnetic density separation*, 39(9):107–116, 2009.

[94] J.R.A. de Koning, E.J. Bakker, and P. Rem. Sorting of vegetable seeds by magnetic density separation in comparison with liquid density separation. *Seed Science and Technology* , 39(3):593–603, 2011.

[95] B. Hu, F. Di Maio, P. Rem, G. Houzeaux, H. Calmet, and H. Owen. Development of inverse magnetic density separation of polyolefin mixtures. *The Journal of Solid Waste Technology and Management*, 26:968–976, 2011.

[96] S. Serranti, A. Gargiulo, and G. Bonifazi. The use of hyperSpectral imaging for quality control in the MDS-based recycling process of polyolefins. *The Journal of Solid Waste Technology and Management*, 26:952–967, 2011.

[97] P. P. Sylvester and R. L. Ferrari. *Finite Elements for Electrical Engineers*. Cambridge University Press, New York, third edition, 1996.

[98] Personal communication of Domenico Lahaye with Peter Rem and his group at the Delft University of Technology, 2012 .

[99] D. Echeverria, D. Lahaye, L. Encica, E.A. Lomonova, P.W. Hemker, and A.J.A. Vandenput. Manifold-mapping optimization applied to linear actuator design. *Magnetics, IEEE Transactions on*, 42(4):1183 –1186, april 2006.

[100] D. Lahaye, A. Canova, G. Gruosso, and M. Repetto. Adaptive manifold-mapping using multiquadric interpolation applied to linear actuator design. *COMPEL-The International Journal for Computation and Mathematics in Electrical and Electronic Engineering*, 26(2):225–235, 2007.

[101] Anders A. Larsen, Martin Bendsøe, Jesper Hattel, and Henrik Schmidt. Optimization of friction stir welding using space mapping and manifold mapping-an initial study of thermal aspects. *Structural and Multidisciplinary Optimization*, 38(3):289–299, 2009.